Multiport Beamforming System Based on Reconfigurable Waveguide Phased Antenna Array For Satellite Communication Applications

Yifang Wei

A dissertation submitted for the degree of Doctor of Philosophy

Heriot-Watt University

School of Engineering and Physical Sciences

October 2022

Abstract

A multiport K/Ka-band beamforming system based on the reconfigurable waveguide phased antenna array is presented in this thesis. The waveguide structure is used to achieve low loss, wideband performance, and simple installation and maintenance. The antenna array is adopted to compensate for the high propagation loss in higher frequency, which also provided flexible functions for multi-user wireless communication applications.

The reconfigurable waveguide transitions are the most crucial component in this beamforming system to achieve dual linear-polarized/left-handed circular-polarized/right-handed circular-polarized functions at K/Ka-band respectively by using the reconfigurable structure. It provided much better performance in bandwidth compared with the recent dual-band/dual-mode waveguide transitions.

The waveguide antenna and antenna arrays are reconfigurable and replaceable to meet the design purposes and requirements for linear-polarized/left-handed circular-polarized/right-handed circular-polarized functions. The ultra-bandwidth from K-band to Ka-band provided advantages in saving cost and flexible functions due to the waveguide antenna array parts being applicable for both transmitting/receiving systems for K/Ka-band.

This advanced beamforming system could provide many merits such as low loss, wideband, compact structure, high functional flexibility, lower cost, simpler installation, and easier maintenance by using the waveguide reconfigurable. These advantages are indicated by the sufficiently good performance in both the simulated and measured results in this thesis, which demonstrated that this beamforming system design is applicable for wireless communication applications in high frequency, especially for satellite communication applications with separated unlink and downlink systems.

The potential and prospect for a MIMO beamforming system with a multilayer PCB feeding network are also demonstrated from the wideband performance of multilayer SICL power divider and SICL-to-waveguide transitions in this thesis to get a more flexible structure for a MIMO beamforming system and more compact structure.

Acknowledgment

Research Thesis Submission

Please note this form should be bound into the submitted thesis.

Name*:*	Yifang Wei		
School:	School of Engineering and Physical Sciences (EPS)		
Version: *(i.e. First, Resubmission, Final)*	Final	Degree Sought:	PhD in Microwave Engineering

Declaration

In accordance with the appropriate regulations I hereby submit my thesis and I declare that:

1. The thesis embodies the results of my own work and has been composed by myself

2. Where appropriate, I have made acknowledgement of the work of others

3. The thesis is the correct version for submission and is the same version as any electronic versions submitted*.

4. My thesis for the award referred to, deposited in the Heriot-Watt University Library, should be made available for loan or photocopying and be available via the Institutional Repository, subject to such conditions as the Librarian may require

5. I understand that as a student of the University I am required to abide by the Regulations of the University and to conform to its discipline.

6. I confirm that the thesis has been verified against plagiarism via an approved plagiarism detection application e.g. Turnitin.

ONLY for submissions including published works

Please note you are only required to complete the Inclusion of Published Works Form (page 2) if your thesis contains published works)

7. Where the thesis contains published outputs under Regulation 6 (9.1.2) or Regulation 43 (9) these are accompanied by a critical review which accurately describes my contribution to the research and, for multi-author outputs, a signed declaration indicating the contribution of each author (complete)

8. Inclusion of published outputs under Regulation 6 (9.1.2) or Regulation 43 (9) shall not constitute plagiarism.

* *Please note that it is the responsibility of the candidate to ensure that the correct version of the thesis is submitted.*

Signature of Candidate*:*	*Yifang Wei*	Date:	27/10/2022

Inclusion of Published Works

Please note you are only required to complete the Inclusion of Published Works Form if your thesis contains published works under Regulation 6 (9.1.2)

Declaration

This thesis contains one or more multi-author published works. In accordance with Regulation 6 (9.1.2) I hereby declare that the contributions of each author to these publications is as follows:

Citation details	Yifang Wei, Christian Arnold and Jiasheng Hong, "A K/Ka-Band Substrate Integrated Coaxial Line Power Divider for 4-input and 16-output Beamforming Multi-Layer Feeding Network," 2020 IEEE Asia-Pacific Microwave Conference (APMC), 2020, pp. 929-931, doi: 10.1109/APMC47863.2020.9331438.
Author 1	Theory, design, simulation experiments and paper write-up
Author 2/ Author 3	Supervision, paper review and finalization
Signature:	*Yifang Wei*
Date:	27/10/2022

Citation details	Yifang Wei, Christian Arnold and Jiasheng Hong, "Reconfigurable Wideband Linear-Polarized and Dual Left/Right-Hand Circularly-Polarized Waveguide Antennas for Beamforming Antenna array," *2022 16th European Conference on Antennas and Propagation (EuCAP)*, 2022, pp. 1-5, doi: 10.23919/EuCAP53622.2022.9769328.
Author 1	Theory, design, simulation experiments and paper write-up
Author 2/ Author 3	Supervision, paper review and finalization
Signature:	*Yifang Wei*
Date:	27/10/2022

Citation details	Yifang Wei, Christian Arnold and Jiasheng Hong, " K/Ka-Band MIMO Beamforming Phased Antenna Array with Multilayer Substrate Integrated Coaxial Line Feeding Network," 2022 Mediterranean Microwave Symposium
Author 1	Theory, design, simulation experiments and paper write-up
Author 2/ Author 3	Supervision, paper review and finalization
Signature:	*Yifang Wei*
Date:	27/10/2022

Citation details	Yifang Wei, Christian Arnold and Jiasheng Hong, "A K/Ka-Band Reconfigurable Substrate Integrated Coaxial Line to Waveguide Transition Technology," IEEE access, 10, pp. 1–1. doi:10.1109/ACCESS.2022.3184020..
Author 1	Theory, design, simulation experiments and paper write-up
Author 2/ Author 3	Supervision, paper review and finalization
Signature:	*Yifang Wei*
Date:	27/10/2022

Contents

LIST OF FIGURES

9

10

LIST OF TABLES

LIST OF ABBREVIATIONS

TESLA – Advanced Technologies for future European Satellite Applications

WP – Work Package

D1.4 – Deliverable 1.4

ESR – Early Stage Researcher

R&D – Research and Development

SIW – Substrate Integrated Waveguide

SICL – Substrate Integrated Coaxial Line

PCB – Printed Circuit Board

MIMO – Multiple-Input and Multiple-Output

LP – Linear-Polarized

CP – Circular-Polarized

LH – Left-Handed

RH – Right-Handed

Tx – Transmit

Rx – Receive

TE – Transverse Electric

TEM – Transverse Electro-Magnetic

IL – Insertion Loss

RL – Return Loss

BTB – Back-To-Back,

MS – Microstrip

WG – Waveguide

SL – Stripline

SISL – Substrate Integrated Suspended Line

TW – This Work

RWG – Ridge Waveguide

CPW – Coplanar Waveguide

GCPW – Grounded Coplanar Waveguide

AWR – Advancing the Wireless Revolution

CST – CST Studio Suite

HFSS – High Frequency Structure Simulator

ADC – Analog-to-digital converter

DAC – Digital-to-analog converter

LIST OF SYMBOLS

g(x) – The distance between the inner conductive lines and the side vias.

φ – The signal phase shifting between each antenna element.

λ – The wavelength.

θ – The beam angle with respect to the boresight direction.

D – The antenna dimension.

L – Cavity height of the waveguide transition.

Dv – Via diameter of the waveguide transition.

W – Stepped transformer width of the waveguide transition.

d1 – Ridge depth d1 of the waveguide transition.

CHAPTER 1

INTRODUCTION

1.1 Motivation

This project is about the research and development (R&D) into an advanced K/Ka-band beamforming system, which consists of the feeding network based on the planar power dividers, waveguide transitions, and reconfigurable waveguide antennas that can be built for an active phased antenna array with a low profile.

With the rapid development of wireless communication technology, people change their interest in research from narrow and crowded low-frequency ranges to higher frequencies. In recent years, with the evolution of 5G technology, the requirements move on towards millimeter-wave. The performance of conventional planar circuit technologies may not satisfying on millimeter waves due to potential radiation loss and surface wave loss. Substrate-integrated waveguide (SIW) and substrate-integrated coaxial line (SICL) are two recent technologies to solve the problem [1] [2] [3]. Compared to the drawbacks of SIW on narrowband, SICL is a better choice for compact broadband applications in wireless communication due to its wideband and smaller size [2] [3]. At low frequencies such as S or C bands, some designs of T-junction power dividers have been published [4], however, they are not applicable on millimeter waves for all designs. There are many problems caused by the limitation of the material and the minimum size of fabrication. At a design point for this project, the power divider feeding network is used for a beamforming antenna array which has the requirement of a working frequency range in K and Ka-band around 17 GHz to 21 GHz and 27 GHz to 31 GHz. To that end, a novel T-junction 3-dB power divider is designed which has a working frequency range of 69% under 20 dB of return loss and provides equal amplitude and equal phase splitting. The power divider design is also applicable to the microstrip structure, whose dimensions will largely depend on the thickness and dielectric constant of the dielectric layer. A stepped impedance transformer is used to increase the bandwidth [4]. Open circuit stub transformer is used to improve the performance of impedance matching in the circuit which has been

presented in many publications in recent years [5] [6]. In this design, an open circuit stub is used to improve in-band impedance matching performance. It provides a novel way to adjust matching frequency which is helpful in wideband applications. The power divider is used as a feeding network for the beamforming antenna array to equally distribute the signals of each element. The actual beamforming can be achieved by connecting the phase shifter and amplifier at the bottom of the PCB network.

In modern satellite communications beamforming technologies, the system needs dual-band operation frequencies for separated uplink and downlink [7], to reduce the influence and interference between them. Active phased antenna arrays are usually used for the "user beam" which serves the end-users and mobile devices. The Rx and Tx are also usually frequency separated, which could also achieve a better downlink margin [8]. Especially the desirable beamforming network system will have inter-satellite links and gateway beams.

In a beamforming system, compared with the coaxial interconnections and transitions to the phased antenna array in a beamforming system, the waveguide transitions have merits in their simple installation and maintenance, which is also popular in RF communication applications for their low loss, wideband performance, and simple structure [9-12]. Therefore, SICL-to-waveguide transition designs are very potential for a multilayer MIMO beamforming technology, especially in satellite communication applications to achieve more flexible functions. The microstrip-to-waveguide transitions developed in this project will also provide wideband performance which will be promising for a beamforming system with a microstrip feeding network. Some microstrip-to-waveguide transitions are designed with good insertion loss and compact structure [9-11]. To be more applicable for a high-frequency multilayer network, some articles about SICL-to-waveguide and Substrate Integrated Suspended Line (SISL)-to-waveguide structures transition designs demonstrated their wideband performance and low loss [13-14].

To achieve dual K/Ka-band operation performance in a satellite communication beamforming system, some dual-band designs are presented in recent years [15-16], which commonly sacrifice the bandwidth and performance to achieve dual-band operations. Furthermore, some of the dual-band waveguide transition designs have operation frequency range limitations [16]. The motivation of this project is to develop

waveguide transitions at K/Ka-band (20GHz/30GHz). For this purpose, the two types of reconfigurable SICL-to-waveguide transitions and microstrip-to-waveguide transitions with two operation frequency modes (K/Ka-band) respectively are designed, which will provide some promising solutions to achieve better wideband performance both for the K/Ka-band separated Rx and Tx, instead of designing two whole systems for Rx and Tx respectively with different dimensions.

These two kinds of SICL-to-waveguide transitions and microstrip-to-waveguide transitions have the same waveguide dimension for the same operation mode, furthermore, the two K/Ka-band modes waveguides will share the same PCB feeding network in beamforming applications. It only needs to easily install or replace the metallic waveguide parts by using screws to achieve K/Ka-band (Tx/Rx) operation modes switching, which will benefit to save cost, simplify the installation and maintenance, and provide flexible functions. The feeding network in PCB is connected by the waveguide transitions with the waveguide antenna array. The waveguide antenna array could be easily installed and replaced on waveguide transitions by using screws.

For a beamforming system, a linear-polarized antenna array and a circular-polarized antenna array have their advantages respectively. Some beamforming designs benefit to use the linear-polarized (LP) antenna on its better cross-polar isolation, lower cost, simpler structure, and lower profile [17]. For satellite communications, the circular-polarized (CP) antenna array has its advantages in terms of polarization mismatch and multi-path interference [18]. Therefore, depending on the different design purposes and requirements, the waveguide transitions and LP/CP waveguide antenna arrays are reconfigurable and replaceable to achieve highly flexible functions. All the waveguides share the same feeding network in the PCB, which is easily installed and connected by screws.

The reconfigurable antenna and dual LH/RH CP waveguide antenna designs are popular recently for their multiple functions and flexibility in application [19-20]. The triangular-shaped slot or stepped transformer is adopted in some dual LH/RH CP waveguide antenna designs [19-20] with around 10% wideband operation performance. However, the beamforming system antenna array is desired to achieve operation frequencies both at 20 GHz and 30 GHz respectively. It will need two waveguide antenna arrays with different antenna dimensions unless the waveguide antenna could

23

achieve bandwidth over 40% (20 GHz-30 GHz). In this project, both the reconfigurable linear-polarized and dual LH/RH CP waveguide antennas are designed with over 40% operation bandwidth for K/Ka-Band, which will be contributed to cost reduction, simple installation, and maintenance.

To work in different situations and requirements in application, the flexible functions of linear-polarized, LH and RH CP modes could be achieved by the replaceable linear polarized and the dual LH/RH CP waveguide antennas with two alternative waveguide inputs, which will be fed by the same waveguide port from the waveguide transition.

In recent years, beamforming designs with single-layer feeding networks have been demonstrated in some articles [17] [21-22] with advantages in their simple structure and lower cost. However, for a massive MIMO beamforming system, the multilayer feeding network is promising to achieve multiple inputs and outputs to provide flexible functions and multiple beams.

1.2 Aims and Objectives

Following the motivation, the aim and objectives of the dissertation are to design a beamforming system with a wideband performance at K/Ka-band for satellite communication applications. There are some tasks to achieve this target:

- K/Ka-band power divider with wideband performance.

- K/Ka-band wideband beamforming feeding networks based on wideband power dividers.

- Reconfigurable waveguide transitions from feed lines in PCB to the waveguide structure which could provide wideband performance at K/Ka-band.

- Reconfigurable waveguide antennas and antenna arrays for LP/LHCP/RHCP operations which could work at K/Ka-band.

- Multiport beamforming system based on the wide-band feeding network, reconfigurable waveguide transitions, reconfigurable waveguide antenna arrays, and phase and gain control section.

1.3 Organization

This thesis is formed into 8 chapters. Following the Chapter 1 introduction, some information about the basic theory, background, and development is included in the review in Chapter 2.

Chapter 3 presents the designs of the wide-band T-junction power divider in single-layer microstrip structure and multilayer SICL structure. The open stub circuit structure is adopted to help the impedance matching and controlling to achieve the required operating frequency range.

Chapter 4 demonstrates the beamforming feeding network designs in the multilayer SICL structure, which is based on the wideband power divider designs from Chapter 3. Moreover, the embedded PCB resistor technology is mentioned in this Chapter to demonstrate its potential for the multilayer SICL-loaded power divider with better isolation.

In this beamforming system design with K/Ka-band modes based on the reconfigurable structure, the waveguide transition designs in Chapter 5 is a very critical component to achieve reconfigurable operation in K/Ka-band. Both the simulated and measured results are presented in this chapter to demonstrate its wideband dual modes operating performance.

The reconfigurable wideband waveguide antennas for linear-polarized/left-handed circular polarized/right-handed circular polarized operations are presented in Chapter 6, which are potential and promising for a waveguide antenna array in a multiport beamforming system application.

Chapter 7 includes the design of a beamforming system sample based on the 2×2 reconfigurable LP/LHCP/RHCP waveguide antenna arrays and the 2×2 K/Ka-band reconfigurable waveguide transition arrays to show the function flexibility. The

measured far-field patterns and s-parameters are illustrated in Chapter 7 to demonstrate the performance.

The last chapter is the conclusion and future work about my research.

CHAPTER 2

FUNDAMENTAL THEORY & LITERATURE REVIEW

2.1 Power Divider

2.1.1 Transmission Line and Open-stub Circuit

For a lossless transmission line, the propagation constant is purely imaginary, $\gamma = j\beta$, hence, the input impedance of a lossless transmission line is [23]:

$$Z_{in}(l) = Z_0 \frac{Z_L + jZ_0 \tan(\beta l)}{Z_o + jZ_L \tan(\beta l)}, \tag{1}$$

where $\beta = \frac{2\pi}{wavelength}$, Z_0 is the characteristic impedance, Z_L is the load impedance and l is the impedance measured distance.

The open-circuited stub and short-circuited stub are commonly adopted in designs to help with impedance matching. The open-circuited stub circuit is an open load, whose input impedance could be given as:

$$Z_{in}(l) = -jZ_0 \cot(\beta l). \tag{2}$$

The short-circuited stub circuit is a shorted load, whose input impedance could be given as:

$$Z_{in}(l) = jZ_0 \tan(\beta l). \tag{3}$$

2.1.2 T-junction Power Divider

The power divider is one of the most widely used basic components in high-frequency applications to split power from one input to several or combine the power from several inputs to an output, which is also the basic unit of the feeding network in a beamforming system.

The T-junction power divider is one of the most commonly used basic structure power dividers, considering the transmission line is lossless, the T-junction power divider is also lossless.
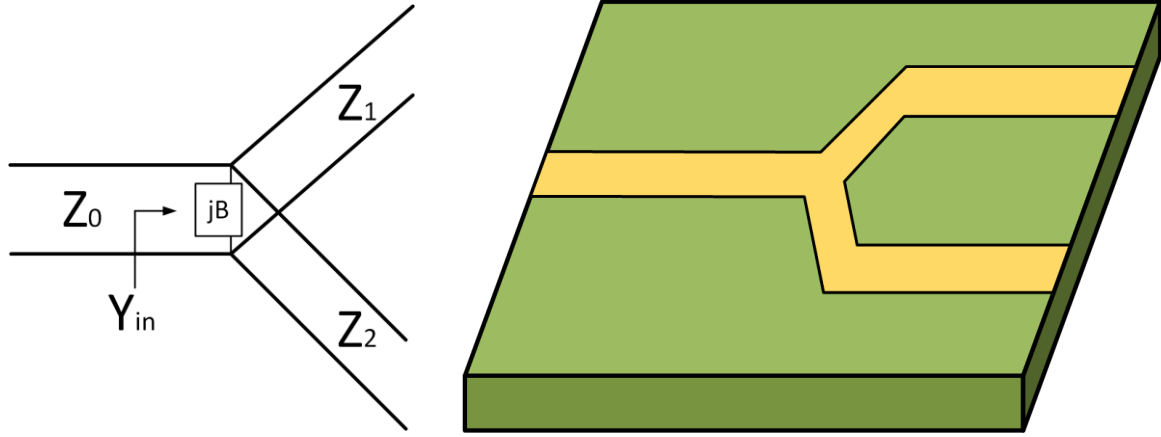
Fig. 2.1 (a) A lossless T-junction power divider and (b) the power divider in microstrip structure [24].

The ideal T-junction equivalent circuit model is shown in Fig. 2.1 (a) and the microstrip T-junction power divider structure is shown in Fig. 2.1 (b) [24]. The junction discontinuity is represented by the susceptance jB at the junction. If B is negligible or compensated, port 1:

$$\frac{1}{Z_0} = \frac{1}{Z_1} + \frac{1}{Z_2} \tag{4}$$

The input impedance at port 1 Z_{in} is given by:

$$Z_{in} = Z_1 || Z_2 = Z_0 \tag{5}$$

Hence, looking at the input, the input impedance is equal to Z_0, however, looking at the outputs, the input impedance is not equal to Z_0. At the same time, the isolation between the two outputs is not good. Therefore, when the T-junction power divider is used to combine the power from two inputs to an output in a feeding network, it needs to keep the same phase and amplitude.

2.1.3 Wilkinson Power Divider

Compare to the T-junction power divider, the Wilkinson power divider is a lossy 3-port network with all ports matched, and with good isolation between two outputs.

The equivalent circuit model of the Wilkinson power divider and its microstrip structure is shown in Fig. 2.2 (a) and (b).
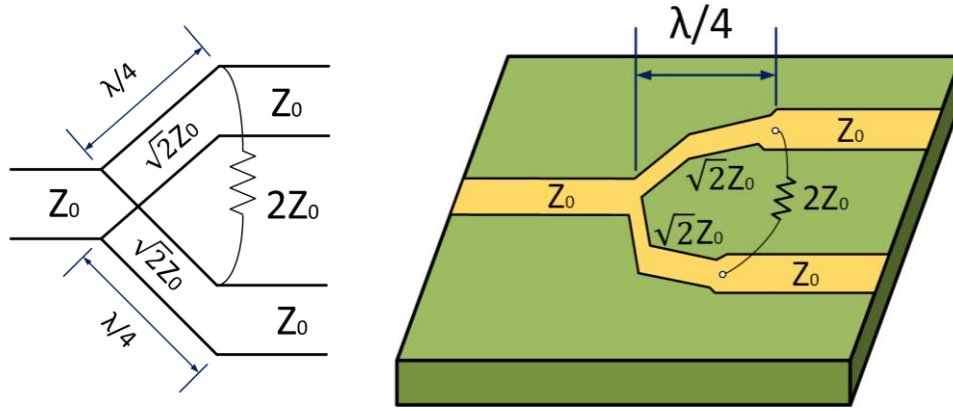
Fig. 2.2 (a) The equivalent circuit model of the Wilkinson power divider and (b) and its microstrip design structure [24].

The quarter-wavelength transformers with the impedance of $\sqrt{2}Z_0$ and isolation resistor with an impedance of $2Z_0$ between two outputs are adopted in the Wilkinson power divider to provide good isolation, which has the advantages of low cost and simple design and manufacture [24].

2.3 Microstrip and SICL Structure

2.3.1 Transmission Line Analysis

A transmission line is the basic passive component for all microwave devices and designs, microstrip structure is one of the most popular planar transmission line structures. It is widely used in single-layer transmission lines and feeding networks due to it is easy to design and manufacture a microstrip structure with the advantages of simple structure, low fabrication cost and compact structure to be integrated [25].

Fig. 2.3 (a) demonstrated the structure of a microstrip line which consists of a top metal line, a middle dielectric layer, and a bottom ground layer. Fig. 2.3 (b) illustrated the E-field distribution.
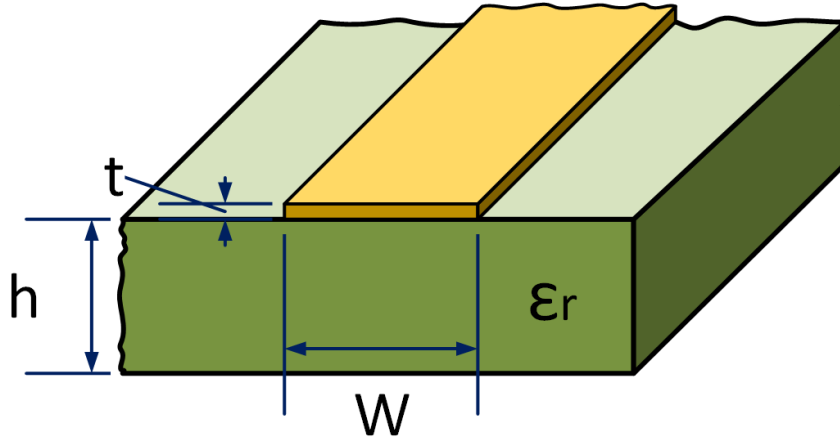
Fig. 2.3 (a) Microstrip line structure [25].
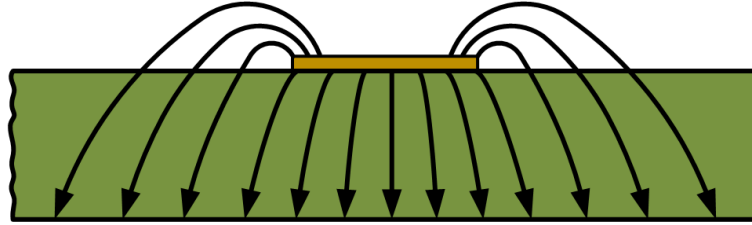
Fig. 2.3 (b) Side view [25].

2.3.2 Analysis of Microstrip Line Structure

For the microstrip line structure, the characteristic impedance $(Z_0)$the closed-form expressions for effective dielectric constant (ε_{eff}) are given in the following equations [26-27]. The h is the height of the substrate layer, W is the width of the microstrip line structure, n is the free-space impedance with the value of 377 ohms, ε_r is the relative permittivity of the dielectric compared to the free space and Z_0 is the characteristic impedance of microstrip.

When W/h<1 (narrow microstrip transmission line),

$$\varepsilon_{eff} = \left(\frac{\varepsilon_r + 1}{2}\right) + \left[\left(\frac{\varepsilon_r - 1}{2}\right) \times \left\{\left(1 + \frac{12h}{W}\right)^{-\frac{1}{2}} + 0.04\left(1 - \frac{W}{h}\right)^2\right\}\right] \qquad (6)$$

$$Z_0 = \left(\frac{n}{2\pi\sqrt{\varepsilon_{eff}}}\right) ln\left(8\frac{h}{W} + 0.25\frac{W}{h}\right) \qquad (7)$$

When W/h≥1 (wide microstrip transmission line),

30

$$\varepsilon_{eff} = \left(\frac{\varepsilon_r + 1}{2}\right) + \left[\left(\frac{\varepsilon_r - 1}{2}\right) \times \left\{\left(1 + \frac{12h}{W}\right)^{-\frac{1}{2}}\right\}\right] \qquad (8)$$

$$Z_0 = \left(\frac{n}{\sqrt{\varepsilon_{eff}}}\right) \times \left[\frac{W}{h} + 1.393 + 0.677\ln\left(\frac{W}{h} + 1.444\right)\right]^{-1} \qquad (9)$$

2.3.3 Substrate Integrated Coaxial Line (SICL) structure

To meet the requirement of a wide operating frequency band in microwave and millimeter-wave applications, the SICL is a popular structure with wideband performance, low insertion loss, and compact structure recently [3][28-30].

Compared to other structures which are widely used in microwave applications, such as microstrip, coaxial line, stripline, and substrate integrated waveguides (SIW), SICL has the advantages of wideband operating frequency performance, low interference, and is suitable for integration simultaneously.

The shielded structure is adopted in the SICL structure to avoid interference between lines especially when the design is compact and integrated, moreover, to avoid the distortion of the propagating signal, the propagation of the fundamental mode should be not dispersive [3].

The microstrip line is not shielded and has radiation loss issues and cross-talk problems. The coaxial line is shielded and not dispersive but not suitable for integration in PCB design. The stripline is similar to the SICL structure but is not shielded to cause lateral leakage and cross-talk problems. The recent substrate integrated waveguides (SIW) structure is shielded and suitable for integrated designs, but it is dispersive, therefore, compared with SIW, the SICL line is more suitable for wideband designs and applications [3][29-30].

From Fig. 2.4 the geometry illustrated that the SICL structure is a planar coaxial transmission line that consists of a middle thin metal film sandwiched between two grounded dielectric layers. The two rows of metallic vias around the thin film from the top and bottom ground are used to avoid interference between adjacent lines. Similar to the stripline structure, the propagation mode in the SICL structure is TEM mode.
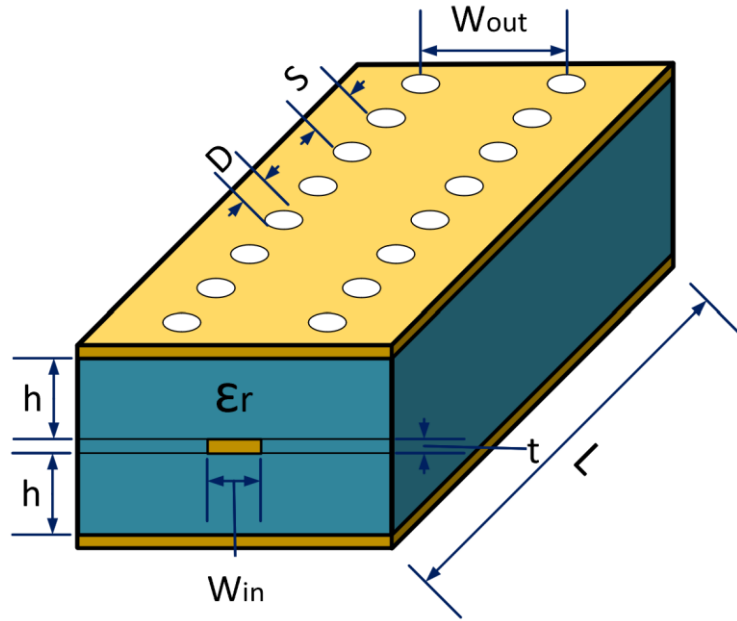
Fig. 2.4 Geometry of a Substrate Integrated Coaxial Line [31].

2.3.4 SICL Structure Analysis

In SICL structure analysis, it could be equivalent to a periodic structure with a combination of stripline and approximate rectangular coaxial line (RCL) [31-32], and Fig. 2.5 shows the top view of the periodic structure of SICL.
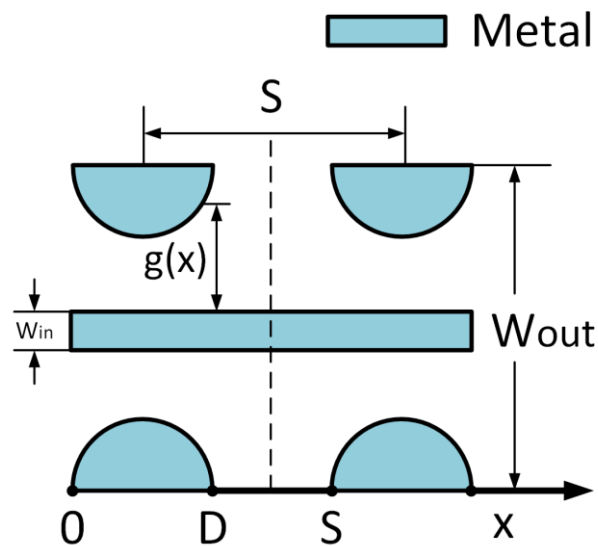
Fig. 2.5 Top view of the periodic structure of a Substrate Integrated Coaxial Line [31-32].

According to the transmission line theory, the general expression for the characteristic impedance of a transmission line is [33]:

$$Z_0 = \left(\frac{\sqrt{R + j\omega L}}{\sqrt{G + j\omega C}}\right),\tag{10}$$

where j is the imaginary unit and ω is the angular frequency. For per unit length, R is the resistance, L is the inductance, G is the conductance of the dielectric, and C is the capacitance.

For a lossless line, R and G are both 0, the imaginary term j also canceled out to make Z_0 become a real expression.

For a stripline, due to the electric and magnetic fields being in a uniform substrate, the characteristic impedance of the transmission line becomes [33]:

$$Z_0 = \left(\frac{\sqrt{\varepsilon_r}}{cC}\right)\tag{11}$$

Where ε_r is the relative permittivity of the dielectric compared to that of free space, C is the capacitance and c is the speed of light in a vacuum.

From Fig. 2.5, x is the position in this periodic structure and the function $g(x)$ is the distance between the inner conductive lines and the side vias. Combined with approximate RCL (0≤x<D) and stripline (D≤x<S), in this SICL unit, $g(x)$ could be written as [31]:

$$g(x) = \frac{w_{out} - w_{in}}{2}\sqrt{\left(\frac{D}{2}\right) - \left(\frac{D}{2} - x\right)^2}\tag{12}$$

When RCL is thin (t < h) [34], it is the same as the general condition in a SICL, the distributed capacitance of the approximate RCL unit can be expressed as:

$$C_{RCL}(x) = 2\frac{\varepsilon_0\varepsilon_r w_{in}}{h} + \frac{4\varepsilon_0\varepsilon_r}{\pi\ln(2)}ln\left[1 + coth\left(\frac{\pi g(x)}{2h + t}\right)\right]$$

$$\cdot\left[\frac{2h + t}{2h}ln\left(\frac{4h + t}{t}\right) + ln\left(\frac{t(4h + t)}{4h^2}\right)\right]\tag{13}$$

The total capacitance of an RCL unit can be written as [31]:

$$C_{RCL} = \int_0^D C_{RCL}(x)dx = 2\int_0^{D/2} C_{RCL}(x)dx \qquad (14)$$

From [35], the capacitance per unit length of the stripline can be calculated as:

$$C_{SL} = \frac{\varepsilon_r \left[\frac{W_{in}}{2h} + C_0/\pi\right] + t}{94.15c} \qquad (15)$$

Where $C_0 = \frac{2h+t}{2h} \ln\left(\frac{4h+t}{2h}\right) - \frac{t}{2h} \ln\left[\frac{t(4h+t)}{4h^2}\right].$

$$C_{SICL} = 2\int_0^{D/2} C_{RCL}(x)dx + C_{SL}(S-D) \qquad (16)$$

The capacitance per unit length of SICL can be expressed as:

$$C = C_{SICL}/S \qquad (17)$$

2.3.5 PCB Embedded Resistor Technology

To improve the low isolation for the T-junction power divider, the loads between outputs are one of the most widely used solutions. However, it is still challenging to design and manufacture the buried resistor on a SICL structure in the dielectric between the top and bottom ground.

The embedded PCB resistor technology is the potential for the SICL structure to develop the loaded power divider to get better isolation [36-37].

To design a SICL power divider with a load, it needs to use embedded resistor PCB technology. For the embedded resistor in PCB, the sheet resistivity will be calculated by:

$$Resistor\ value\ =\ sheet\ resistivity\ \times\ ratio\ of\ element\ length\ to\ width \qquad (18)$$

This means 20 ohms per square ($\frac{\Omega}{square}$) sheet resistance.

$$R = R_S \times \frac{L}{W}\ ;\ where\ \frac{L}{W} = number\ of\ squares\ N \qquad (19)$$
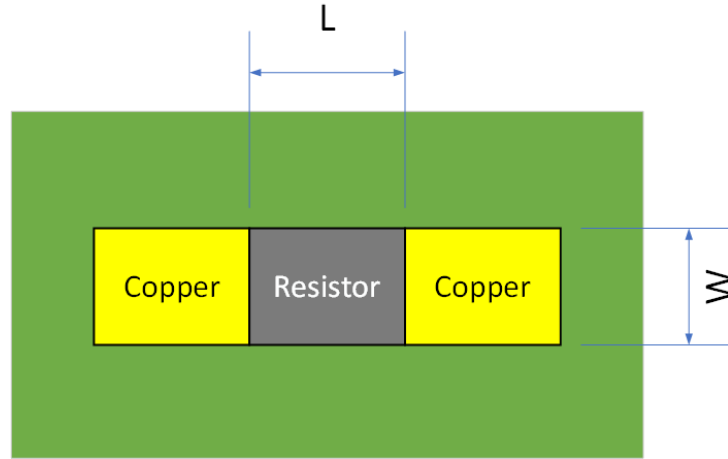
Fig. 2.6. (a) Explanation of the sheet resistivity.
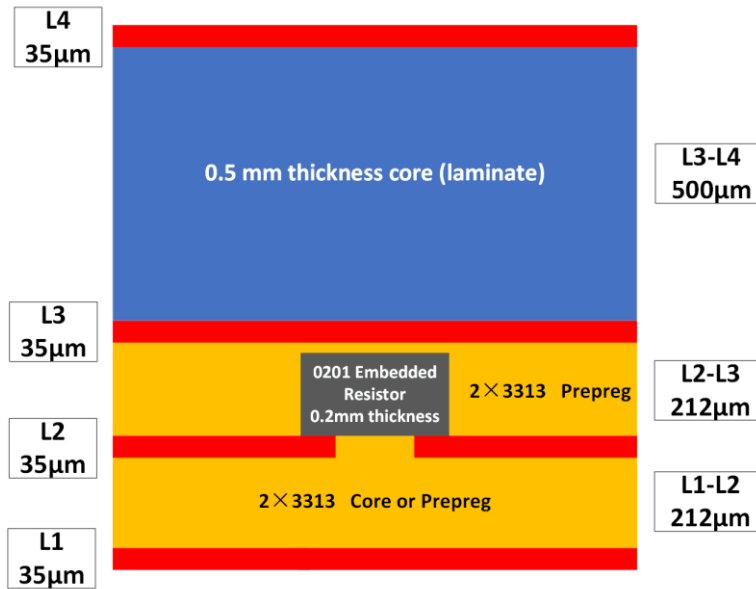
Fig. 2.6. (b) The stackup of the power divider with the embedded PCB resistor.

The explanation of the sheet resistivity is illustrated in Fig. 2.6 (a) and the stackup of the SICL power divider with the embedded PCB resistor is in Fig. 2.6. (b) However, the cost for manufacturing the stackup of the SICL power divider with the embedded PCB resistor is much higher than without the embedded resistor. So, the SICL power divider with an embedded PCB resistor is not cost-effective for the beamforming feeding network. The SICL power divider without the load would be a better choice for a multilayer beamforming system feeding network.

2.4 Waveguide Transitions

For a system in a microwave application, the transition designs are commonly used to connect the planar transmission lines and designs to the devices in the next section. Compared with coaxial interconnections and transitions, waveguide transitions are commonly used due to their advantages in simple installation and maintenance. The waveguide structure transitions also have merits in low loss, wideband performance, and simple structure in RF communication applications [9-12].

There are some horizontal transition designs [9][38-39], which are demonstrated in Fig. 2.7 (a) and (b).

(a)   *(b)*
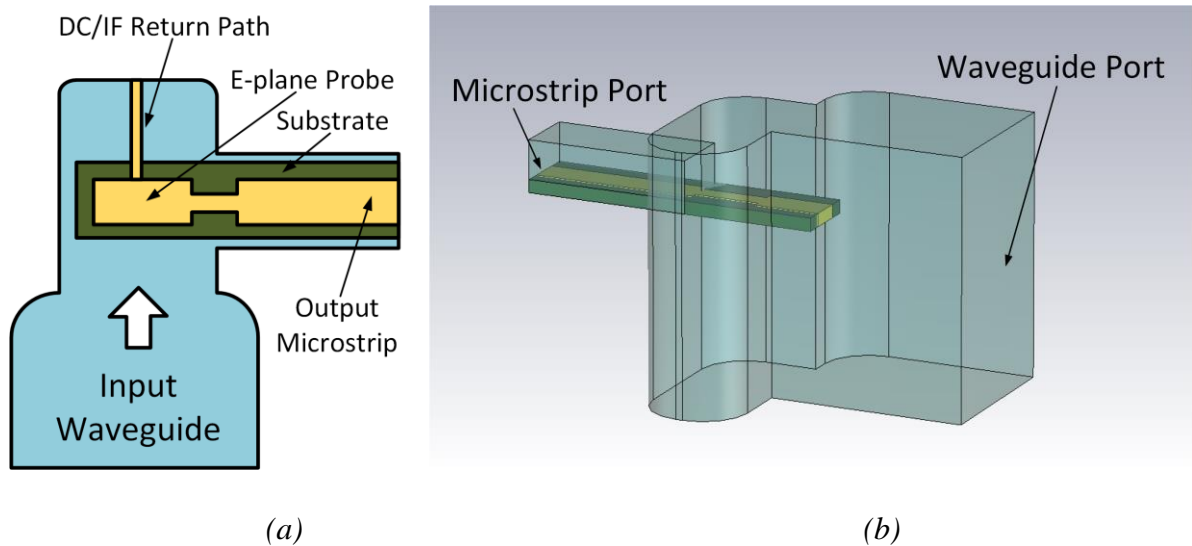
Fig. 2.7 Two horizontal waveguide transition designs in recent years [38-39].

However, for a system device with PCB feeding networks and waveguide devices, the vertical transitions are more suitable for design and installation. Fig. 2.8 (a) illustrated a vertical microstrip-to-waveguide design, which is popular for single-layer feeding networks in a microwave system design with merits in low cost, simple structure, and easy design and manufacture.

Fig. 2.8 (b) showed a vertical SICL-to-waveguide design, which is suitable for a multilayer MIMO feeding network in a microwave system with advantages in more flexible structures and functions in design and smaller plane dimensions. However, it is still challenging to design and manufacture multilayer SICL designs with many kinds of buried vias.
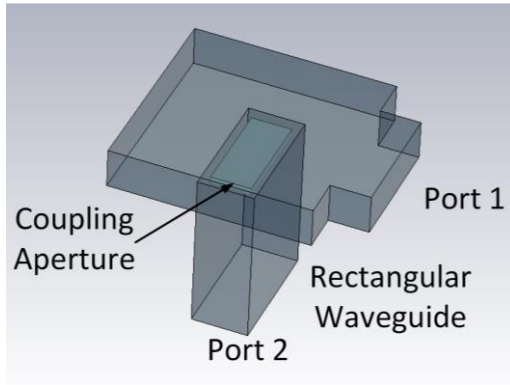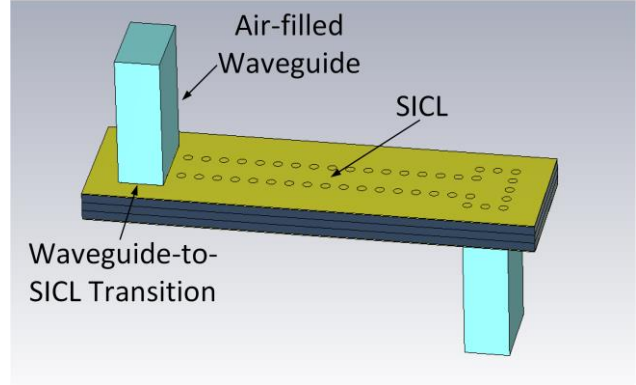
(a)   (b)

Fig. 2.8 (a) A microstrip-to-waveguide transitions design [10] and (b) a SICL-to-waveguide transition design in recent years [13].

To transform the propagation mode and connect from a planar microstrip line or a SICL line to a vertical waveguide structure, the stepped impedance transformers are adopted in the design [40-41] as Fig. 2.9 (a). To analyze these stepped impedance transformers, the configuration of a step junction is shown in Fig. 2.9 (b) and the equivalent circuit model is demonstrated in Fig. 2.9 (c) [41]. The reactive energy of the fringing fields at each waveguide step is represented by susceptance B, The Y_{01} and Y_{02} represent the admittances of stepped transformers.
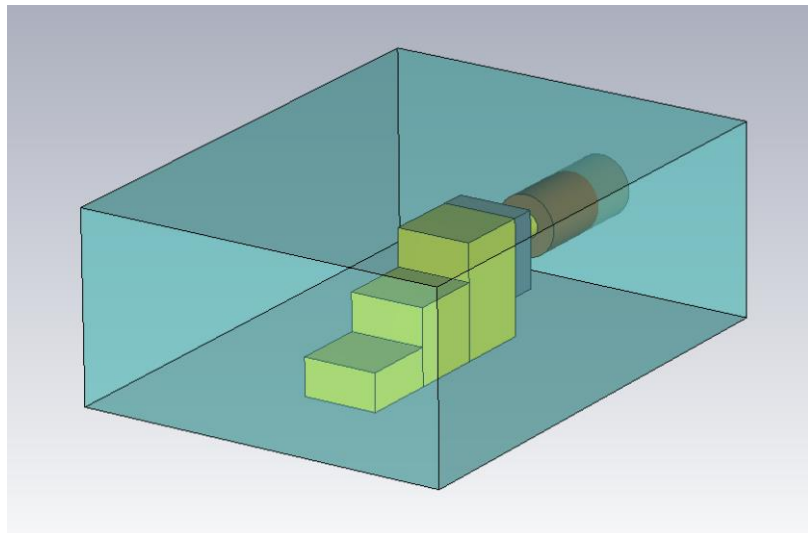
(a)
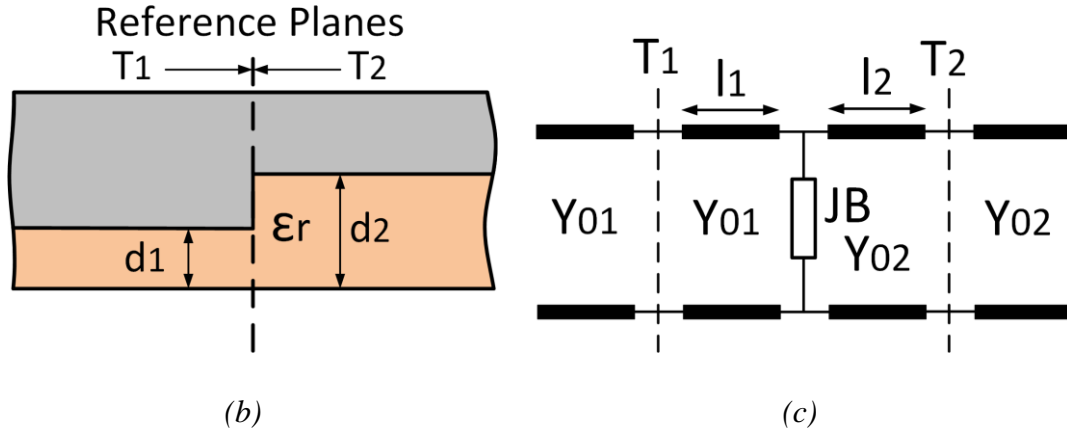
Fig. 2.9 (a) A stepped transformers design in recent waveguide transition [40], (b) the structure of a ridge waveguide step junction [41] and (c) Equivalent circuit [41].

2.5 Antenna Theory

2.5.1 Antenna Description

The antenna is the device to radiate and receives electromagnetic waves, which is shown in Fig. 2.10. There are some important parameters for an antenna design. Many of the parameter definitions are from the IEEE Standard Definitions of Terms for Antennas (IEEE Std 145-1983).
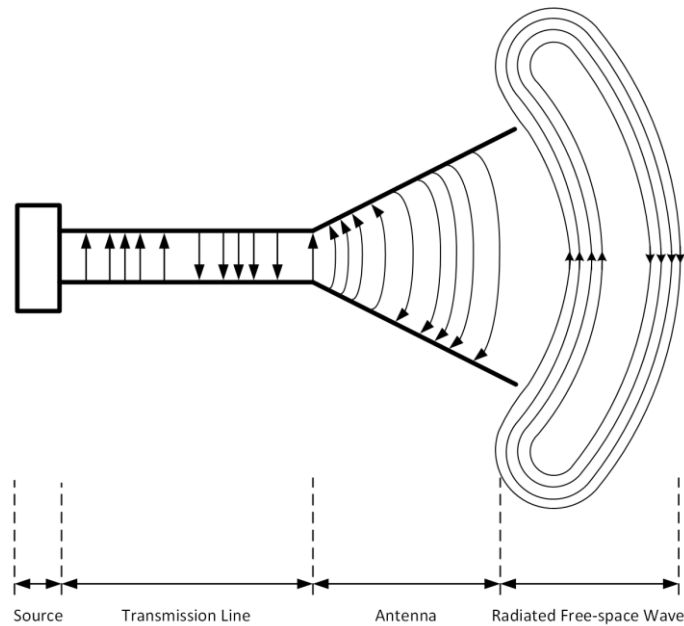
Fig. 2.10 Antenna components description [25].

38

2.5.1.1 Bandwidth

Bandwidth in an antenna design is defined as "the range of frequencies within which the performance of the antenna conforms to a specified standard with respect to some characteristic" [42]. Bandwidth most of the time represents impedance bandwidth, however, polarization bandwidth, directivity bandwidth, efficiency bandwidth, and axial ratio bandwidth are also used in an antenna design.

2.5.1.2 Gain

The gain of the antenna is defined as "The ratio of the radiation intensity in a given direction to the antenna input power that would be produced if the power accepted by the antenna were isotropically radiated" [42]. It could be expressed as:

$$Gain = 4\pi \frac{Radiation\ Intensity}{Antenna\ Input\ Power} = 4\pi \frac{U(\theta,\emptyset)}{P_{in}}\ (dimensionless) \qquad (20)$$

2.5.1.3 Beamwidth

In a radiation pattern, the beamwidth means mainly half-power beamwidth, which is demonstrated in Fig. 2.11 and is defined as "In a radiation pattern cut containing the direction of the maximum of a lobe, the angle between the two directions in which the radiation intensity is one-half the maximum value" [42]. Another commonly used beamwidth is the angle between the first nulls of the pattern, which is called first-null beamwidth.
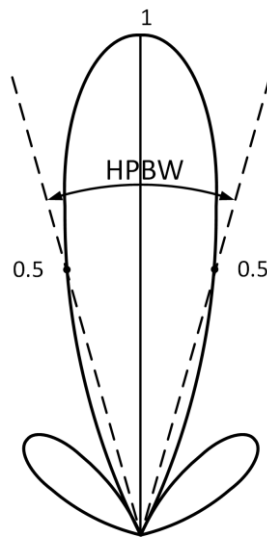
Fig. 2.11 Two-dimensional power pattern of Half-Power Beamwidth [25].

2.5.1.4 Directivity

Directivity is the ratio of the radiation intensity in a particular direction from the antenna to the radiation intensity averaged over all directions. Its average radiation intensity is equal to the total power radiated by the antenna divided by 4π. The direction of maximum radiation intensity is implied if the direction is not specified [42], which could be expressed as:

$$D = \frac{U}{U_0} = \frac{4\pi U}{P_{rad}} \tag{21}$$

The maximum directivity (if the direction is not specified) could be written as:

$$D_{max} = D_0 = \frac{U|max}{U_0} = \frac{U_{max}}{U_0} = \frac{4\pi U_{max}}{P_{rad}} \tag{22}$$

Where D is the directivity (dimensionless), D_0 is the maximum directivity (dimensionless), U is the radiation intensity (W/unit solid angle), U_{max} is the maximum radiation intensity (W/unit solid angle), U_0 is the radiation intensity of isotropic source (W/unit solid angle) and P_{rad} is the total radiated power (W).

2.5.1.5 Radiation Pattern

Radiation pattern means "The spatial distribution of a quantity which characterizes the electromagnetic field generated by an antenna" [42]. The far-field pattern is the radiation pattern obtained in the far-field region.

2.5.1.6 Polarization

Polarization of an antenna is the polarization of the wave transmitted by the antenna, which is a property of transverse waves [42]. In antenna designs, the linear-polarized antenna and circular-polarized antenna are two kinds of antenna operation polarization designs mainly used in applications.

In a linear-polarized antenna, it is a plane electromagnetic wave, which means the electric field or magnetic field is confined to a plane along the direction of propagation.

The circular-polarized wave consists of two perpendicular electromagnetic plane waves with equal amplitude and 90 degrees phase difference. Right-handed circular polarization and left-handed circular polarization are determined by the rotation of the phase-leading component toward the phase-lagging component [25]. If the rotation is clockwise, it will generate a right-handed circular-polarized wave; if the rotation is counter-clockwise, it will generate a left-handed circularly polarized wave. The linear-polarization and circular-polarization are shown in Fig. 2.12.
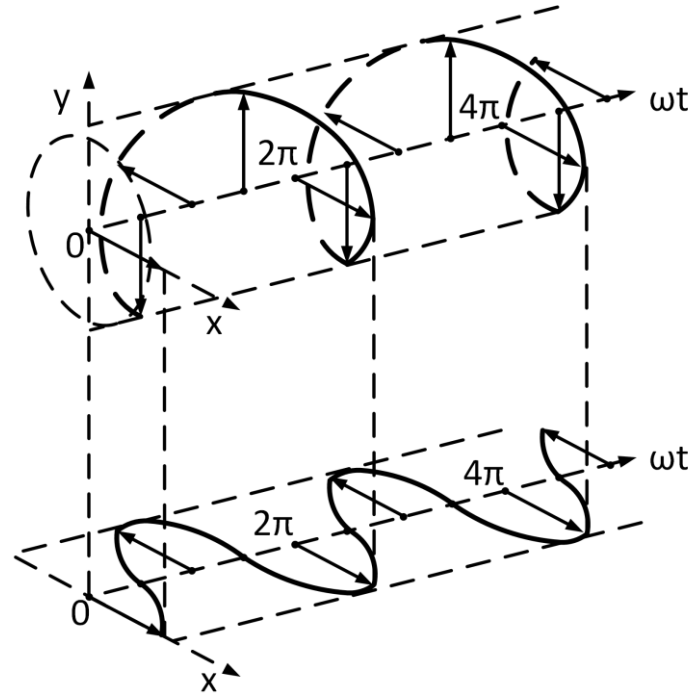
Fig. 2.12 Linear-polarized and circular-polarized wave [25].

2.5.2 Microstrip Patch Antenna

Since the 1950s, the microstrip patch antenna was introduced by Deschamps and became popular to be investigated [43]. Nowadays, it is one of the most widely used antennae in applications, due to its merits in simple structure, easy manufacture, low fabricated cost, and lightweight [43-45]. Many investigations are continuing to focus on its gain, bandwidth, beamwidth, shape, operating frequency, feeding, and reconfigurable structure to develop its performance in high-frequency applications [46-52].

2.5.3 Horn Antenna

Since the 1900s, the horn antenna is widely used to improve the bandwidth and gain [53-54]. The horn structure is easy to be fed by the waveguide and easy to design and construct, which makes it more popular in antenna applications. Combined with the SIW structure, the horn antenna could improve its advantages of compact structure and light weight [55-58]. There are some typical horn structures demonstrated in Fig. 2.13.

(a)   (b)

(c)   (b)
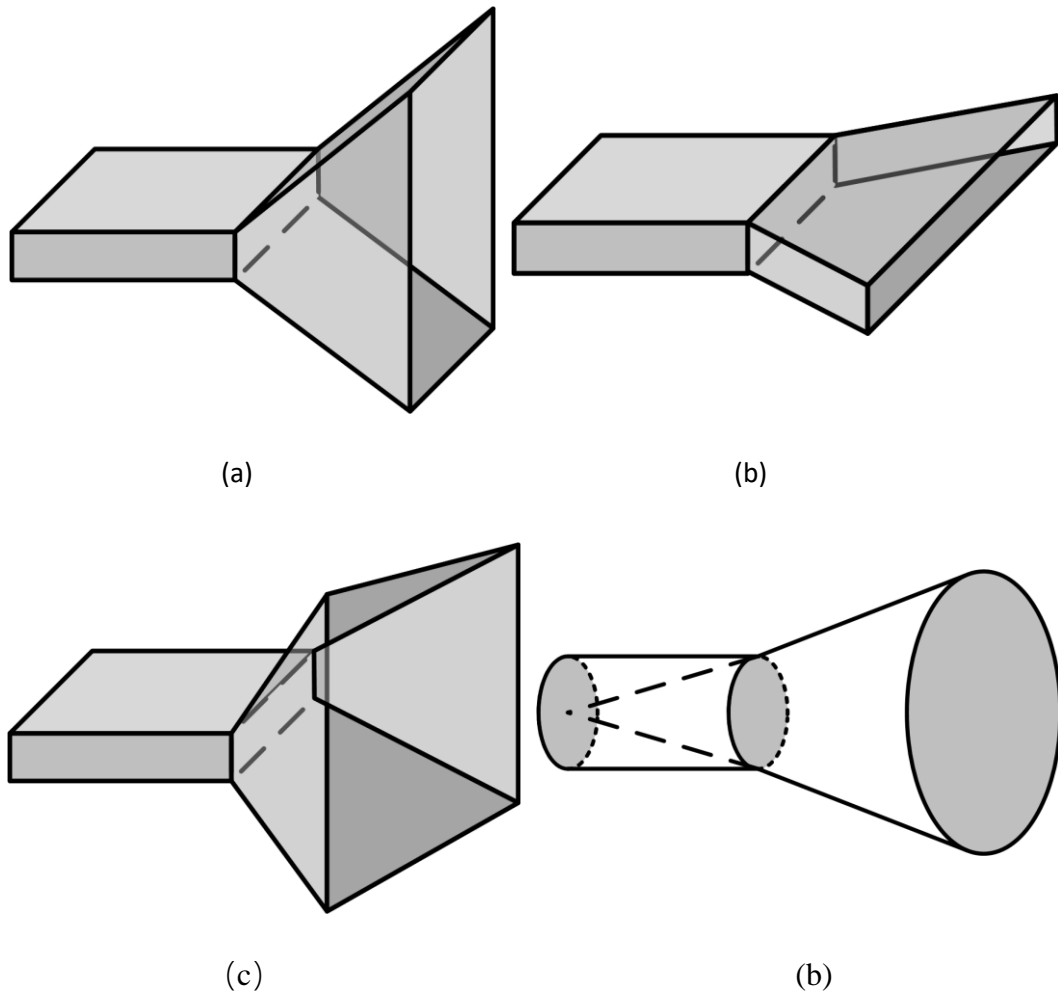
Fig. 2.13 Typical horn antenna structures [25].

2.5.4 Antenna Arrays

Antenna array design is adopted to achieve better gain, to overcome and compensate for the higher propagation loss in high-frequency applications such as 5G technology [59-60].

Antenna arrays are also commonly used in beamforming applications based on phased antenna arrays to change the radiation main lode direction by controlling the phase and gain

of each antenna element, which demonstrated its merits on low profile and electronically steerable array functions compared with the traditional mechanically steered antennas with drawbacks of high maintenance cost and unreliable mechanical positioning and limits [61-63].

2.5.5 Antenna Far-field Pattern Measurement and Antenna Regions.
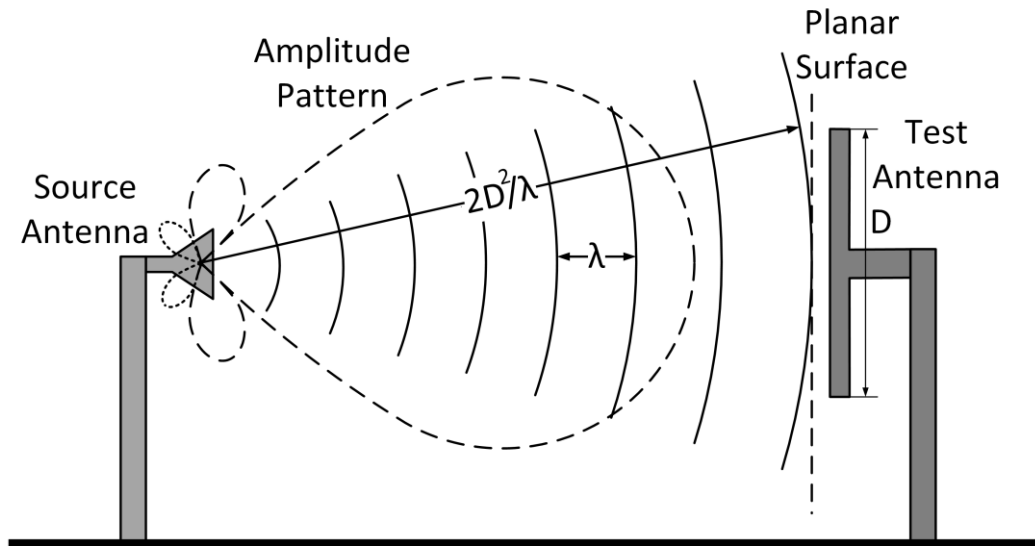
Fig.2.13 Antenna measurement regions [25].

To measure the antenna, there are two commonly used measurements, which are far-field pattern measurement and near-field pattern measurement.

The critical point for both two measurements is the distance between the referenced antenna and the tested antenna. The far-field range starts from [25]:

$$d = \frac{2D^2}{\lambda}$$

(23)

Where d is the Fraunhofer distance, λ is the wavelength of the radio wave and D is the antenna dimension.

2.6 Phased Antenna Array

The phased array technique was designed in 1905 to enhance radio waves transmission in one direction [64], which adjusts the phase and amplitude to control the main lobe to the required direction at specific angles, which is demonstrated in Fig. 2.14.

43
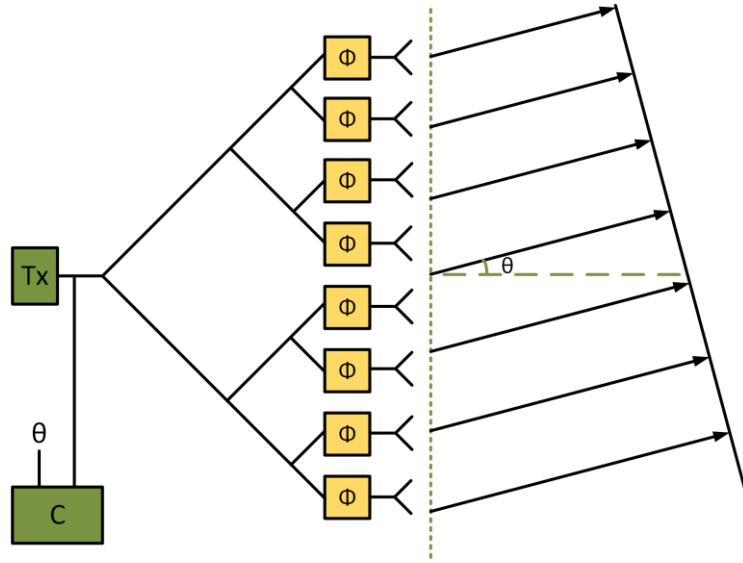
Fig. 2.14 Phased antenna array basic theory [65].

The phased array beam angle could be calculated from the formula [66]:

$$\varphi = \frac{2\pi d sin\theta}{\lambda},$$ (24)

where φ is the signal phase shifting between each antenna element, d is the distance from each element, λ is the wavelength and θ is the beam angle with respect to boresight direction.

There are two kinds of phased arrays commonly used: active phased array and passive active array. In a passive active array, typically use large amplifiers for all the antenna elements and microwave transmit signal [67-68]. However, in an active phased array, each antenna element has a phase shifter and a gain control section (amplifier) [69-71].

2.7 Beamforming Architectures

In a phased array, there are three types of beamforming techniques: analog beamforming [72-74], digital beamforming [75-76], and hybrid beamforming [77-79].

In an analog beamforming system, the beam is controlled by analog phase shifters adjustment. Each antenna element needs a radio-frequency (RF) power divider or combiner, a phase shifter (and a gain control section) to control the phase difference between each element [72-73].

In digital beamforming, the phase and amplitude of each antenna element are digitally controlled by the baseband processing [80]. Digital beamforming could break the limitation placed on the number of beams and antenna elements, moreover, it could provide more possibility and functional flexibility to improve the performance of bandwidth, sidelobe, degrees of freedom, and beam control. However, each antenna element has one RF chain and a digital-to-analog converter (DAC) or analog-to-digital converter (ADC) in the digital beamforming architecture, so, it has drawbacks on high power consumption, high complexity for massive antenna elements and signalling overheads [81].

Combined with the advantages of both analog and digital beamforming architectures, hybrid beamforming becomes a promising solution in beamforming applications. In a hybrid structure, the cost is significantly reduced by reducing the number of RF chains and ADC/DAC, which will also make the power consumption and architecture complexity lower [80-81].

2.8 MIMO Beamforming

The massive MIMO structure is popular in cellular communication applications to serve mobile users simultaneously with a large number of antennas in a beamforming system.

Digital beamforming has merits in flexibility, performance optimality, and adaptability, however, the high cost of a large number of RF chains and ADCs/DACs and high power consumptions make the digital beamforming not suitable to be applied in massive a MIMO system [82]. Therefore analog beamforming and hybrid beamforming are more appropriate to the MIMO structure in applications [82-84].

CHAPTER 3

SICL AND MICROSTRIP POWER DIVIDER

3.1 Basic Structure and Dimensions

A T-junction power divider is a basic building component for RF communication applications and an advanced multiple-input and multiple-output (MIMO) feeding network in an antenna array. Fig. 3.1 shows the designed circuit layout of the proposed K/Ka-band SICL wideband 3-dB power divider with an open-circuit stub, which is sandwiched between the top and bottom ground to avoid unwanted radiation from the feed network as well as to preserve the desired TEM wave propagation. The SICL structure shown in Fig. 3.1 shows the two side rows of metallic vias to reduce interference with resonance in the network. The dimensions of the SICL power divider are shown in Table 1. According to limitations on fabrication, the ideal cross-section structure is replaced by a realistic one for fabrication, the front view of the cross-section with a single circuit layer is illustrated in Fig. 3.2 (a) and (b).

According to the physical structure of the T-junction power divider, when the input has a 50-ohm feed line, the two parallel arms are 100 ohms ideally to be matched 50-ohm feed line for the outputs [4]. Each stepped impedance transformer length is used around 1/8 wavelength and the size of the stepped impedance transformer needs to be adapted for different working frequencies.

The microstrip T-junction power divider has a very similar structure and basic theory as the SICL power divider, the dimensions will largely depend on the thickness and the dielectric constant of the PCB dielectric layer.

Fig. 3.1. Prototype design of the K-Ka band power divider.

Table 1: Dimensions of the K-Ka band power divider (all in millimeters).

L1	L2	L3	L4	L5
0.79	0.93	0.13	0.37	3.16
L6	L7	L8	W1	W2
0.40	1.37	6.71	0.27	0.30
W3	W4	W5	W6	W7
0.54	0.13	0.13	0.19	0.25

3.2 Equivalent Circuit Model

The equivalent circuit model is shown in Fig. 3.3 (a), the junction is ignored due to its negligible influence. To simplify the power divider into an ideal equivalent circuit model, the formula (25) is used to represent every part of the transmission line in the power divider with different widths (impedance Z) and lengths (electrical length θ), which is derived from formula (1).

$$Z_{i+1} = Z_{0,i} \frac{Z_i + jZ_{0,i}\tan(\beta_i l_i)}{Z_{o,i} + jZ_i\tan(\beta_i l_i)}, \tag{25}$$

To improve the reliability of this equivalent circuit model, Matlab software is used to run the calculations based on formulas (2) and (25) and plots the results in Fig.

47

3.3 (b). The demonstrated result plot is very similar to the simulation result of the power divider in AWR and CST software.

For this symmetrical circuit, the two output ports (i.e., ports 1 and 2) exhibit the same magnitude and phase while good matching at the input port over the operating frequencies is required. To that end, an open circuit stub transform is used in this design to help to match impedance while adjusting the matching frequency points.

The relationships between impedance matching and circuit parameters of the open circuit stub or stepped impedance transformer are shown in Fig. 3.4 (a), (b), (c), and (d). The AWR software is used to get simulated results and analysis, which is suitable to build a circuit and network. From the charts, the performance of impedance matching is related to the width (impedance Z) and length (electrical length θ) of the stub. From the formula (2) and (25), the input impedance of the power divider largely depends on the open circuit stubs (impedance Z3, electrical length θ_3) and the stepped impedance transformers (impedance Z2 and Z1, electrical length θ_2 and θ_1) to help the impedance matching at required frequencies.

For the stepped impedance transformers, at the lower frequency matching point, the matching frequency is increased due to the increase of Z1; at the higher frequency matching point, the matching frequency is decreased due to the increase of Z2.

(a)   (b)
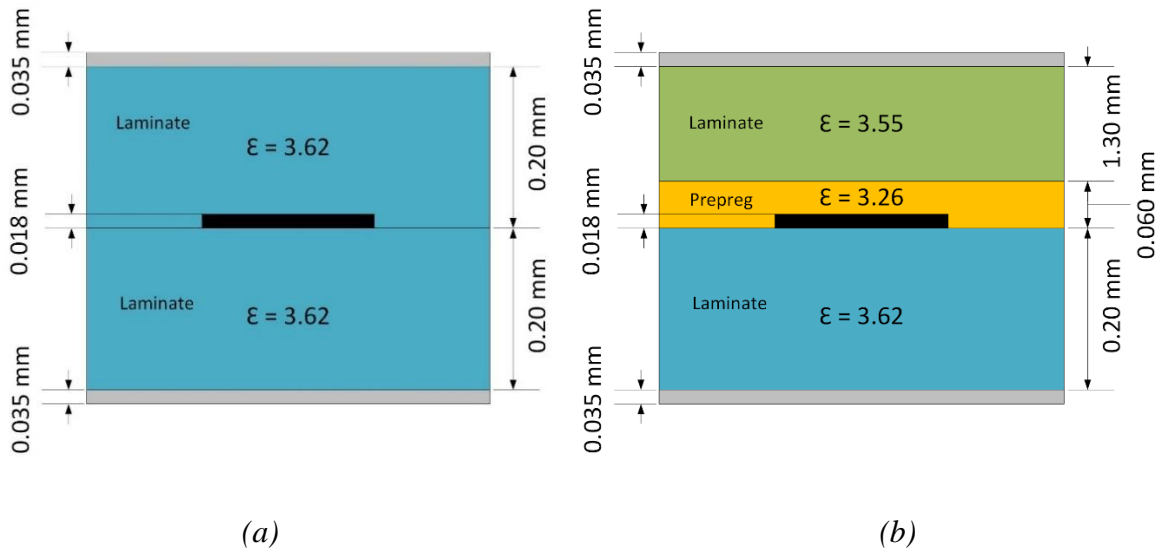
Fig. 3.2. (a) Front view of ideal structure; (b) front view of the structure.

48
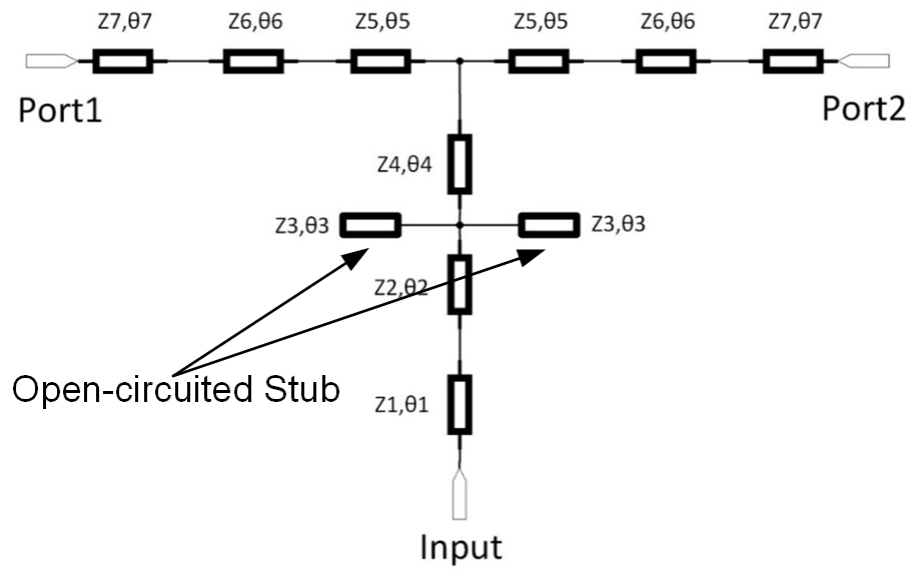
Fig. 3.3. (a) Equivalent circuit model of the power divider.
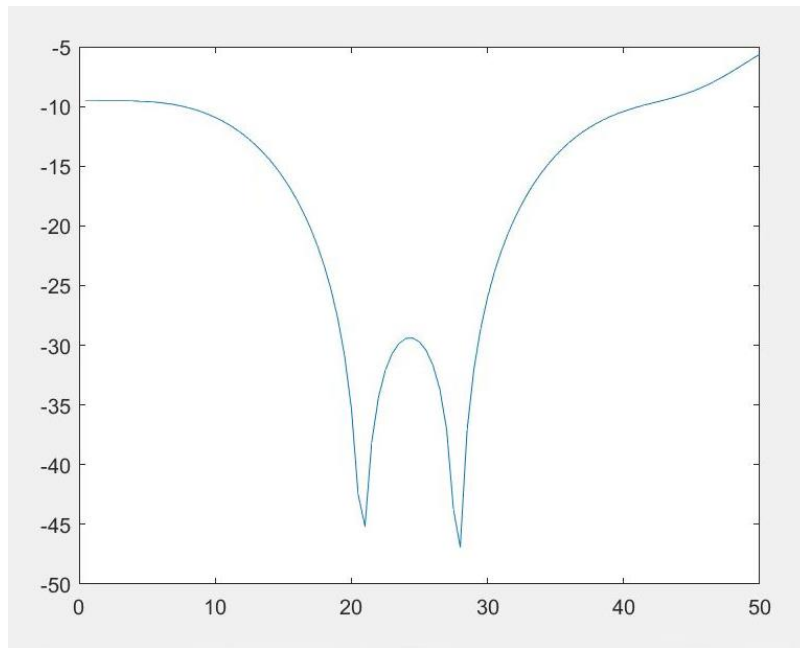
Fig. 3.3. (b) Equivalent circuit model calculation of the power divider based on the formulas (2) and (25).
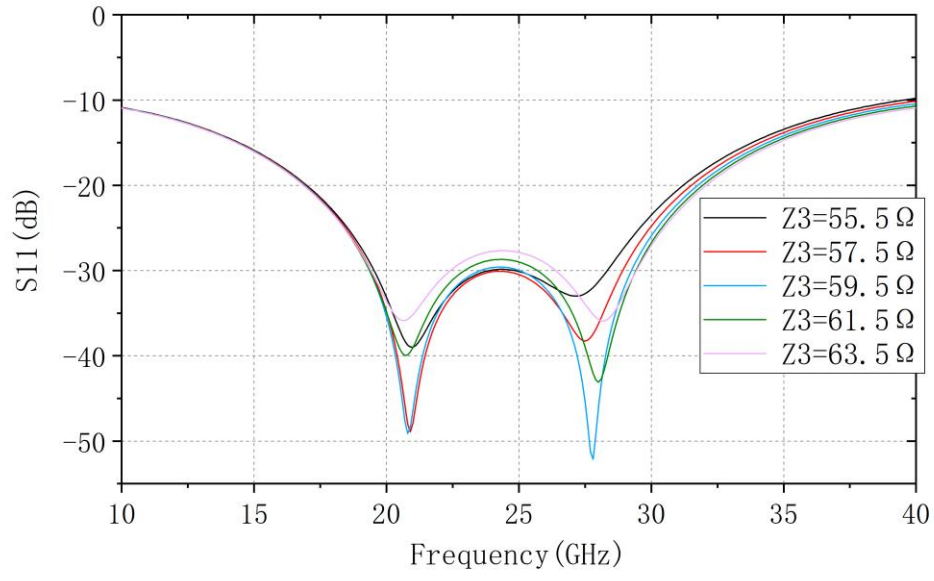
(a)
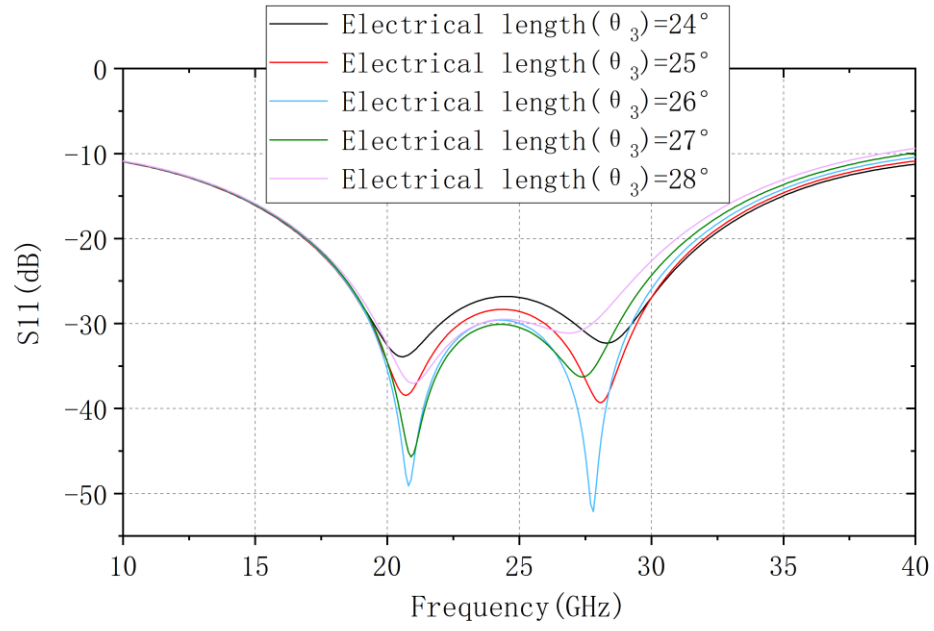
(b)
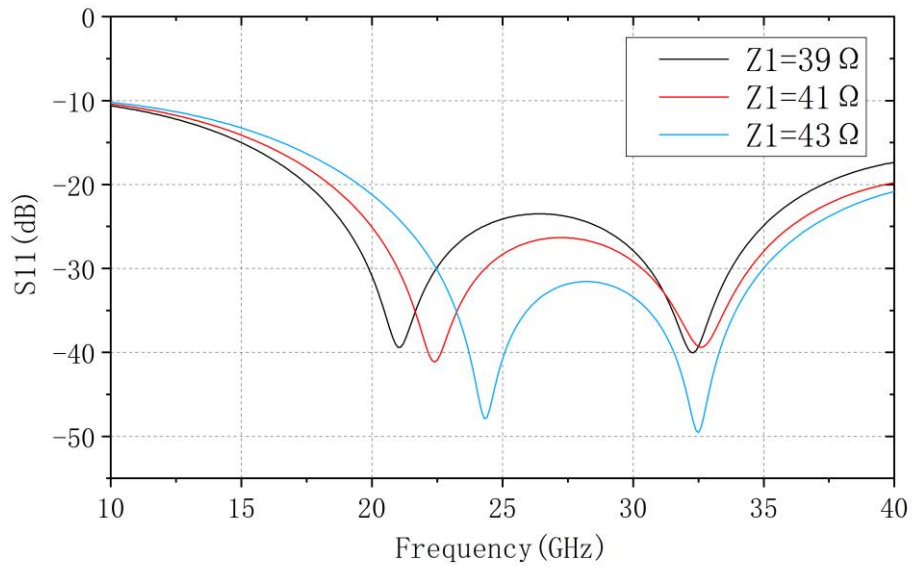
(c)
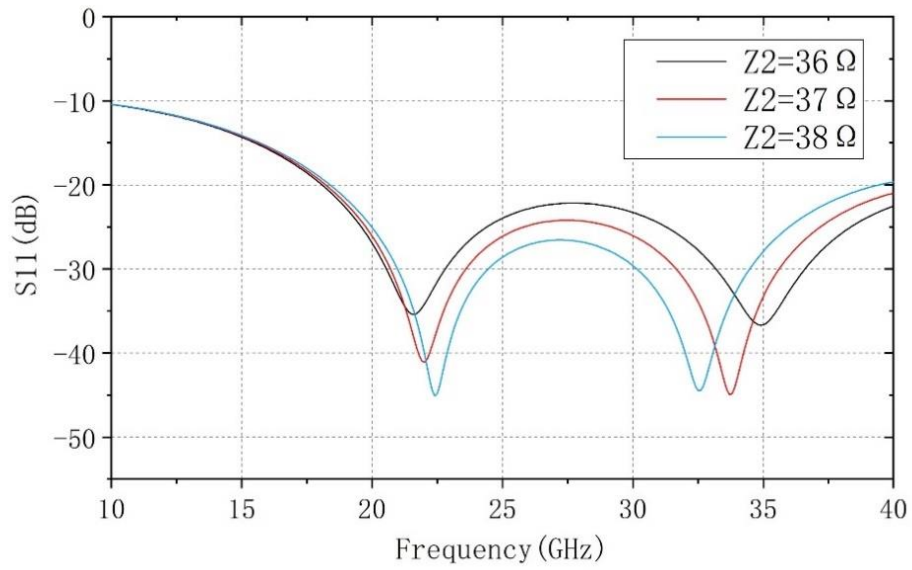
(d)

Fig. 3.4. (a) Equivalent circuit model simulation S11 when (a) the impedance of a stub is changing and (b) the electrical length of the stub is changing (keeps other variables the same at 25 GHz); when (c) Z1 and (d) Z2 of the stepped impedance transformer is changing and adjust the size of the stub to match impedance.

3.3 Results and Discussion

The simulation results are shown in Fig. 3.5, the operational frequency range with return loss better than 20 dB is 69% (16 GHz-33 GHz). In the desired frequency range from 17 GHz to 22 GHz (K transmit band) and 27 GHz to 32 GHz (Ka receive band), the return loss is better than 23 dB. Compared with the simulation result of the power divider matched at the required frequency without open stubs, it illustrated the improved performance for matching at the required frequency by using the open stubs.
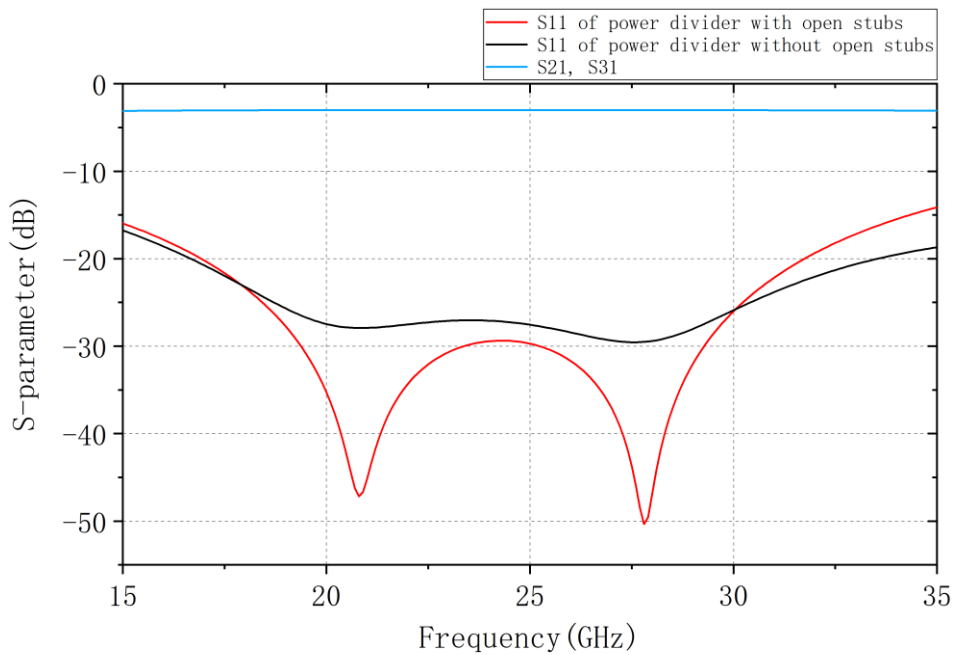
Fig. 3.5. Simulation results on CST software.

To facilitate experimental testing of the designed power divider, three grounded coplanar waveguides (GCPW) are deployed and extended from the power divider ports to the edge test ports on K-connectors.
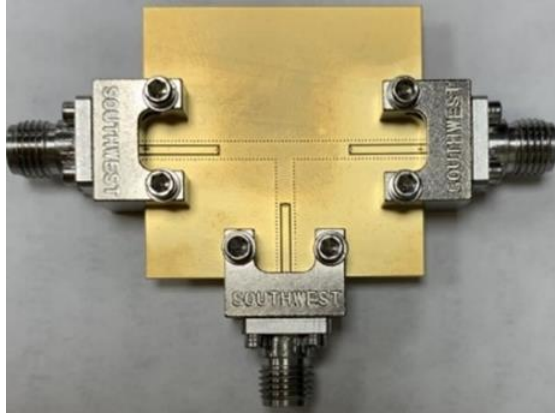
(a)
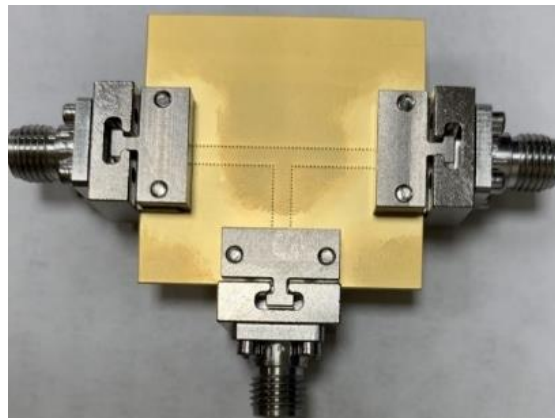
(b)

Fig. 3.6. Fabricated prototype (a) top view and (b) bottom view.
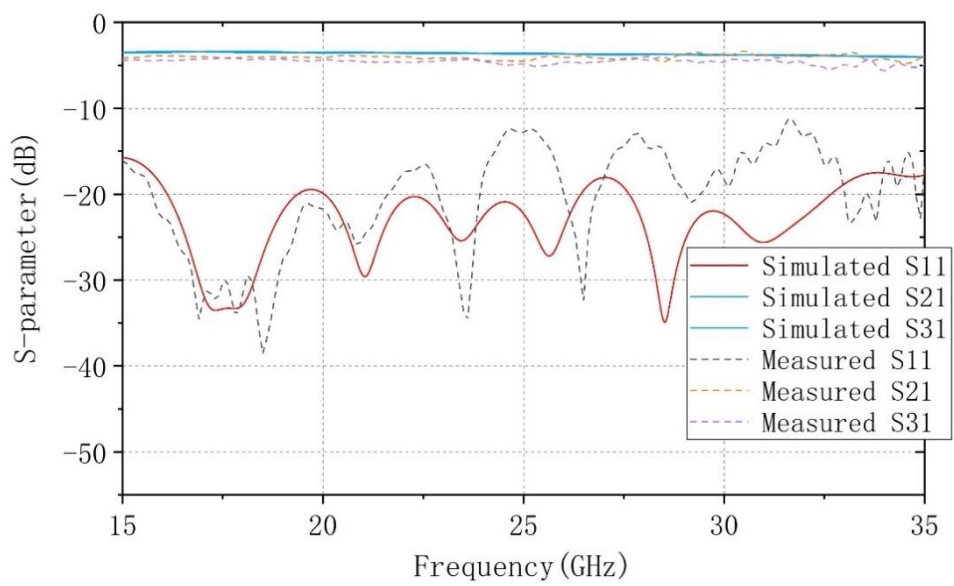
Fig. 3.7. Simulated and measured performance of the test prototype.

The fabricated prototype for the testing is illustrated in Fig. 3.6 with the test port connectors assembled. The measured results are plotted in Fig. 3.7, together with the simulated ones from CST software for comparison. In general, the measured frequency responses by using a PNA-L device demonstrate the desired characteristics of the designed K/Ka-band power divider, at the required operational frequencies K-band and Ka-band, the measured results of return loss and insertion loss are both very similar to the simulated results. Some mismatches may be attributed to the tolerance in fabrication/assembling, such as multilayer PCB thickness difference between design and fabrication due to the manufacturing accuracy, and loss of cables and connectors in measurements at high frequency. Comparing the measured results and simulated results to adjust the designs and planning the measurements more carefully and scientifically will be helpful to get better performance and more similar results to simulations in the next measurement.

CHAPTER 4

SICL BEAMFORMING NETWORK

4.1 Beamforming Network Based on T-junction Power Divider

In a beamforming system, compared with the simple structure of the microstrip feeding network based on the microstrip power divider, the multilayer feeding network based on the SICL power divider is more suitable for a MIMO beamforming structure.

The designed power divider above is deployed as an essential building component for developing a 4-input and 16-output feeding network for antenna arrays for beamforming. The proposed scheme is easily scalable for massive antenna arrays with hundreds of elements and several inputs, the structure of a 16×8 outputs feeding network example is shown in Fig. 4.2 (d). The 4-input-16-output network is a 5-layer design (4 layers with 4 inputs and a top layer for the 16 outputs), each layer has one input. The input signal is split into 16 outputs at each layer. The feeding network combines the corresponding outputs signals at each layer (such as combining signals from output 1 in layer 1, output 1 in layer 2, output 1 in layer 3 and output 1 in layer 4 to one output 1 signal at the top PCB feeding network layer) into 16 final outputs signals at the top PCB layer, which is shown in Fig. 4.1. The combined 16 final outputs are located on the top layer to fit a 4×4 antenna array. For a shorter transmission line to reduce loss of the circuit, appropriate shifting between each layer is a good solution. The top and front views are illustrated in Fig. 4.2 (a), (b), and (c), the example in Fig. 4.2 (d) illustrated the scalable layout of the feeding network with hundreds of outputs. The simulated result of the 4-16 network from AWR software is shown in Fig. 4.3, which illustrated the wideband performance both at required K/Ka-band operational frequencies. The total insertion loss of the feeding network is better than 1.2 dB (the ideal simulated insertion loss is 6 dB due to the power dividers splitting the input signals) and the return loss is better than 15 dB at the required frequency range (17GHz – 22GHz, 27GHz – 32GHz).
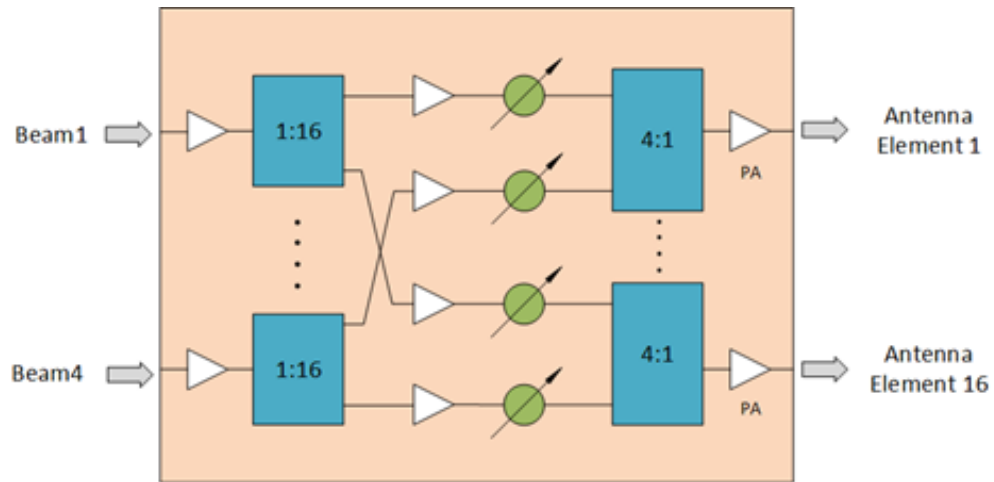
Fig. 4.1. The basic concept of the complex network.

(a)

(b)

Transmission Line
Power Divider
Vias to Top Layer
Vias to upper Layer
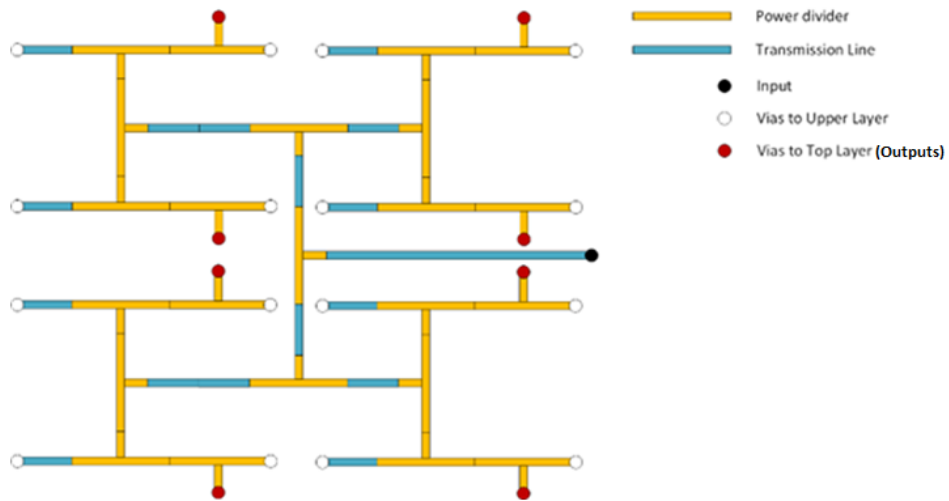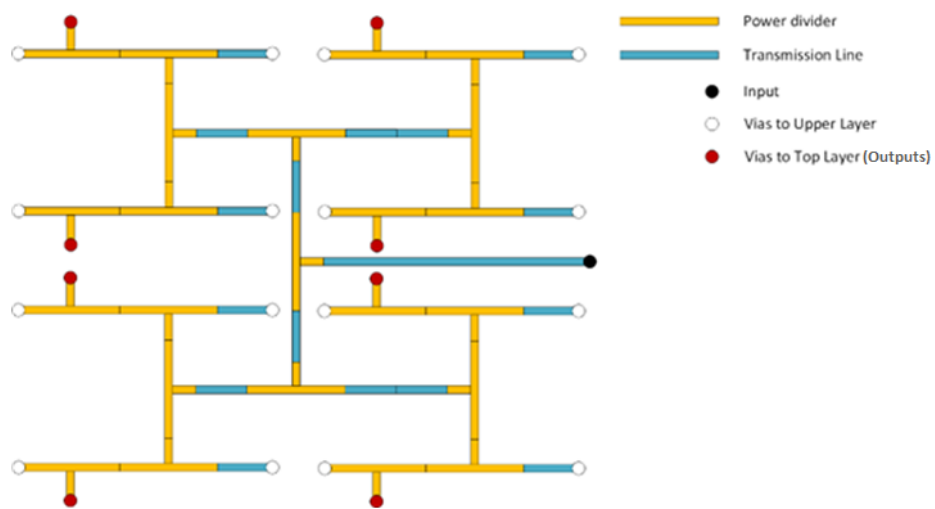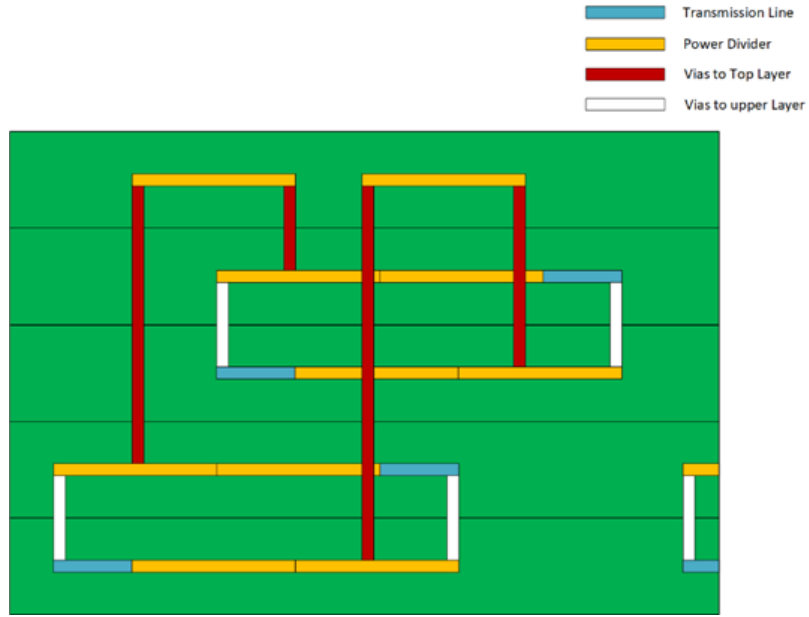
(c)
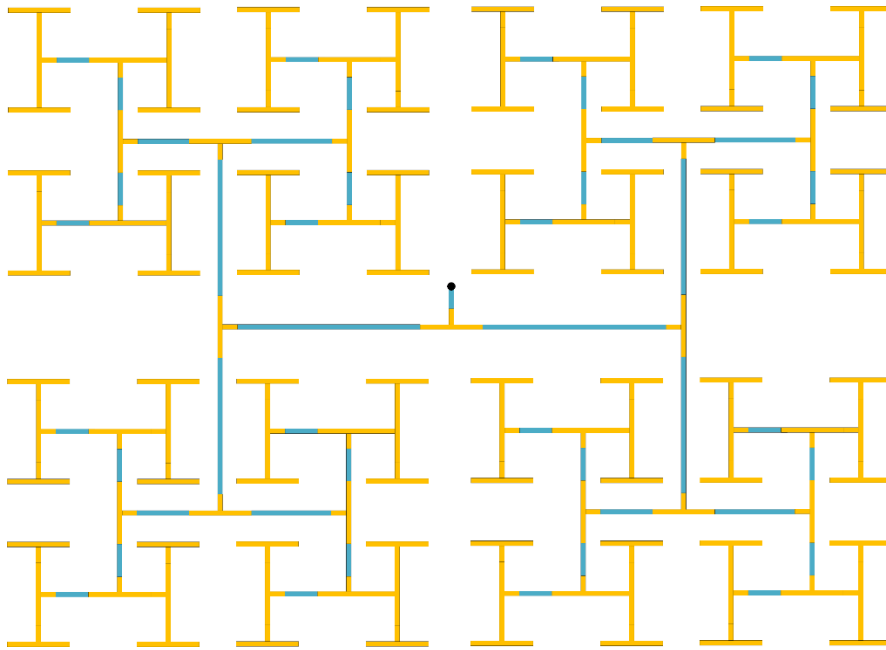
(d)

Fig. 4.2. Proposed 4-input and 16-output multi-layer feeding network (a) Top view of the first layer; (b) Top view of the second layer; (c) Front view of the part of the network; (d) Example of feeding network with 16×8 outputs from the bottom input layer to the layer under top output layer.

Equal-length transmission lines are designed for all corresponding inputs due to the feature of low isolation for the power divider without the resistor between outputs [4].
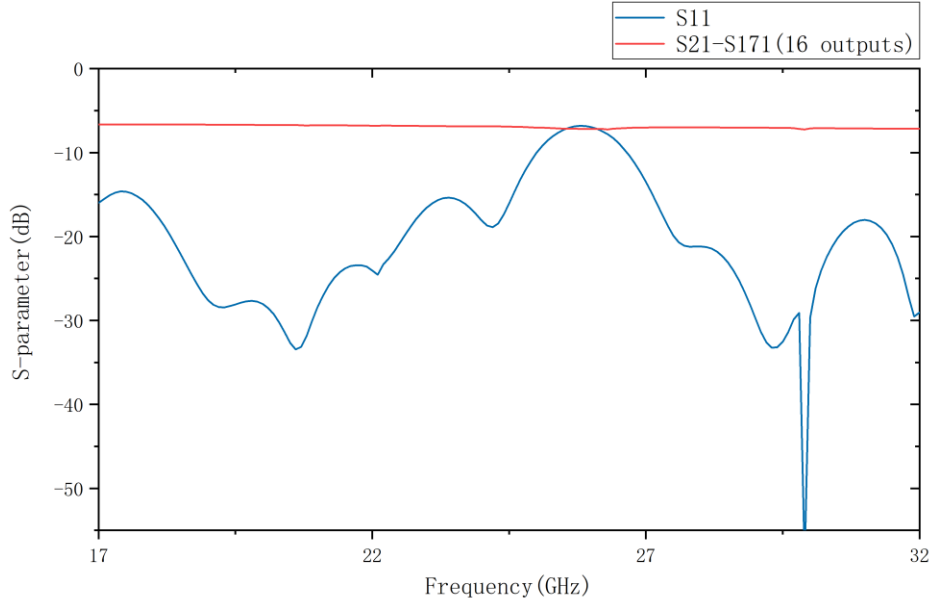
Fig. 4.3. Simulated S-parameter of the 4-16 feeding network.

4.2 Prospect and Potential of the Loaded Power Divider in Multilayer Beamforming Feeding Network

The characteristic of the low isolation for the T-junction power divider causes some limitations in feeding network applications, which need to keep the same phase and amplitude on the two outputs to divide signals and two inputs to combine signals.

Some designs used the load to improve the isolation performance, such as the Wilkinson power divider. However, it is still challenging to design and manufacture the resistor in a multilayer PCB structure, such as in the SICL structure.

The embedded PCB technology is used to design buried resistors and capacitors in recent years [36-37]. When the isolation is increased, the two outputs/inputs will not influence and interfere with each other so much. Therefore, in a feeding network, the limitation of the same phase, amplitude, and length of the transmission line could also

58

be improved. The simulated results from AWR software are demonstrated in Fig. 4.4 and Fig. 4.5 for comparison.
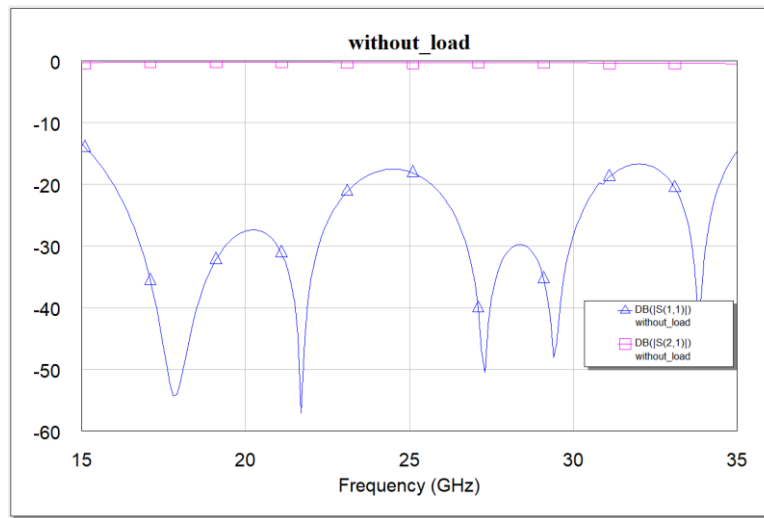
(a)
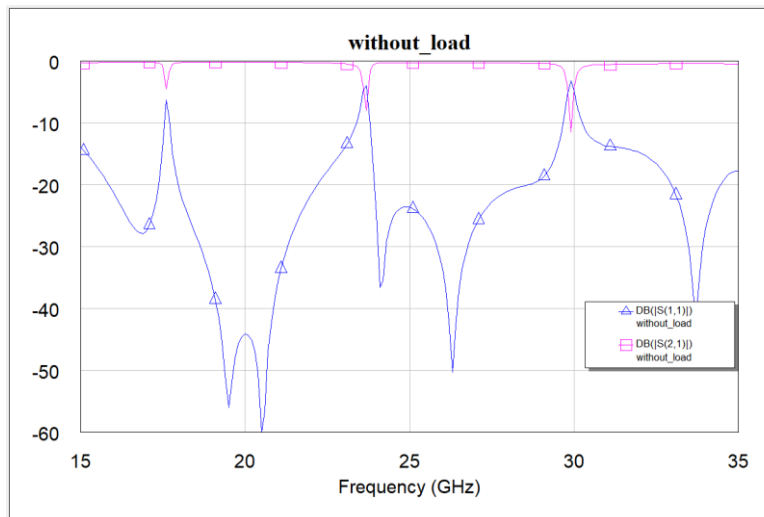
(b)
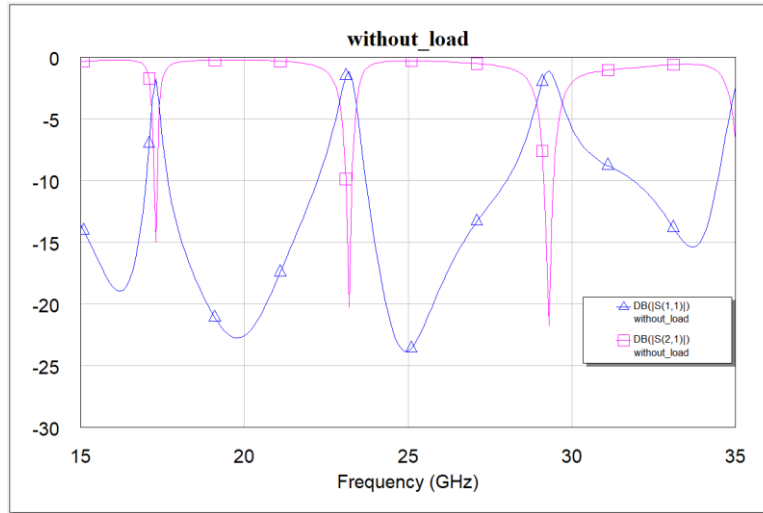
(c)
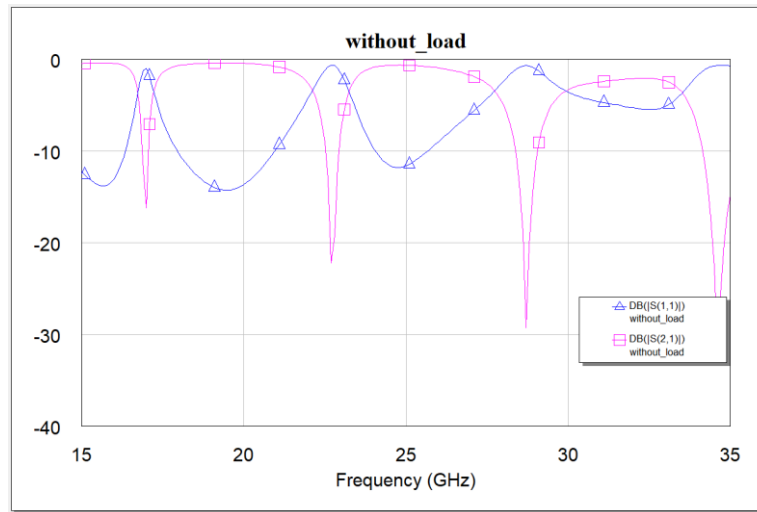
(d)

Fig. 4.4. The results for two power dividers without loads back-to-back connected to transmission lines with electrical length differences of (a) 0-degree, (b) 30-degree, (c) 60-degree, and (d) 90-degree.

(a)

(b)

(c)

61
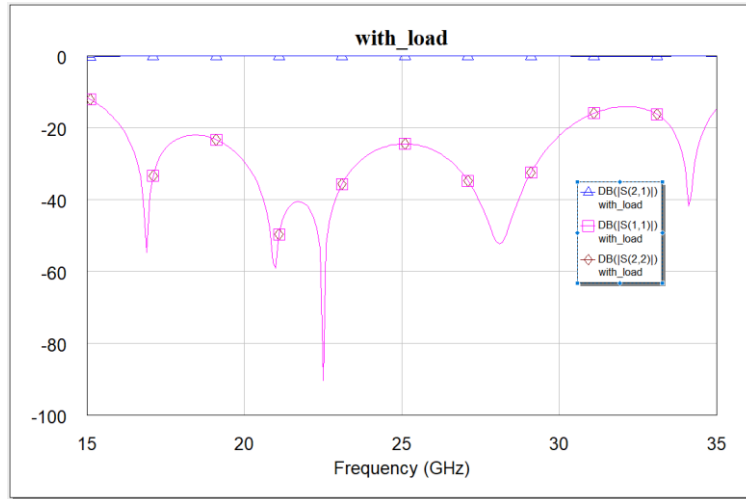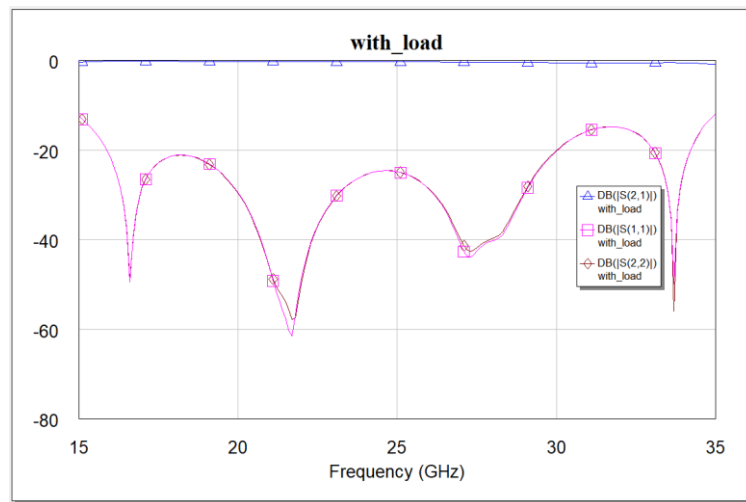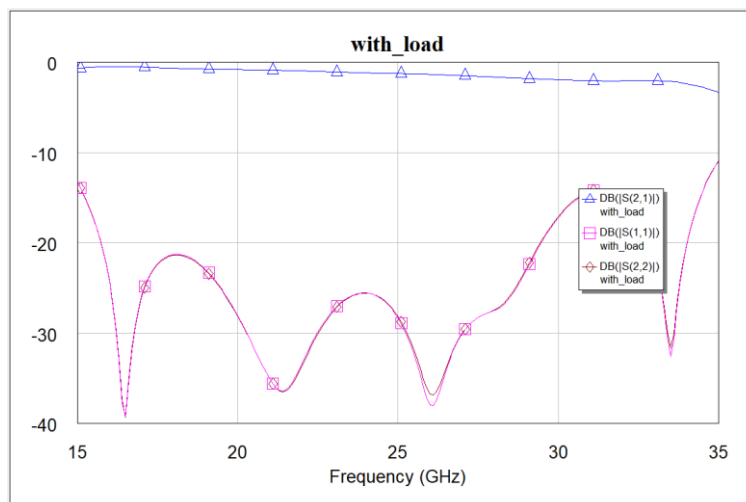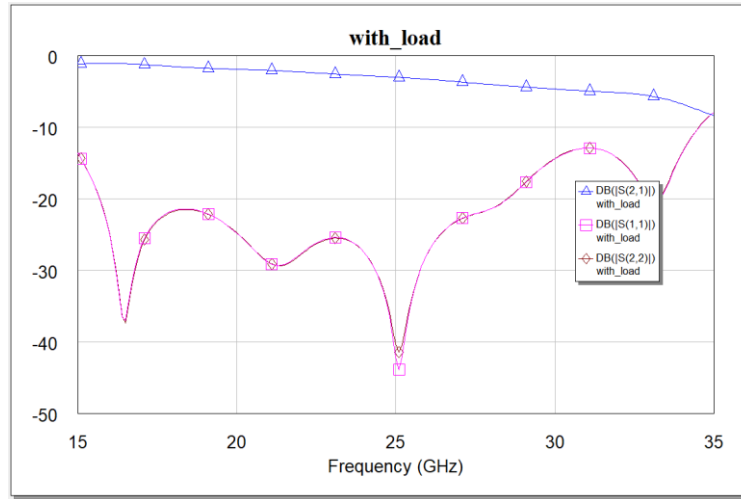
(d)

Fig. 4.5. The results for two power dividers with loads back-to-back connected to transmission lines with electrical length differences of (a) 0-degree, (b) 30-degree, (c) 60-degree, and (d) 90-degree.

The charts showed the improved performance and tolerance when the loaded power divider with better isolation to reduce the influence caused by a phase shift on the power dividers connection in a feeding network.

For the network based on the power dividers without loads, when the phase difference occurred between the power dividers, even only 30 degrees phase difference, it caused mismatching in the network to affect the performance a lot. For the network based on the power dividers with loads and high isolation, it kept good results when there is a 60-degree or 90-degree phase difference occurred in the network at required frequencies.

It demonstrated the potential and prospect of the loaded power divider based on embedded PCB technology for multilayer feeding network designs and applications.

CHAPTER 5

WAVEGUIDE TRANSITIONS

5.1 Design of the SICL-to-waveguide Transition

In a beamforming system, the SICL-to-waveguide transition or the microstrip-to-waveguide transition will connect the feeding network in PCB and the waveguide antenna array. An example 2×2 beamforming antenna array is illustrated in Fig. 5.1. to show the beamforming system network. The phase and gain control section will be installed at the bottom of the multilayer PCB feeding network.
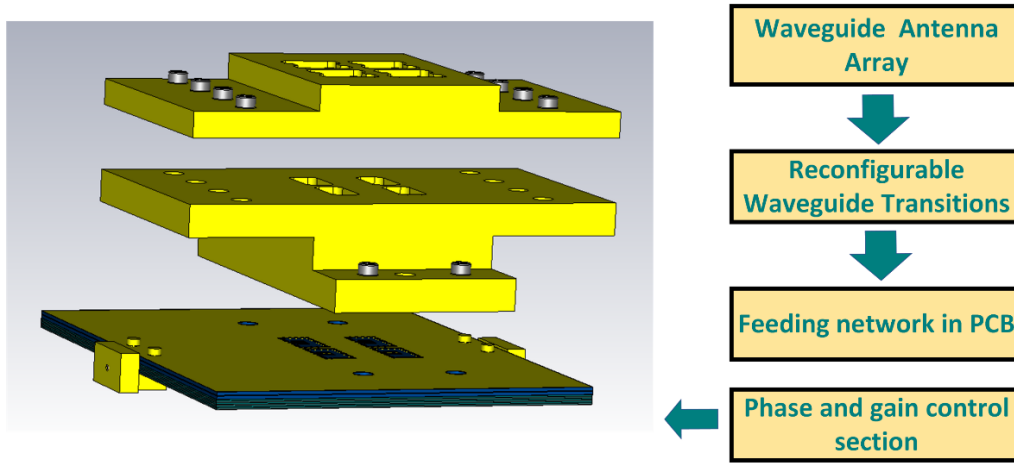
Fig. 5.1. Beamforming system network.

5.1.1. Rectangular Waveguide Transitions with Stepped Transformers

For a high-frequency multilayer PCB feeding network in a beamforming system, the SICL structure will provide low loss and wideband performance due to its two side rows of metallic vias to reduce interference of resonance in the beamforming feeding network in a compact structure [85]. The SICL structure is shown in Fig. 5.2. To achieve dual-mode operations at K/Ka-band respectively, the adaptable patches on top of the PCB could help to match the impedance for two modes and reduce the interference between them, which is shown in Fig. 5.3 (a) and (b). Distinguished from conventional designs, the two modes for K/Ka-Band will share the same PCB feeding network. The

commercial beamforming chips ADAR-3000 and ADAR-3001 [86-87] are planned to use to provide the K/Ka-band phase shift in the beamforming system in applications.
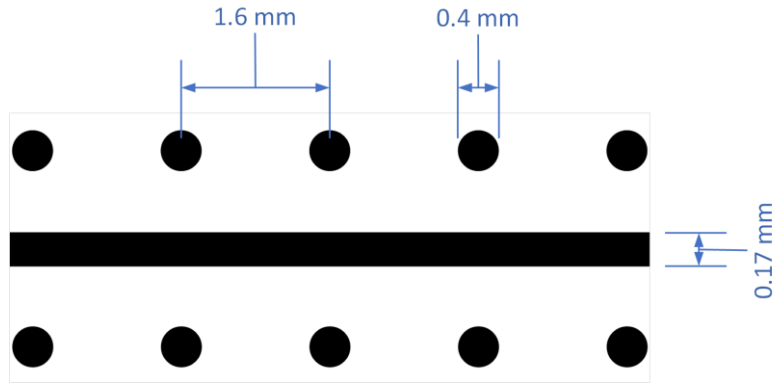
Fig. 5.2. SICL structure with dimensions.

The waveguide parts with two different dimensions for K/Ka-band respectively will be connected to the same PCB. They could be installed and replaced easily by screws to achieve different modes of operations in different frequencies, which is already demonstrated in Fig. 5.1.

(a)

Ka-band mode waveguide range
Dielectric
Patches on top of PCB
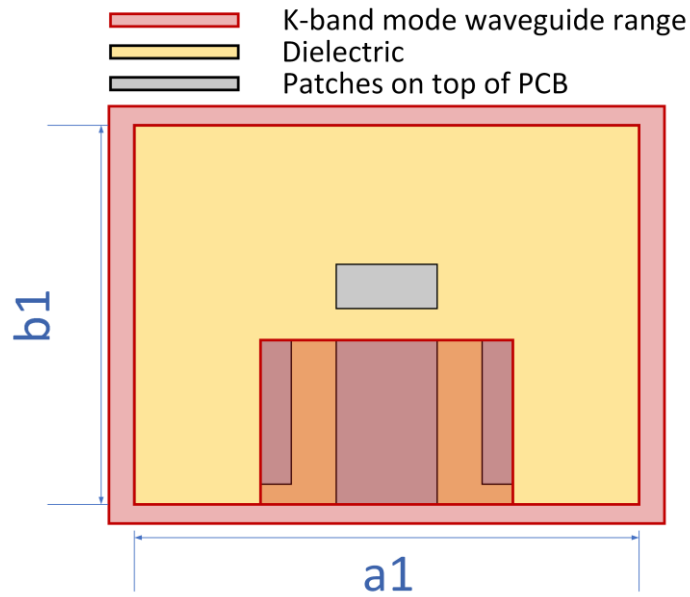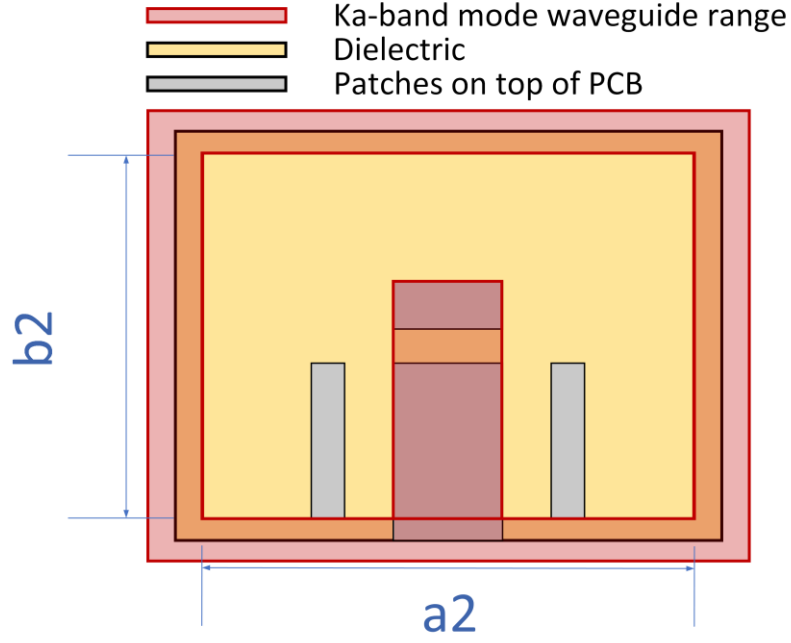
(b)

Fig. 5.3. Concept of two modes switched for the SICL-to-waveguide transition for (a) K-band mode and (b) Ka-band mode. The dimensions are a1 = 9, b1 = 4.5, a2 = 8.5, b2 = 4.25, all in millimeters.

The stepped transformers are adopted in this waveguide transition design to increase the impedance from SICL to the waveguide and convert the propagation mode from quasi-TEM in a SICL to TE10 in a waveguide. The side view and top view of the rectangular SICL-to-waveguide transition with stepped transformers are illustrated in Fig.5.4 (a) and (b) with the dimensions in Table 2, the E-field distributions from HFSS software are shown in Fig. 5.5 (a) and (b) to demonstrate its TE10 propagation mode in waveguide. To meet the requirements in a beamforming system to provide a better antenna elements distance for better performance, there is a dimension limitation of 10 mm for every element. Therefore, the broad wall width of the K-band and Ka-band modes waveguides in this design are 9 mm and 8.5 mm respectively. When the board wall is 9 mm, the cut-off frequency is around 16.7 GHz, the waveguide still could work in the required frequency range. The narrow wall width is around half of the broad wall width. The SICL structure and the waveguide are connected by a via, whose equivalent circuit model is shown in Fig. 5.6 (a) [88]. To build an equivalent circuit model of a via, the effect of via switching on signal transmission quality need to be considered in high frequencies, and the resonator effect of parallel-plate is considered firstly in the

65

modeling method [88]. It included the capacitance and inductance between the vias and the top/bottom ground, the capacitance of the vias and pads, and the impedance of the vias. The stepped transformers from via (Zvia) to waveguide (Zws) could be represented by the equivalent circuit model of Fig. 5.6 (b). The stepped transformer is a series cascade of ridge waveguide step junctions that are separated by ridge waveguide transmission lines lengths with different ridge depths, and a ridge-to-rectangular waveguide discontinuity [41]. This equivalent circuit model of the ridge stepped transformers and junctions is derived from Fig. 2.9 (b) and (c). The reactive energy of the fringing fields at each waveguide step is represented by susceptance B1, B2, B3, and B4. The Zd1, Zd2, and Zd3 represent the impedance of stepped transformers. The simulation result from Fig. 5.7 (a) and (b) shows the wideband performance both on K/Ka-band operation modes with the bandwidth of 36.6% (18.1 GHz - 26.2 GHz) and 38.1% (21.7 GHz - 31.9 GHz) respectively for return loss better than 10 dB.
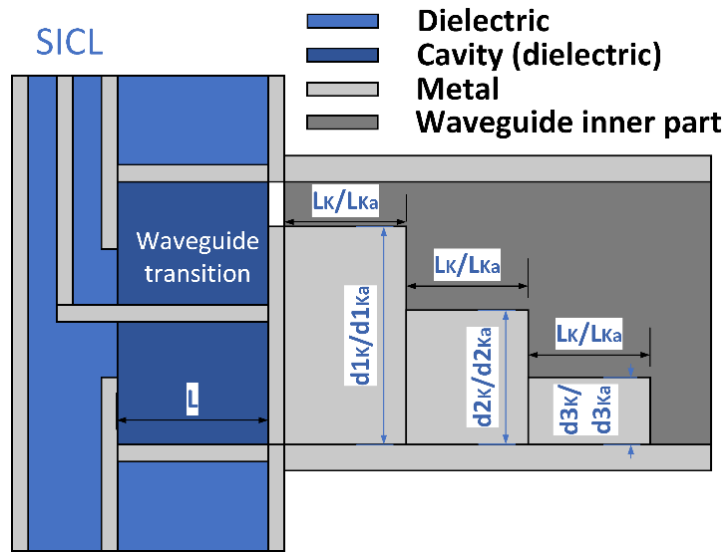
(a)
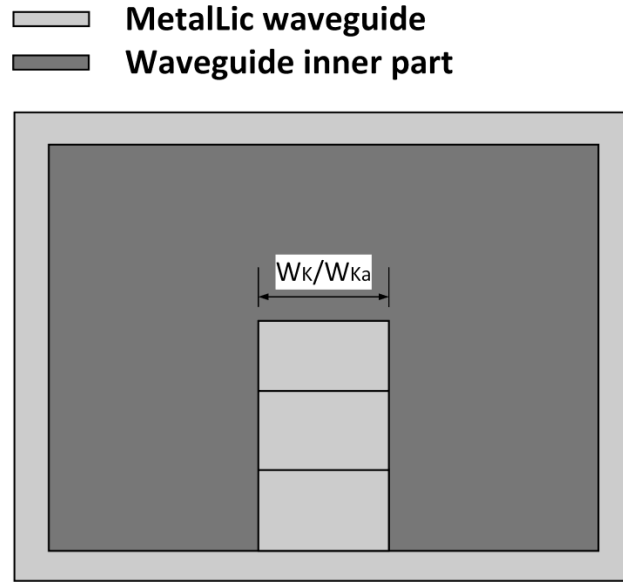
(b)

Fig. 5.4. (a) Side view and (b) top view of the rectangular SICL-to-waveguide transition with stepped transformers.

Table 2: Dimensions of the rectangular SICL-to-waveguide transition with stepped transformers (all in millimeters).

L	WK	WKa	d1K
1.1	28	12	26.5
d1Ka	*LK*	*LKa*	
29	37	21	
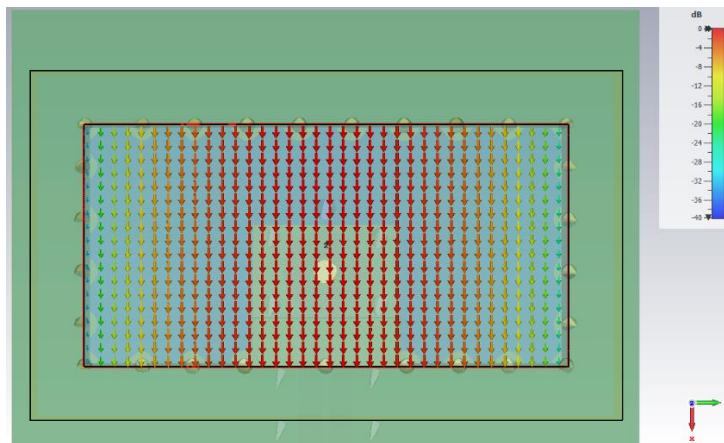
(a)
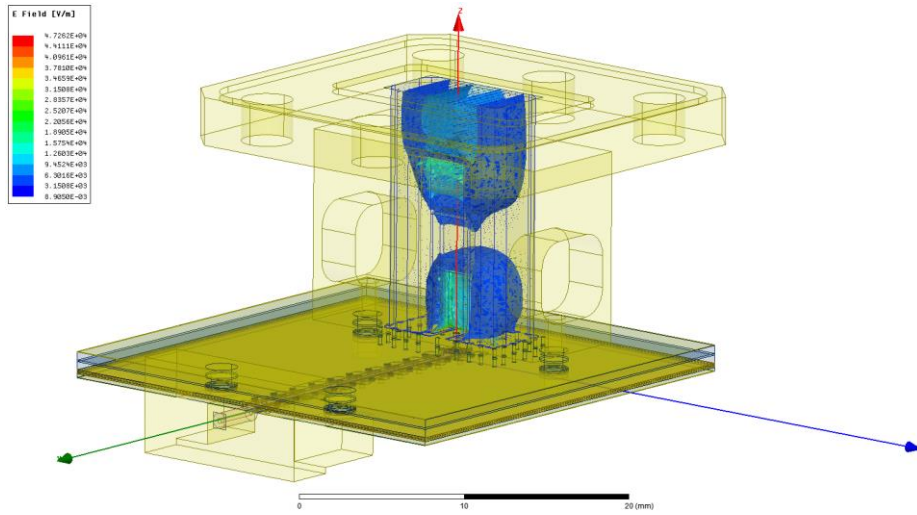
(b)

Fig. 5.5. E-field distributions of (a) the waveguide port and (b) the waveguide part in the SICL-to-waveguide transition with stepped transformers.
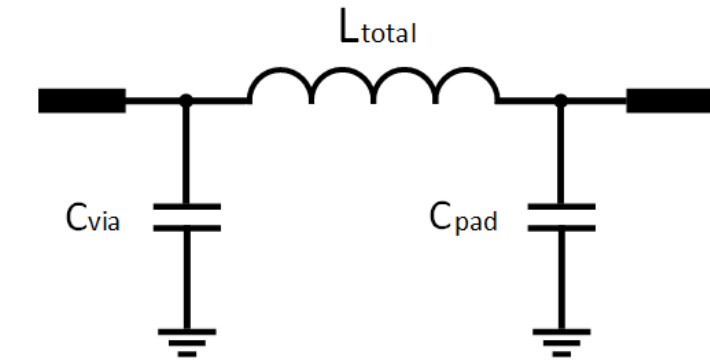
(a)
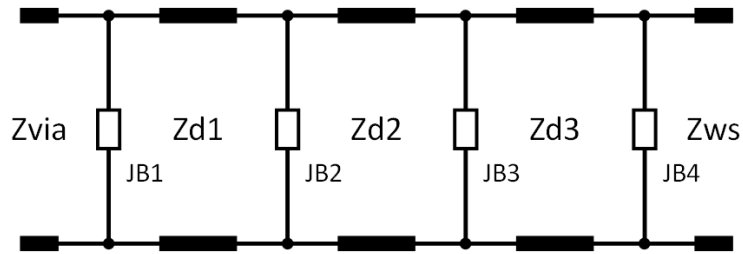
(b)

Fig. 5.6. Equivalent circuit models of (a) Via and (b) stepped transformers.
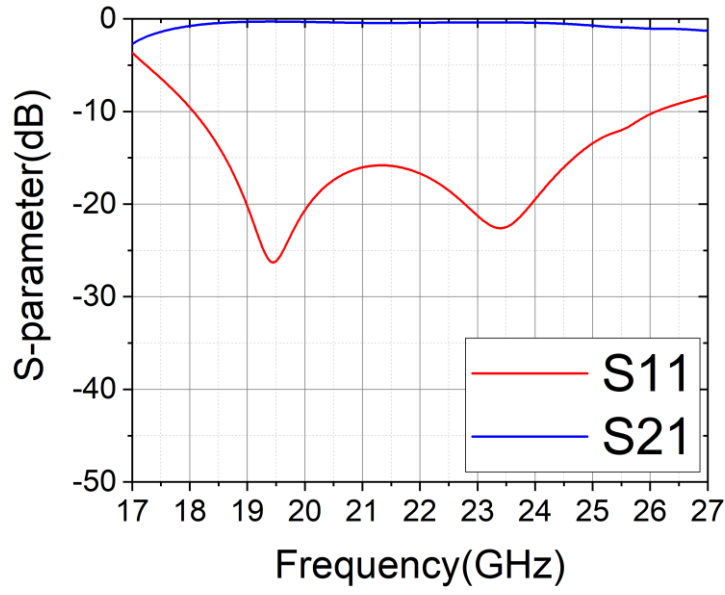
(a)
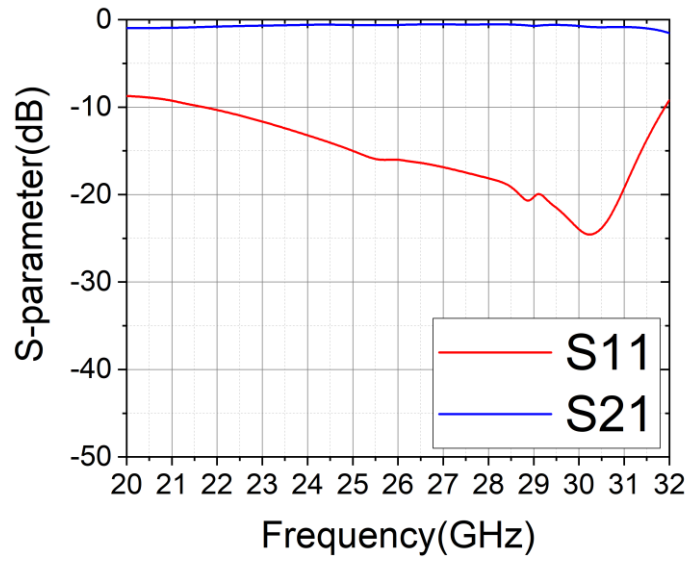
(b)

Fig. 5.7. Simulated results of waveguide transition with stepped transformers for (a) K-band mode and (b) Ka-band mode.

5.1.2. Ridge Waveguide Transitions

The reconfigurable ridge waveguide transitions have a similar design to the waveguide transitions with stepped transformers to achieve K/Ka-band dual-mode operations by using the adaptable patches on top of the PCB. For the same operation mode, the same dimensions of the

69

waveguides and adaptable patches will make these two types of SICL-to-waveguide transitions match the same PCB feeding network in a beamforming system. The ridge waveguide structure is adopted in this design to get wider bandwidth performance [89-90]. The loss of waveguide transitions with stepped transformers for K-band mode below 18 GHz will increase a lot, due to its cut-off frequency being around 16.7 GHz. For the same board wall width, the ridge waveguide structure will provide a lower TE10 cut-off frequency to get better performance on bandwidth in the limited waveguide dimensions to meet the requirements for a beamforming system. The side view and top view of the ridge structure SICL-to-waveguide transition are illustrated in Fig. 5.8 (a) and (b) with the dimensions in Table 3, the E-field distributions from HFSS software are shown in Fig. 5.9 (a) and (b) to demonstrate its TE10 propagation mode in waveguide. The simulation results of the ridge SICL-to-waveguide transition are shown in Fig. 5.10 (a) and (b), they demonstrated the wider bandwidth performance both on K/Ka-band operation modes with the bandwidth of 50.5% (16.3 GHz - 27.3 GHz) and 43.7% (20.4 GHz - 31.8 GHz) respectively for return loss better than 10 dB compared with the SICL-to-waveguide transition with stepped transformers.


(a)
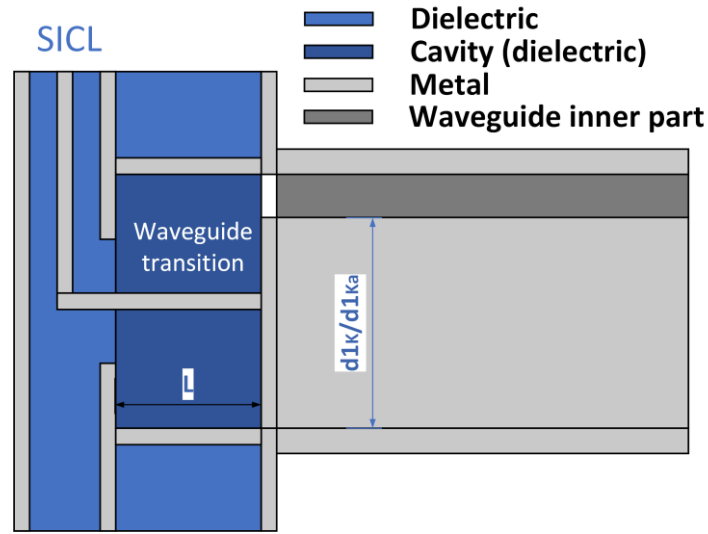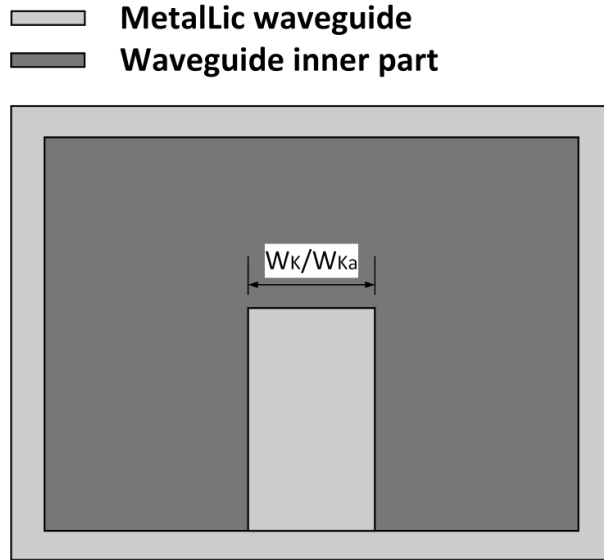
WK/WKa

(b)

Fig. 5.8. (a) Side view and (b) top view of the ridge SICL-to-waveguide transition.

Table 3: Dimensions of the ridge SICL-to-waveguide transition (all in millimeters).

| *L*	*WK*	*WKa*	*d1K*	*d1Ka*
1.1	28	12	26.5	29

(a)

71
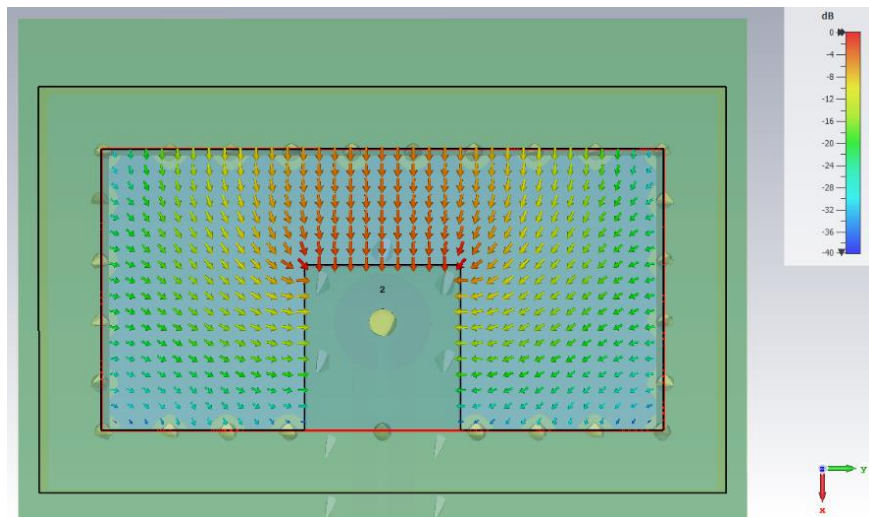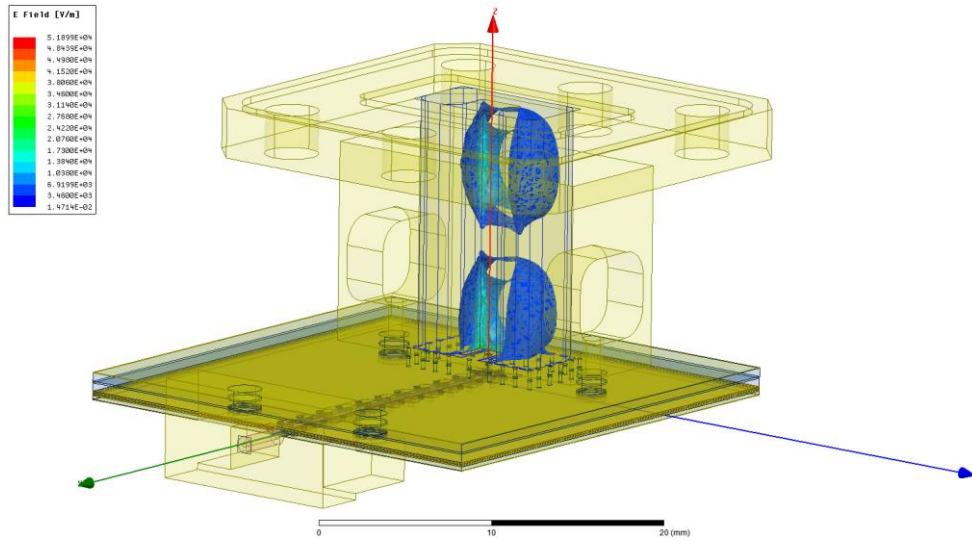
(b)

Fig. 5.9. E-field distributions of (a) the waveguide port and (b) the waveguide part in the ridge SICL-to-waveguide transition.

In a beamforming application, adding an 8.5mm × 4.25mm to 9mm × 4.5mm waveguide transition to the K-band mode waveguide port will not influence the performance a lot and help the two modes designs have the same waveguide dimension on both K/Ka-band. Therefore, the two K/Ka-band modes waveguides could connect and feed the same wideband waveguide antenna array in a beamforming system with separated Rx and Tx to bring more benefits on flexibility, cost-efficiency, and simplified installation.
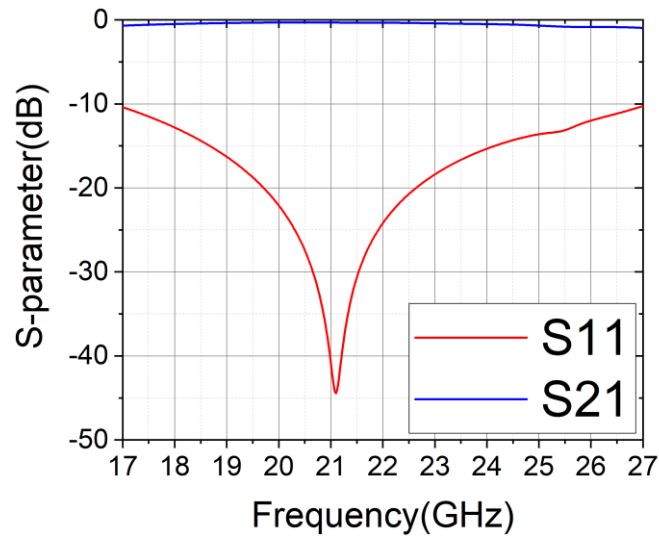
(a)
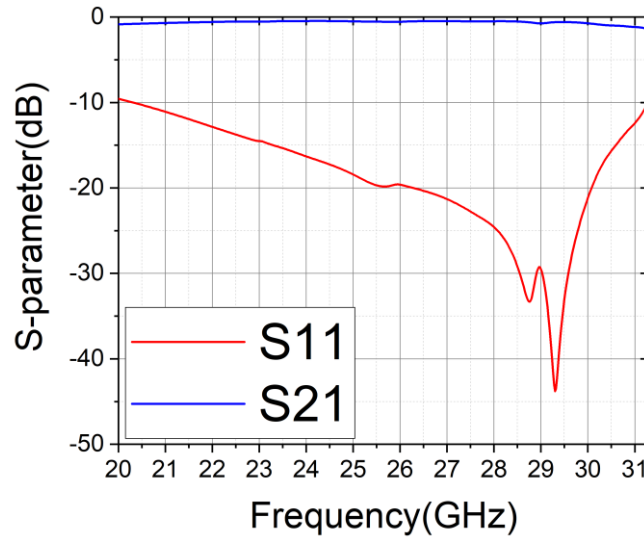
(b)

Fig. 5.10. Simulated results of ridge waveguide transition for (a) K-band mode and (b) Ka-band mode.

5.1.3. Simulations and Analysis

The cavity height L, via diameter Dv, ridge depth d1, and stepped transformer width W are critical to these two SICL-to-waveguide transition designs. The analysis in Fig. 5.11 (a), (b), (c), and (d) demonstrated the effects on varieties of these transition parameters for the exampled K-band mode ridge SICL-to-waveguide transition. The cavity height L is critical for the propagation mode transform from a SICL to a waveguide. The via diameter Dv and width W of the ridge (or the stepped transformer) will significantly influence the operation frequency range. The operation range will move to a higher frequency when the via diameter Dv increases or the ridge width W decreases. The ridge depth d1 will help the impedance matching to get better performance.

73
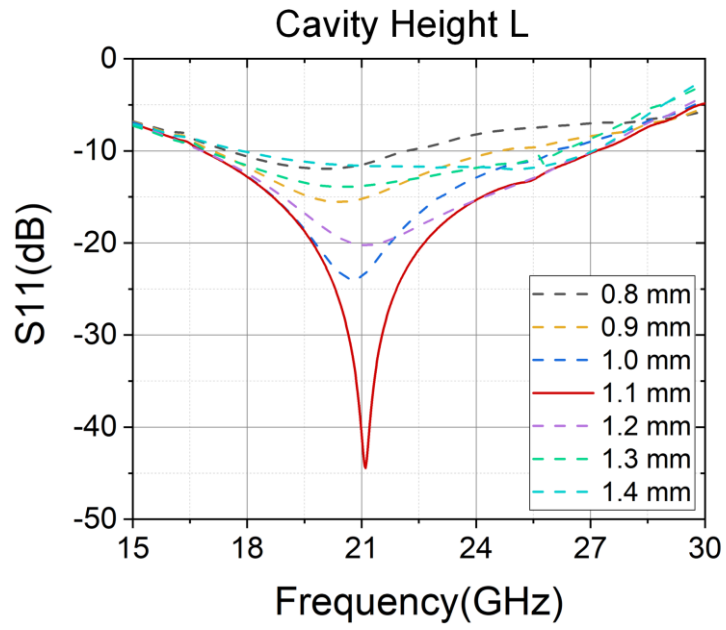
(a)
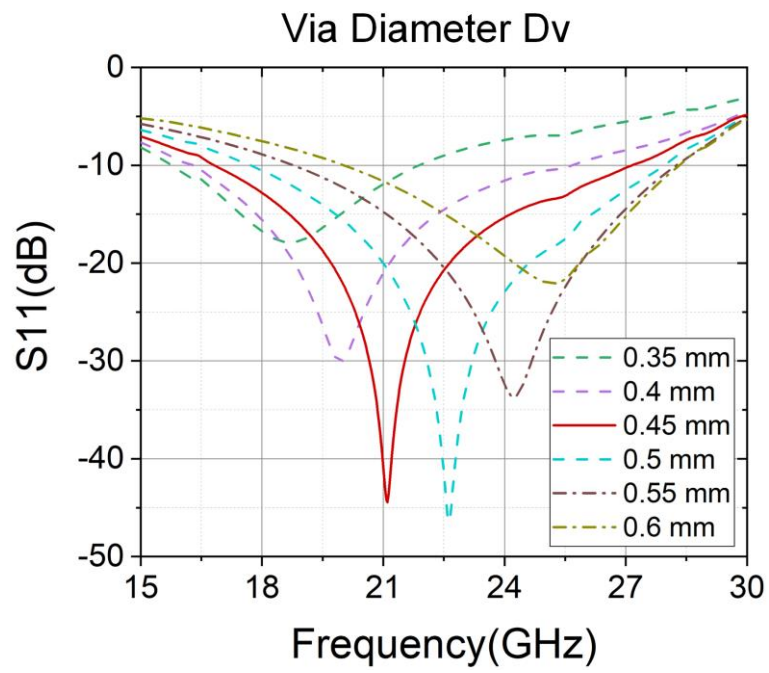
(b)
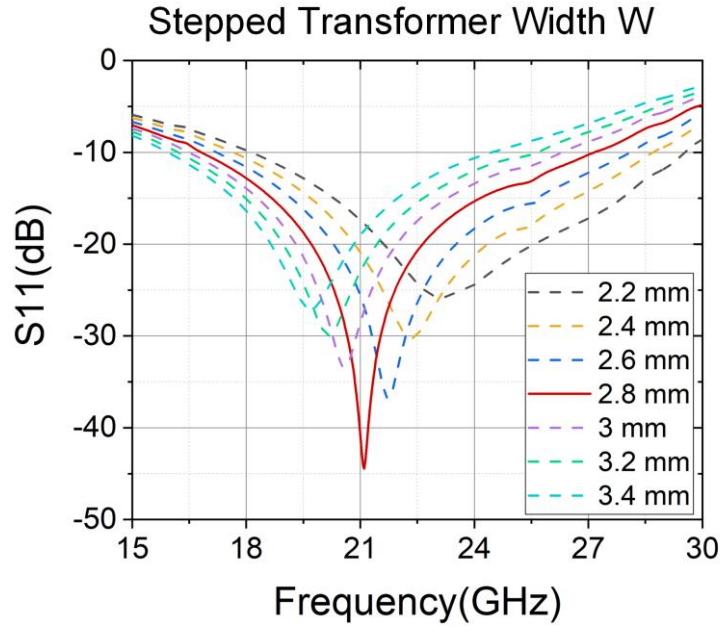
(c)
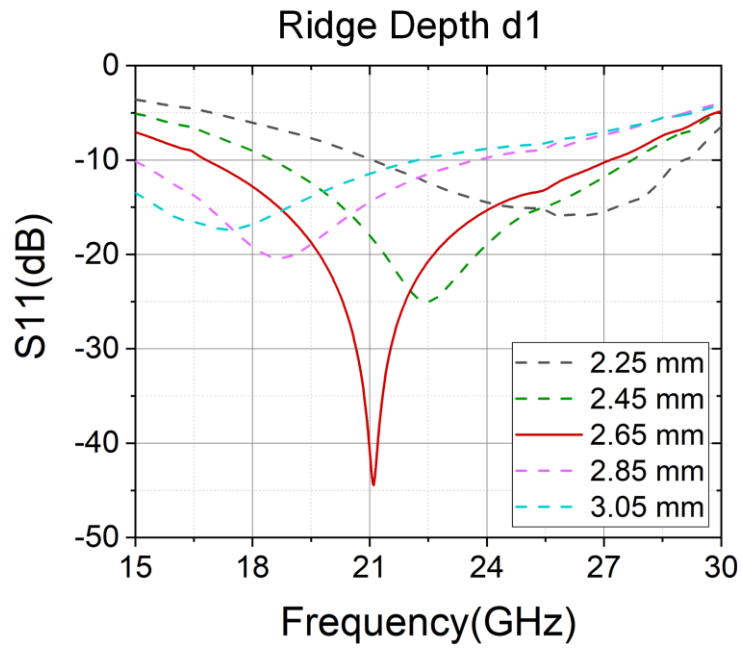
(d)

Fig. 5.11. Simulated reflection coefficient for different parameters. (a) Various values of cavity height L, (b) various values of via diameter Dv, (c) various values of stepped transformer width W, and (d) various values of ridge depth d1.

5.1.4. Experiment Results

A grounded coplanar waveguide (GCPW) structure was deployed and extended from the SICL to the edge of the test ports on a K-connector to facilitate experimental testing of the two kinds of designed SICL-to-waveguide vertical transitions. The measured S-parameter results are tested by using the PNA-L device. The fabricated SICL-to-waveguide transition is shown in Fig. 5.12. (a). The back-to-back structure was used in the measurement, shown in Fig. 5.12. (b). The measured and simulated results of the SICL-to-waveguide transition with stepped transformers and the ridge SICL-to-waveguide transition are shown in Figs. 5.13. (a) and (b) and Figs. 5.13. (c) and (d), respectively. The measured insertion loss and return loss results agree relatively well with the simulations (including the connectors and the GCPW structures). The higher insertion loss and the small difference are due to the fabrication tolerance.
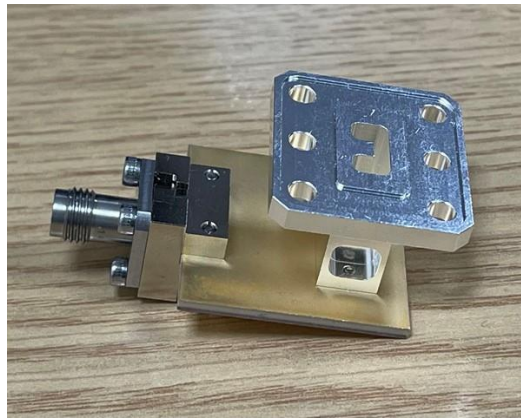
(a)

(b)

Fig. 5.12. (a) Fabricated SICL-waveguide transition and (b) back-to-back structure in the measurement.

(a)

(b)

(c)

(d)

Fig. 5.13. Measured results of waveguide transition with stepped transformers for (a) K-band mode and (b) Ka-band mode; Measured results of ridge waveguide transition for (c) K-band mode and (d) Ka-band mode.

The SICL-to-waveguide transition with stepped transformers measured minimum insertion loss (per transition) as 1.2 dB for K/Ka-band. The measured back-to-back structure bandwidths (return loss below 10 dB) are around 35.8% (17.4 GHz-25.0 GHz) and 25.0% (24.5 GHz-31.5 GHz) for K/Ka-band, respectively.

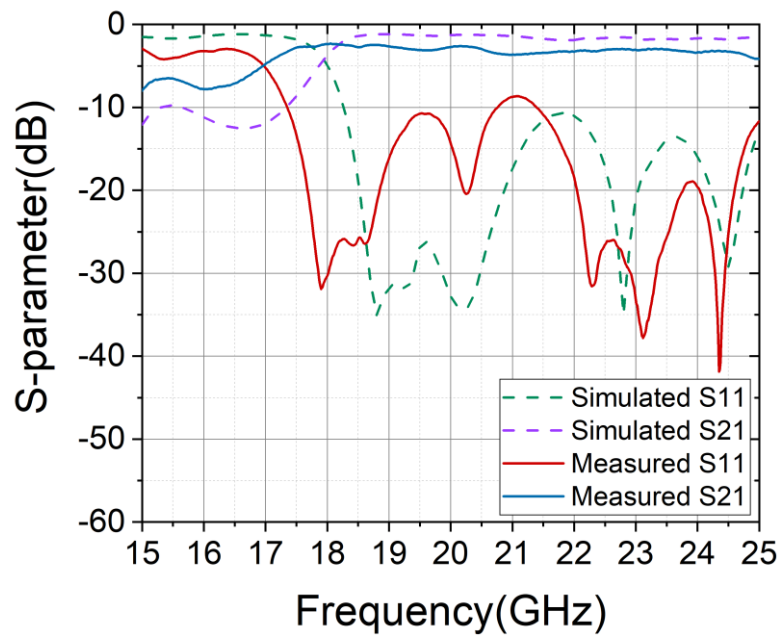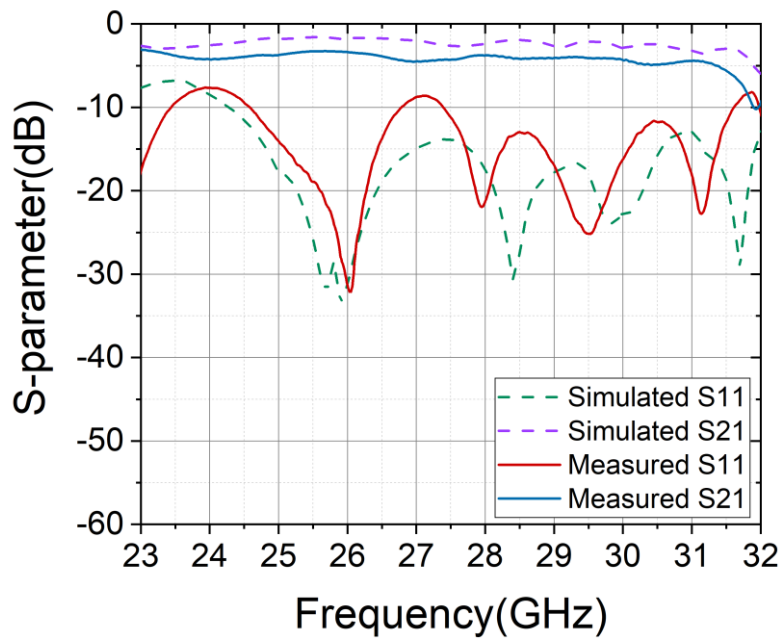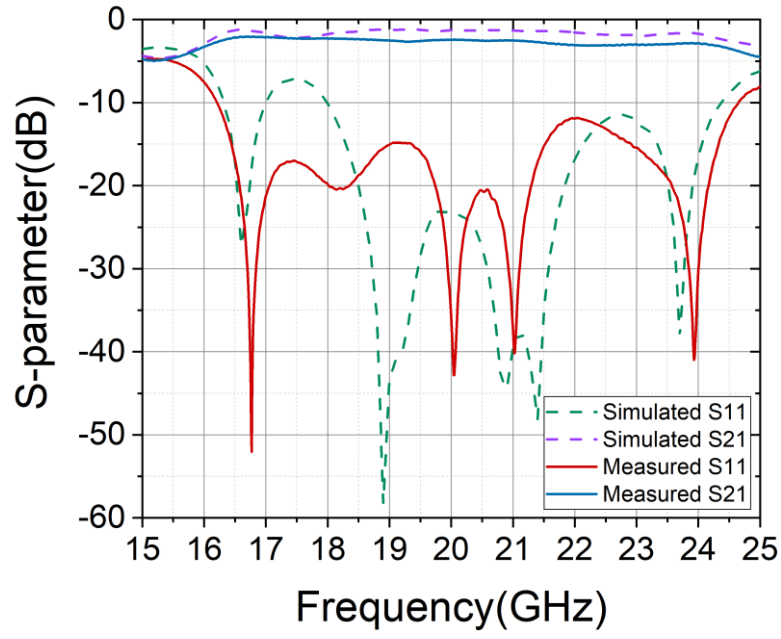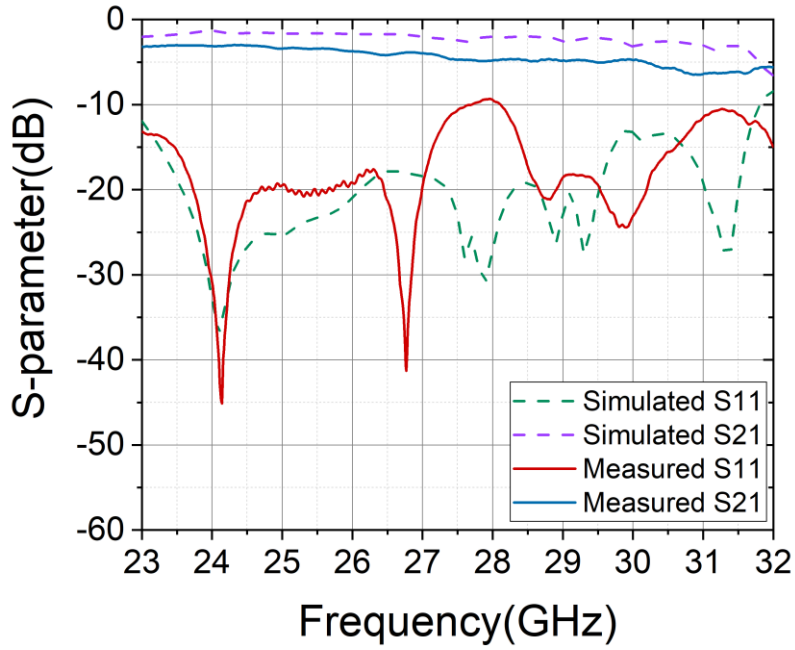The ridge SICL-to-waveguide transition measured minimum insertion loss (per transition) is 1.0 dB and 1.1 dB for K/Ka-band, respectively. The measured back-to-back structure bandwidths (return loss below 10 dB) are around 41.2% (16.2 GHz-24.6 GHz) and 45.2% (20.2 GHz-32.0 GHz) for K/Ka-band, respectively.

Both reconfigurable SICL-to-waveguide vertical transitions with stepped transformers and ridge SICL-to-waveguide vertical transitions provided wideband performance at K/Ka-band. Table 4 summarized and demonstrated the performance of recently published waveguide transition designs. Compared with the recent dual-band waveguide transition designs (with around 3% to 16% bandwidth), most waveguide transition designs with a single operational frequency band mode have better wideband performance and insertion loss. The comparison shows that the two presented designs have considerably better wideband performance than the recent dual-band waveguide transitions with around 25% to 45% measured bandwidth and could achieve the dual-band operation at K/Ka-band simultaneously by using the reconfigurable structure. Furthermore, the sizes (estimated dimensions of the transition designs which exclude the 50-ohm input and waveguide output) of all cited designs and these two proposed designs are listed in the table. The proposed designs have a compact footprint with 0.7λ and 0.9λ dimensions for K/Ka-band, respectively, applicable for an antenna array in MIMO beamforming applications at K/Ka-band.

Table 4: Data of different waveguide transitions.

Ref.	Transition	IL per transition (dB)	10 dB RL (%)	Freq. band	Vertical transition	Dual-band	Layers before WG transition	Size	Reconfigurable
[9]	MS-WG	<0.52	26.0	W	No	No	Single-layer	1.5λ	No
[10]	MS-WG	<0.95	11.5	Ka	Yes	No	Single-layer	1.4λ	No
[11]	MS-WG	<0.6	15.0	W	Yes	No	Single-layer	1.0λ	No
[12]	MS-WG	<1.0	20.0	V	Yes	No	Single-layer	0.9λ	No
[38]	MS-WG	<0.32	37.4	W	No	No	Single-layer	0.8λ	No
[39]	MS-WG	<0.5	37.8	W	No	No	Single-layer	0.8λ	No
[13]	SICL-WG	<0.85	21.5	W	Yes	No	Multilayer	0.8λ	No
[14]	SISL-WG	<0.34	45.7	Ka	Yes	No	Multilayer	0.8λ	No
[91]	CPW-WG	<1.2	31.5	W	Yes	No	Single-layer	1.0λ	No
[92]	SIW-WG	<1.2	40.0	K	Yes	No	Single-layer	0.9λ	No
[93]	GCPW-WG	<2.0	6.2	W	Yes	No	Single-layer	0.8λ	No
[93]	SL-WG	<2.6	33.8	W	Yes	No	Multilayer	0.7λ	No
[94]	SIW-WG	<1.0	43.0	K	Yes	No	Single-layer	0.9λ	No
[15]	GCPW-WG	<1.2 <1.0	3.0 6.7	K/Ka	Yes	Yes	Single-layer	0.7λ 1.1λ	No
[16]	SL-WG	<1.4 <1.4	8.0 15.9	K/Ka	Yes	Yes	Multilayer	0.9λ 1.0λ	No
[95]	SL-WG (Simulated)	N/A	12.3 12.9	K/Ka	Yes	Yes	Multilayer	0.6λ 1.0λ	No
TW	SICL-WG	<1.2 <1.2	35.8 25.0	K/Ka	Yes	Yes	Single-layer	0.7λ 0.9λ	Yes
TW	SICL-RWG	<1.0 <1.1	41.2 45.2	K/Ka	Yes	Yes	Single-layer	0.7λ 0.9λ	Yes

IL - Insertion Loss, RL - Return Loss, MS - Microstrip, WG - Waveguide, SL - Stripline, SICL - Substrate Integrated Coaxial Line, SISL - Substrate Integrated Suspended Line, CPW - Coplanar Waveguide, GCPW - Grounded Coplanar Waveguide, SIW - Substrate Integrated Waveguide, TW - This Work, RWG - Ridge Waveguide.

5.2 Design of The Microstrip-to-waveguide Transition

The microstrip-to-waveguide transitions have a similar design theory to the SICL-to-waveguide transitions designs in Fig. 5.3. The microstrip-to-waveguide transitions and the SICL-to-waveguide transitions have their advantages respectively for a beamforming system.

For the microstrip-to-waveguide transitions, they have a simpler structure, much lower cost and it is easier to manufacture due to their single-layer microstrip structures.

For the SICL-to-waveguide transitions, they are more suitable for the MIMO beamforming system with a multilayer feeding network, which could provide more flexibility in functions and structures.

5.2.1. Rectangular Waveguide Transitions with Stepped Transformers

Fig. 5.14 (a) and (b) showed the structure of the microstrip-to-waveguide transition with stepped transformers, the dimensions are shown in Table 5.
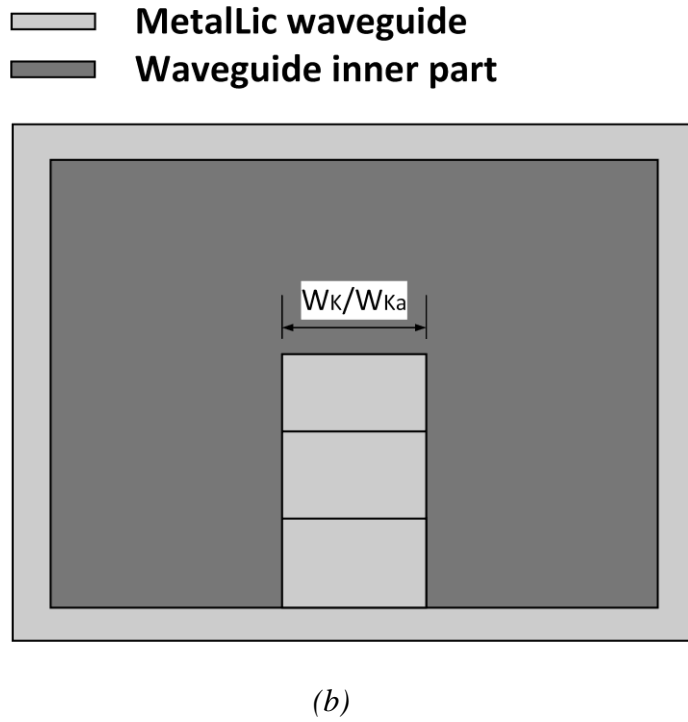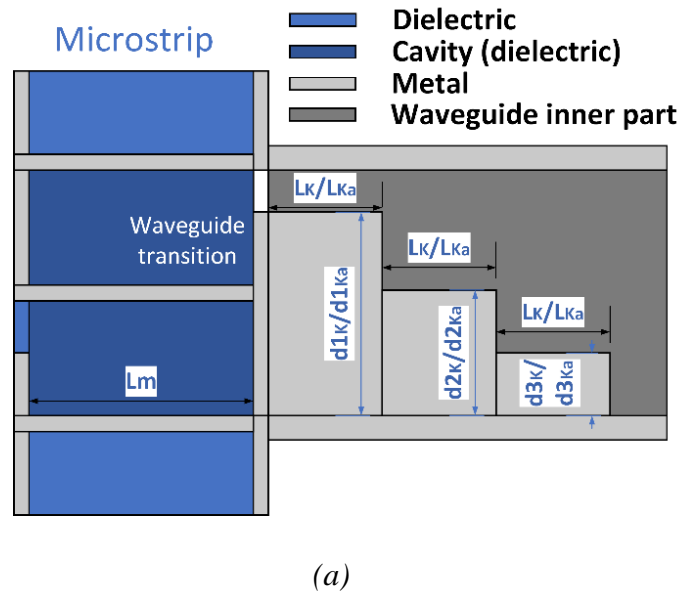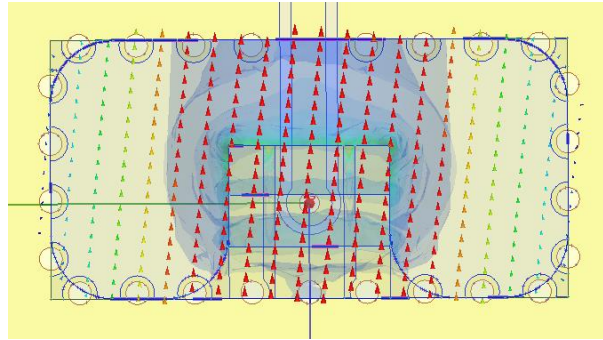
(a)

(b)

Fig. 5.14. (a) Side view and (b) top view of the rectangular microstrip-to-waveguide transition with stepped transformers.
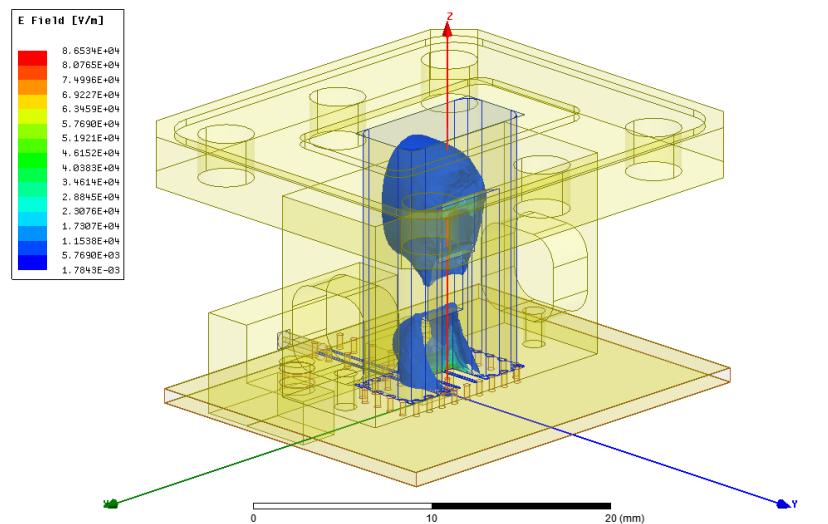
Table 5: Dimensions of the rectangular microstrip-to-waveguide transition with stepped transformers (all in millimeters).

Lm	WK	WKa	d1K
0.8	28	12	26.5
d1Ka	LK	LKa	
29	37	21	

The E-field distributions of the waveguide port and waveguide part in the simulation from HFSS software are demonstrated in Fig. 5.15 (a) and (b) to show its TE10 propagation mode in the waveguide.
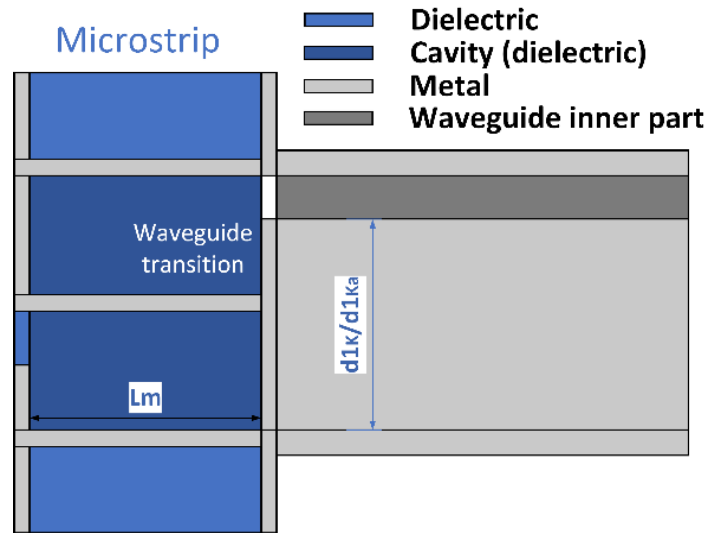

(a)

(b)

Fig. 5.15. E-field distributions of (a) the waveguide port and (b) the waveguide part in the microstrip-to-waveguide transition with stepped transformers.

82

5.2.2. Ridge Waveguide Transitions

Fig. 5.16 (a) and (b) showed the structure of the ridge microstrip-to-waveguide transition, the dimensions are shown in Table 6.


(a)

(b)

Fig. 5.16. (a) Side view and (b) top view of the ridge microstrip-to-waveguide transition.
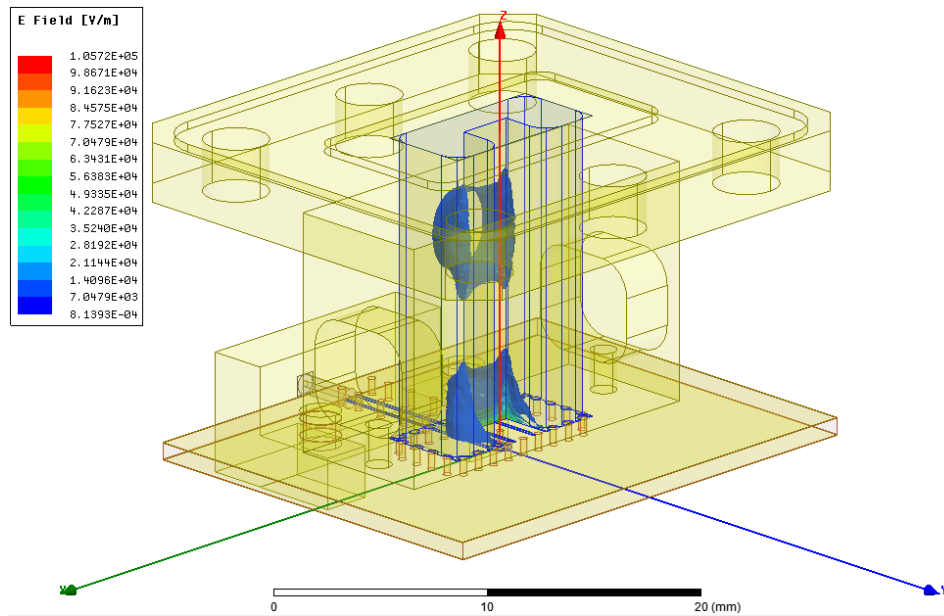
Table 6: Dimensions of the ridge microstrip-to-waveguide transition (all in millimeters).

Lm	WK	WKa	d1K	d1Ka
0.8	28	12	26.5	29

The E-field distributions of the waveguide port and waveguide part in the simulation from HFSS software are demonstrated in Fig. 5.17 (a) and (b) to show its TE10 propagation mode in the waveguide.
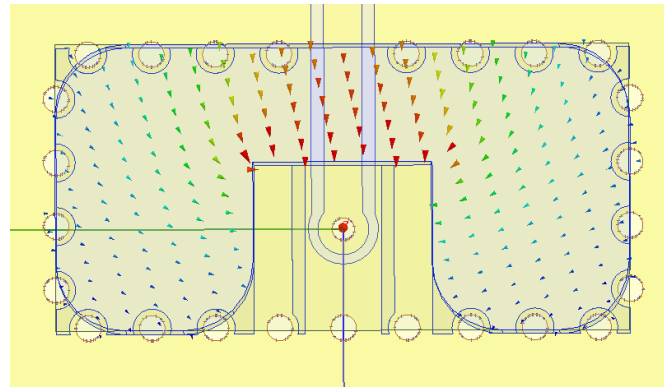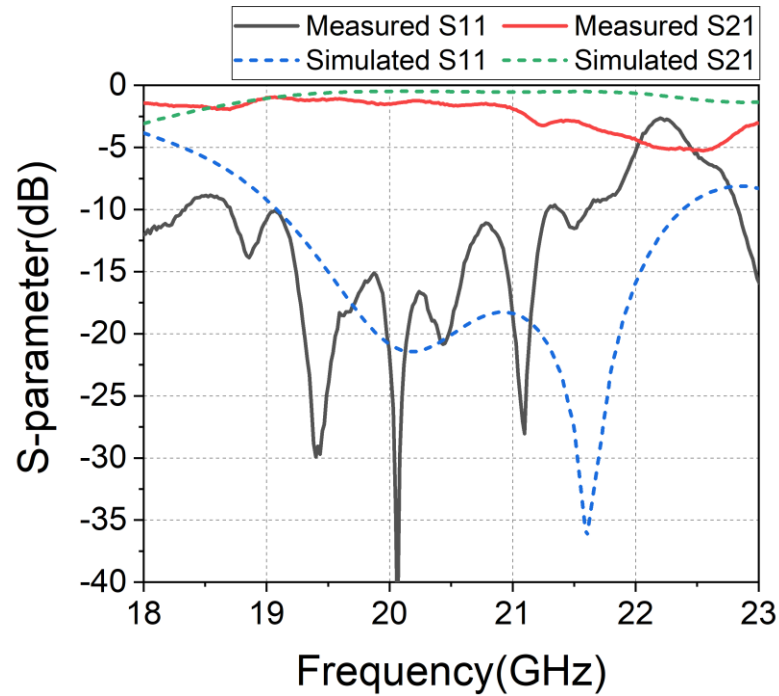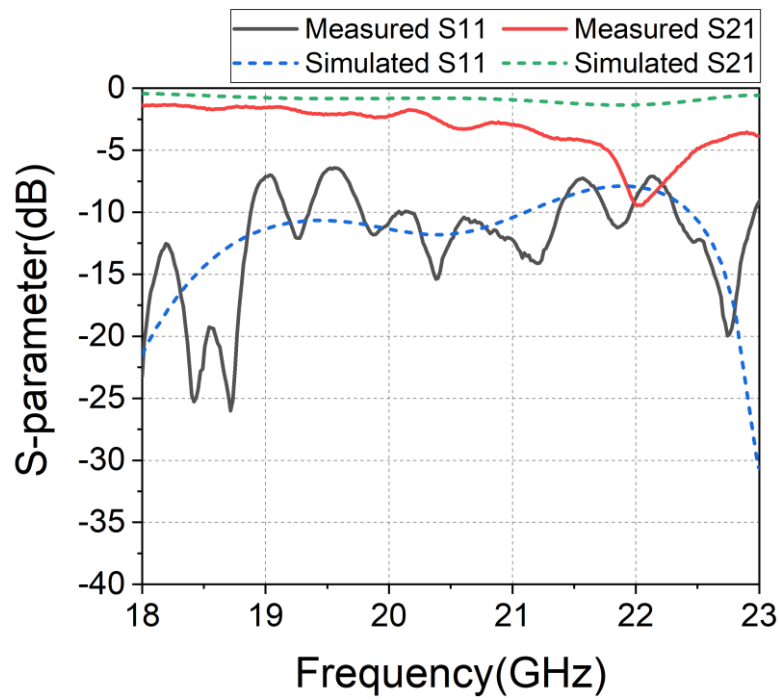

(a)

(b)

Fig. 5.17. E-field distributions of (a) the waveguide port and (b) the waveguide part in the ridge microstrip-to-waveguide transition.

84

5.2.3. Experiment Results

The measured S-parameter results in the back-to-back structure of two kinds of microstrip-to-waveguide transitions are demonstrated in Fig. 5.18.

(a)

(b)
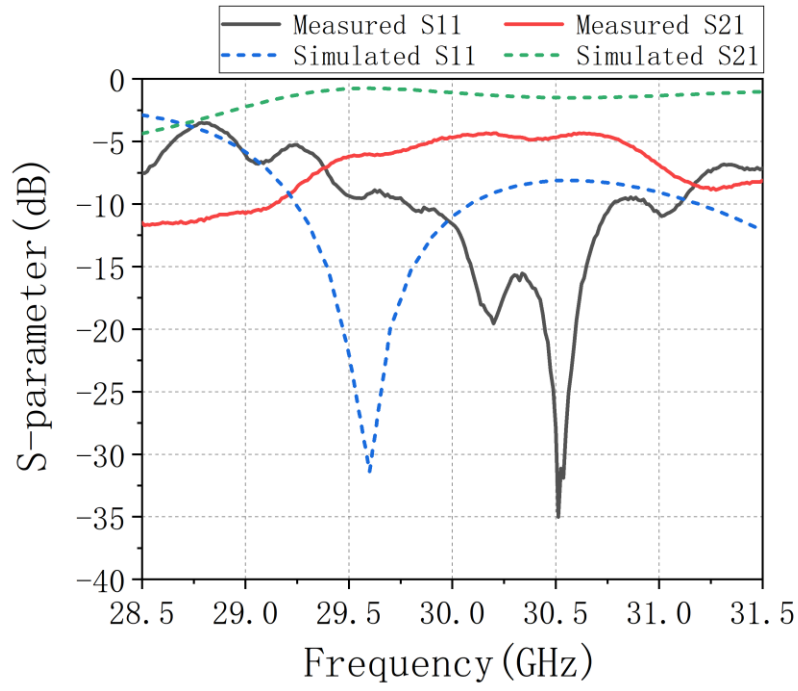
(c)

(d)

Fig. 5.18. Comparison between measured and simulated S-parameter results of microstrip-to-waveguide transitions (a) with stepped transformers for K-band mode (b) with the ridge structure for K-band mode, (c) with stepped transformers for Ka-band mode (d) with the ridge structure for Ka-band mode.

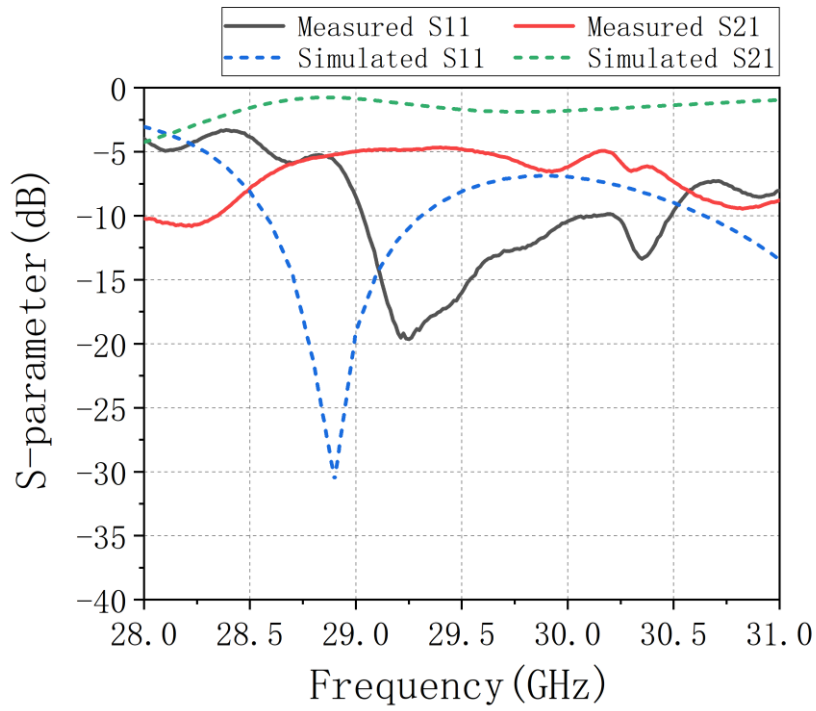These results also demonstrated the wideband performance of the two microstrip-to-waveguide transition designs at the required K/Ka-band respectively. Some discrepancy between the simulation and measurement would attribute to the tolerance in material and fabrication. The mismatch and shifting in frequencies between measured results and simulated results are mainly caused by the PCB layer thickness difference between design in simulations and manufacture.

Comparing the measured and simulated results will be helpful to adjust and optimize the designs such as actual design thickness (especially for multilayer PCB designs), dimensions, and accuracy in manufacture, to get better-measured performance and more similar results to simulated results with less shift in the next step.

To get better results in measurement, there are many feasible ways such as careful and scientific equipment setup and calibration, checking the condition of cables and connectors before the test, and making a good measurement plan and consideration to reduce loss in the measured environment.

CHAPTER 6

WAVEGUIDE ANTENNAS

6.1 Reconfigurable Linear-Polarized Waveguide Antenna

To be applicable in a MIMO beamforming system antenna array, there is a dimension limitation for the waveguide antenna designs. In this project, the waveguide antenna elements in the array are required to be restricted to a maximum dimension of 10 mm. The antennas will be fed by the 9×4.5 mm waveguides from the waveguide transitions which connect the PCB feeding network.
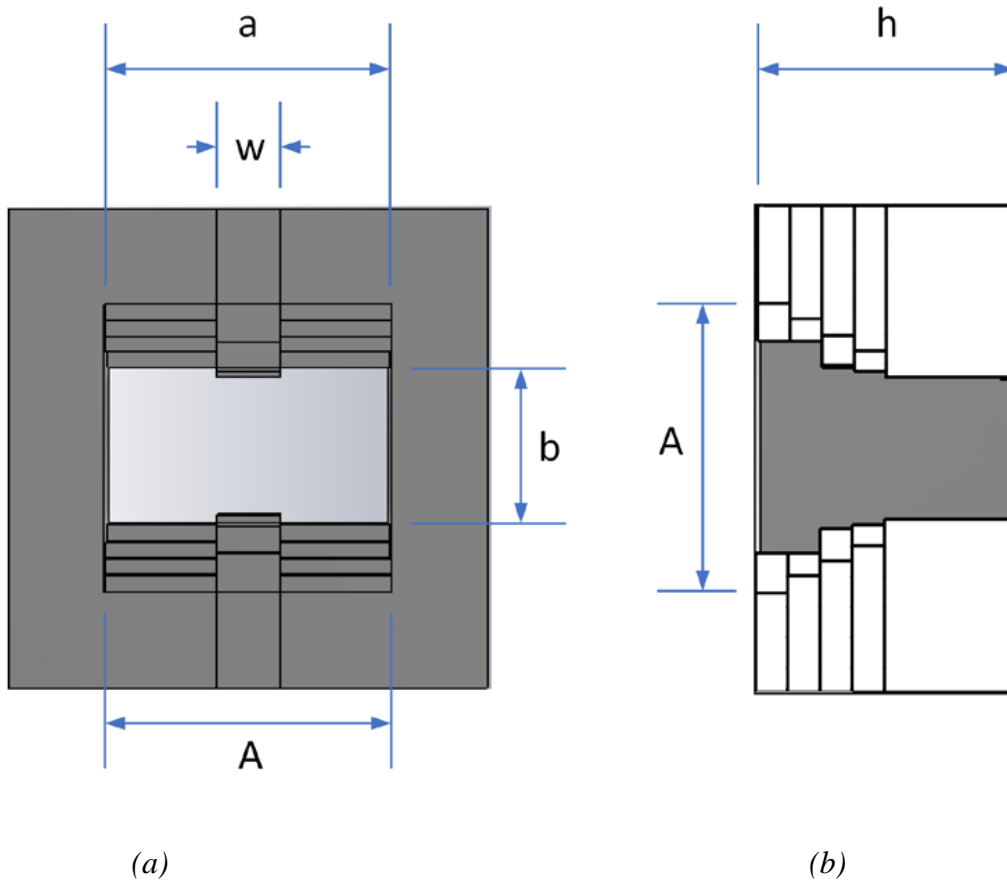

(a) *(b)*

Fig. 6.1. Structure of the horn waveguide antenna as the (a) front view. (b) cross-section. The dimensions are A = a = 9, b = 4.5, h = 8, w = 2, all in millimeters.
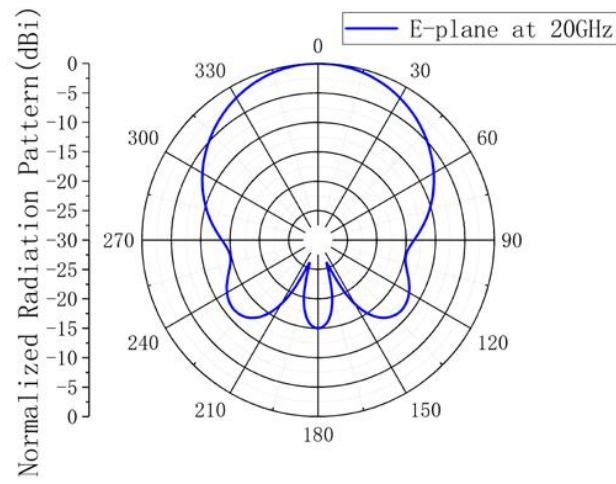
The linear-polarized waveguide antenna is designed as a horn waveguide structure to achieve higher gain and wideband performance as Fig. 6.1 (a) and (b) [96].

The stepped ridge structure is adopted to improve the bandwidth, reduce the size and help impedance matching [97]. Compared to a rectangular waveguide of the same size, a ridge waveguide could have a lower cut-off frequency of the fundamental mode, which means it will have a smaller size for the same operating frequency. The propagation mode is TE10 due to the waveguide length $0.5\lambda<a<\lambda$.
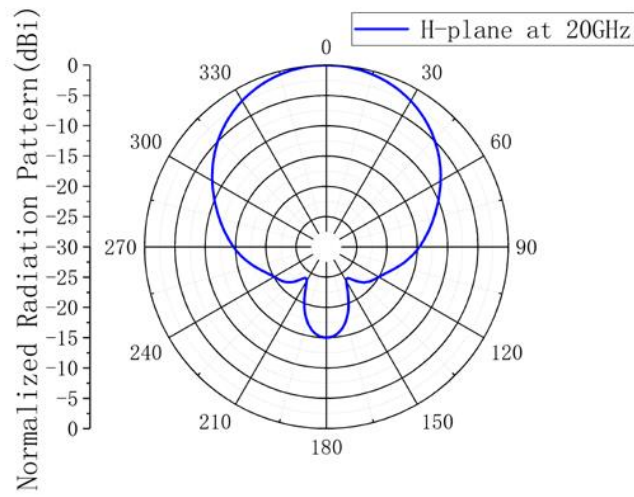
The linear-polarized waveguide antenna simulated return loss and far-field patterns from CST software are demonstrated in Fig.6.2 (a), (b), (c), (d), and (e). For a phased antenna array, the gain and the main lobe angular width will largely depend on the numbers, distributions, and distances of each antenna array element. An example of the 2×2 waveguide antenna array simulated far-field pattern is shown in Fig. 6.3, which could demonstrate the difference between the 2×2 array and an individual waveguide antenna. The simulated gain is 7.99 dBi and the angular width (3 dB) is 72.2 degrees for the individual waveguide antenna. The simulated gain is 14.5 dBi and the angular width (3 dB) is 34.8 degrees for the 2×2 waveguide antenna. The array's main lobe direction will be controlled by the phase control sections of each antenna array element in a beamforming system.
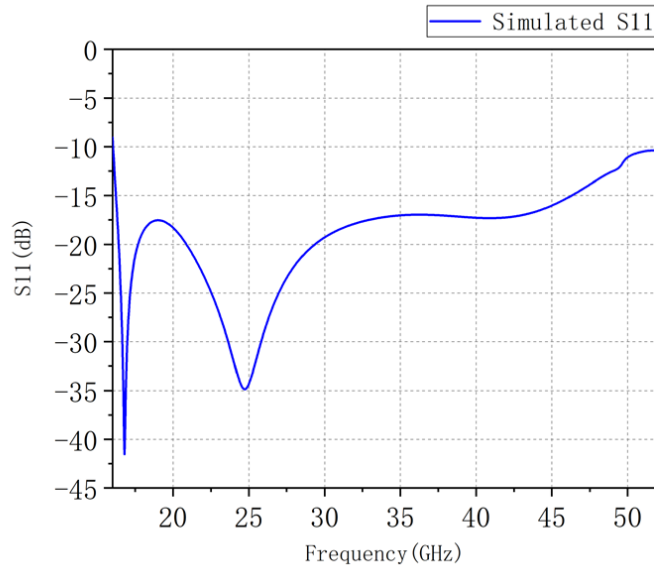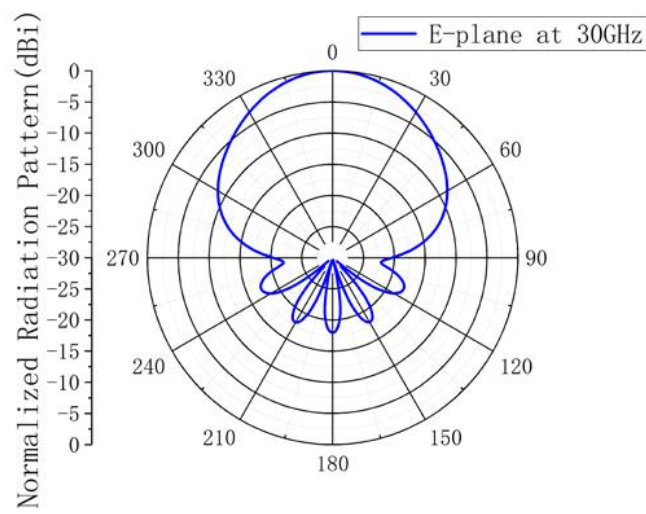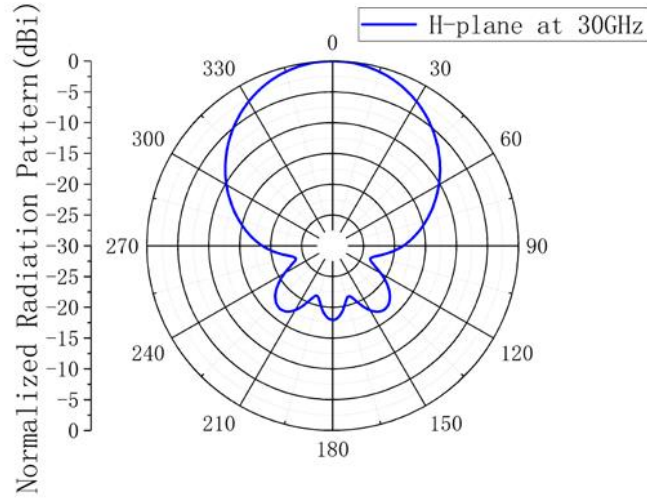

(a)

(b)

(c)

(d)

(e)

Fig. 6.2. (a) Simulated S11 of the linear-polarized horn waveguide antenna. Simulated far-field patterns at (b) E-plane at 20 GHz; (c) H-plane at 20 GHz; (d) E-plane at 30 GHz; (e) H-plane at 30 GHz
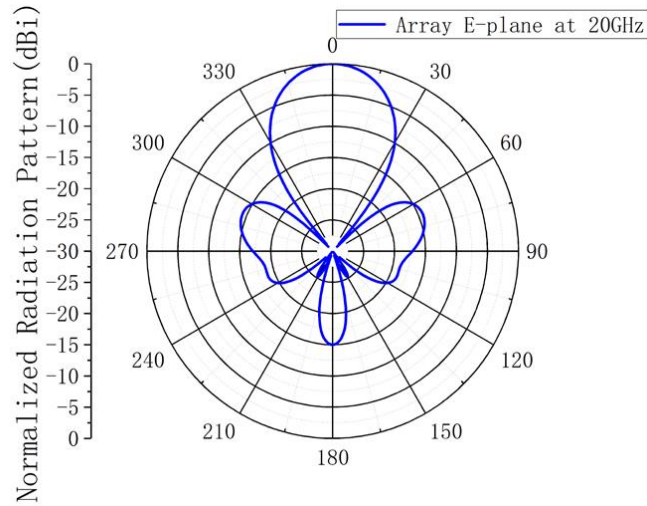

Fig. 6.3. Simulated E-plane far-field pattern of a 2×2 array at 20 GHz.

The linear-polarized waveguide antenna provided a wideband performance from 16 GHz to 52 GHz from the demonstrated simulation results, which could achieve wideband operations in both K/Ka-band beamforming applications.

6.2 Reconfigurable Dual Left-Handed/Right-Handed Modes Circular-Polarized Waveguide Antenna

The triangular-shaped slot or stepped transformer is used in many recent designs to achieve a CP operation by a combination of two orthogonal modes with equal amplitude and a 90-degree phase shift. The structure of the dual LH/RH CP waveguide antenna is shown in Fig. 6.4 (a) and (b). An orthogonal mode TE01 will be combined with the primary fundamental mode TE10, the principle theory to excite the CP wave is based on the odd/even-mode analyses [19-20].

When port 1 is excited, the decomposed even mode field and odd mode field are shown in Fig. 6.5. The same field directions in two layers of waveguides in even mode will lead to the unchanged TE10 mode at the output. The inverted field directions in odd mode will cause mode coupling at the triangular-shaped stepped transformers and lead to horizontal TE01 mode gradually. The different guided wavelengths of the two propagation modes (TE10 and TE01) will bring the required 90-degree phase shift to achieve a CP wave. The phase shift and the circular polarization performance will largely depend on the length of each part (L1, L2, L3).

By exciting port 2 instead, the only difference is the field directions in odd mode are reversed, which could develop an opposite rotation direction. Therefore, the LH/RH CP operations could be alternative by exciting two antenna waveguide ports respectively in beamforming applications. Meanwhile, an approximate hexagon structure is adopted in this waveguide design to achieve wider bandwidth and lower profile [98].

The two propagation modes caused by the hexagon waveguide structure are illustrated in Fig. 6.6, the different guided wavelengths of the two modes will cause a phase lag, which will also help to achieve the CP operation. Combined with the traditional two-layer waveguide with a triangular-shaped stepped transformers structure, the novel dual LH/RH CP waveguide antenna will achieve wider bandwidth and shorter height (Lh = L1+L2+L3). The simulated S11 from CST software when port 1 and port 2 are excited respectively are shown in Fig. 6.7. The far-field patterns at 20 GHz/ 30GHz by exciting port 1 from CST software are illustrated in Fig. 6.8 (a), (b),

(c), (d) and the far-field patterns at 20 GHz/ 30GHz by exciting port 2 are illustrated in Fig. 6.9 (a), (b), (c), (d). It demonstrated the CP antenna could provide a wideband performance for the required K/Ka-Band operation frequency range (20 GHz/30 GHz) with S11 better than -12.5 dB. Meanwhile, the 3dB Axial Ratio bandwidths are both 47.7% (20 GHz-32.5 GHz) for LH/RH CP modes due to their symmetrical structure, which is illustrated in Fig. 6.10. The height significantly decreased to 26 mm. Compared with previous designs [19-20], to achieve circular polarization from 20 GHz, it will commonly require around 45 mm height (3λ) to develop a CP wave.
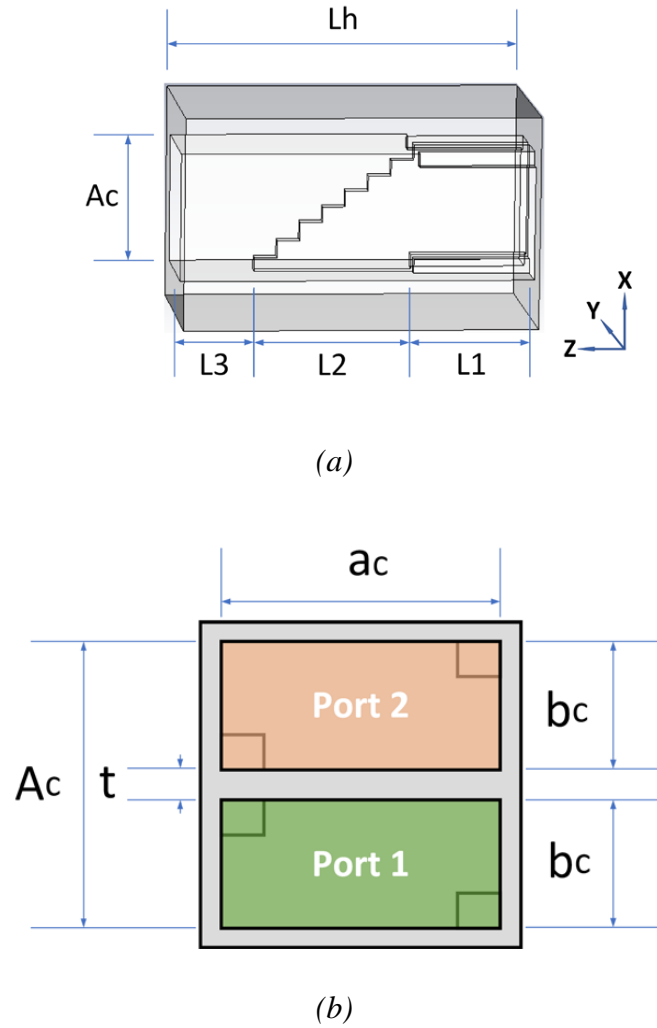

(a)

(b)

Fig. 6.4. Structure of the (a) dual LH/RH CP waveguide antenna and (b) two input ports. The dimensions are Ac = ac = 9, L1 = 10.2, L2 =11.2, L3 = 5.6, t = 1, bc = 4, all in millimeters.
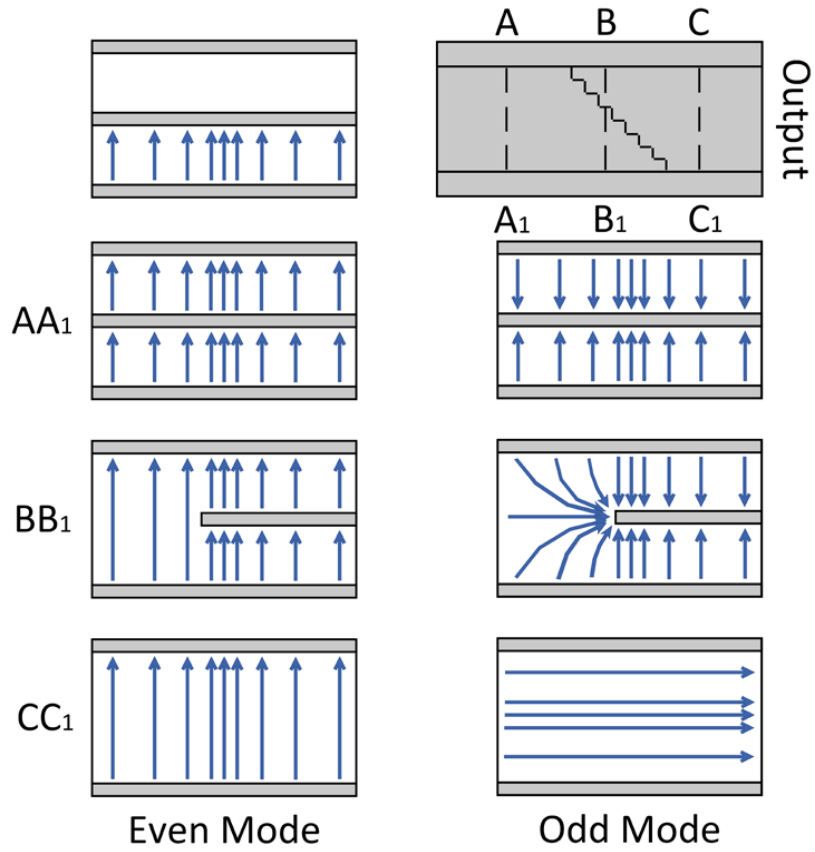
Fig. 6.5. The odd/even-mode analyses.
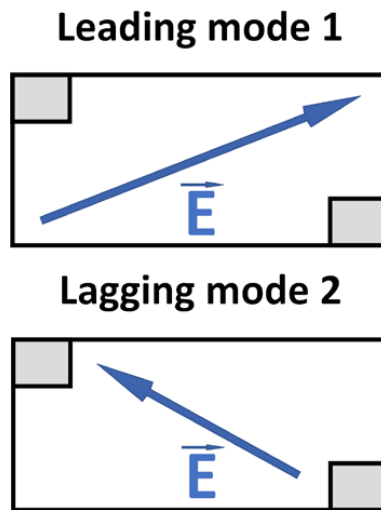
Leading mode 1

Lagging mode 2

Fig. 6.6. Two modes in the approximate hexagon waveguide.

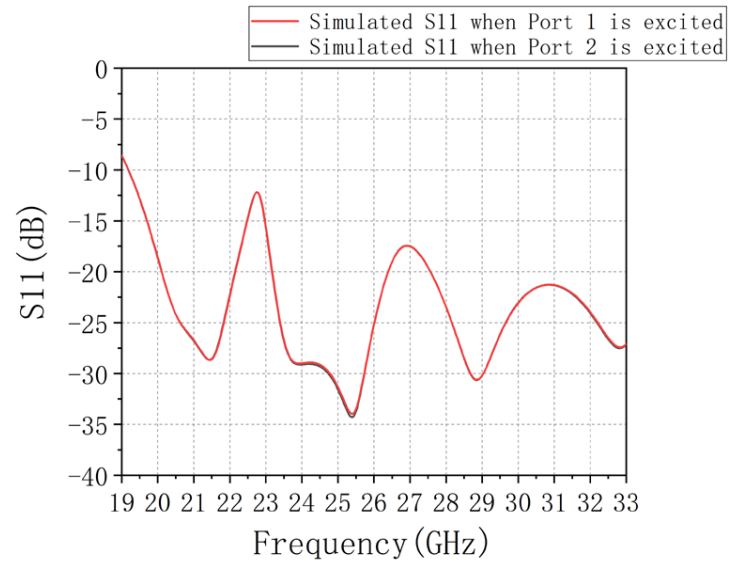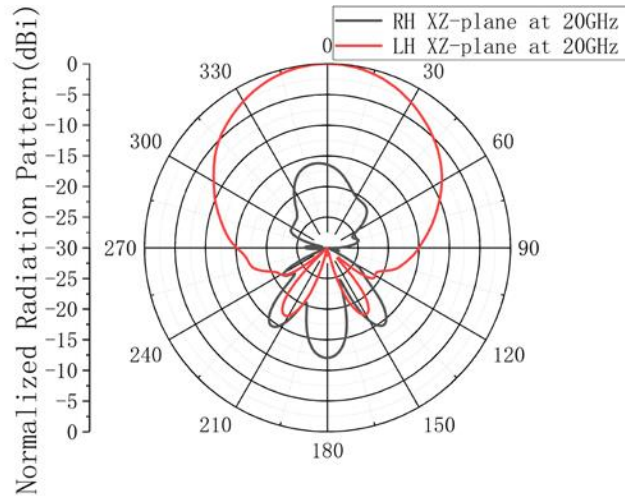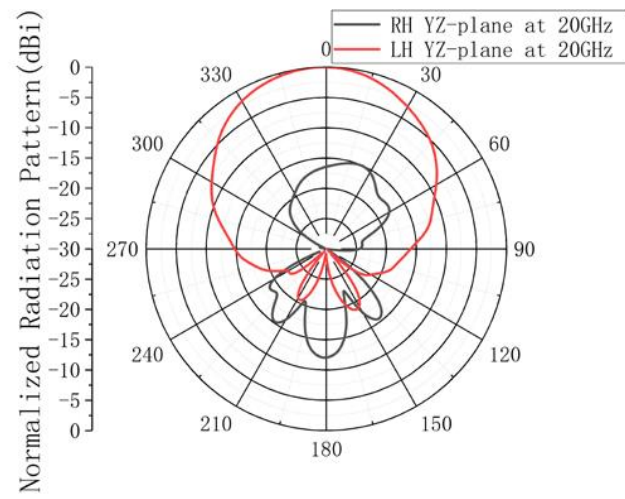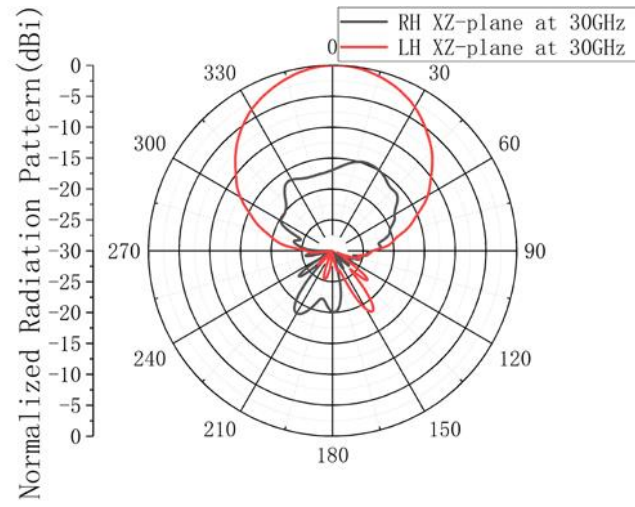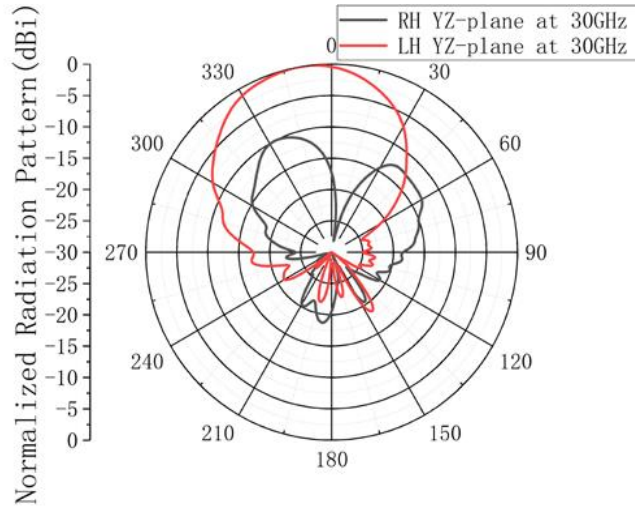*Fig. 6.7. Simulated S11 of the dual LH/RH CP waveguide antenna.*

(a)

(b)

95

(c)

(d)

Fig. 6.8. When port 1 is excited, (a) xz-plane pattern and (b) yz-plane pattern at 20 GHz;

(c) xz-plane and (d) yz-plane at 30 GHz.

(a)

(b)

(c)
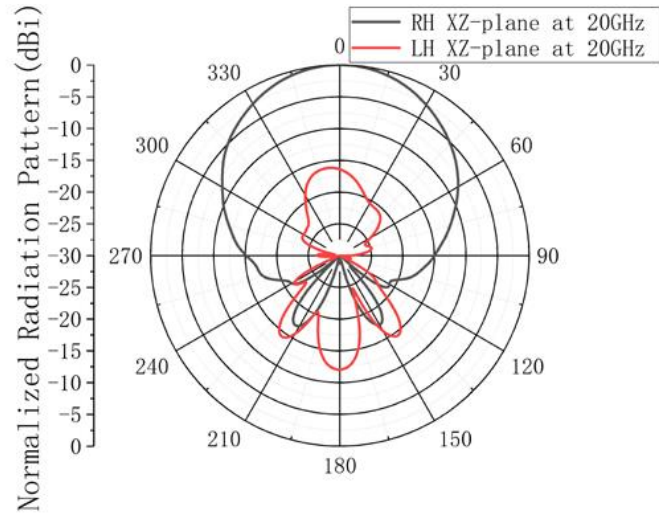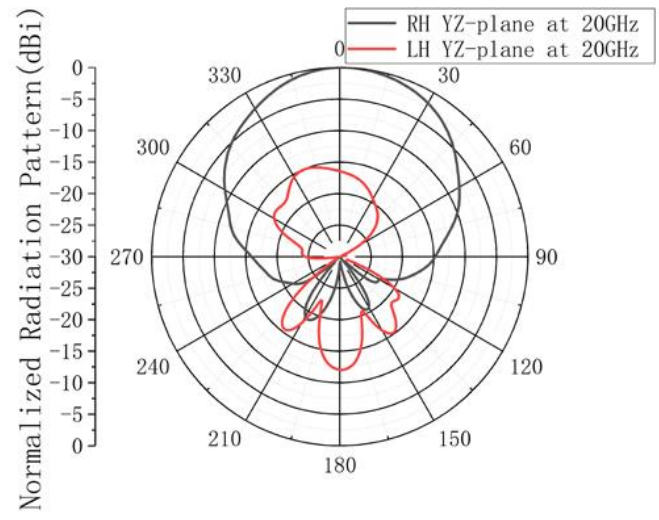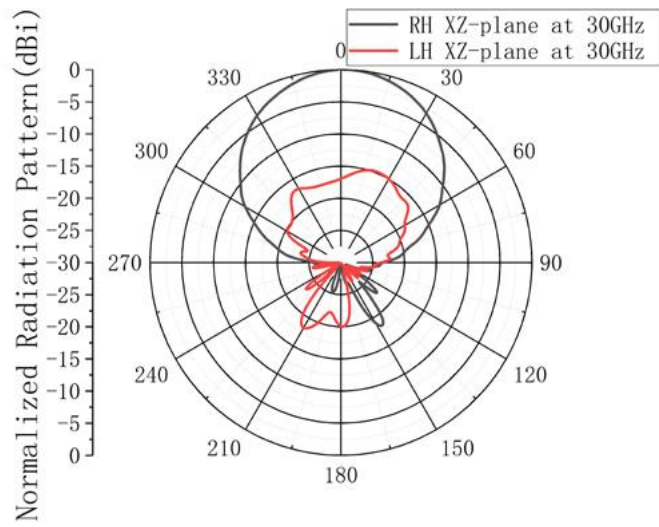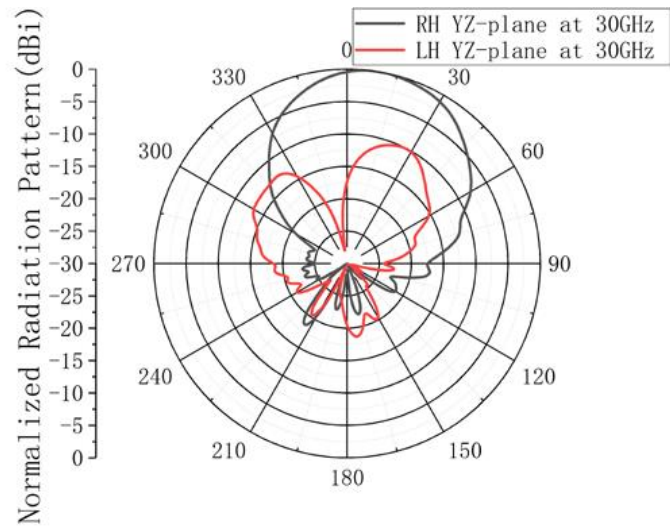
97

(d)

Fig. 6.9. When port 2 is excited, (a) xz-plane pattern and (b) yz-plane pattern at 20 GHz;

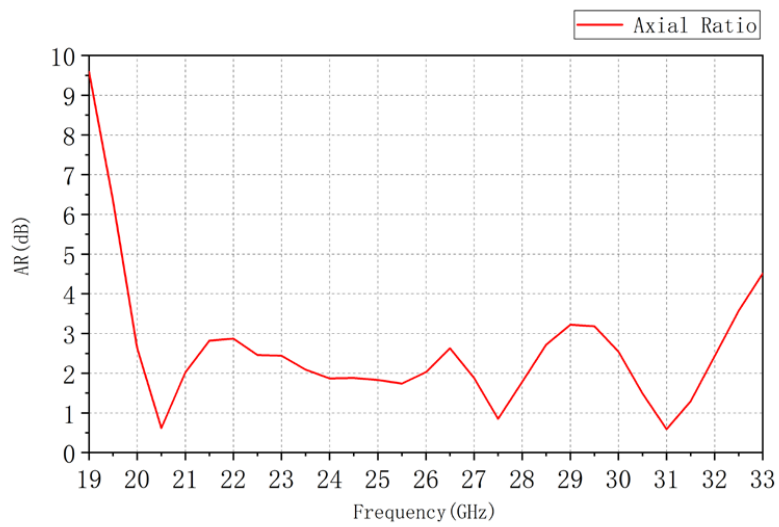*(c) xz-plane and (d) yz-plane at 30 GHz.*

Fig. 6.10. Axial Ratio.

6.3 Fabricated and Measured Results

To get some preliminary experimental results, the single LP waveguide antenna and CP antenna are connected to the SICL-to-waveguide transitions for 20/30 GHz modes respectively, which are illustrated in Fig. 6.11 (a) and (b).
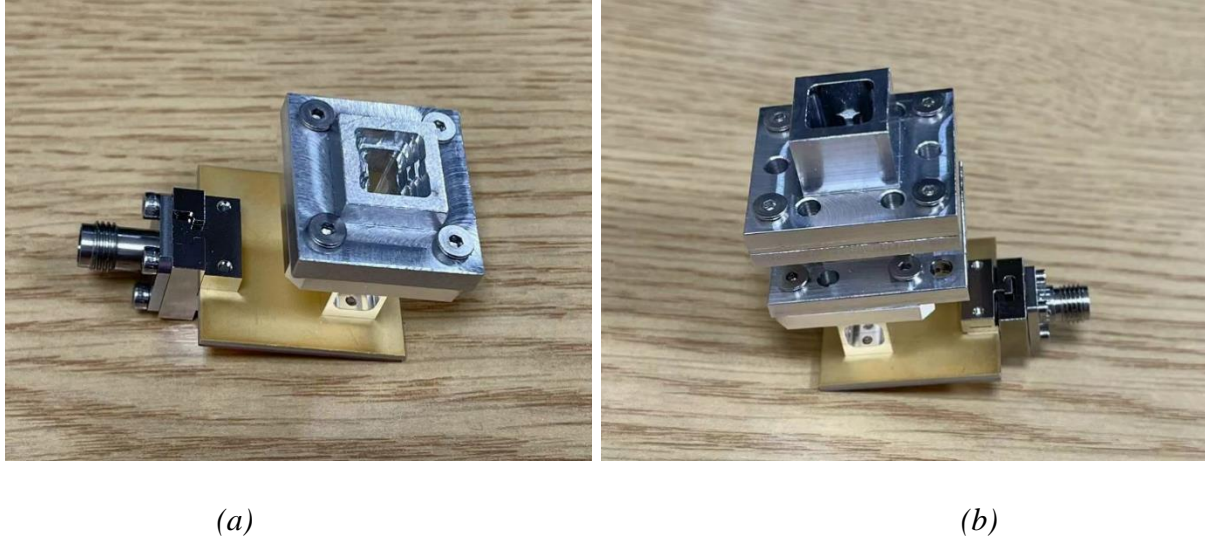

(a)   *(b)*

Fig. 6.11. (a) Fabricated linear-polarized waveguide antenna and (b) fabricated circular-polarized waveguide antenna with SICL-to-waveguide transitions.

There are some preliminary experimental results about the fabricated single LP/CP waveguide antenna. The drilling diameter is 1 mm for both the LP waveguide antenna and the CP antenna. There is a drilling thickness limitation for fabrication, so the CP waveguide antenna is split into two parts to make it easier to manufacture. The DAMS Antenna Measurement Studio in a chamber with wave-absorbing material and a PNA-L device is used to test the far-field pattern of the antennas. The measured S11 of the LP/CP waveguide antenna is illustrated in Fig. 6.12 (a), (b), (c), and (d) for K/Ka-band respectively, the co-polar and cross-polar measured far-field patterns of the single LP waveguide antenna are shown in Fig. 6.13 (a), (b), (c) and (d) for K/Ka-band at E-plane and H-plane respectively. The left-handed/right-handed CP waveguide antenna far-field patterns are shown in Fig. 6.14 (a), (b), (c) and (d) and Fig. 6.15 (a), (b), (c) and (d) for K/Ka-band at XOZ-plane and YOZ-plane respectively.
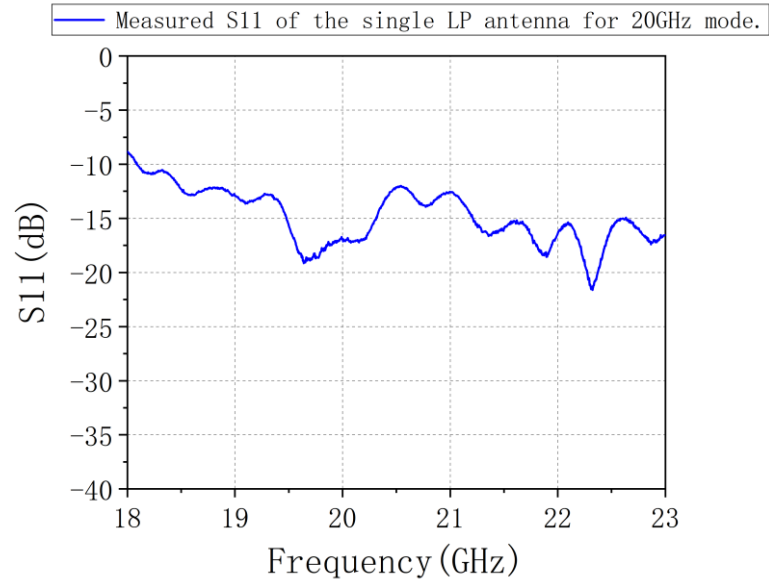
(a)
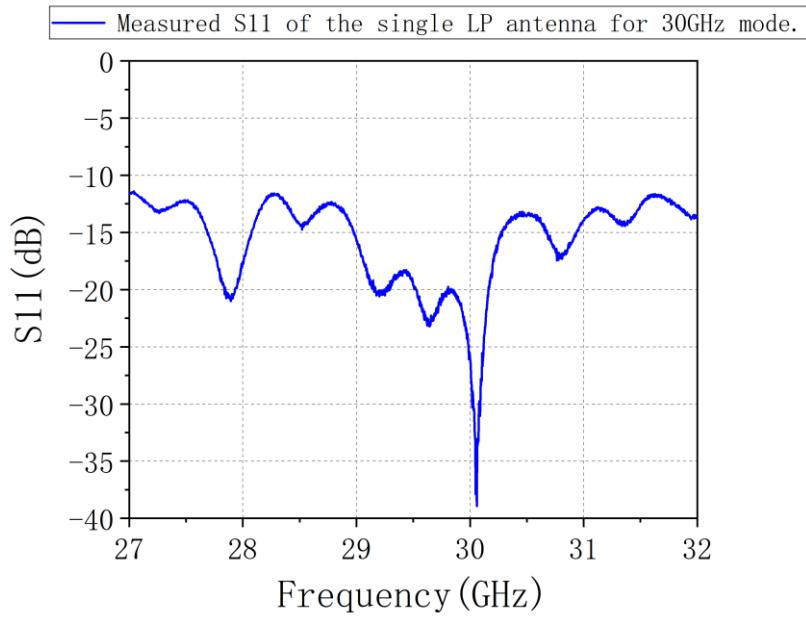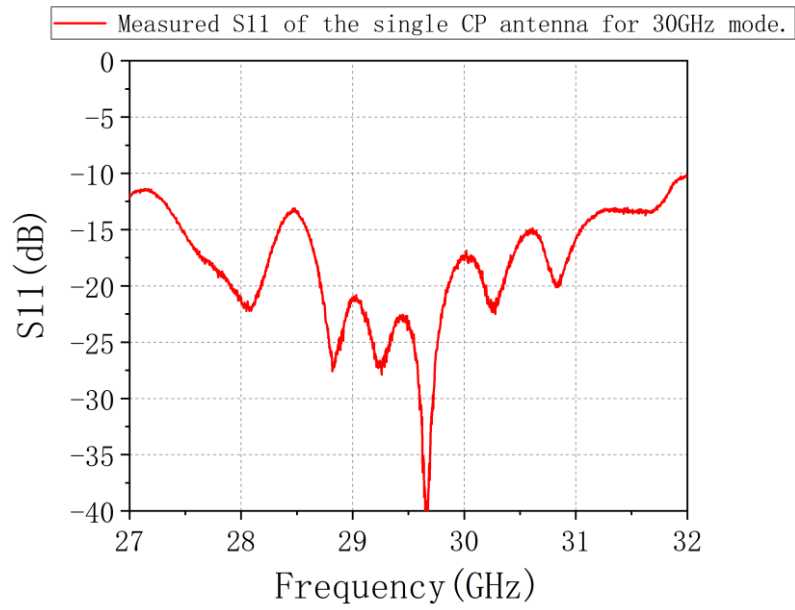

(b)
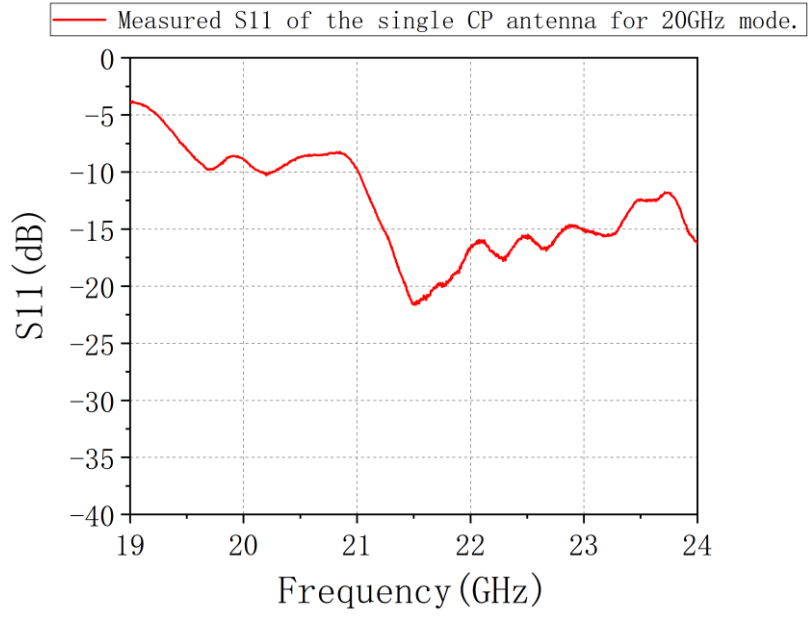
(c)

(d)

Fig. 6.12. Measured S11 of (a) LP antenna for 20GHz mode; (b) LP antenna for 30GHz mode; (c) CP antenna for 20GHz mode and (d) CP antenna for 30GHz mode.
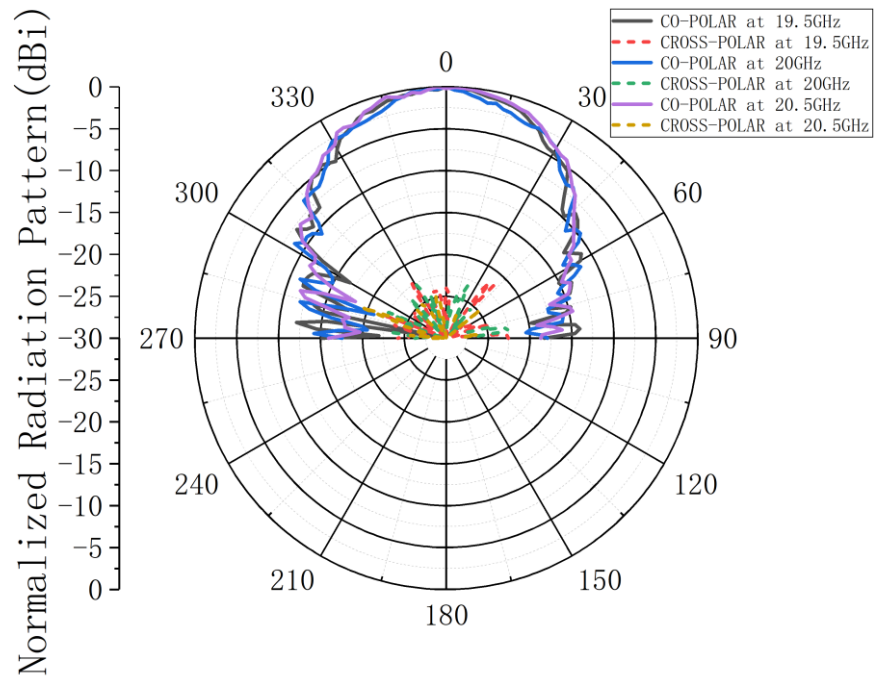
(a)
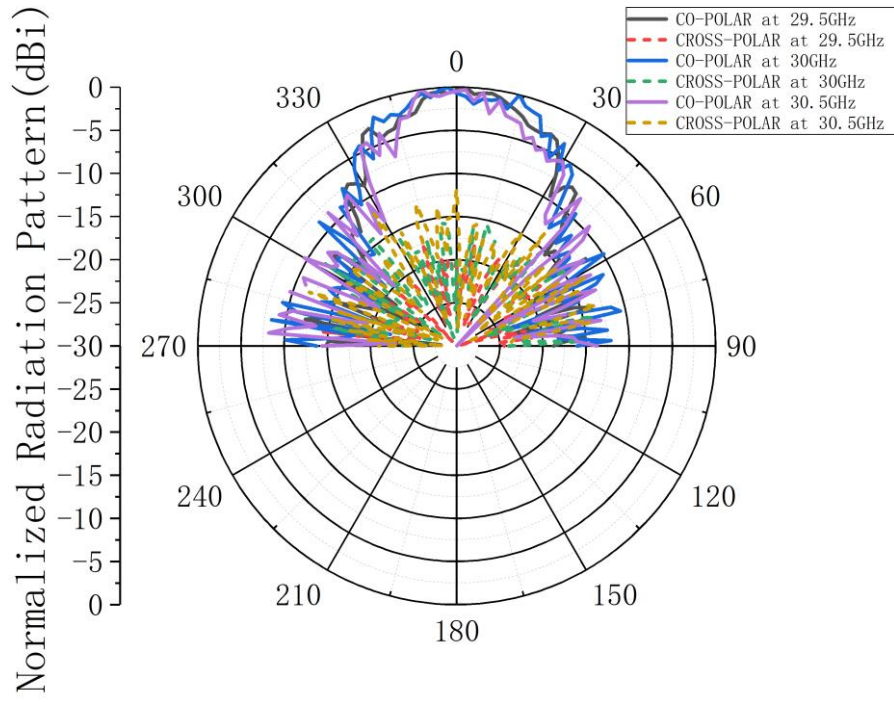
(b)
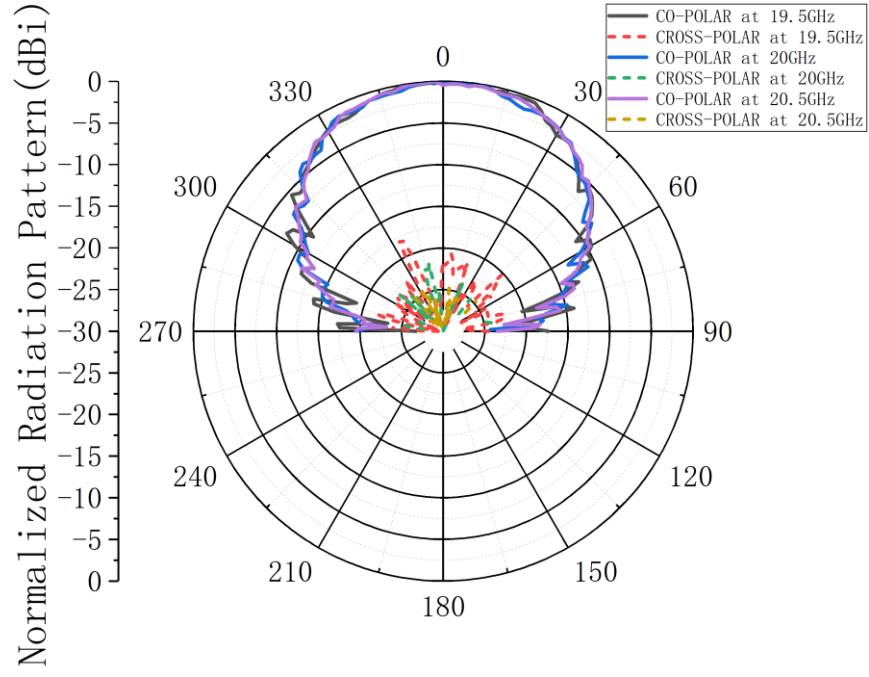
(c)
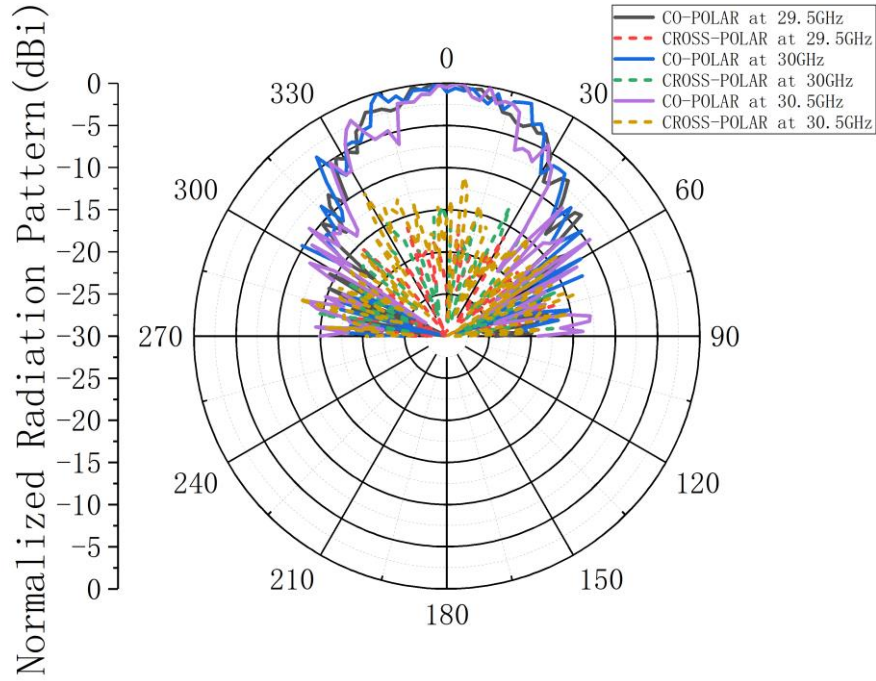
(d)

Fig. 6.13. Measured far-field patterns of single LP waveguide antenna at (a) 20GHz at E-plane, (b) 30GHz at E-plane, (c) 20GHz at H-plane, and (b) 30GHz at H-plane.
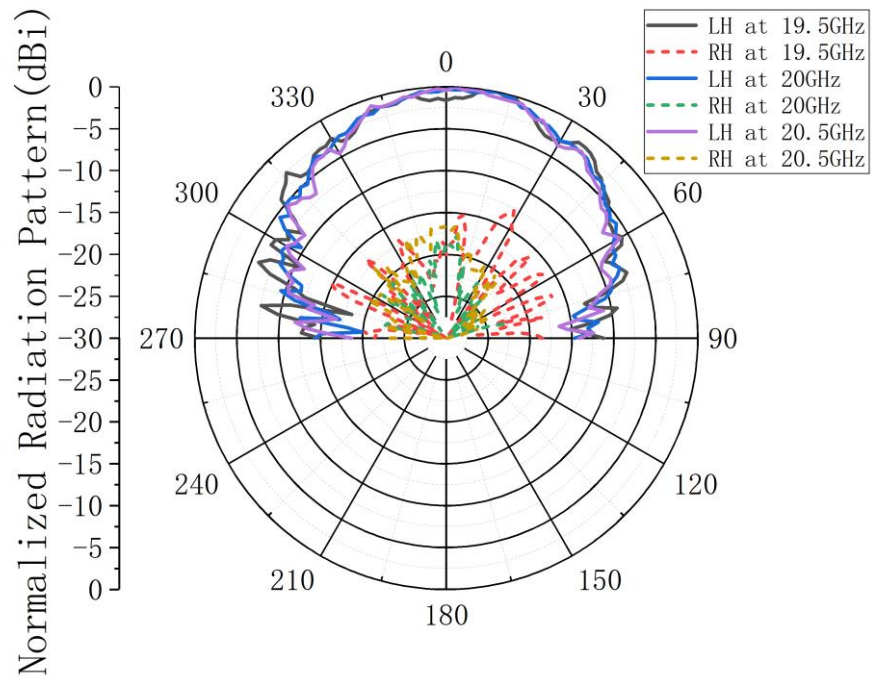
(a)
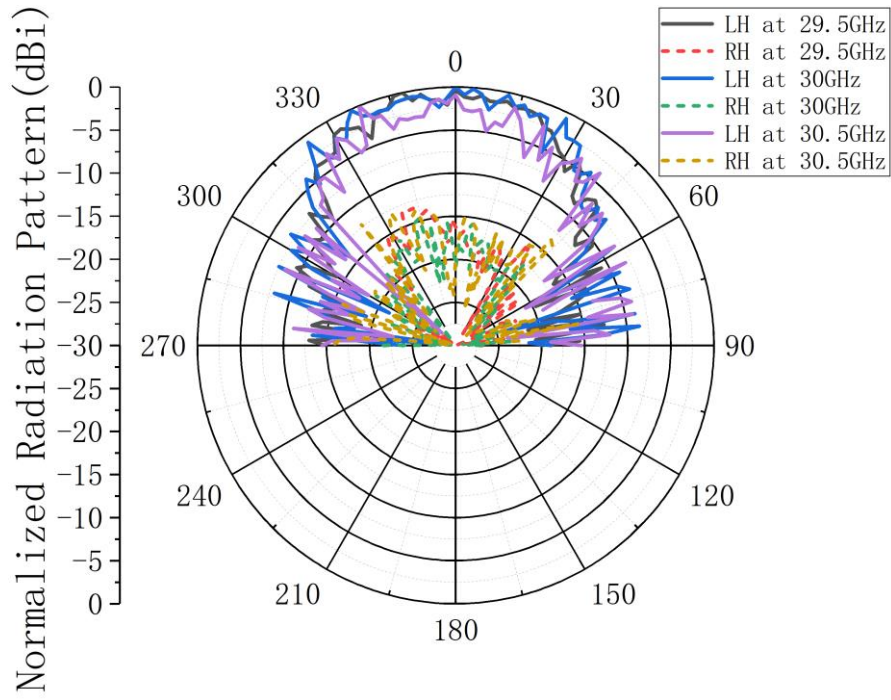
(b)
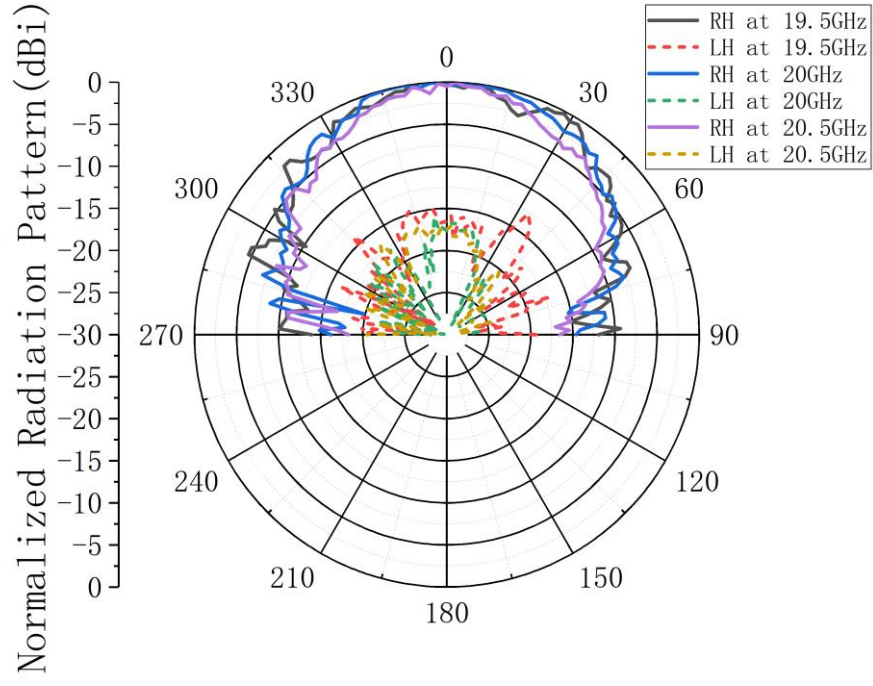
(c)
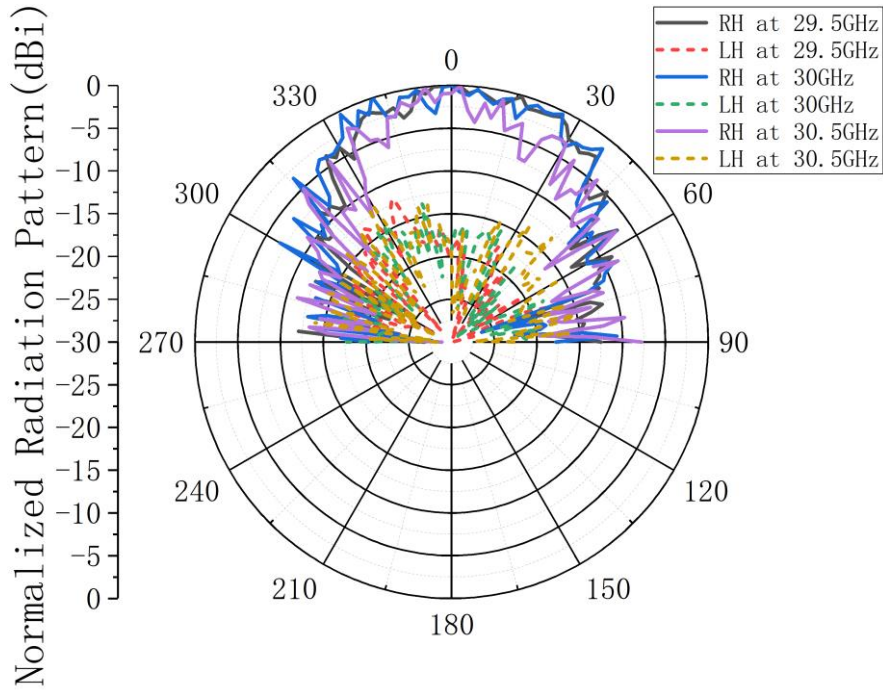
(d)

Fig. 6.14. Measured far-field patterns of left-hand single CP waveguide antenna at (a) K-band and (b) Ka-band at XOZ-plane; Measured far-field patterns of right-handed single CP waveguide antenna at (c) K-band and (d) Ka-band at XOZ-plane.
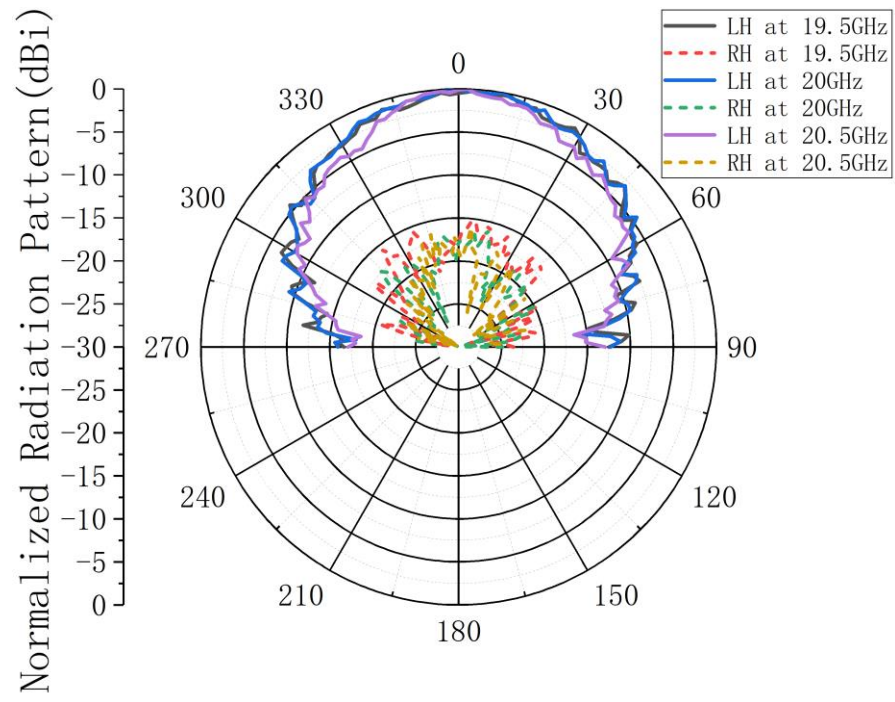
(a)
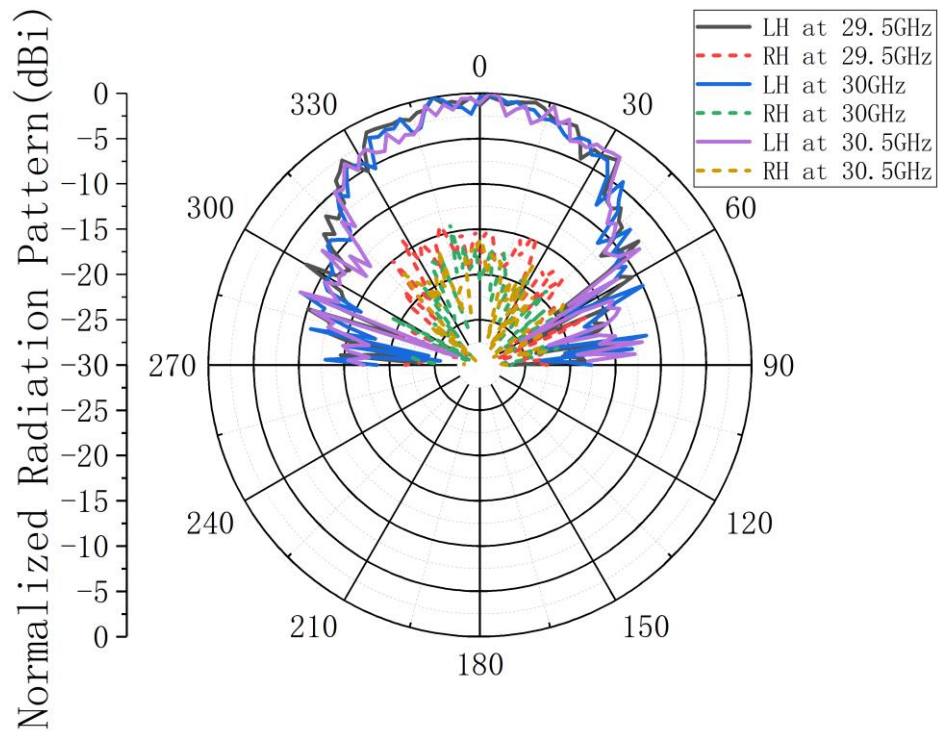
(b)
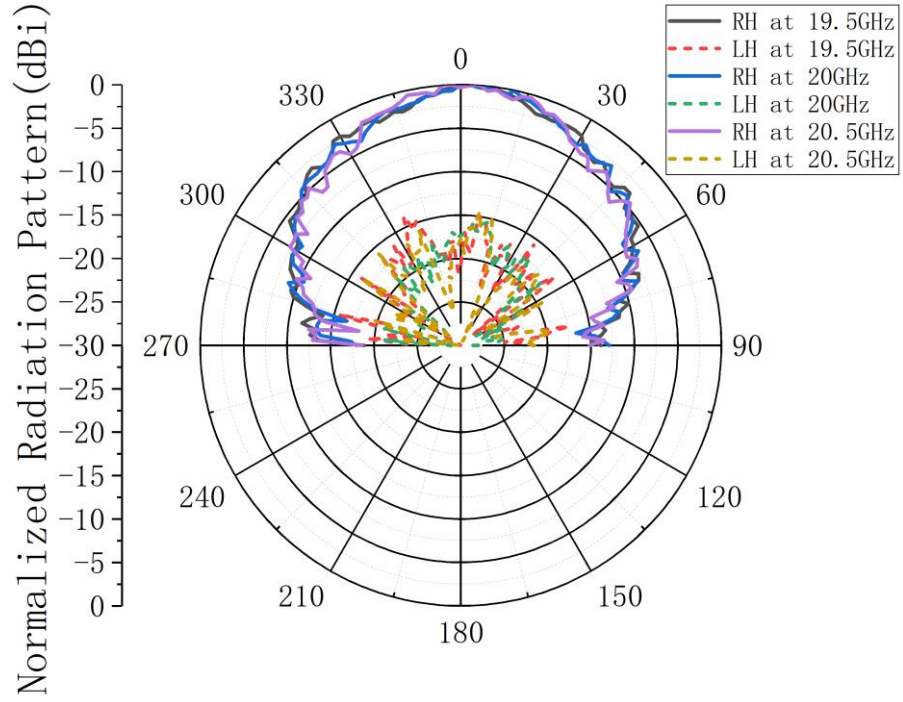
(c)
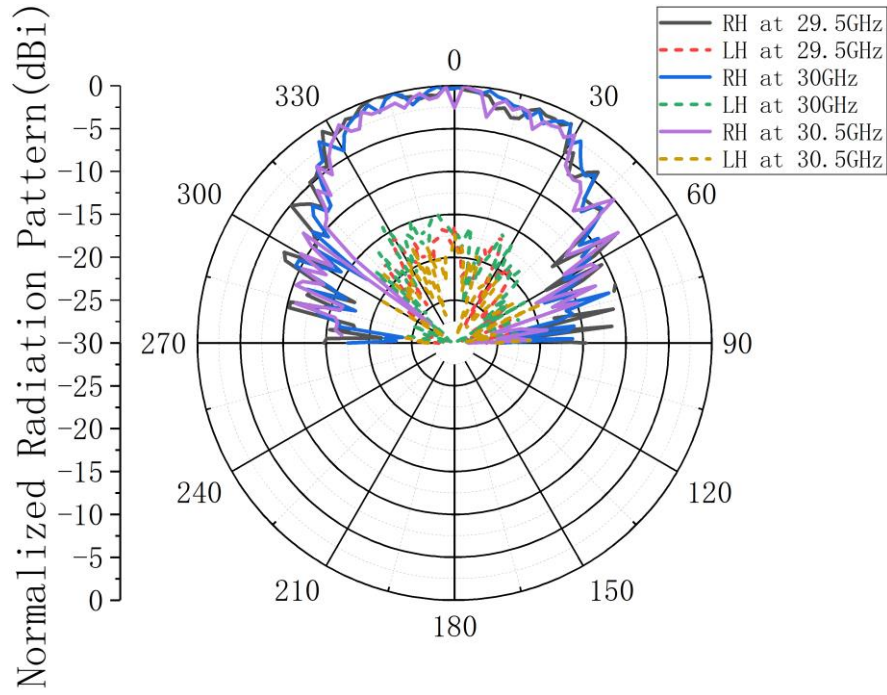
(d)

Fig. 6.15. Measured far-field patterns of left-handed single CP waveguide antenna at (a) K-band and (b) Ka-band at YOZ-plane; Measured far-field patterns of right-handed single CP waveguide antenna at (c) K-band and (d) Ka-band at YOZ-plane.

The measured axial ratios for the left-handed CP antenna and right-handed CP antenna are shown in Fig. 6.16 (a) and (b) for K/Ka-band mode respectively.

The measured results demonstrated good performance on wideband and circular-polarized operations at K/Ka-band.
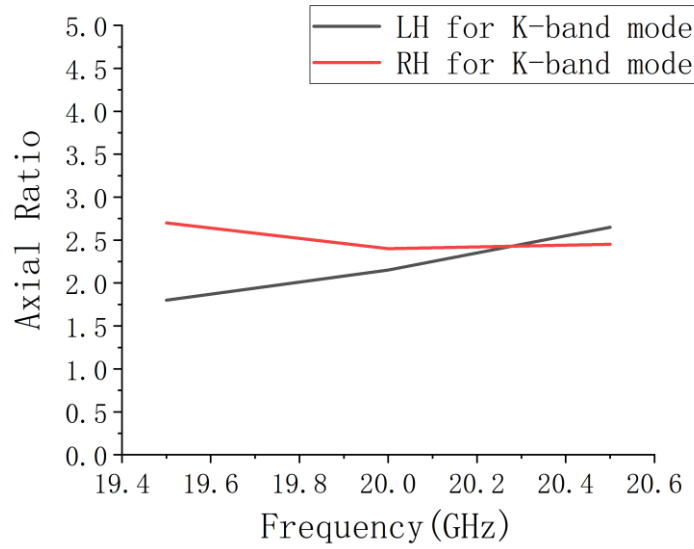
(a)
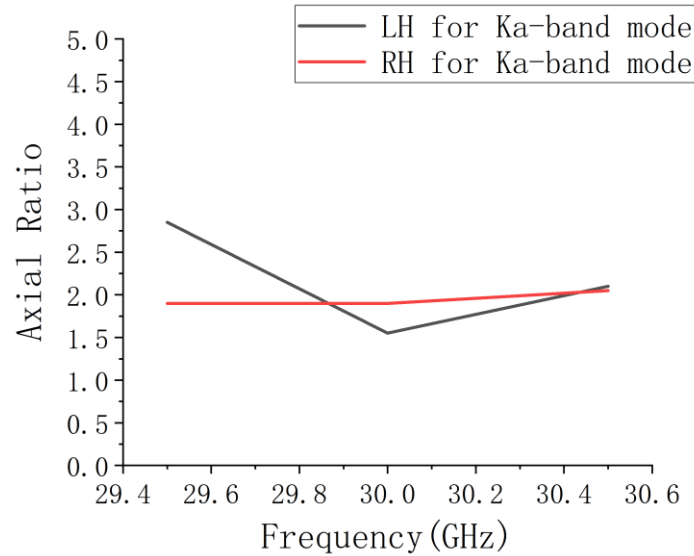
(b)

Fig. 6.16. Measured axial ratios of left-handed/right-handed CP antenna at (a) K-band mode and (b) Ka-band mode.

CHAPTER 7

Multi-Port Beamforming System for Reconfigurable Antenna Array

7.1 Design of One-Input-Four-Output Beamforming System Sample with Single-Layer Microstrip Structure Feeding Network

7.1.1. Reconfigurable Waveguide Linear-Polarized Antenna Array
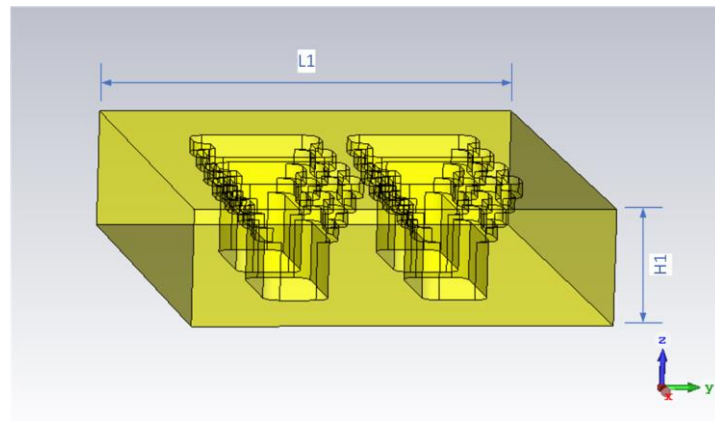
(a)
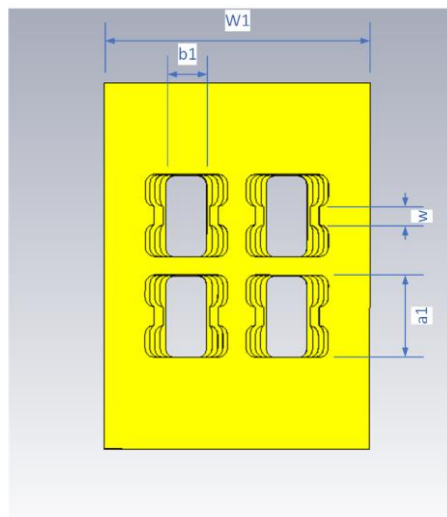
(b)

Fig. 7.1. (a) 3D structure of the 2×2 LP antenna array and (b) Top view of the 2×2 LP antenna array.

Table 7: Dimensions of the 2×2 LP antenna array (all in millimeters).

L1	W1	a1
40	29	9
b1	w	H1
4.5	2	8

The structure of a 2×2 LP antenna sample is demonstrated in Fig. 7.1 (a) and (b) with all dimensions in Table 7.

The simulated S-parameters of the 2×2 LP antenna array from CST software are shown in Fig. 7.2. (a) and (b). The far-field patterns from CST software are demonstrated in Fig. 7.3. (a), (b), (c), and (d).

The simulated gain is 14.3 dBi and the angular width (3 dB) is 34.9 degrees for the 2×2 LP waveguide antenna at 20 GHz, the simulated gain is 15.7 dBi and the angular width (3 dB) is 24.2 degrees for the 2×2 LP waveguide antenna at 30 GHz. The antenna array's main lobe direction will depend on the phase difference of each antenna element which is controlled by the phase and gain control sections.

(a)

110
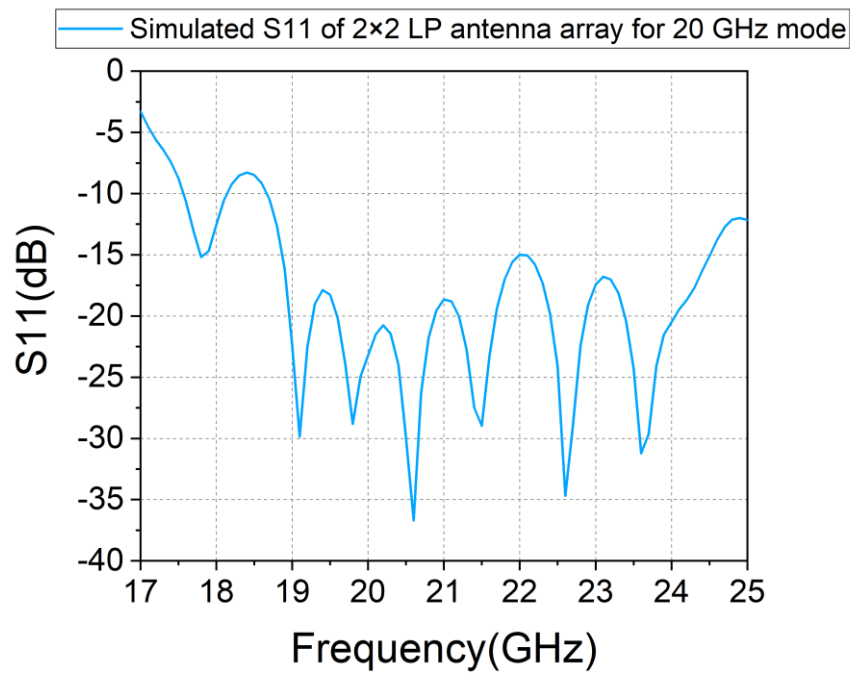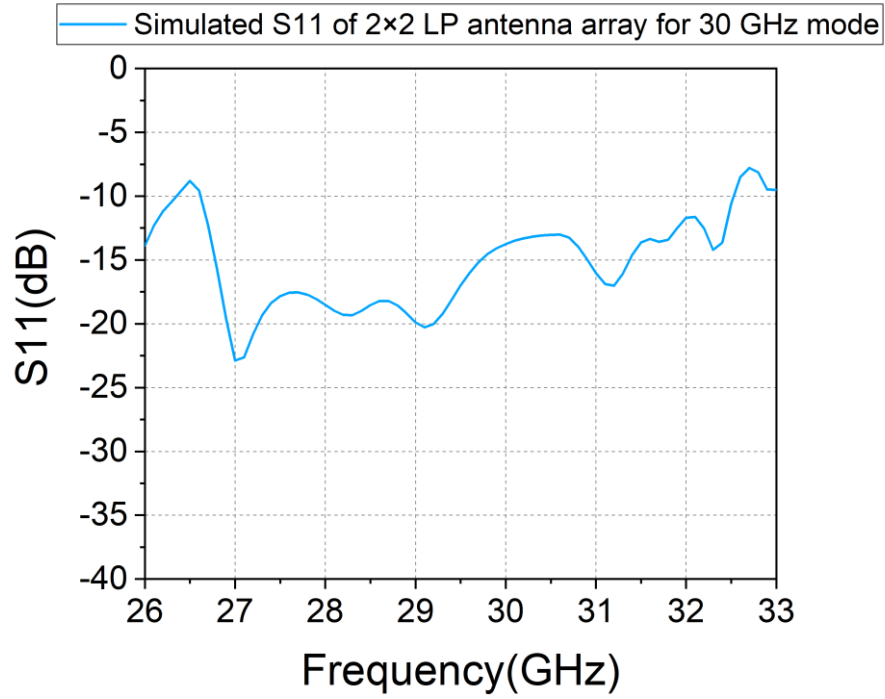
(b)

Fig. 7.2. Simulated S11 of 2×2 LP antenna array for (a) 20GHz mode and (b) 30GHz mode.
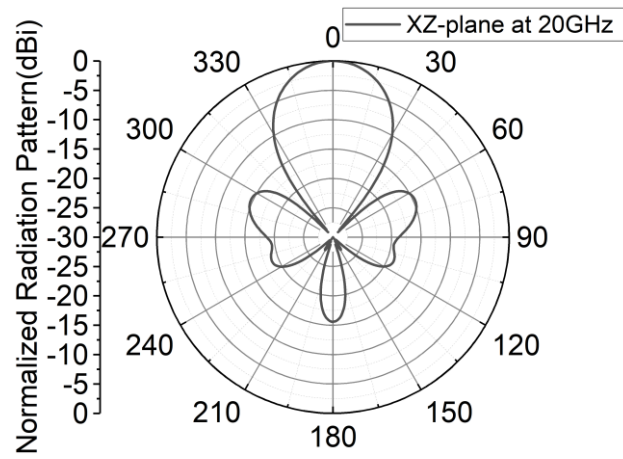
(a)
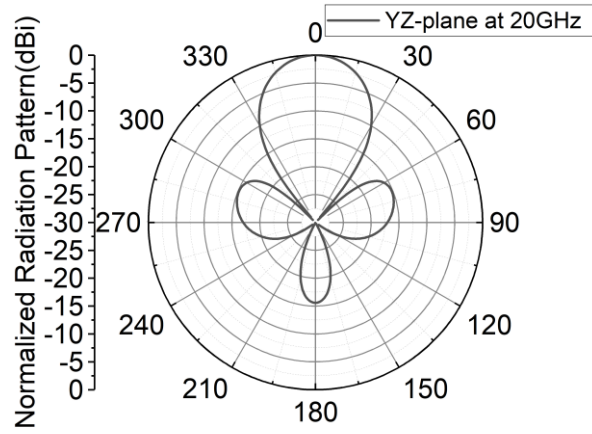
(b)
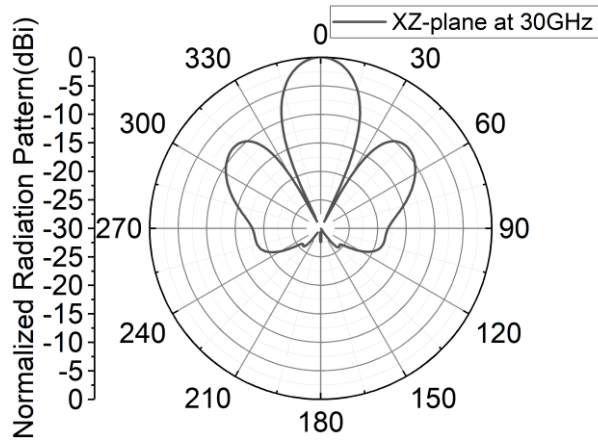
(c)

(d)

Fig. 7.3. Co-polar far-field patterns of 2×2 LP antenna array at 20GHz at (a) XOZ plane and (b) YOZ plane; Co-polar far-field patterns of 2×2 LP antenna array at 30GHz at (c) XOZ plane and (d) YOZ plane.

7.1.2. Reconfigurable Waveguide Dual Left-Handed/Right-Handed Modes Circular-Polarized Antenna Array

The structure of the 2×2 CP waveguide antenna array is illustrated in Fig. 7.4 (a) and (b) with all dimensions in Table 8. The right-handed/left-handed CP wave will be controlled by replacing the reconfigurable CP waveguide antenna array to choose port 1/port 2 to be fed by the waveguide ports from the waveguide transitions as Fig. 7.5.

The simulated S-parameters of the 2×2 CP antenna array from CST software are shown in Fig. 7.6. (a) and (b). The right-handed antenna array far-field patterns from CST software are demonstrated in Fig. 7.7. (a), (b), (c), and (d), the left-handed antenna array far-field patterns are demonstrated in Fig. 7.8. (a), (b), (c) and (d), the Axial Ratio is shown in Fig. 7.9. (a) and (b).

The simulated gain is 13.1 dBi and the angular width (3 dB) is 41.7 degrees for the 2×2 CP waveguide antenna at 20 GHz, the simulated gain is 15.8 dBi and the angular width (3 dB) is 23.2 degrees for the 2×2 CP waveguide antenna at 30 GHz.
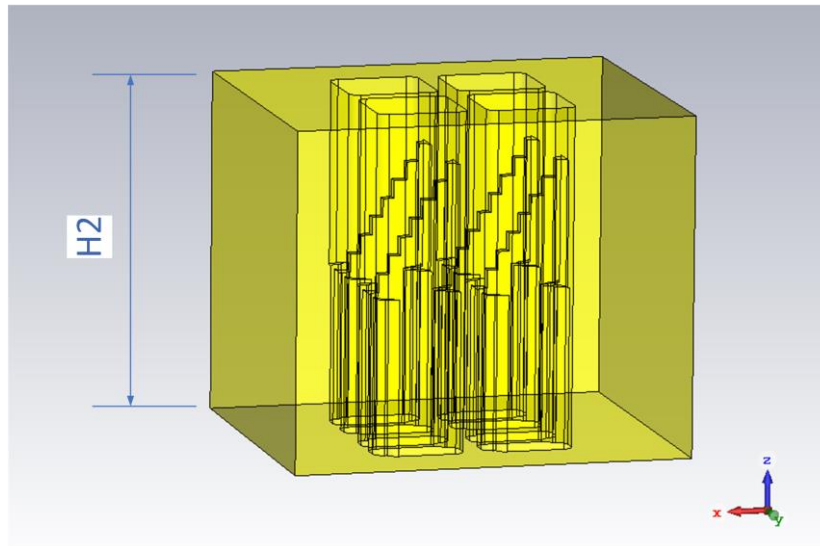
(a)
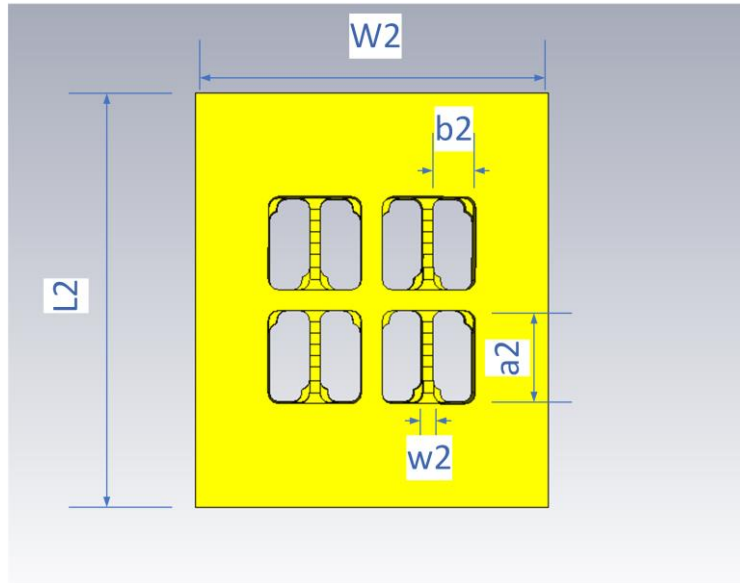
(b)

Fig. 7.4. (a) 3D structure of the 2×2 CP antenna array and (b) Top view of the 2×2 CP antenna array.

Table 8: Dimensions of the 2×2 CP antenna array (all in millimeters).

L2	W2	a2
40	34	9
b2	w2	H2
4	1	34
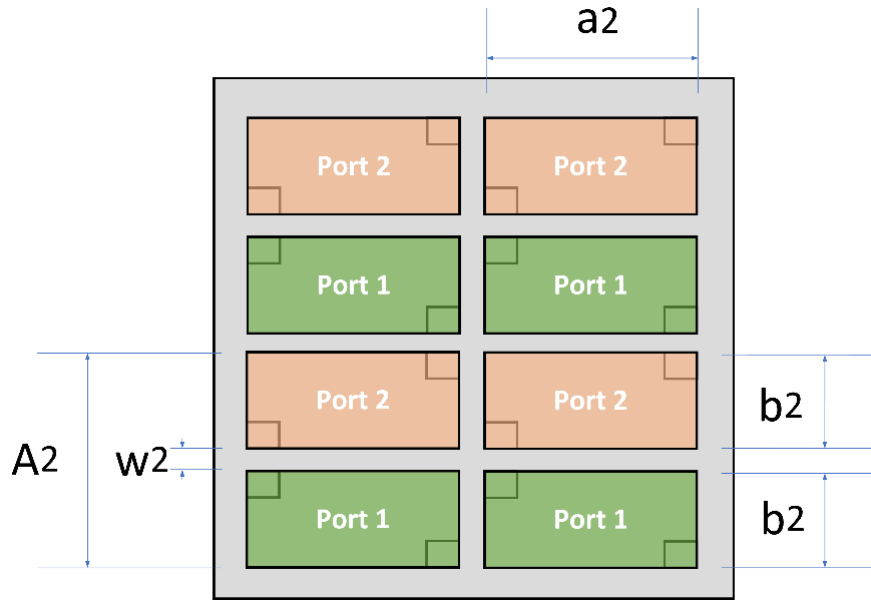
Fig. 7.5. The sketch of CP waveguide antenna ports. The dimensions are A2 = 9, w2 = 1, a2 = 9, b2 = 4, all in millimeters.
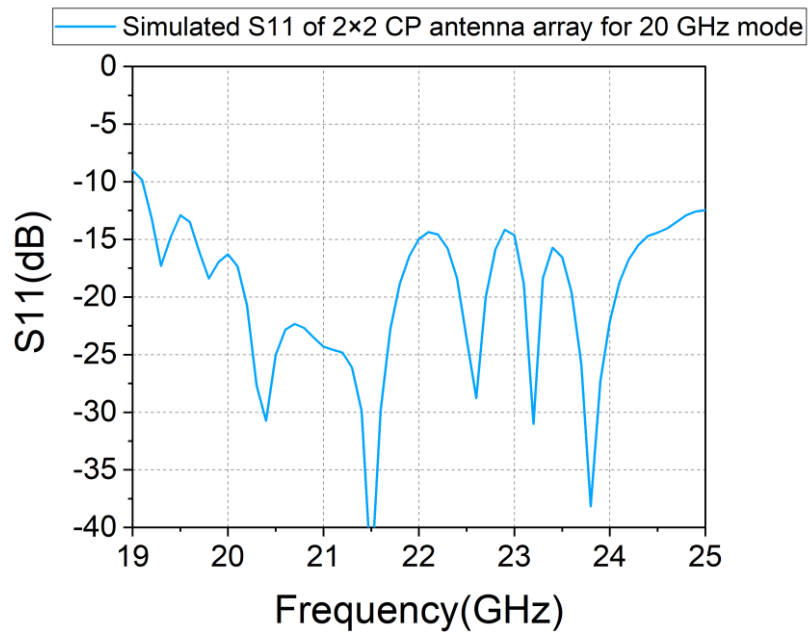

(a)
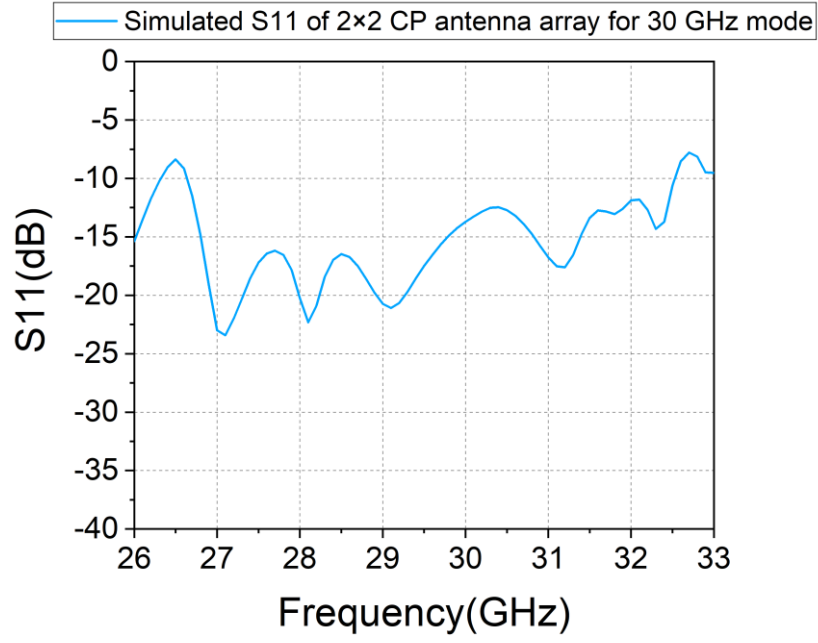
(b)

Fig. 7.6. Simulated S11 of 2×2 CP antenna array for (a) 20GHz mode and (b) 30GHz

mode.

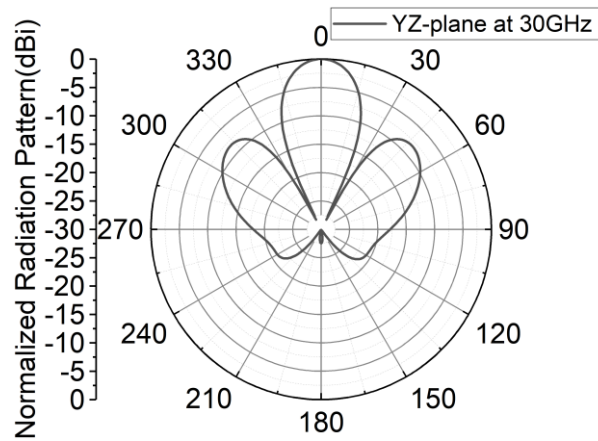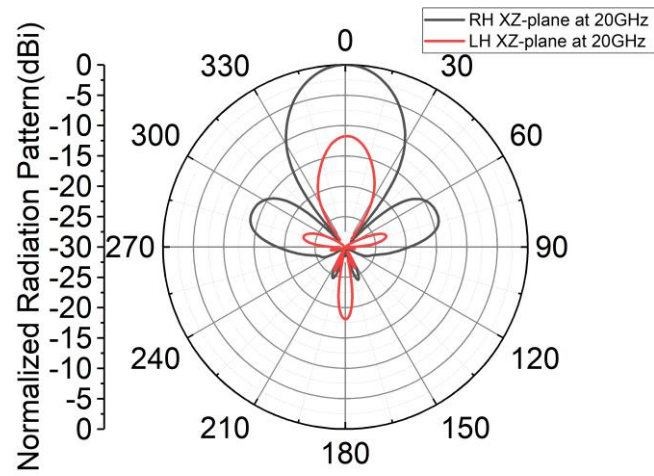*(a)*
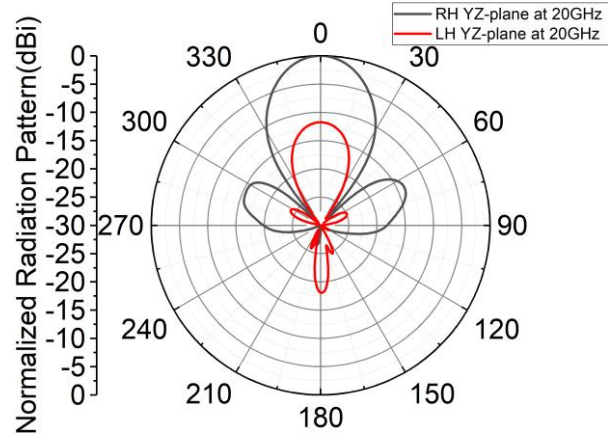
(b)
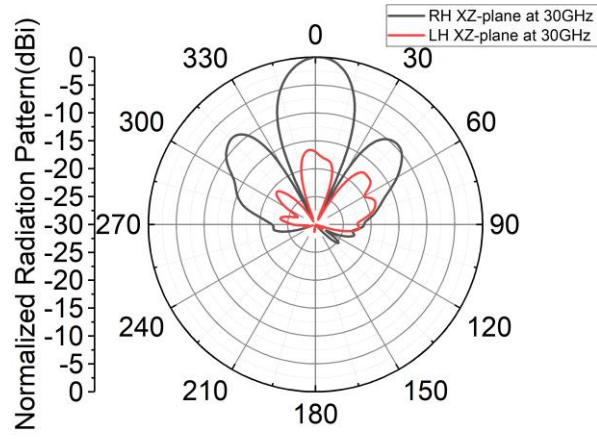
(c)
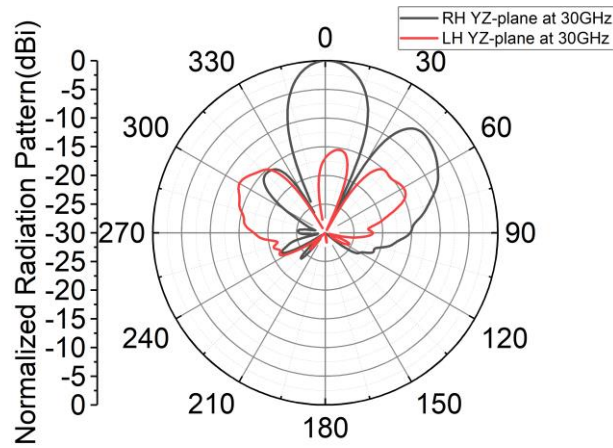
(d)

Fig. 7.7. Far-field patterns of 2×2 CP right-handed waveguide antenna array at 20GHz at (a) XOZ plane and (b) YOZ plane; Far-field patterns of 2×2 CP right-handed waveguide antenna array at 30GHz at (c) XOZ plane and (d) YOZ plane.

117

(a)

(b)

(c)

118
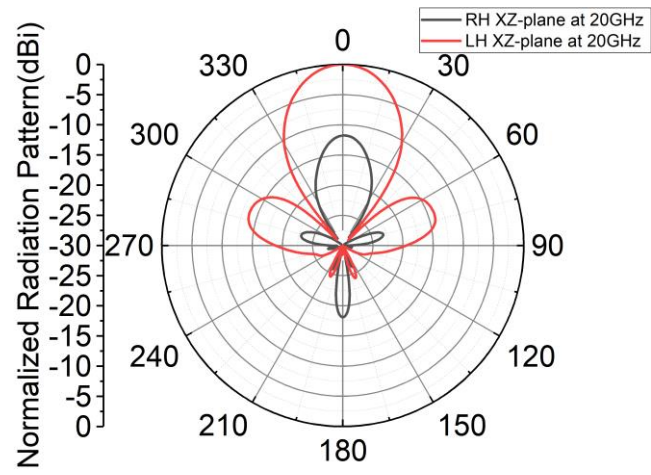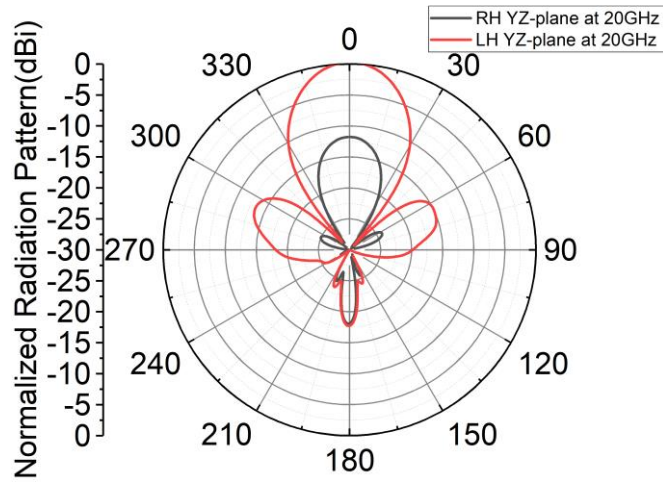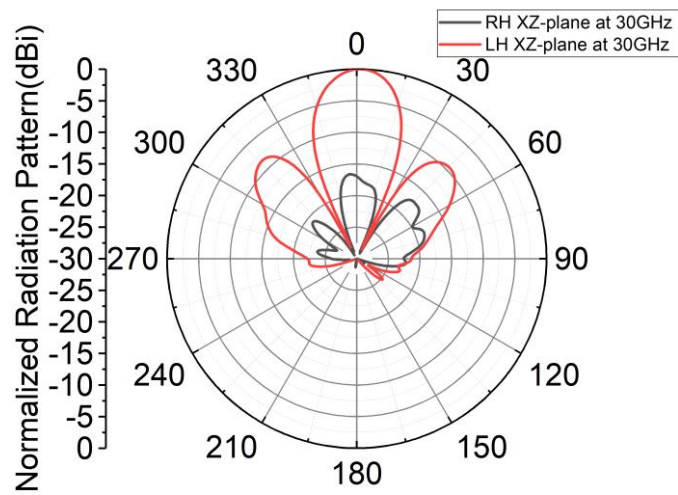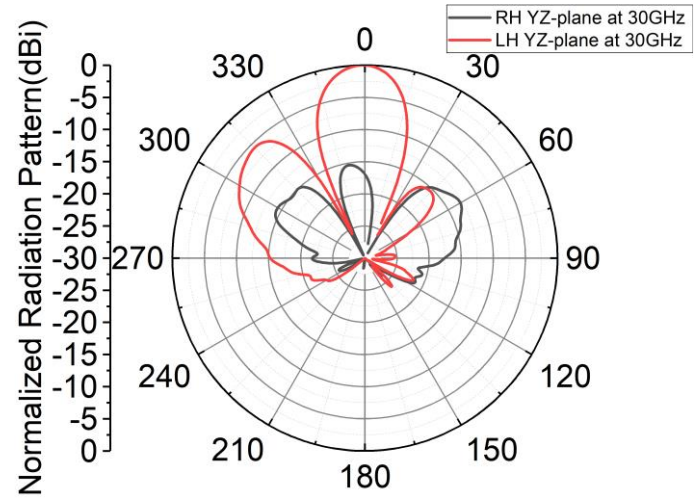
(d)

Fig. 7.8. Far-field patterns of 2×2 CP left-handed waveguide antenna array at 20GHz at (a) XOZ plane and (b) YOZ plane; Far-field patterns of 2×2 CP left-handed waveguide antenna array at 30GHz at (c) XOZ plane and (d) YOZ plane.
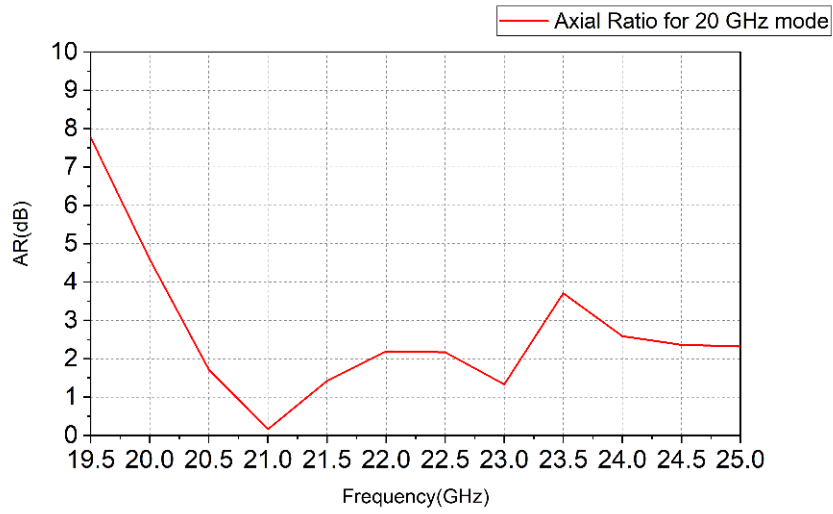
(a)
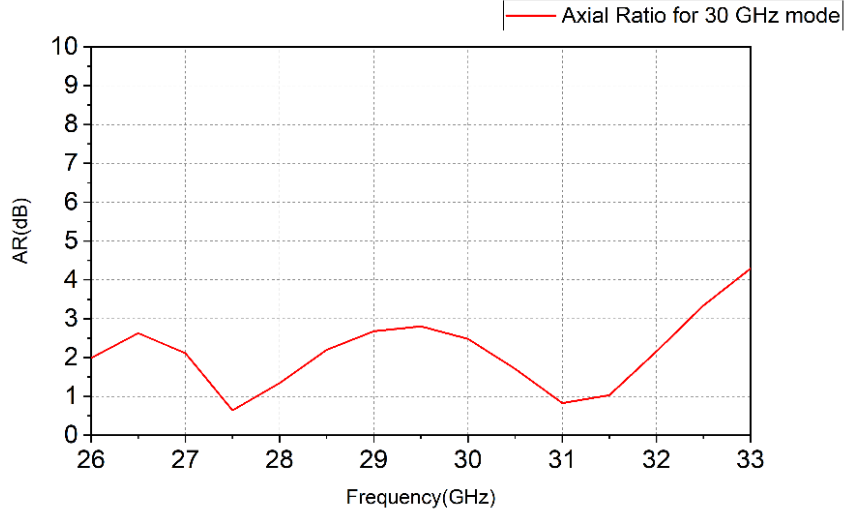
(b)

Fig. 7.9. Axial Ratio of the CP antenna array for (a) 20 GHz mode and (b) 30GHz mode.

7.1.3. Beamforming Analysis

The antenna array beam angle could be calculated from the formula [66]:

$$\varphi = \frac{2\pi d sin\theta}{\lambda}, \tag{24}$$

where φ is the signal phase shifting between each antenna element, d is the distance from each element, λ is the wavelength and θ is the beam angle with respect to boresight direction.

The beam angle could be calculated as 13.1 and 8.7 degrees at 20 GHz and 30 GHz respectively when the phase difference is 60-degree, which are familiar with the main lobe direction from simulated far-field patterns from CST software in Fig. 7.10 (a) and (b).

120
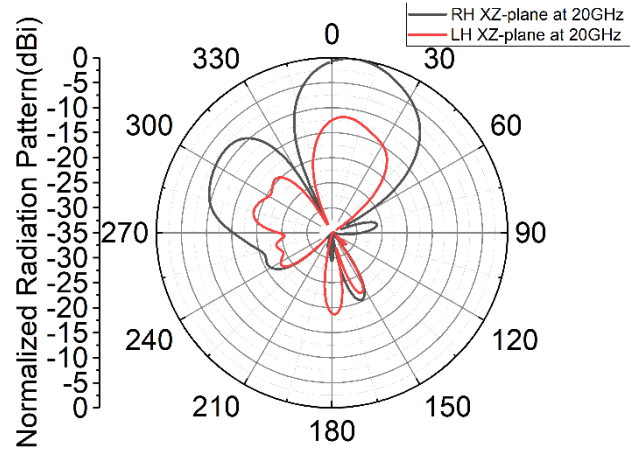
(a)
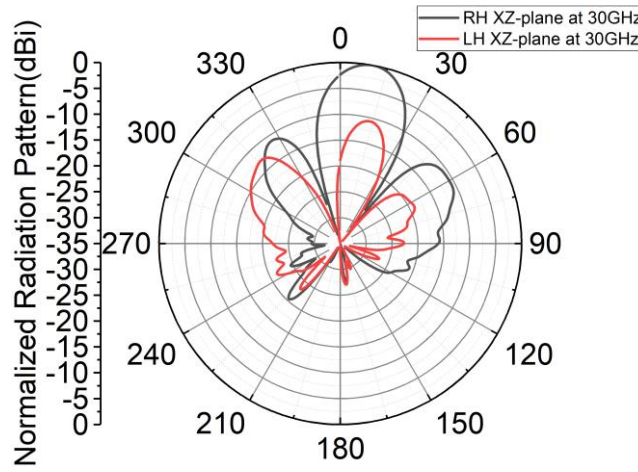
(b)

Fig. 7.10. Example of the far-field patterns of 2×2 right-handed CP antenna array with 60 degrees phase difference at XOZ plane at (a) 20 GHz and (b) 30GHz.

7.1.4 Fabricated and Measured Results

The fabricated PCB feeding network and the LP/CP waveguide antenna array are illustrated in Fig. 7.11 (a) and (b), the measurement environment is shown in Fig. 7.11 (c). All the waveguide parts are fabricated of aluminum. To get the measured far-field patterns of the beamforming system samples, The DAMS Antenna Measurement Studio in a chamber with wave-absorbing material and a PNA-L device is used.
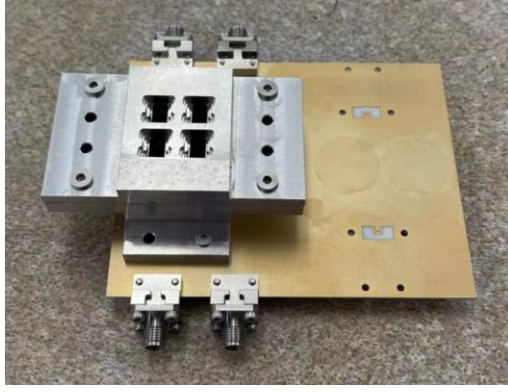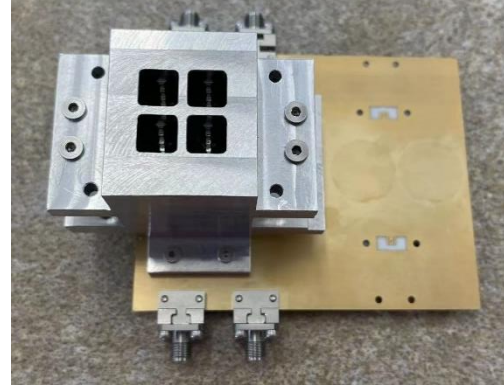
(a)   (b)
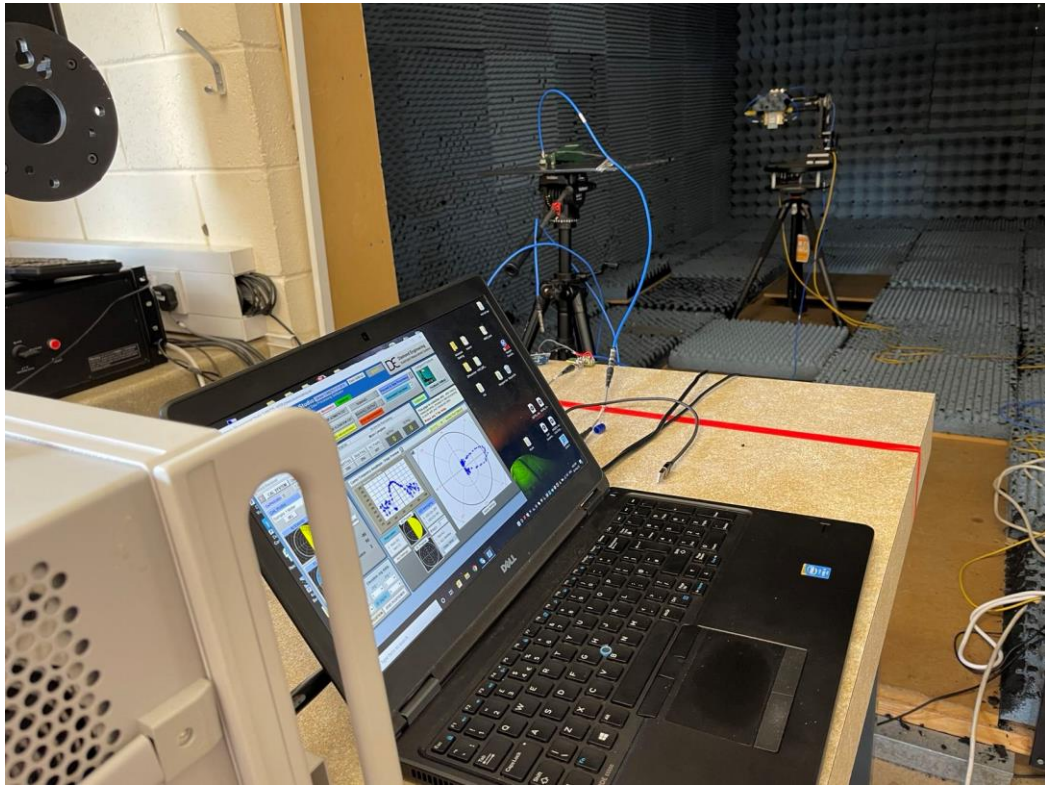
(c)

Fig. 7.11. Fabricated PCB feeding network with (a) LP waveguide antenna array, (b) CP waveguide antenna array, and (c) the far-field pattern measurement.

It is expensive and not cost-efficient to use the evaluation kit of the commercial beamforming chips in the measurement, which will cost more than 2,000 Euros. The 1-4 microstrip feeding network will provide the phase difference between the antenna array elements. Fig. 7.12. (a) illustrated the 1-4 feeding network to feed the antenna array and provide phase shift, the Fig. 12. (b) showed the fabricated 1-4 feeding network sample.
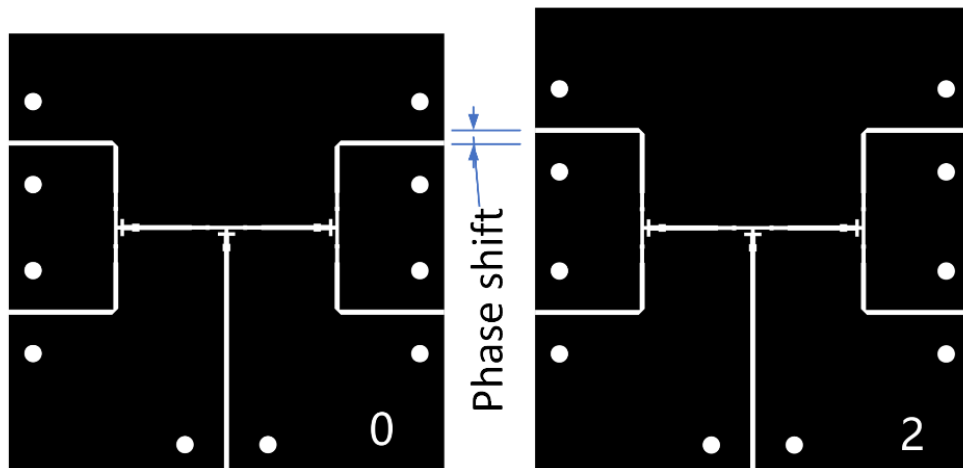
(a)
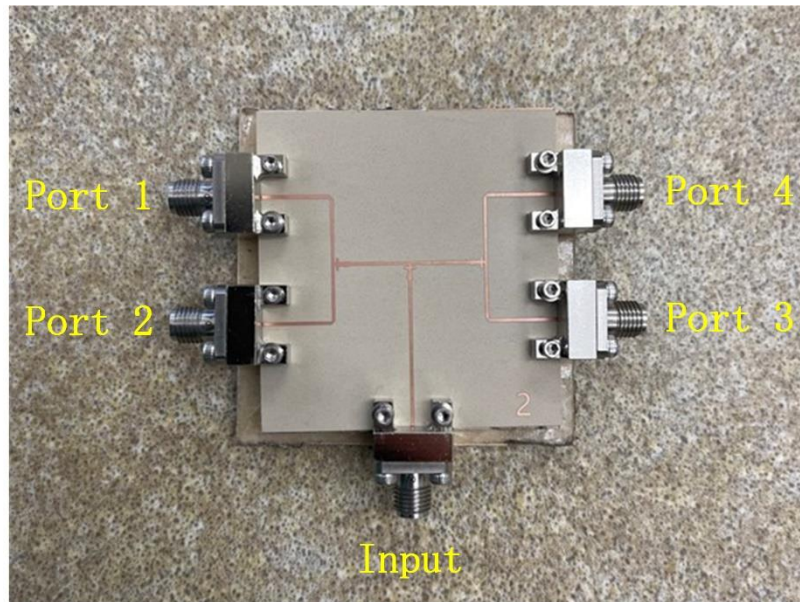
(b)

Fig. 7.12. (a) The 1-4 feeding network to feed the antenna array and provide phase shift and (b) the fabricated 1-4 feeding network sample.

The measured phase results from Fig. 7.13. demonstrated that the 1-4 feeding network could provide a 30-degree/60-degree phase difference around 20 GHz, and a 45-degree/90-degree phase difference around 30 GHz.
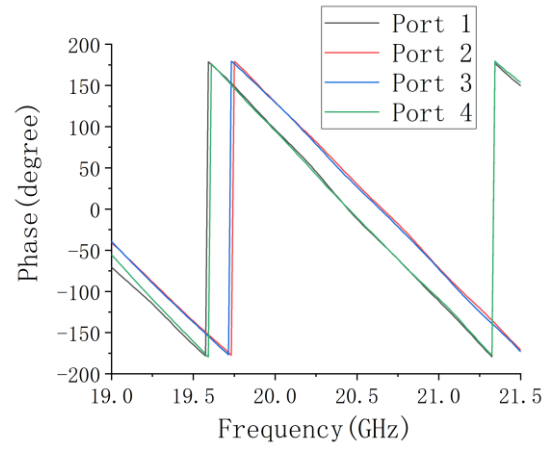
(a)
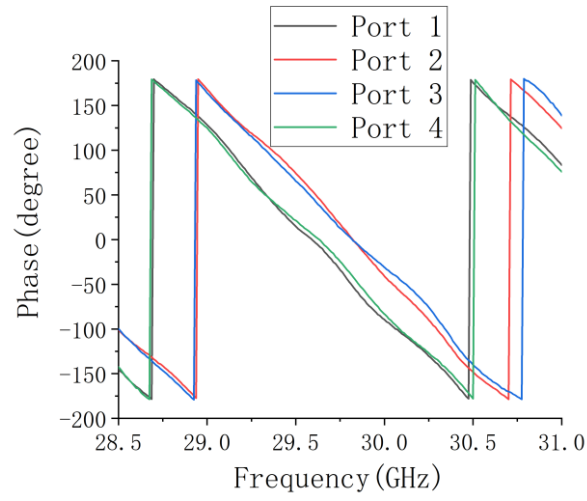
(b)
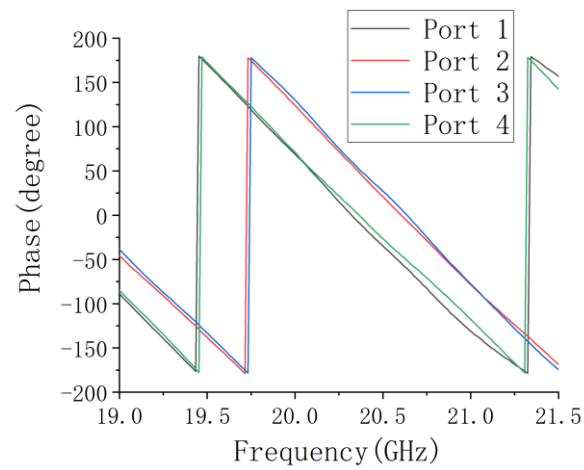
(c)
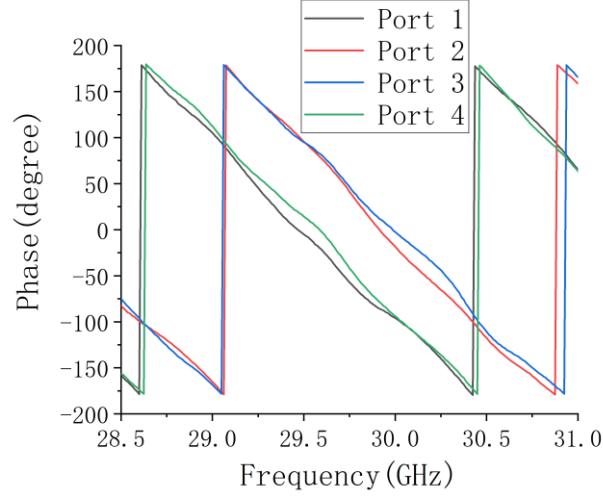
(d)

Fig. 7.13. Measured insertion loss phase results of the 1-4 feeding network mode 1 at (a) K-band (around 30-degree phase difference) and (b) Ka-band (around 45-degree phase difference); Measured insertion loss phase results of the 1-4 feeding network mode 2 at (a) K-band (around 60-degree phase difference) and (b) Ka-band (around 90-degree phase difference).
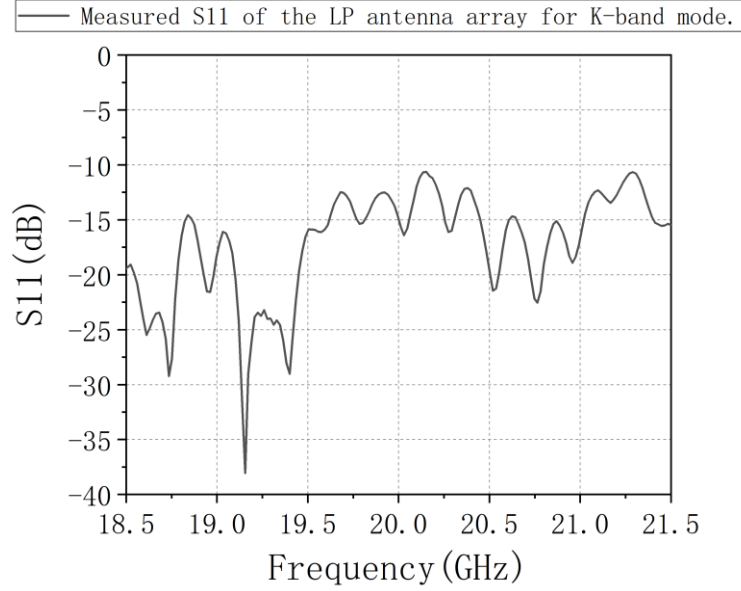
(a)
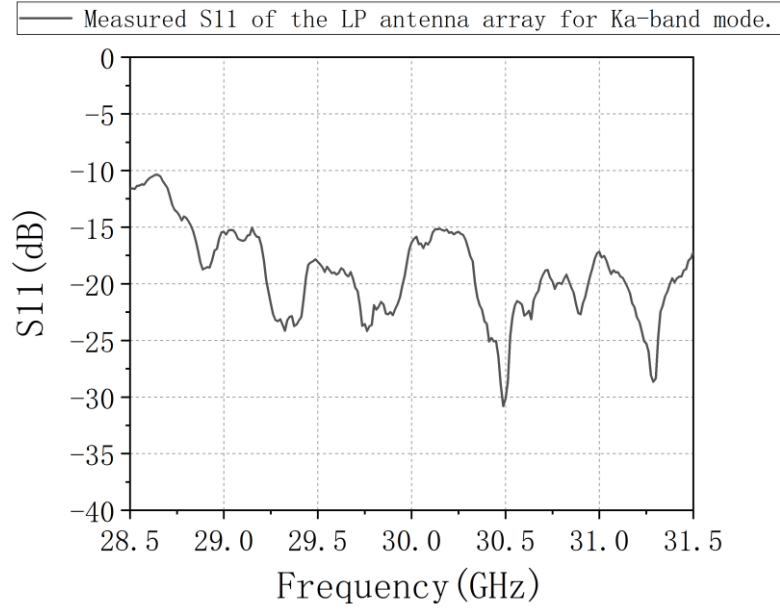
(b)

Fig. 7.14. Measured S11 of the beamforming system with LP antenna array for (a) K-band mode and (b) Ka-band mode.

Measured S11 of the CP antenna array for K-band mode.
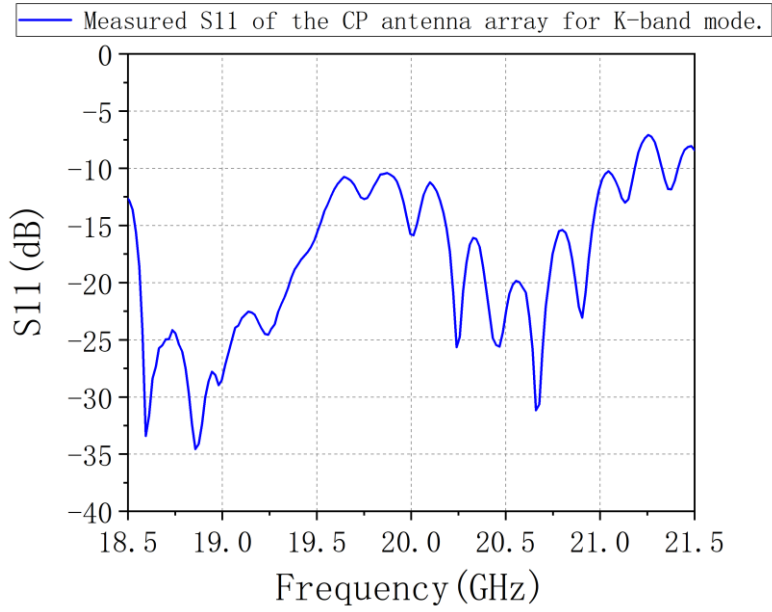
(a)
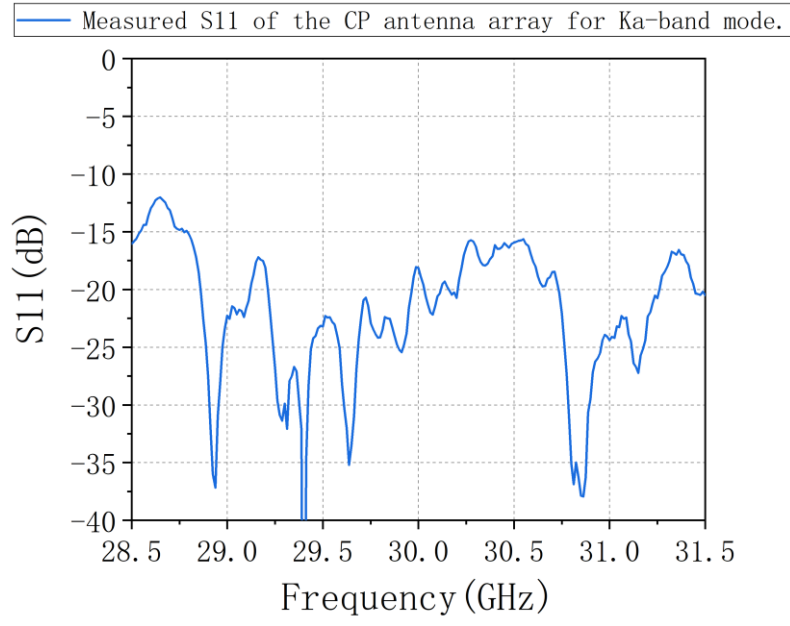
(b)

Fig. 7.15. Measured S11 of the beamforming system with CP antenna array for (a) K-band mode and (b) Ka-band mode.
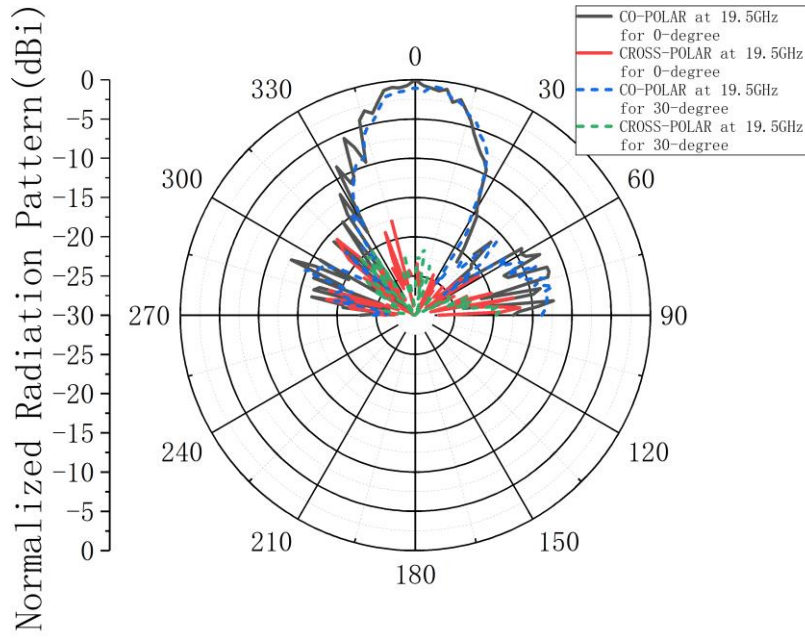
(a)
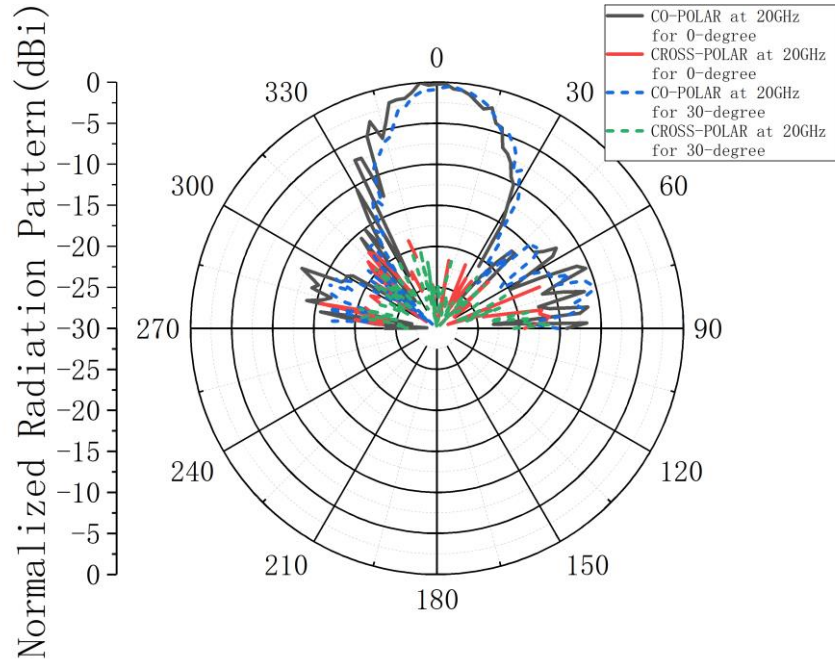
(b)
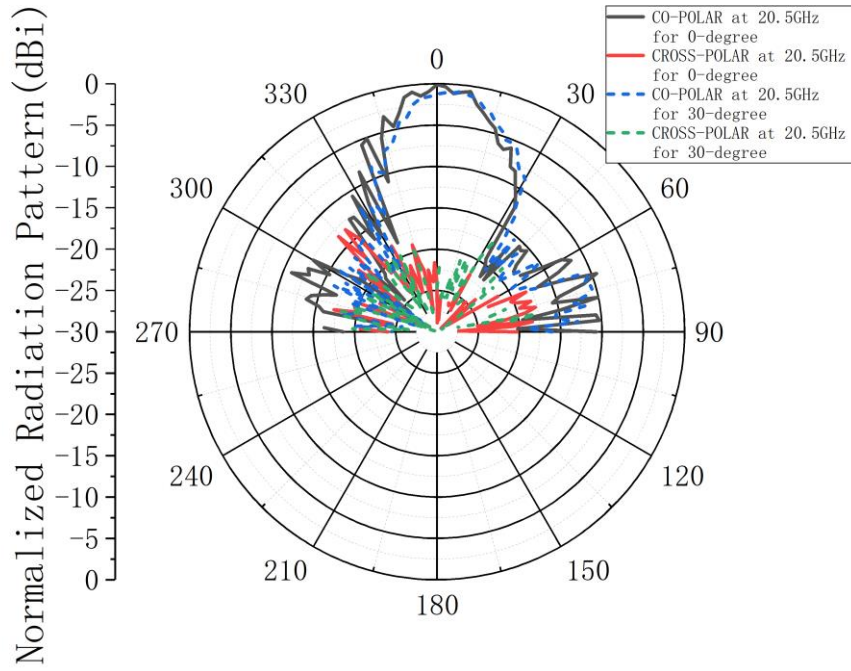
(c)

Fig. 7.16. Measured far-field patterns of beamforming system with LP antenna array when the antenna element phase shift is 0-degree and 30-degree for K-band mode at (a) 19.5 GHz, (b)20 GHz, and (c) 20.5 GHz.
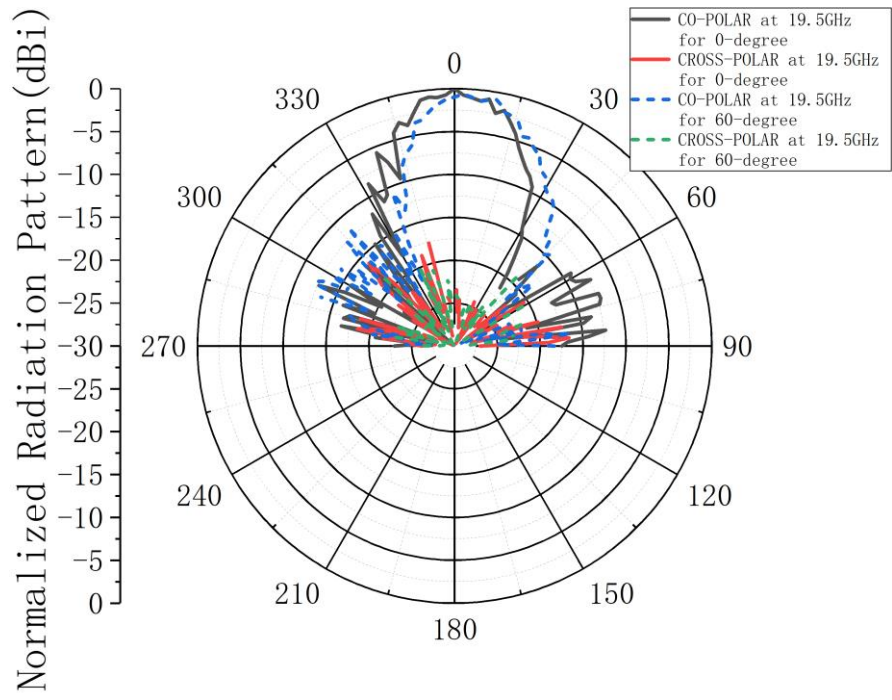
(a)
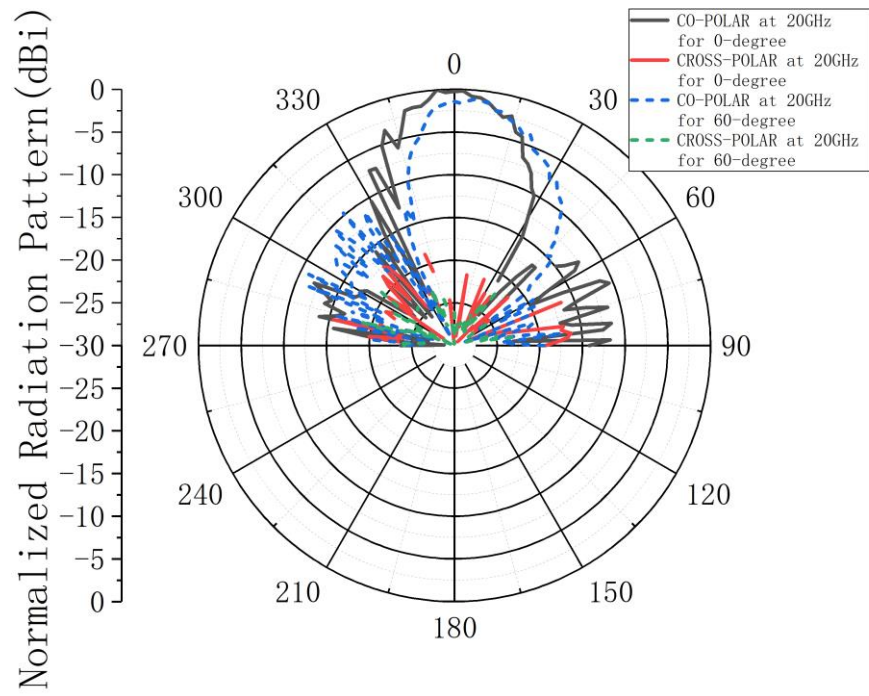
(b)
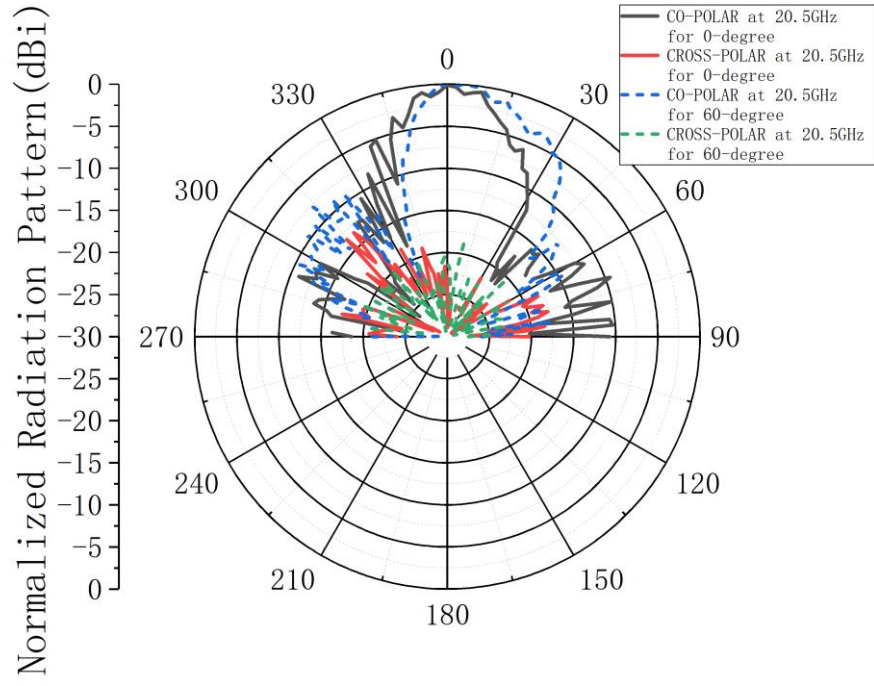
(c)

Fig. 7.17. Measured far-field patterns of beamforming system with LP antenna array when the antenna element phase shift is 0-degree and 60-degree for K-band mode at (a) 19.5 GHz, (b)20 GHz, and (c) 20.5 GHz.
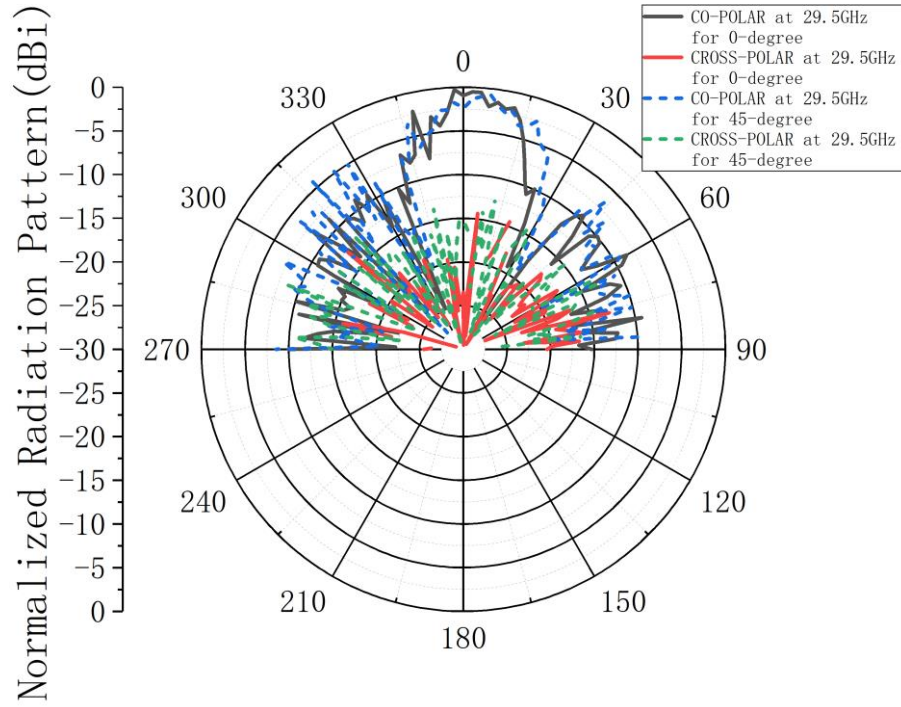
(a)
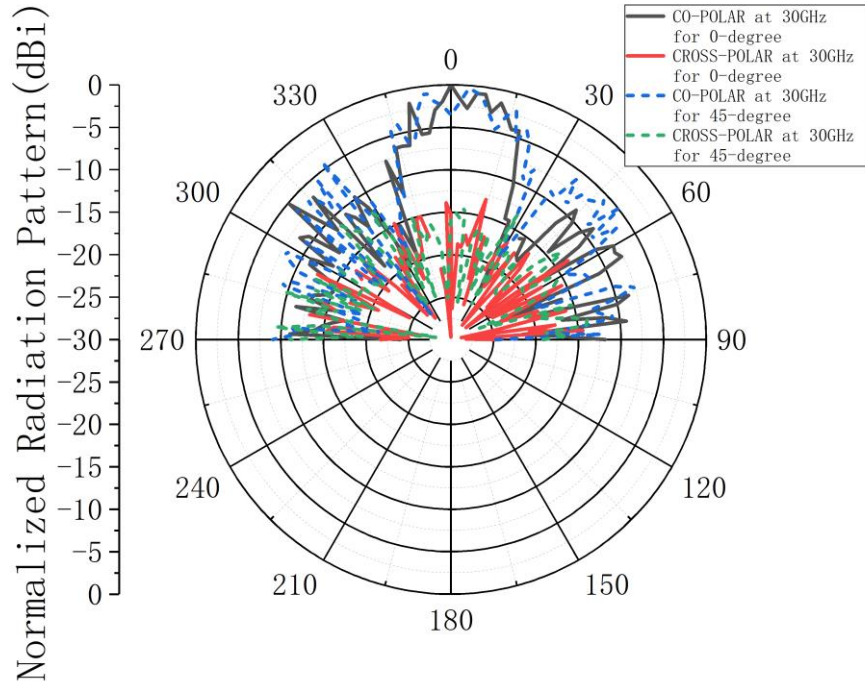
(b)
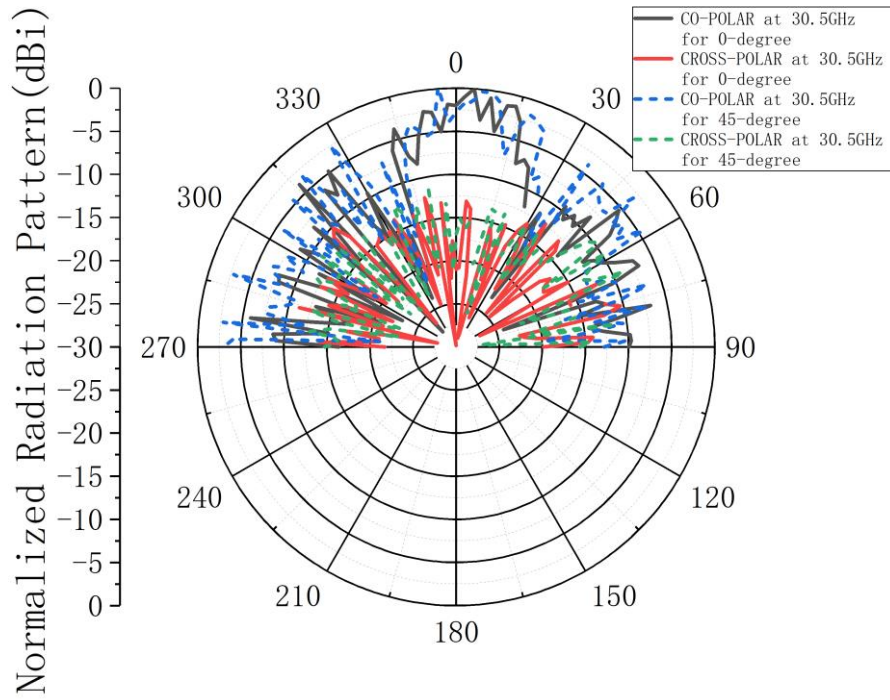
(c)

Fig. 7.18. Measured far-field patterns of beamforming system with LP antenna array when the antenna element phase shift is 0-degree and 45-degree for Ka-band mode at (a) 29.5 GHz, (b)30 GHz, and (c) 30.5 GHz.

131

(a)

(b)

Legend (panel c):
- CO-POLAR at 30.5GHz for 0-degree
- CROSS-POLAR at 30.5GHz for 0-degree
- CO-POLAR at 30.5GHz for 90-degree
- CROSS-POLAR at 30.5GHz for 90-degree
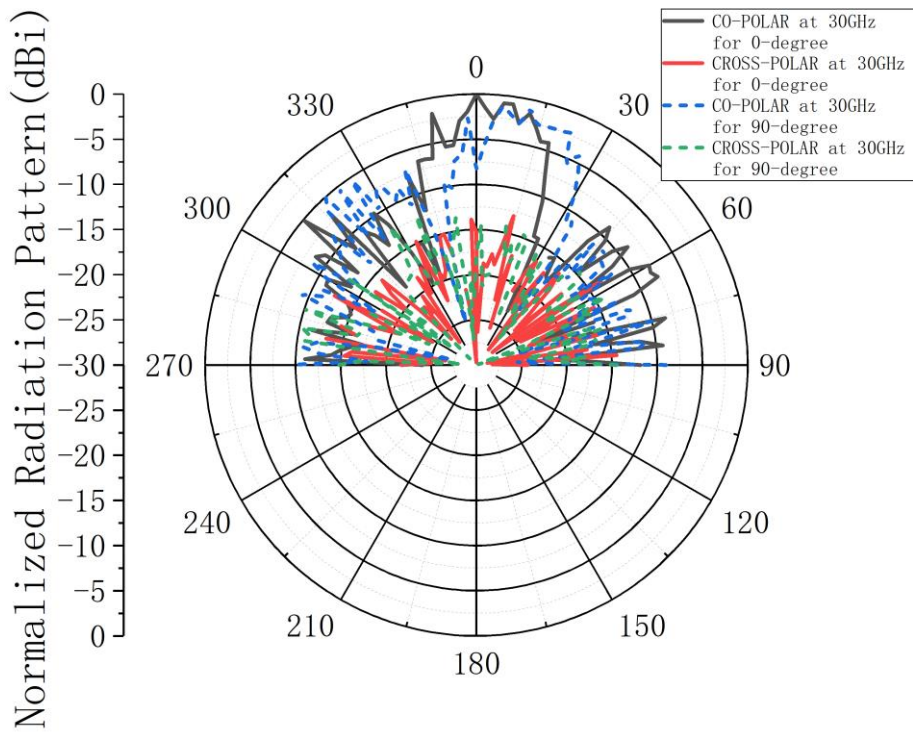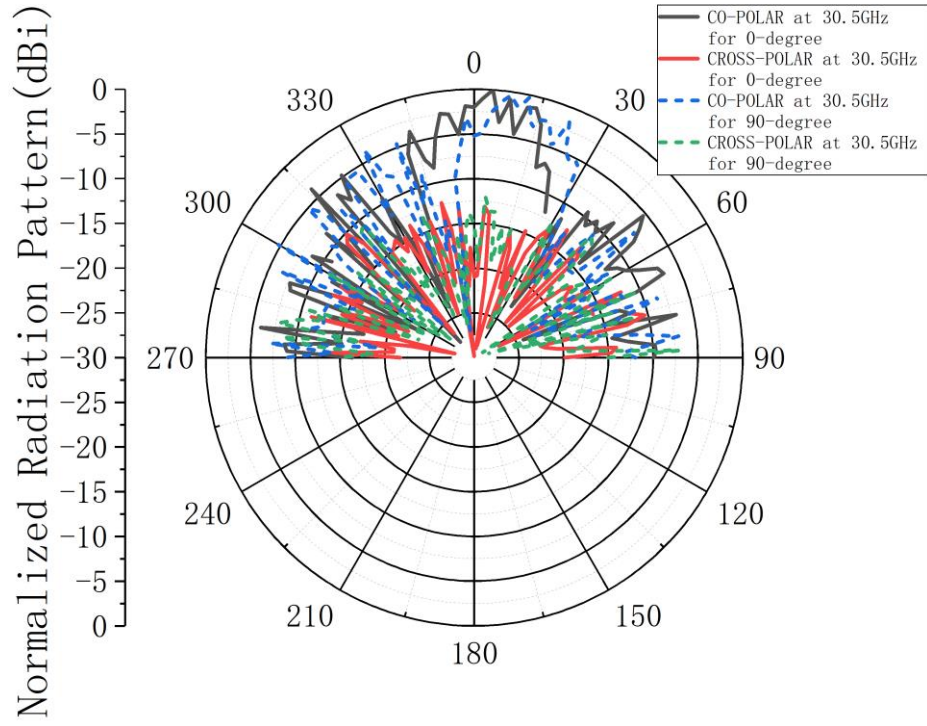
(c)

Fig. 7.19. Measured far-field patterns of beamforming system with LP antenna array when the antenna element phase shift is 0-degree and 90-degree for Ka-band mode at (a) 29.5 GHz, (b)30 GHz, and (c) 30.5 GHz.

Legend (panel a):
- LH at 19.5GHz for 0-degree
- RH at 19.5GHz for 0-degree
- LH at 19.5GHz for 30-degree
- RH at 19.5GHz for 30-degree

(a)

133
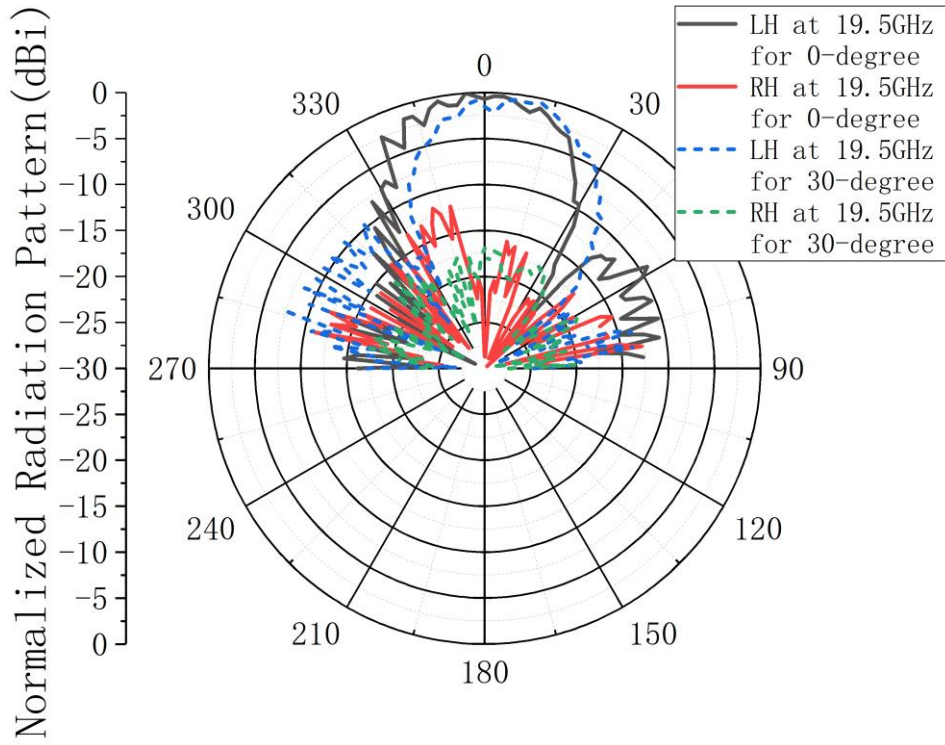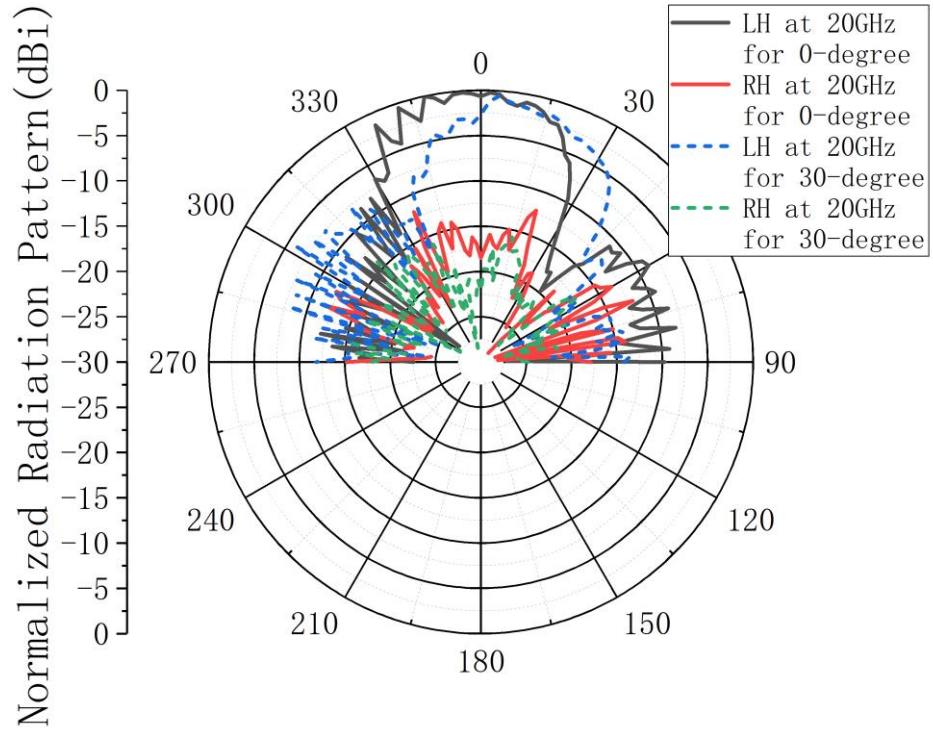
(b)
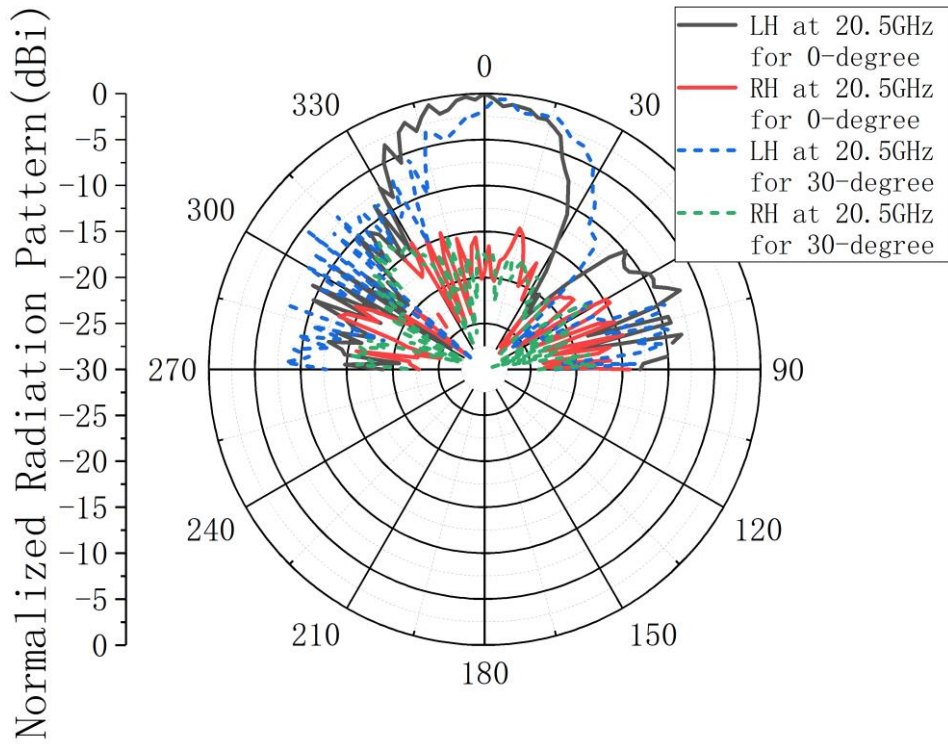
(c)

Fig. 7.20. Measured far-field patterns of beamforming system with CP antenna array when the antenna element phase shift is 0-degree and 30-degree for K-band mode left-handed circular-polarization at (a) 19.5 GHz, (b) 20 GHz and (c) 20.5 GHz.

134
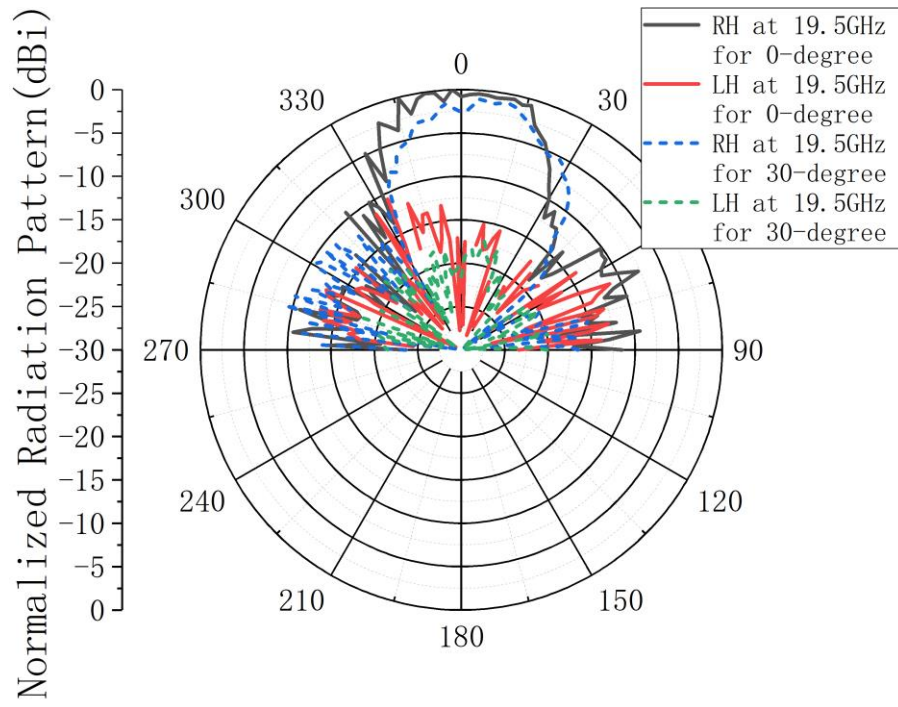
(a)
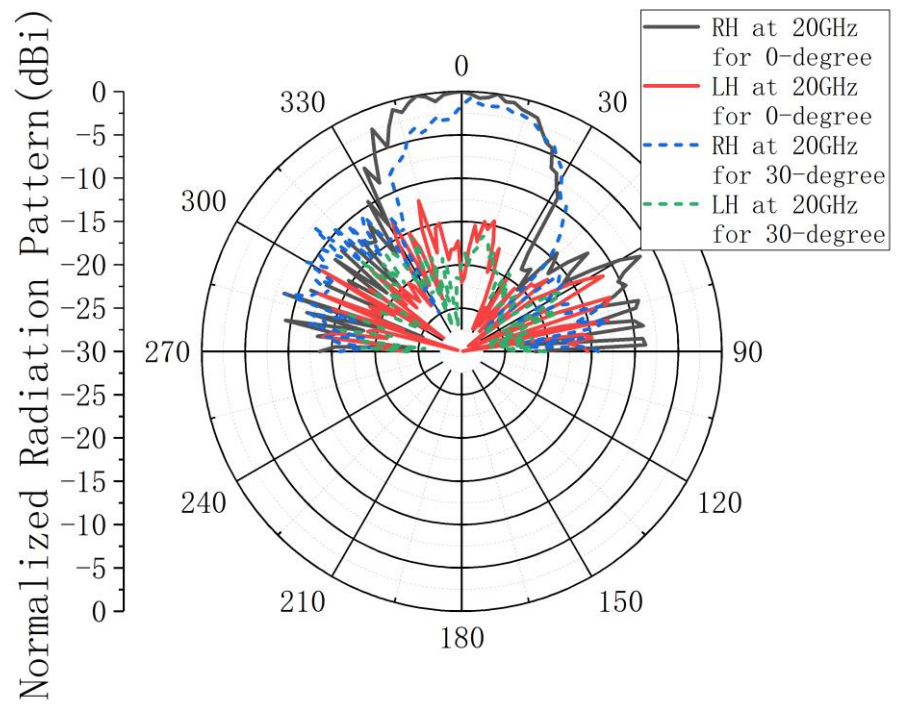
(b)
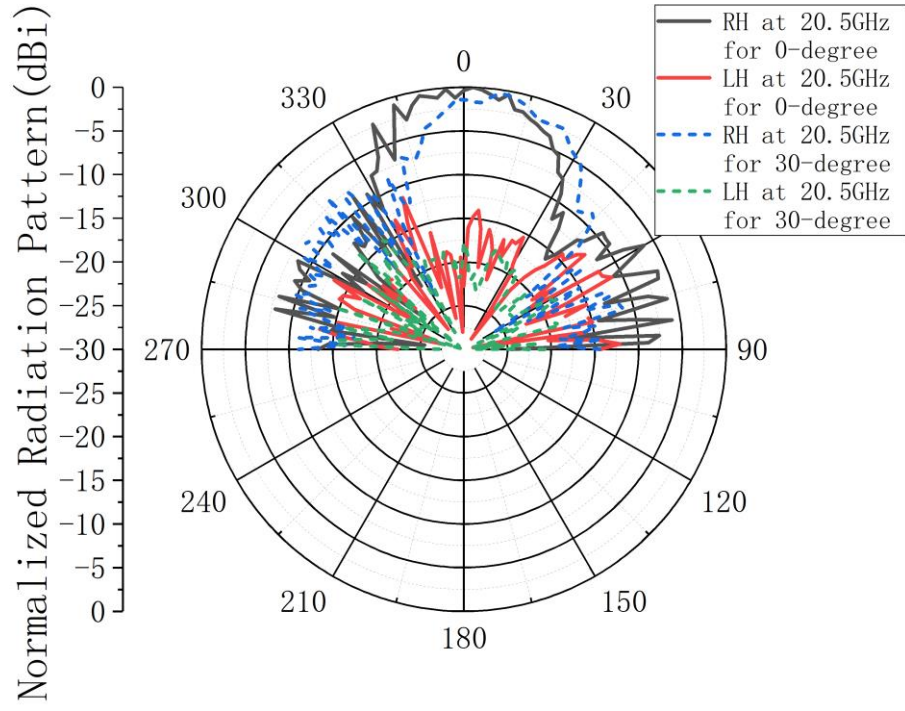
(c)

Fig. 7.21. Measured far-field patterns of beamforming system with CP antenna array when the antenna element phase shift is 0-degree and 30-degree for K-band mode right-handed circular-polarization at (a) 19.5 GHz, (b) 20 GHz and (c) 20.5 GHz.
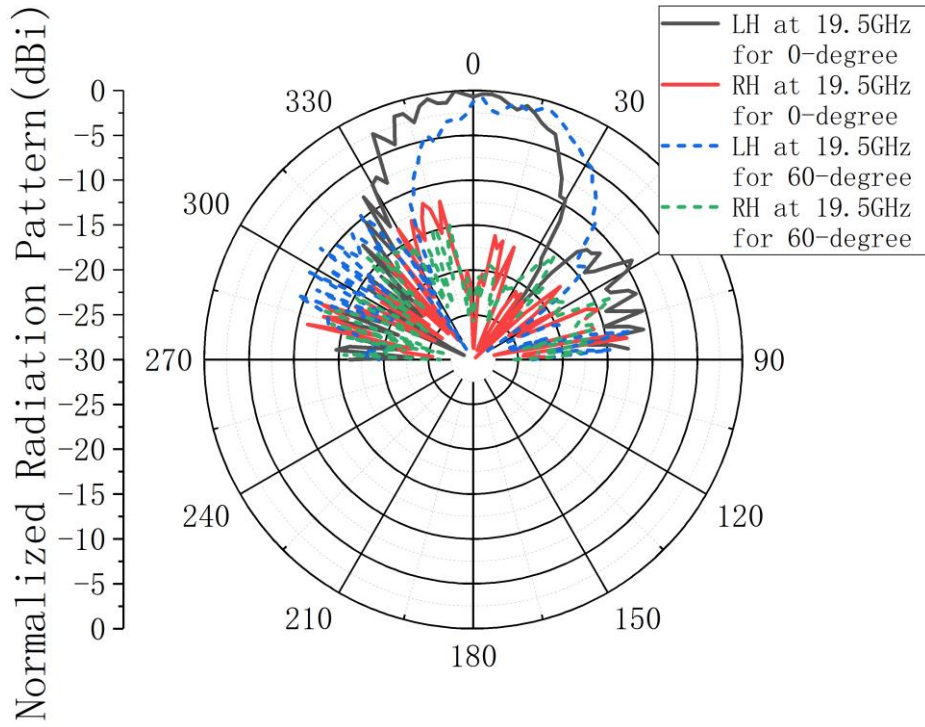
(a)
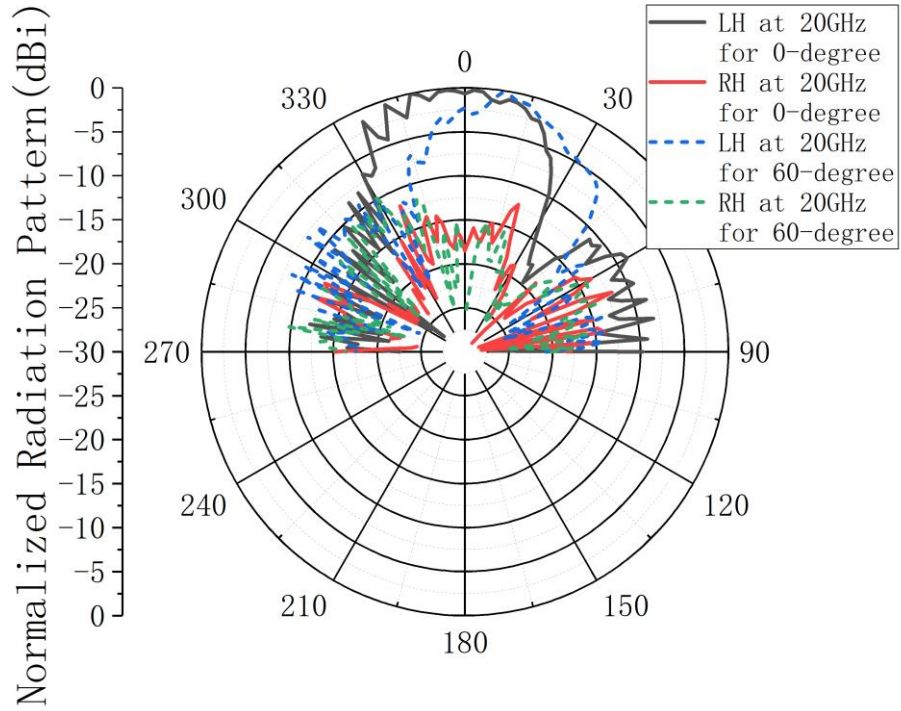
(b)
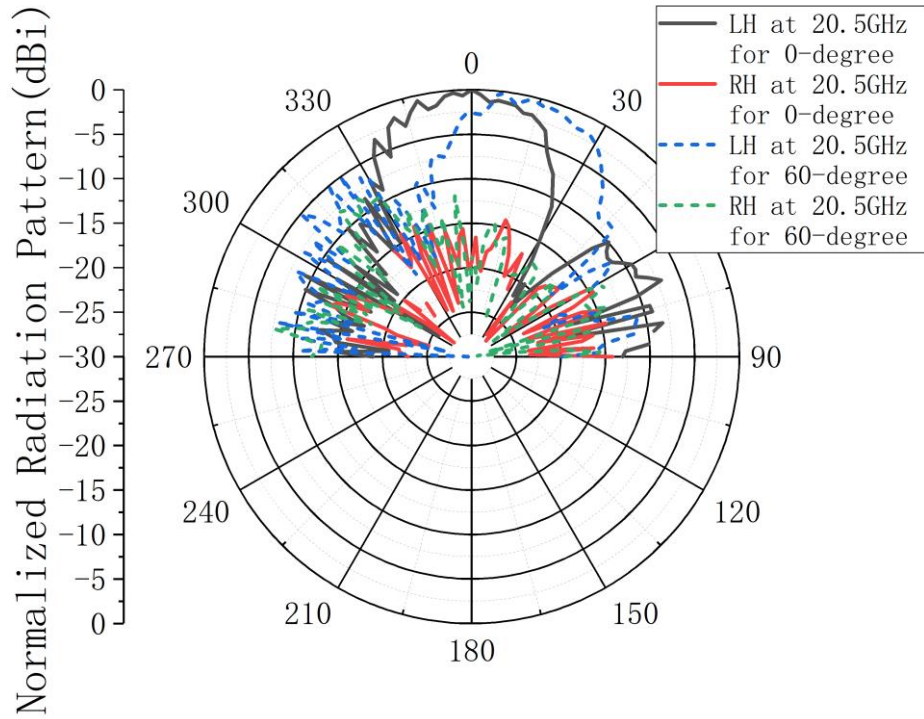
(c)

Fig. 7.22. Measured far-field patterns of beamforming system with CP antenna array when the antenna element phase shift is 0-degree and 60-degree for K-band mode left-handed circular-polarization at (a) 19.5 GHz, (b) 20 GHz and (c) 20.5 GHz.

137
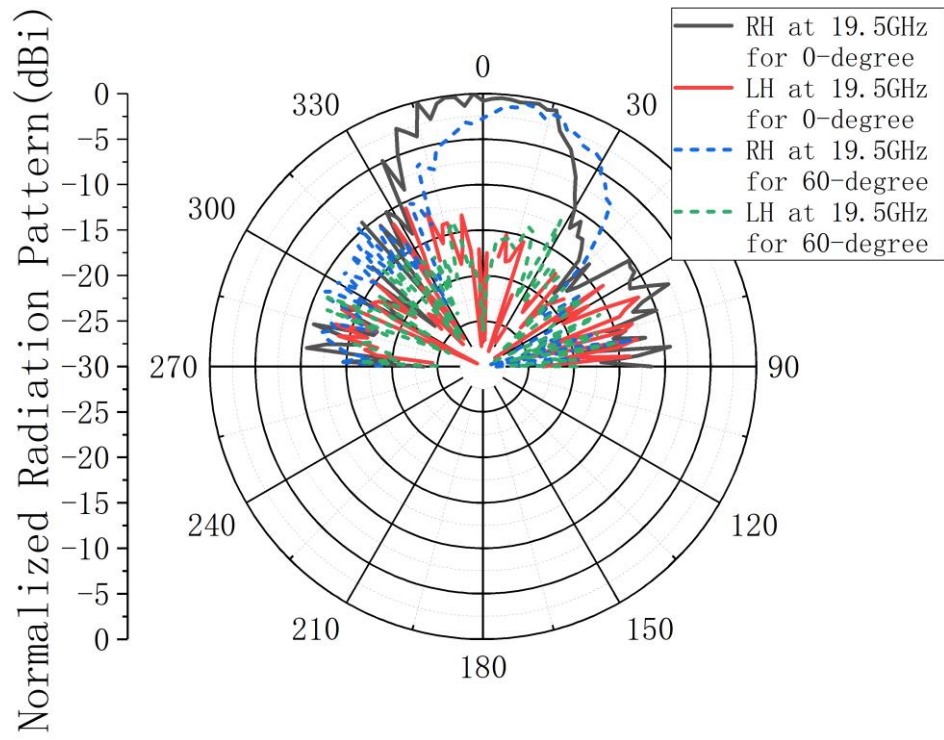
(a)
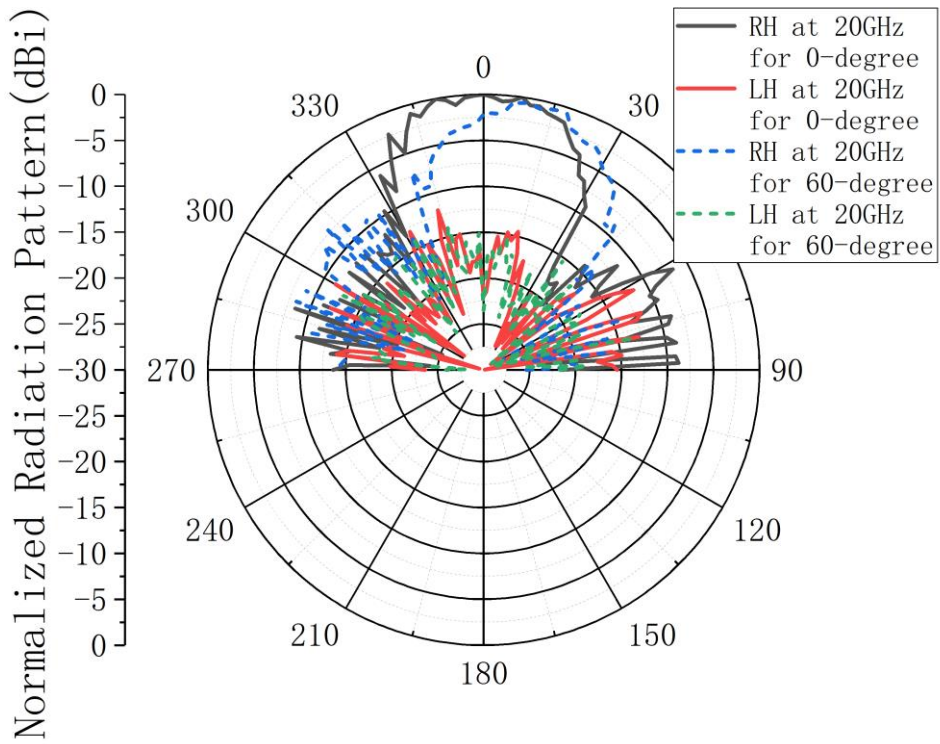
(b)
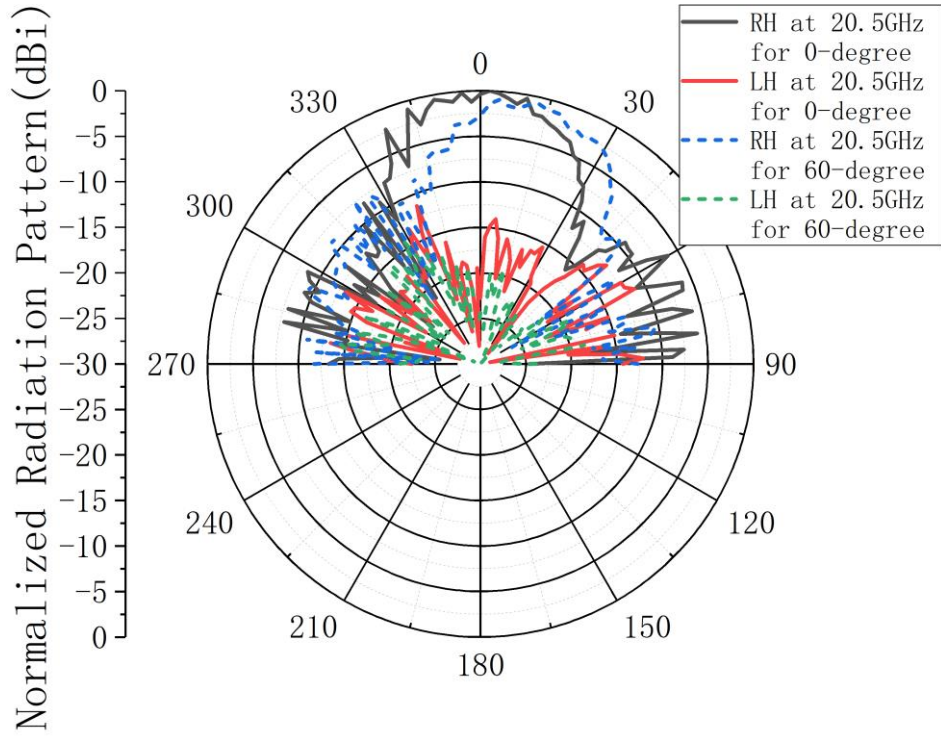
(c)

Fig. 7.23. Measured far-field patterns of beamforming system with CP antenna array when the antenna element phase shift is 0-degree and 60-degree for K-band mode right-handed circular-polarization at (a) 19.5 GHz, (b) 20 GHz and (c) 20.5 GHz.

(a)

139
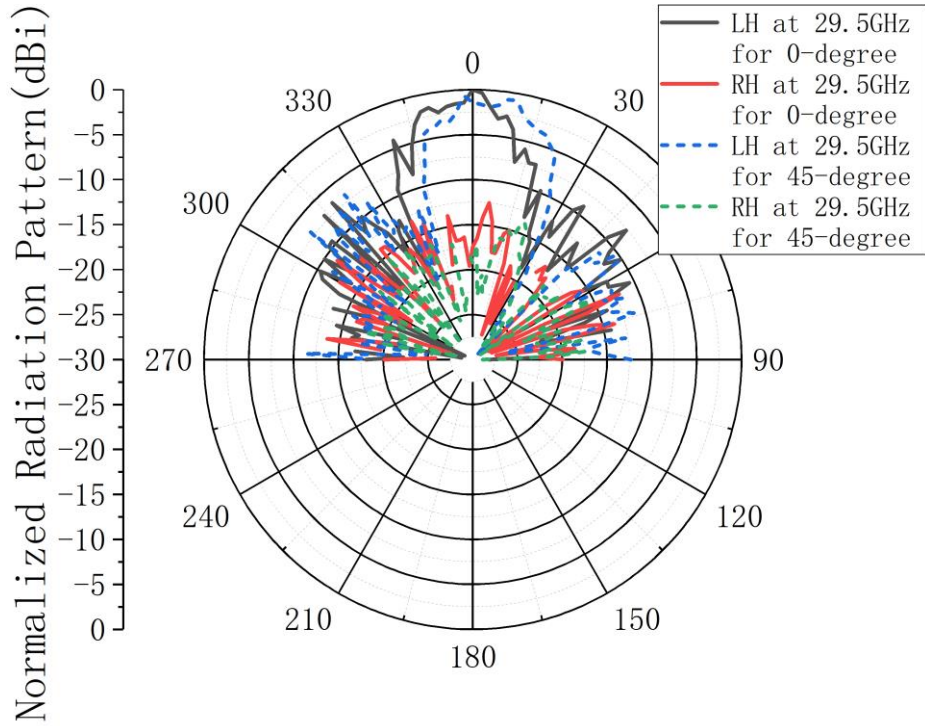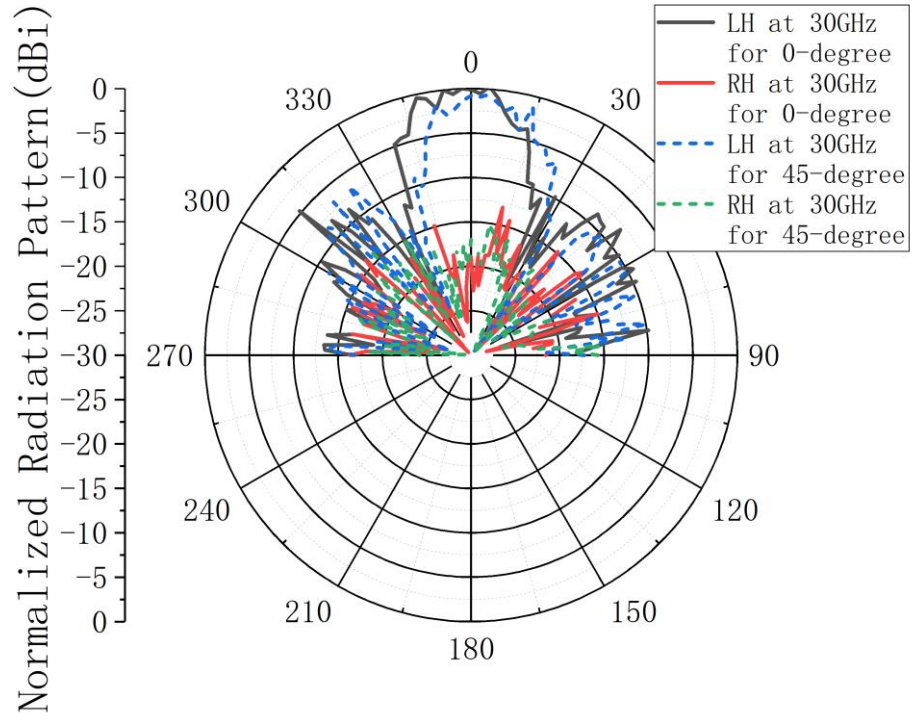
(b)
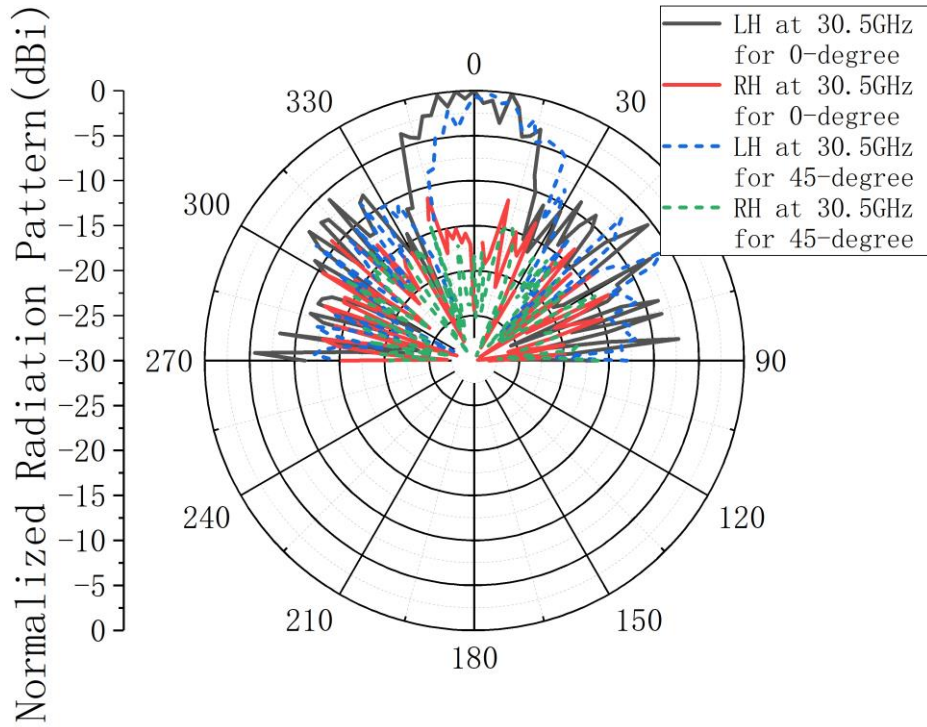
(c)

Fig. 7.24. Measured far-field patterns of beamforming system with CP antenna array when the antenna element phase shift is 0-degree and 45-degree for Ka-band mode left-handed circular-polarization at (a) 29.5 GHz, (b) 30 GHz and (c) 30.5 GHz.

(a)

(b)

141
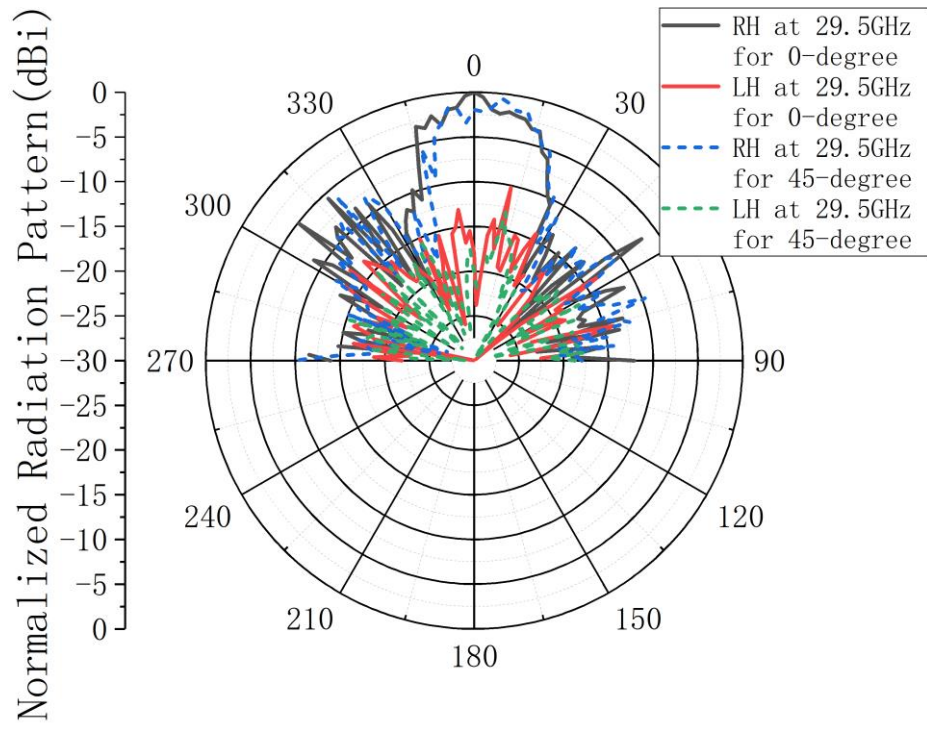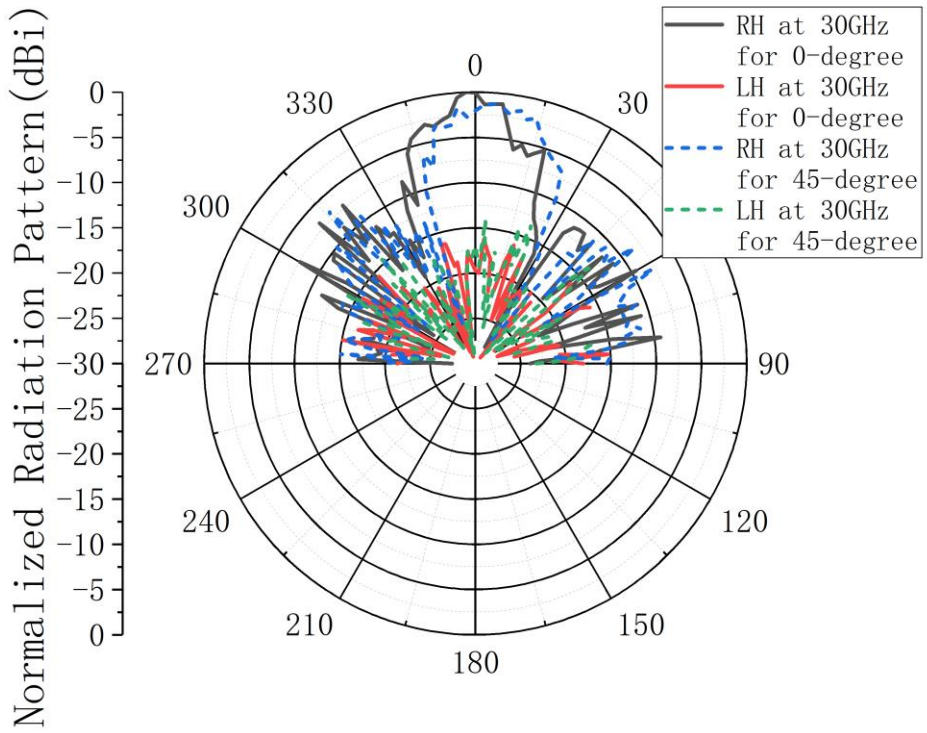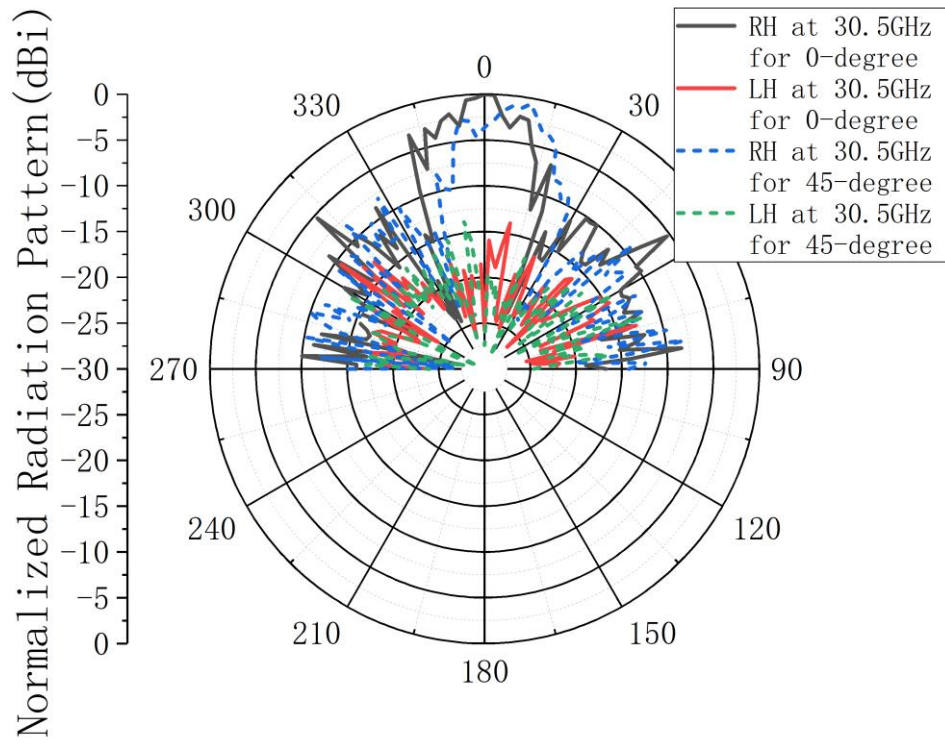
(c)

Fig. 7.25. Measured far-field patterns of beamforming system with CP antenna array when the antenna element phase shift is 0-degree and 45-degree for Ka-band mode right-handed circular-polarization at (a) 29.5 GHz, (b) 30 GHz and (c) 30.5 GHz.
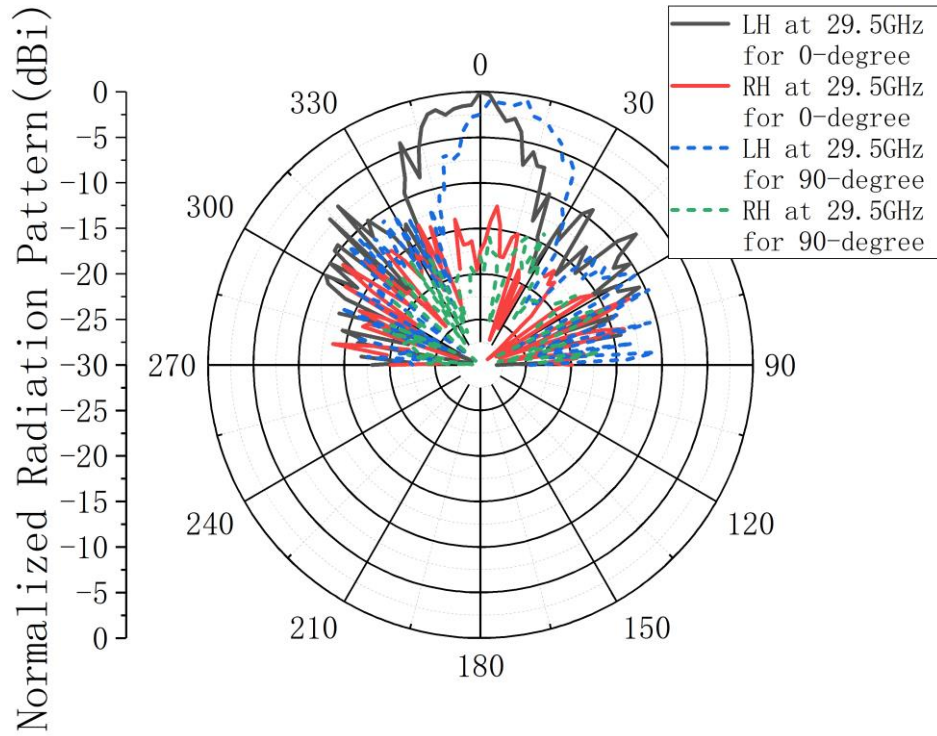
(a)
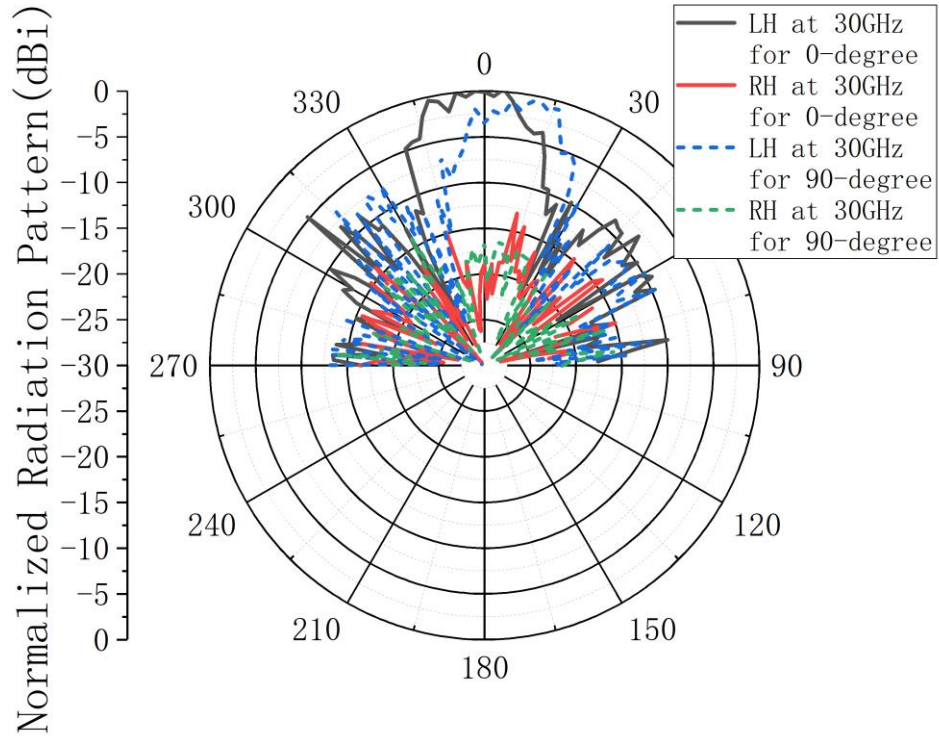
(b)
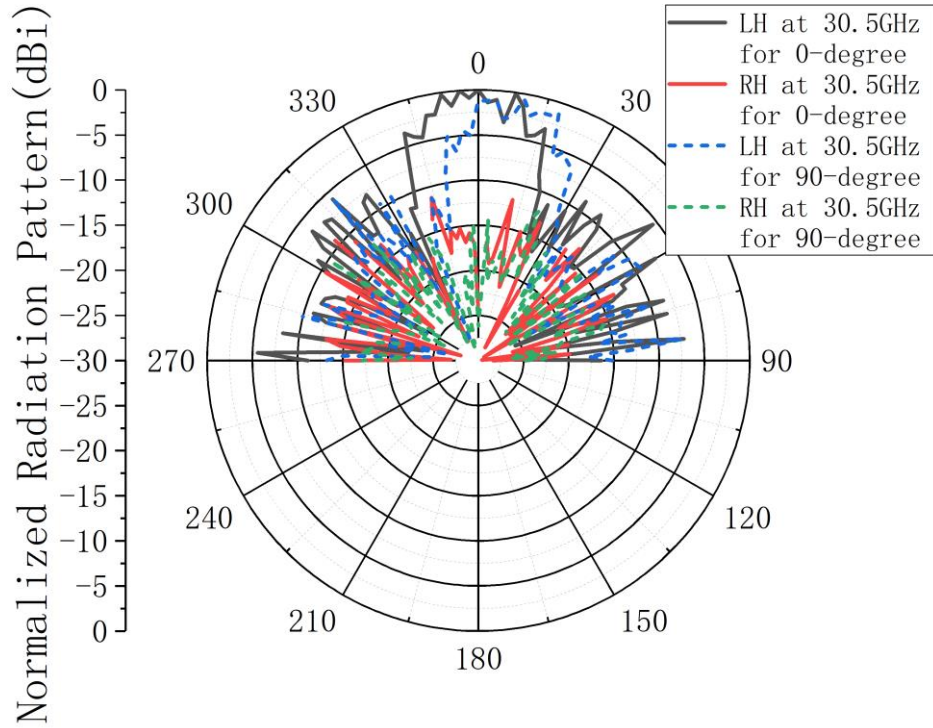
(c)

Fig. 7.26. Measured far-field patterns of beamforming system with CP antenna array when the antenna element phase shift is 0-degree and 90-degree for Ka-band mode left-handed circular-polarization at (a) 29.5 GHz, (b) 30 GHz and (c) 30.5 GHz.

143
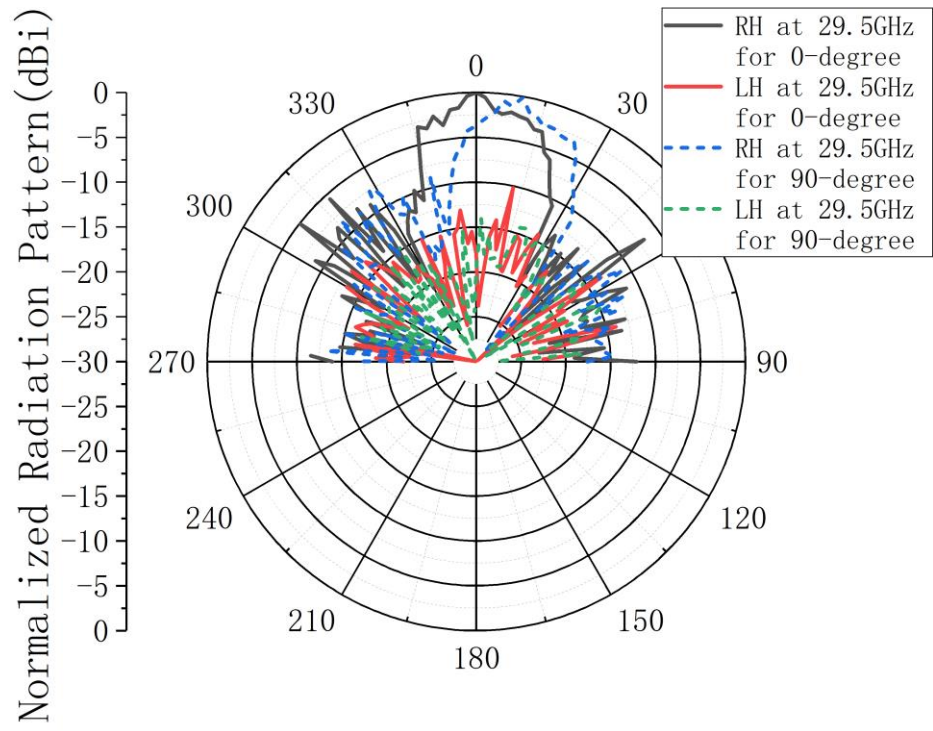
(a)
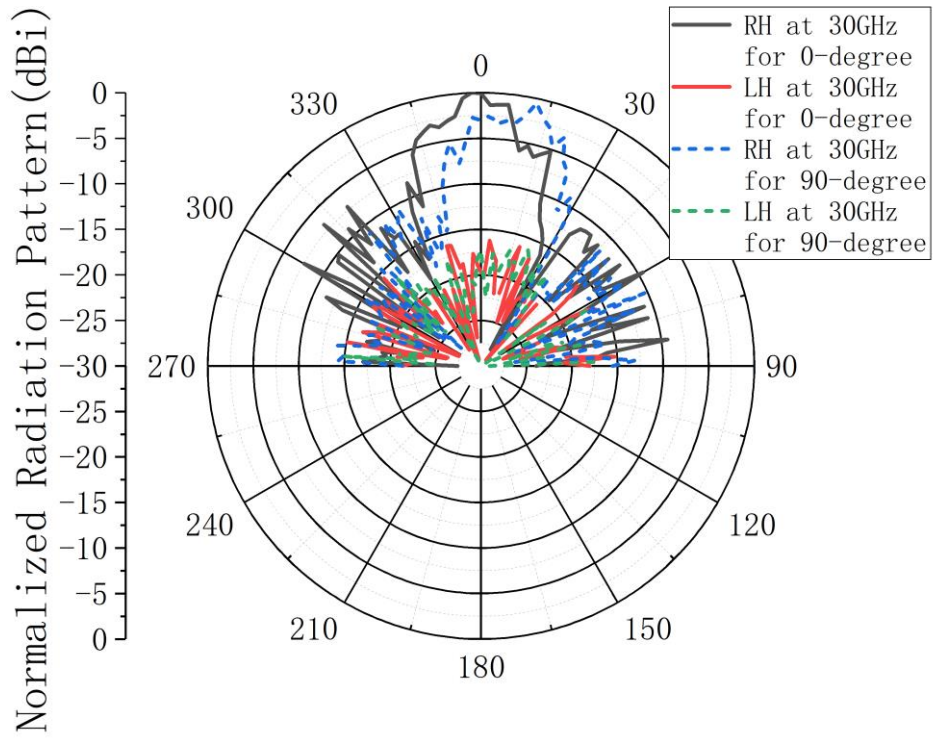
(b)
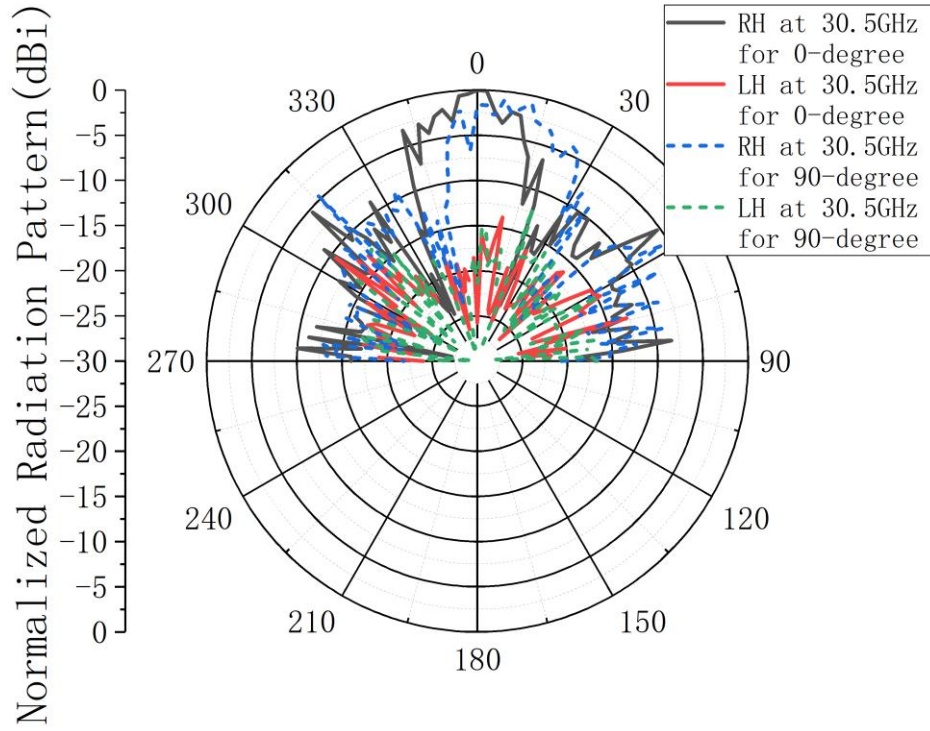
(c)

Fig. 7.27. Measured far-field patterns of beamforming system with CP antenna array when the antenna element phase shift is 0-degree and 90-degree for Ka-band mode right-handed circular-polarization at (a) 29.5 GHz, (b) 30 GHz and (c) 30.5 GHz.
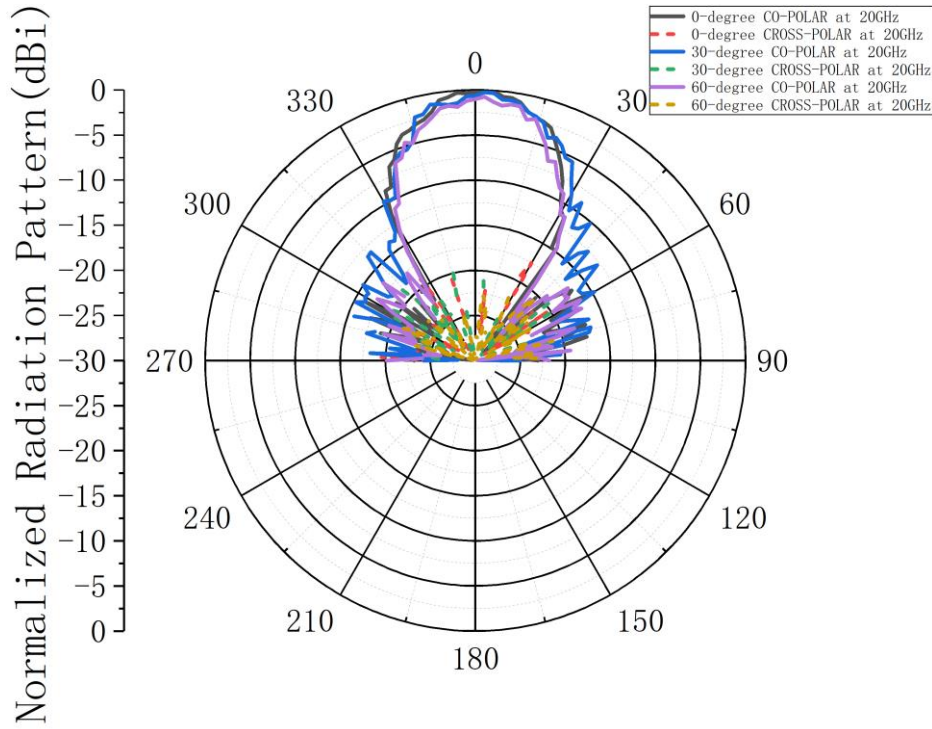
(a)
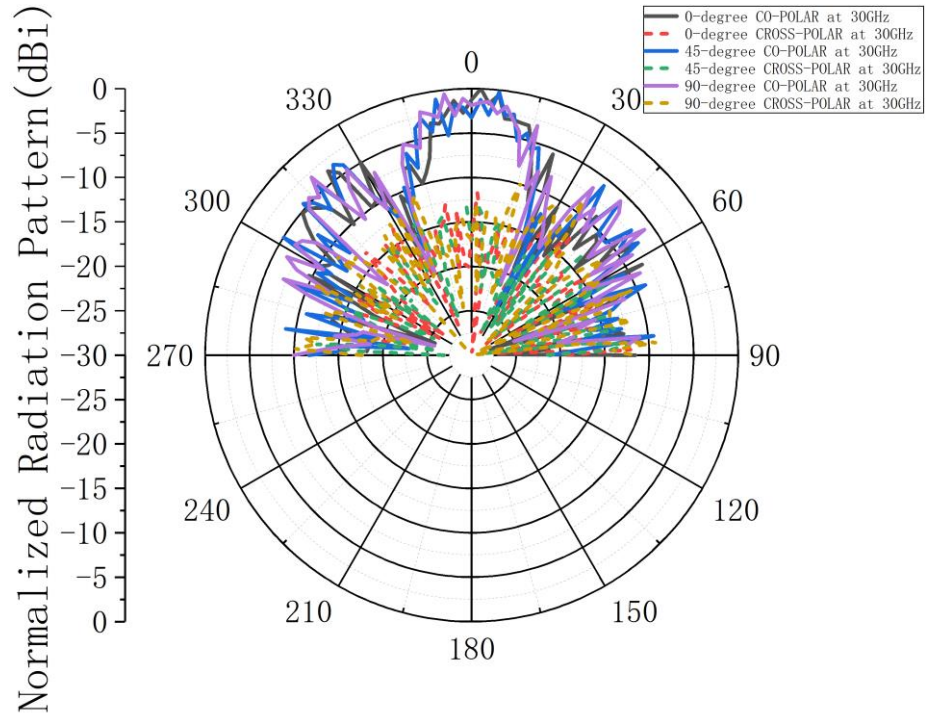
(b)

Fig. 7.28. Measured far-field patterns of beamforming system with LP antenna array when the antenna element phase shift is (a) 0-degree, 30-degree, and 60-degree at 20 GHz and (b) 0-degree, 45-degree, and 90-degree at 30 GHz at YOZ-plane.

(a)

146

(b)
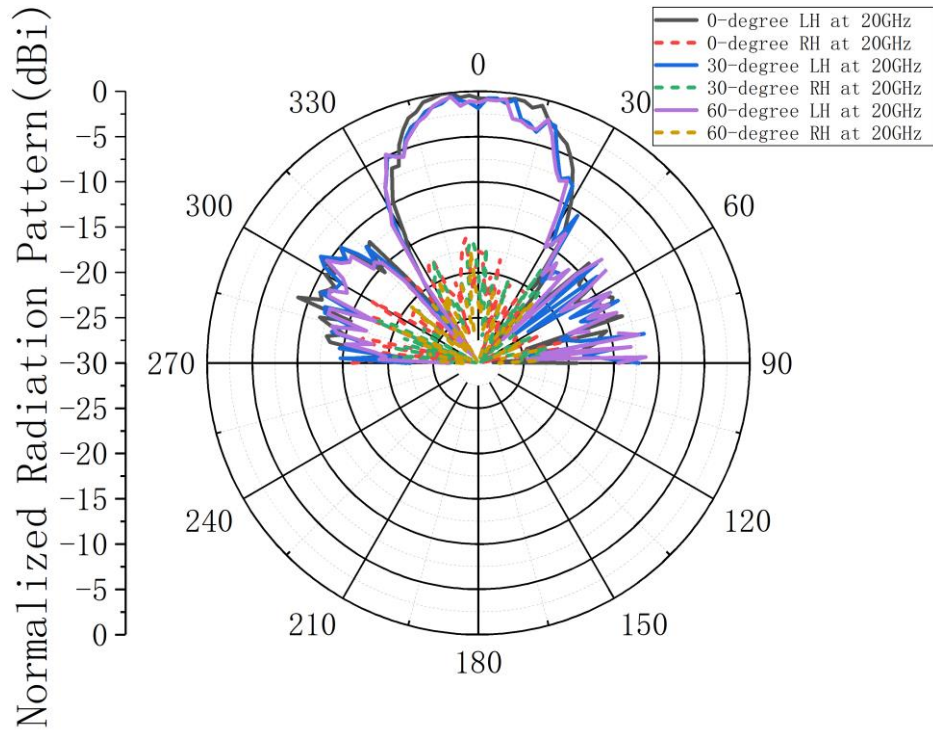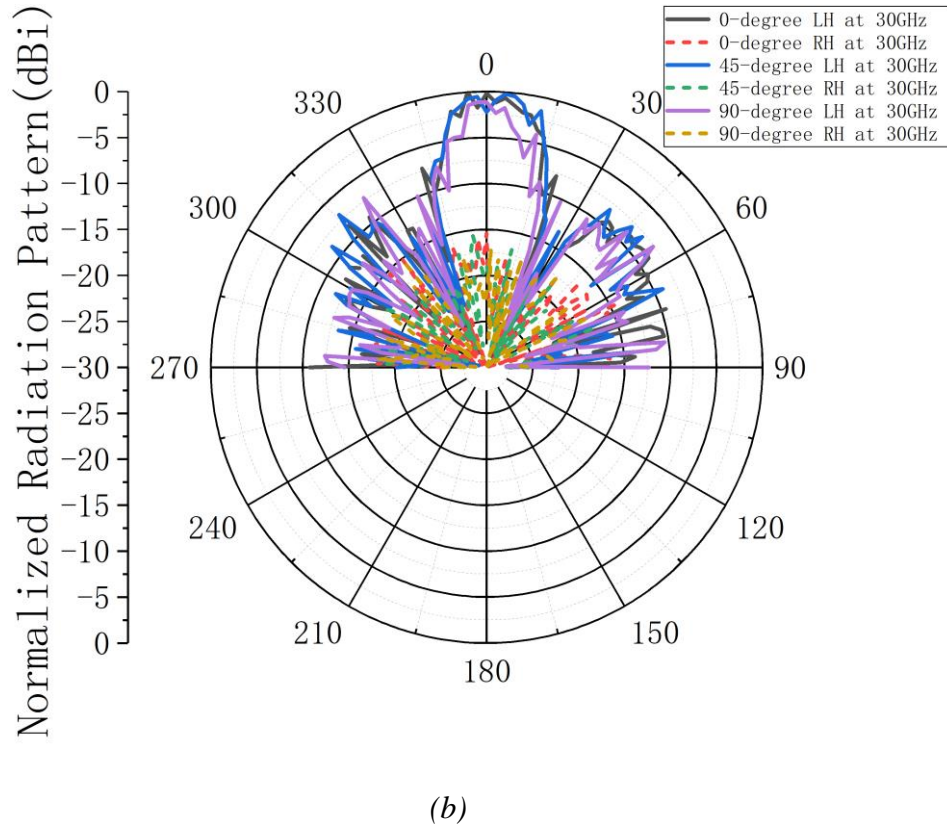
Fig. 7.29. Measured far-field patterns of beamforming system with left-handed CP antenna array when the antenna element phase shift is (a) 0-degree, 30-degree, and 60-degree at 20 GHz and (b) 0-degree, 45-degree, and 90-degree at 30 GHz at YOZ-plane.

(a)
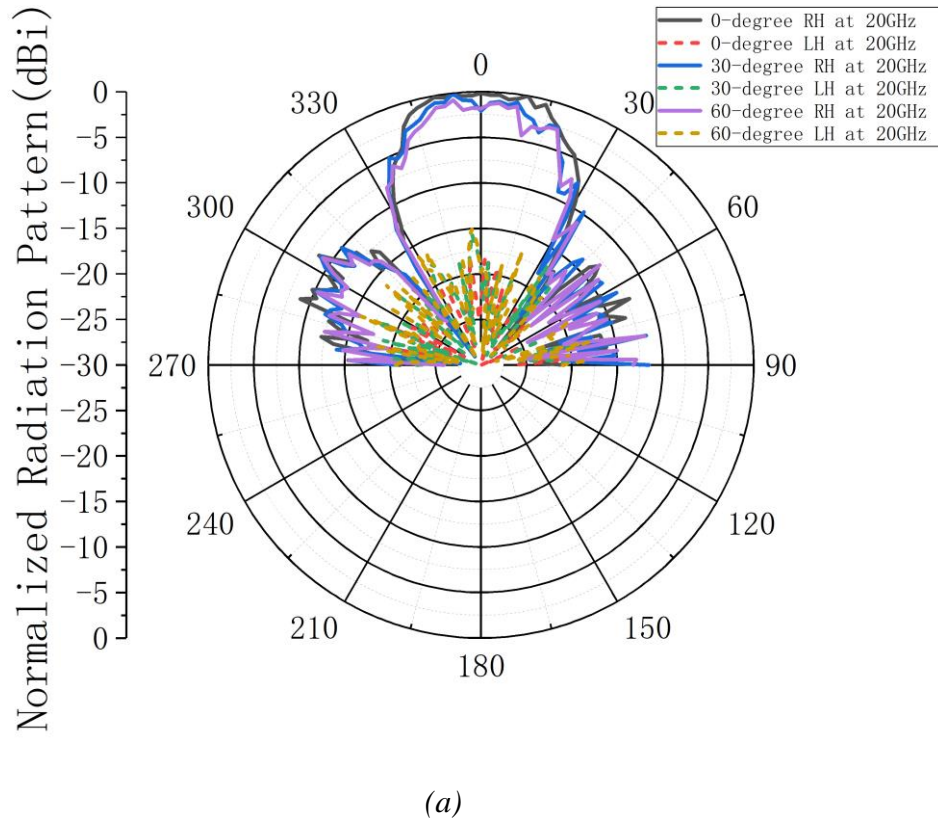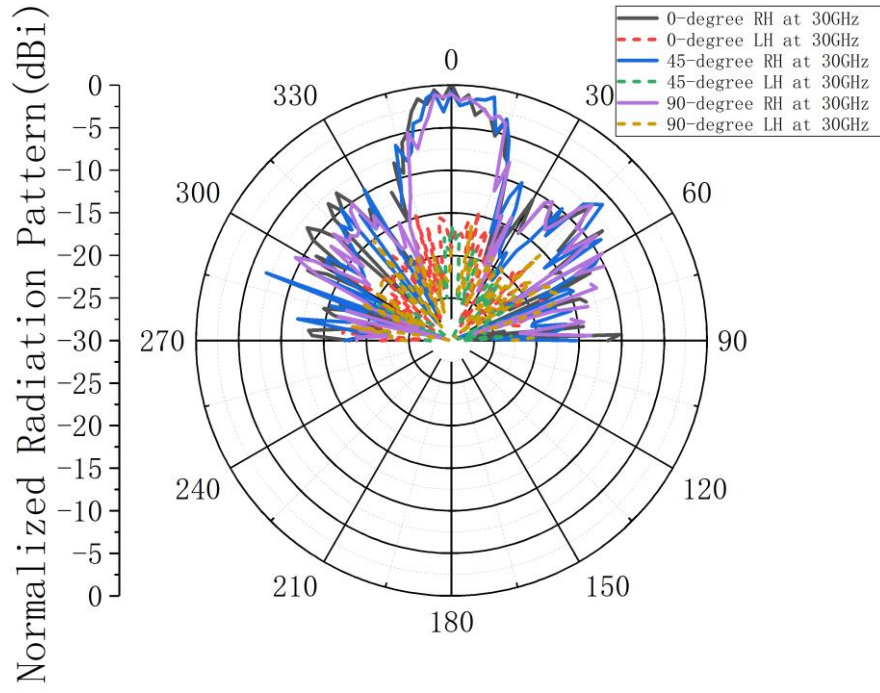
(b)

Fig. 7.30. Measured far-field patterns of beamforming system with right-handed CP antenna array when the antenna element phase shift is (a) 0-degree, 30-degree, and 60-degree at 20 GHz and (b) 0-degree, 45-degree, and 90-degree at 30 GHz at YOZ-plane.

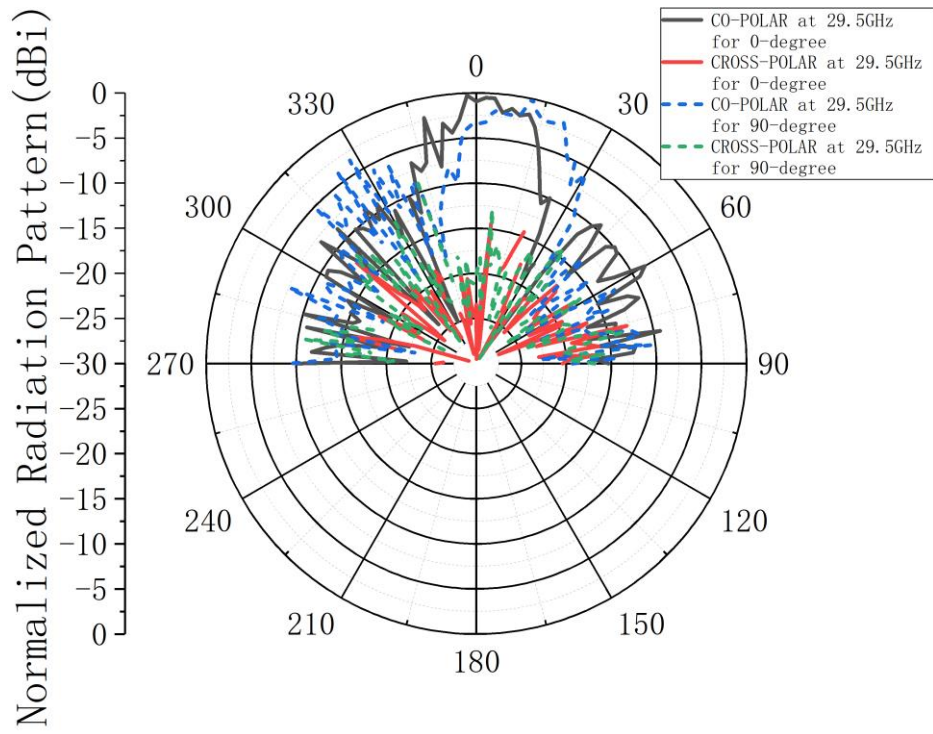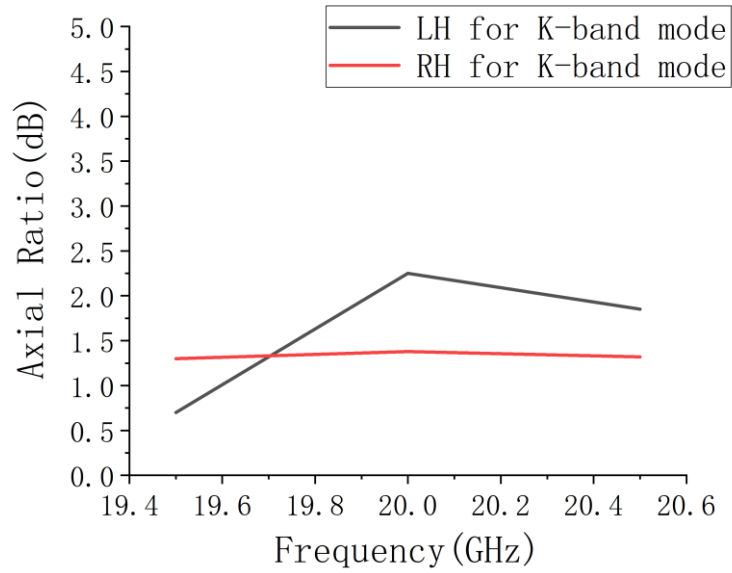(a)
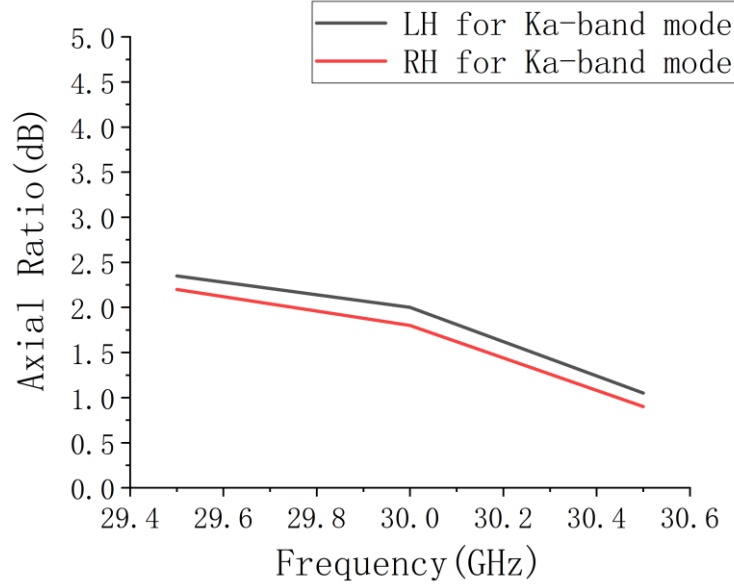
(b)

Fig. 7.31. Measured axial ratios of the beamforming system samples with left-handed/right-handed CP antenna arrays at (a) K-band mode and (b) Ka-band mode.

The measured S11 in Fig. 7.14. and Fig. 7.15. illustrated that both the beamforming system samples with reconfigurable waveguide LP antenna array and CP antenna array provided wideband performance for K/Ka-band.

Compared with the beamforming system samples with no element phase shift, the measured far-field patterns of the two kinds of beamforming system samples demonstrated that both the LP antenna array beamforming system and CP antenna array beamforming system have around the 4-6 degrees beam angle shifts when there are a 30-degree or the 10-12 degrees beam angle shifts when there is a 60-degree antenna element phase shift for K-band mode; The 4-6 degrees beam angle shifts when there are a 45-degree or the 10-12 degrees beam angle shifts when there is a 90-degree antenna element phase shift for Ka-band mode in Fig. 7.16. to Fig. 7.27 at XOZ-plane. At YOZ-plane, for both the LP antenna beamforming system and the CP antenna beamforming system, when the beam angle was controlled and changed by the phase difference, the beam directions kept the same, which are illustrated in Fig. 7.28, Fig. 7.29. and Fig. 7.30.

149

The measured axial ratios for the beamforming system samples with the left-handed CP antenna array or the right-handed CP antenna are shown in Fig. 7.31 (a) and (b) for K/Ka-band mode respectively. Both at the required K-band and Ka-band frequency ranges, the axial ratios are less than 3 dB, which meets the requirement of a circular-polarized antenna at the operational frequencies for this beamforming system design.

The measured results illustrated that both the beamforming system samples with reconfigurable waveguide LP antenna array and CP antenna array provided wideband performance for K/Ka-band.

7.2 Design of Two-Input-Four-Output Beamforming Sample with Multilayer SICL Structure Feeding Network

It is still challenging to design and manufacture a multilayer SICL PCB, especially with many types of vias. The manufacturing cost is also very high, a 10-layer 10cm by 10cm dimensions multilayer SICL PCB board will cost thousands of Euros.

The 2-input-4-output (2-4) feeding network simulation structures from CST software are shown in Fig. 7.32. (a) and (b). The fabrication stackup of the design is demonstrated in Fig. 7.33. (a).

To manufacture a multilayer 2-4 network PCB with many buried vias, the back-drilling vias and pads need to be added to the top and bottom of the PCB in manufacture progress, and the minimum diameter of the back drilling via is around 1.5 mm in manufacture. The fabrication stackup of the 2-4 multilayer PCB SICL feeding network with back-drilling vias is shown in Fig. 7.33. (b).

The simulation from CST software showed that the performance in a 2-4 network PCB with 1.5 mm diameter back drilling and added pads is not good, due to the impedance matching will be affected a lot by the added pads and when the diameter is larger than 1 mm, which is demonstrated in Fig. 7.34.
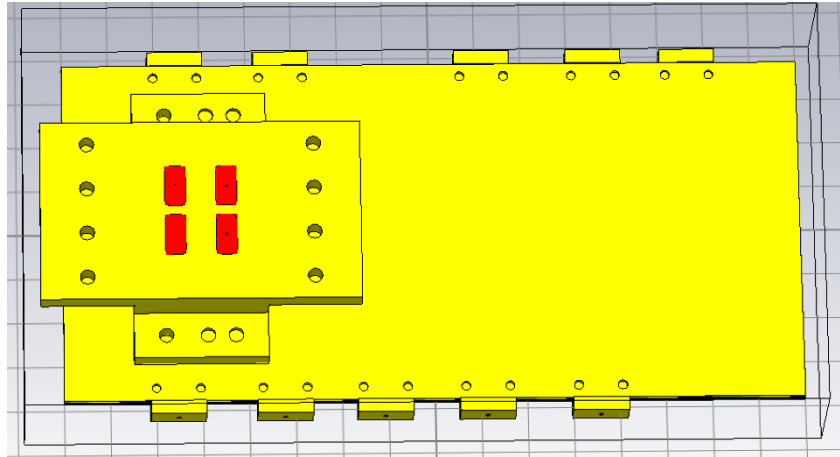
Fig. 7.32. (a) Multilayer 2-4 network PCB structure with waveguide transitions and ports.
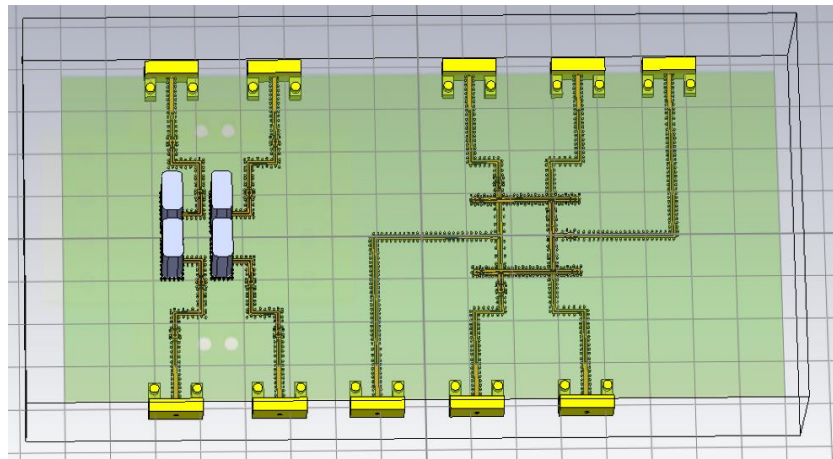
Fig. 7.32. (b) Multilayer 2-4 network PCB inner structure with ports.

Fig. 7.33. (a) Designed stackup of the 2-4 multilayer PCB SICL feeding network.
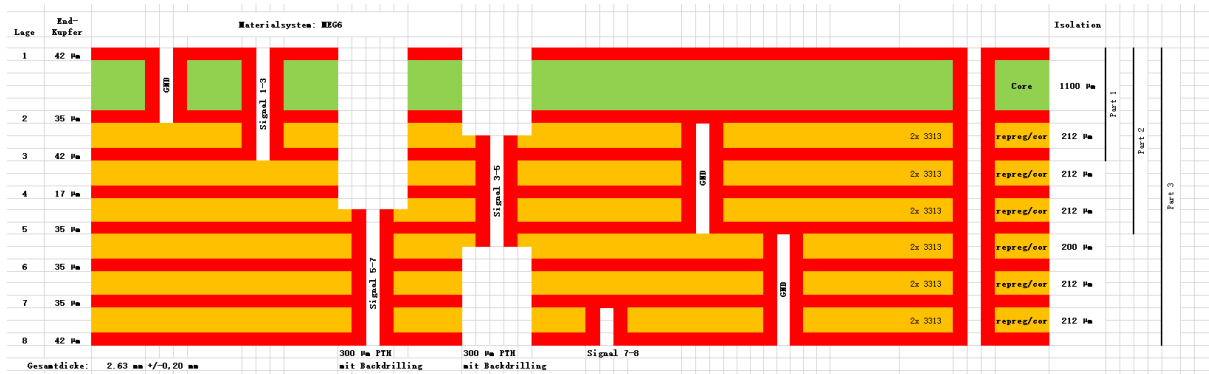
Fig. 7.33. (b) Stackup of the 2-4 multilayer PCB SICL feeding network with back-drilling vias.
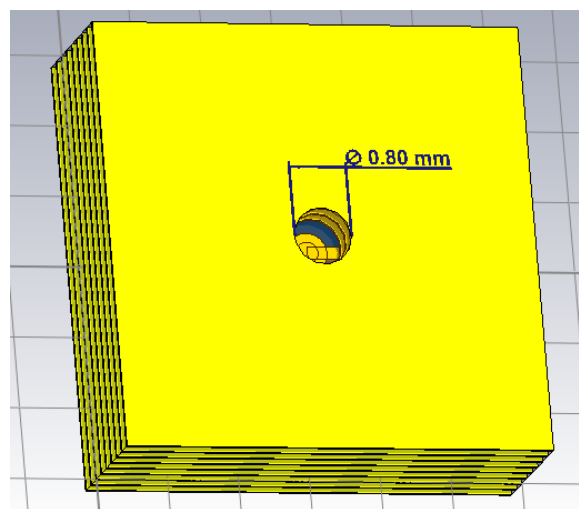
Fig. 7.34. (a) Simulated structure when the back drilling diameter is 0.8 mm and no pads were added on top and bottom of the PCB.
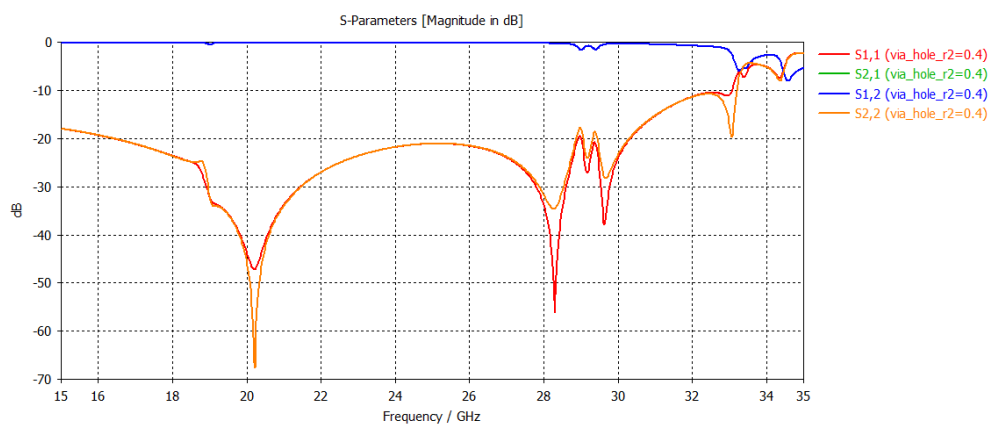
Fig. 7.34. (b) Simulated results when the back drilling diameter is 0.8 mm and no pads were added on the top and bottom of the PCB.

152
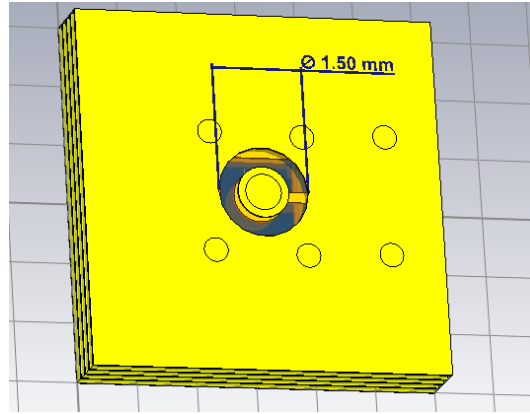
Fig. 7.34. (c) Simulated structure when the back drilling diameter is 1.5 mm and added pads on top and bottom of the PCB.
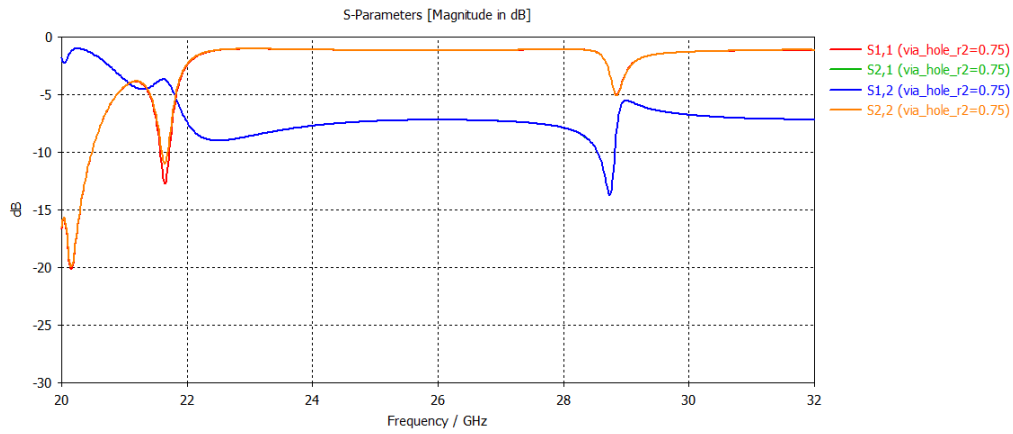
Fig. 7.34. (d) Simulated results when the back drilling diameter is 1.5 mm and added pads on top and bottom of the PCB.

Similar to the simulation, the measured s-parameters and far-field patterns demonstrated the performance of the SICL 2-4 network and the beamforming system with the 2-4 network which were affected a lot due to the back-drilling vias and the added pads. Fig. 35. (a) and (b) showed the fabricated 2-4 network and its measurement using the PNA-L device.

153
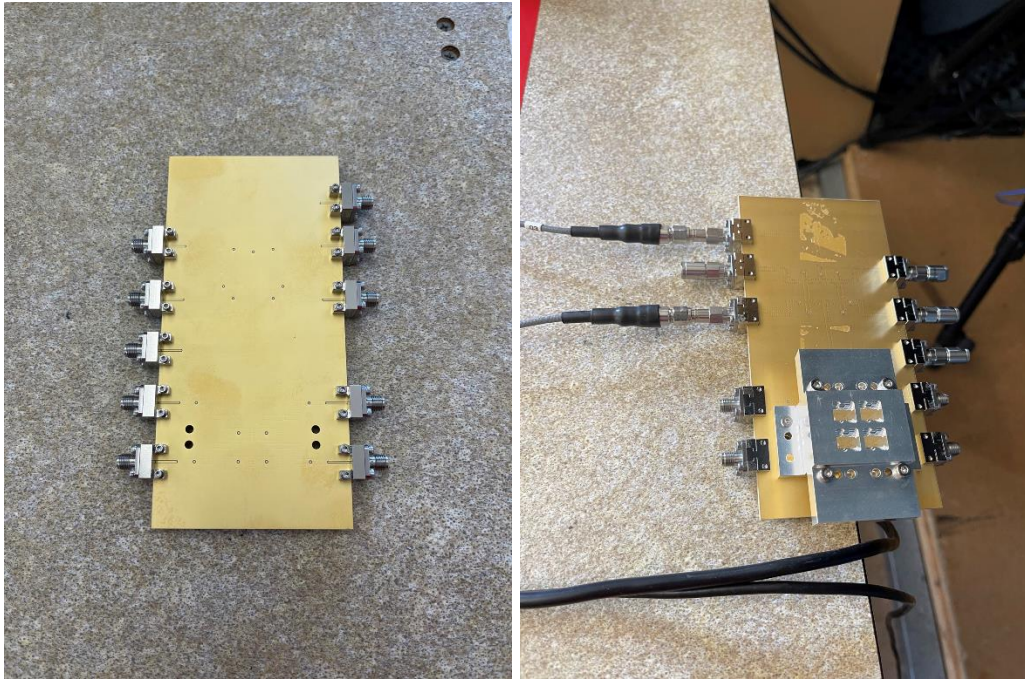
Fig. 7.35. (a) Fabricated 2-4 network PCB and (b) beamforming sample with 2-4 network PCB feeding network, waveguide transitions, and waveguide antenna array.

The measured s-parameters and far-field patterns are shown in Fig. 7.36, Fig. 7.37, and Fig. 7.38, to demonstrate that the measured performance of the 2-4 feeding network with a 1.5mm back drilling diameter and added pads is not good, which is also similar to the simulations (the measured S21 of SICL 2-4 networks already -6 dB in measurement).

The noise from the measured results is large, due to the 2-4 feeding network impedance being affected a lot by the added pads and 1.5mm diameter back drilling, which cause the beamforming system could not transmit/receive the signal well.
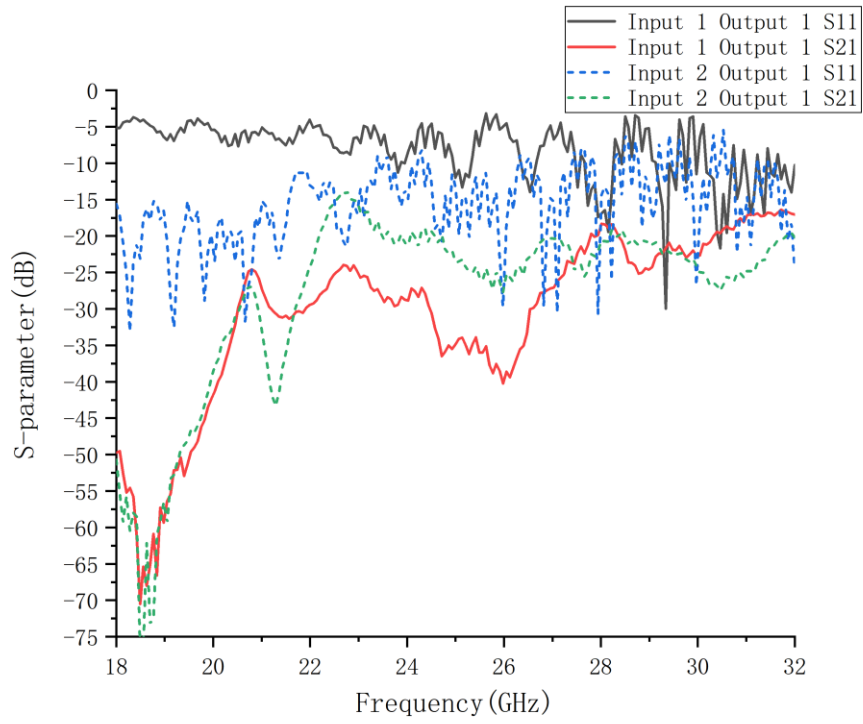
Fig. 7.36. (a) Measured s-parameters of fabricated 2-4 network when only connecting input 1/input 2 and output 1 (other 4 ports connect with 50-ohm loads).
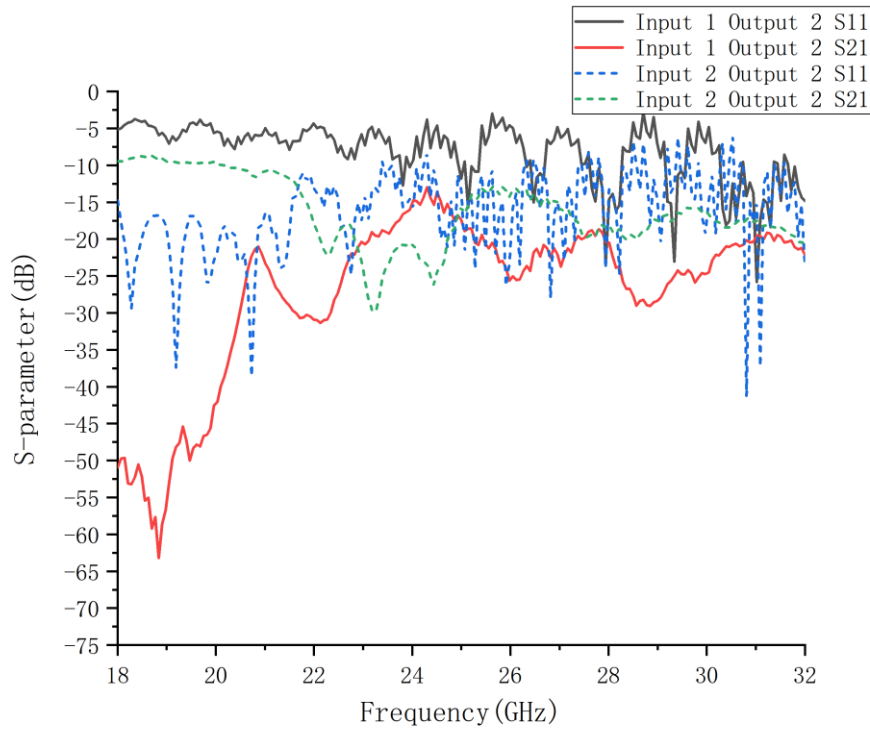
Fig. 7.36. (b) Measured s-parameters of fabricated 2-4 network when only connecting input 1/input 2 and output 2 (other 4 ports connect with 50-ohm loads).
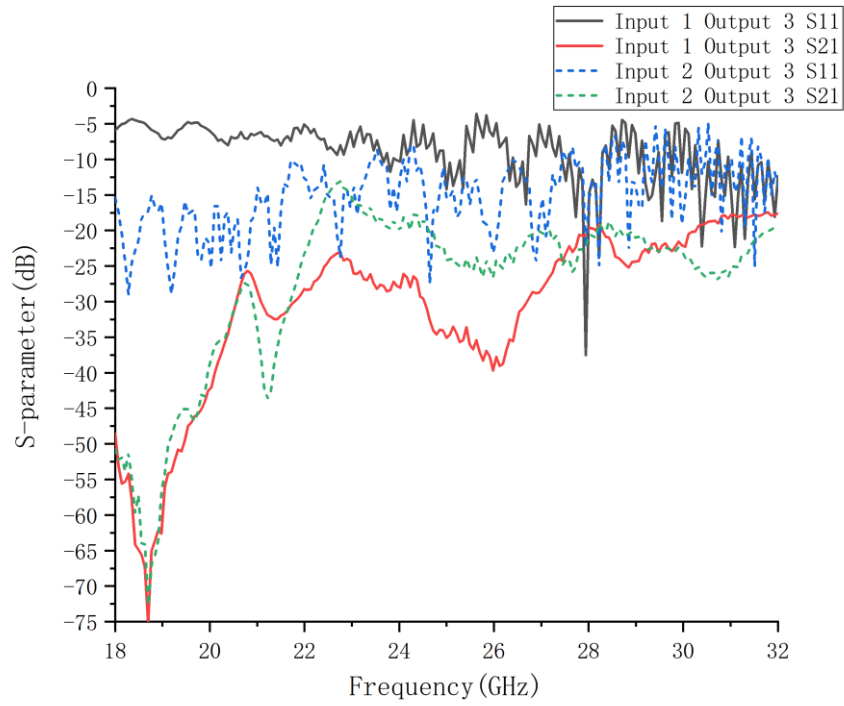
Fig. 7.36. (c) Measured s-parameters of fabricated 2-4 network when only connecting input 1/input 2 and output 3 (other 4 ports connect with 50-ohm loads).
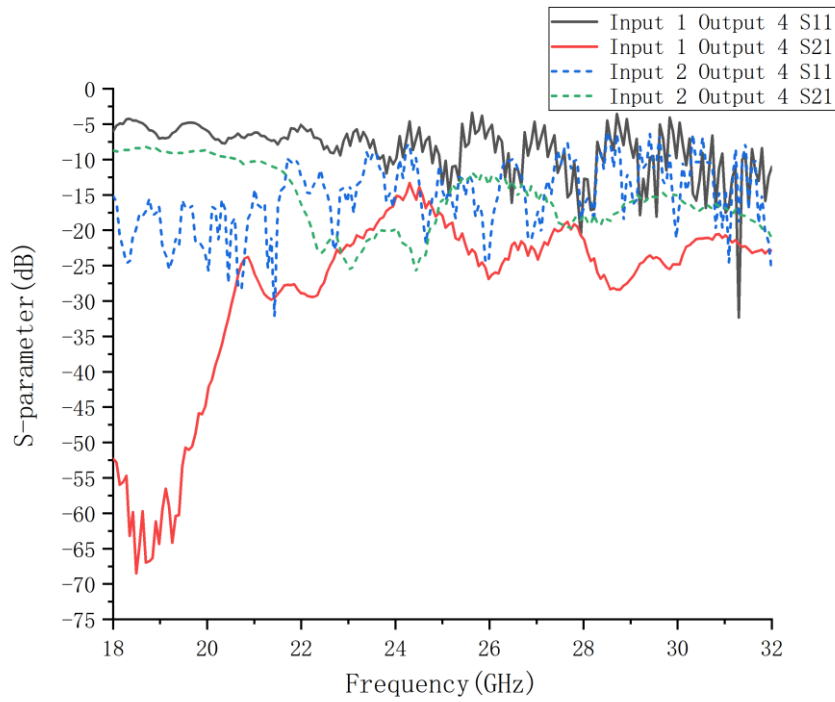
Fig. 7.36. (d) Measured s-parameters of fabricated 2-4 network when only connecting input 1/input 2 and output 4 (other 4 ports connect with 50-ohm loads).

The SICL 2-4 network beamforming far-field patterns also showed that the measured results of the beamforming system with a SICL 2-4 feeding network are not good.
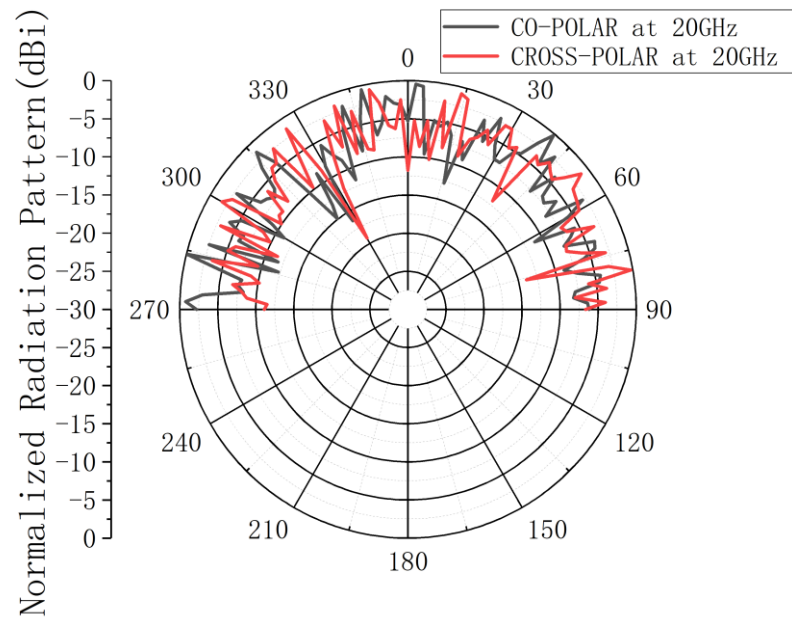
(a)
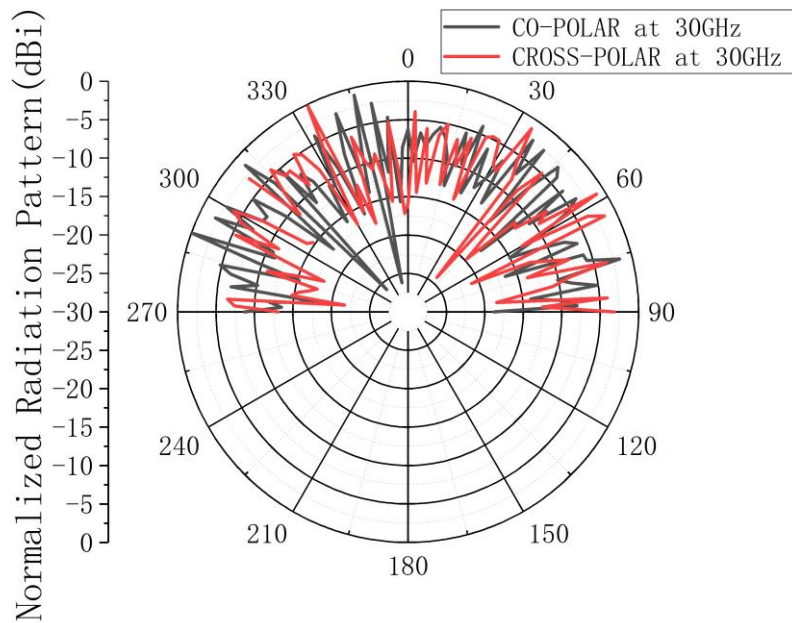
(b)

Fig. 7.37. Measured LP far-field patterns for the beamforming system with the 2-4 feeding network at (a) 20 GHz and (b) 30 GHz.
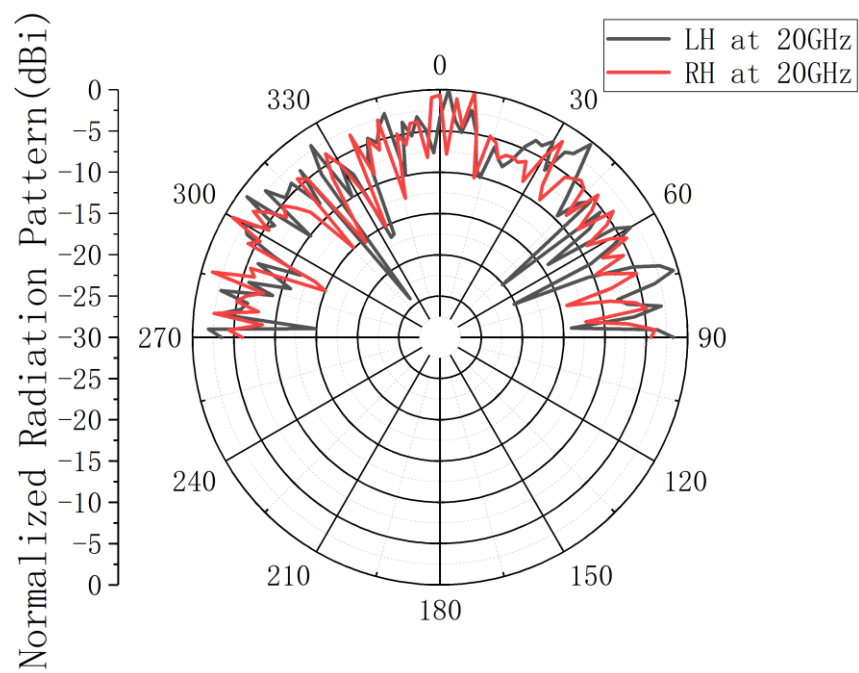
(a)
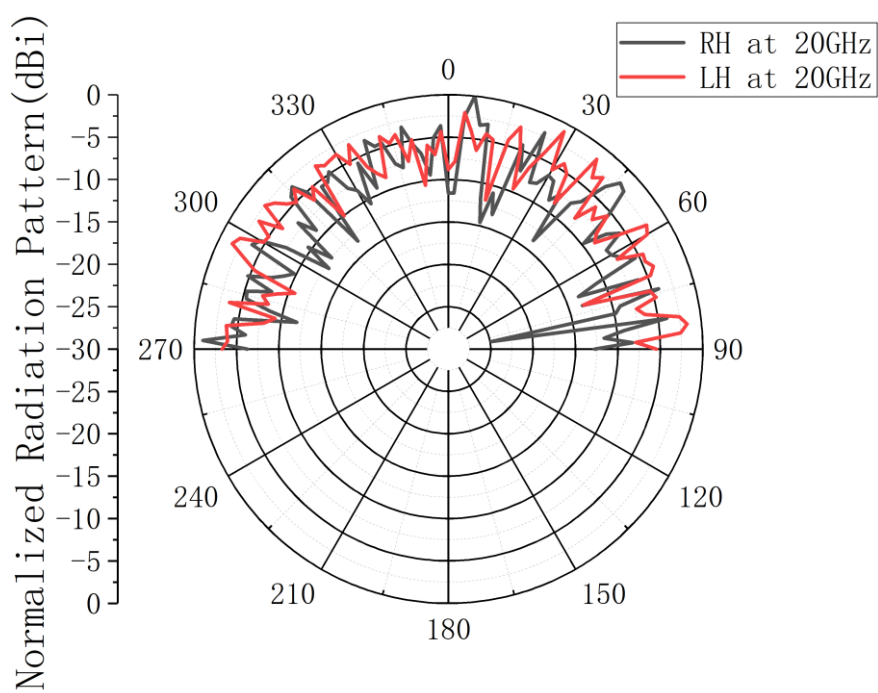
(b)
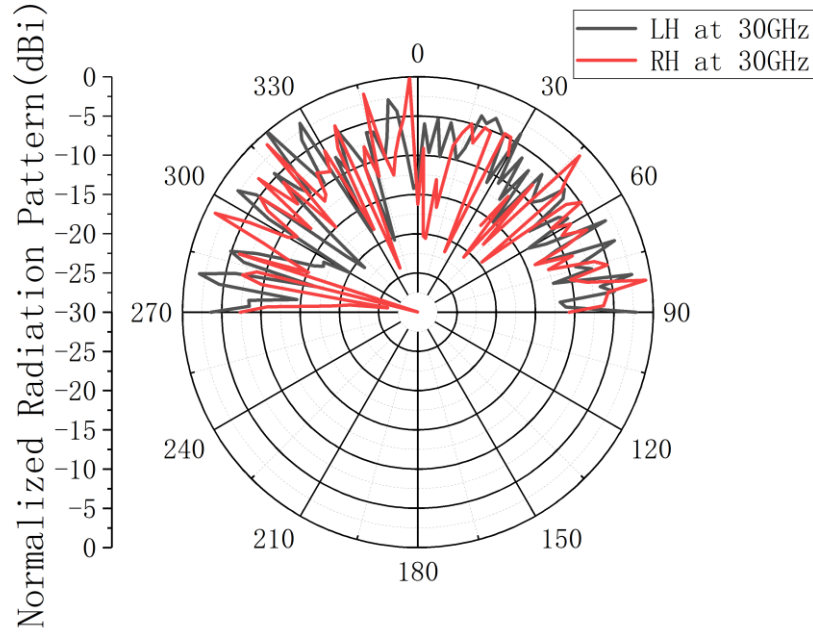
(c)
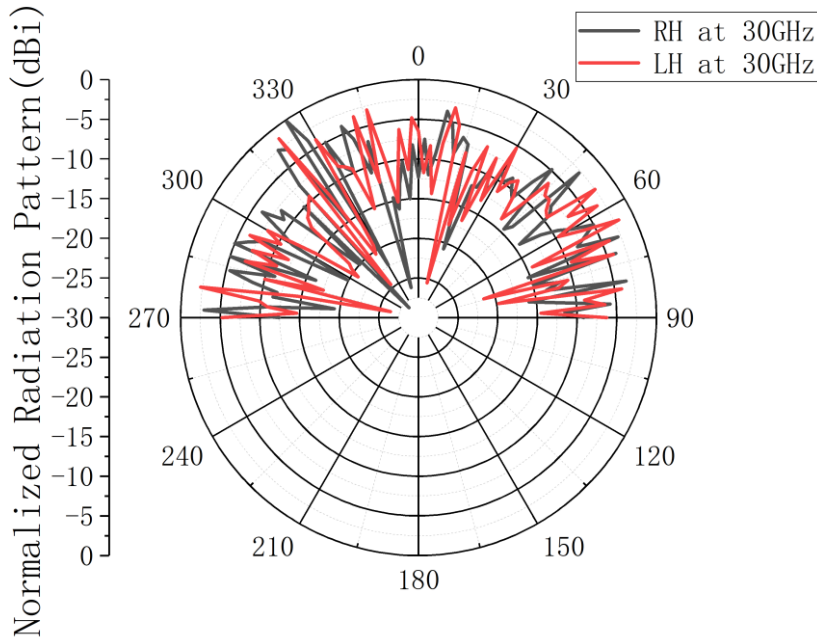
(d)

Fig. 7.38. Measured CP far-field patterns for the beamforming system with the 2-4 feeding network for (a) LH CP antenna at 20 GHz, (b) RH CP antenna at 20 GHz, (c) LH CP antenna at 30 GHz and (d) RH CP antenna at 30 GHz.

A beamforming system with a single-layer microstrip PCB feeding network (1-4 network), it has advantages in its low cost, simple stricture, and easier design and manufacture. However, the microstrip single-layer feeding network will have many

limitations on MIMO structure designing in beamforming applications and it is not suitable for massive MIMO structures with massive inputs and outputs.

For a beamforming system with a multilayer SICL PCB feeding network (2-4 network), it has advantages in the MIMO beamforming network design with more function flexibilities for multi-beam and multi-user applications, especially in a massive MIMO beamforming network with multiple inputs and hundreds of outputs. It has smaller dimensions and a compact structure which is appropriate for integration. However, the SICL multilayer PCB designs and manufacture are still very challenging and expensive when it has many kinds of buried vias and massive layers.

CHAPTER 8

CONCLUSIONS AND FUTURE WORK

8.1 Conclusion

In this thesis, a novel multiport K/Ka-band beamforming system based on the reconfigurable waveguide phased antenna array is designed, which consists of the low-profile planar feeding network, planar circuit-to-waveguide transitions, reconfigurable LP/CP dual left-handed/right-handed waveguide antenna arrays that can facilitate the integration with commercial beamforming core chips.

The waveguide structure is used for its advantages of low loss, wideband single mode operational performance, simple installation, and simple maintenance. To compensate for high loss at high-frequency applications, the antenna array is adopted, which also provided high functional flexibility in wireless communication applications with massive antenna elements to serve multi-user.

For a satellite communication application, the separated uplink and downlink system is usually adopted to reduce the influence and interference. This reconfigurable dual K/Ka-band beamforming system demonstrated its high practicability and flexibility for the separated transmitting/receiving system by using the reconfigurable waveguide structure. The reconfigurable waveguide transitions are the most critical component in this reconfigurable beamforming system to achieve dual-band functions at K/Ka-band with much better performance in bandwidth compared with the recent dual-band/dual-mode waveguide transitions.

The wideband waveguide antennas and antenna arrays are reconfigurable and replaceable to meet the design purposes and requirements for linear-polarized/left-handed circular-polarized/right-handed circular-polarized functions. The advantages of saving cost and flexible functions are provided due to the waveguide antenna array parts could achieve multi-mode operations at required frequencies in a beamforming system.

Both the waveguide transition designs and the beamforming system designs are not only suitable for satellite communication applications but also applicable for various

of the latest applications such as the 5G mobile communication and the radar system in automatic drive applications.

To reduce the power consumption, system complexity and high cost of the ADC/DAC devices for a digital beamforming network in a beamforming system with massive antenna elements, the analog beamforming or hybrid beamforming system based on the phased antenna array became more popular recently. Combined with the beamforming core chips to provide phase and gain control, this beamforming system also has the potential for high-performance beamforming designs based on the active antenna array. Moreover, to combine the advantages of analog and digital beamforming to build a hybrid beamforming architecture, this design provided analog beamforming hardware parts that could be combined with the digital beamforming devices to realize better performance in beamforming accuracy and flexibility in beamforming applications with massive antenna elements.

Although it is still challenging and not cost-efficient to manufacture and design the multilayer SICL feeding network based on the SICL power dividers, the potential and prospect for MIMO beamforming system with multilayer PCB feeding network is also demonstrated from the wideband performance of the multilayer SICL power divider and SICL-to-waveguide transitions in this thesis to get a more flexible and compact structure. The multilayer SICL power divider with loads using the embedded resistor PCB technology will also attract more attention and interest for its merits in better isolation and high tolerance in a multilayer network.

8.2 Future Work

There is some feasible and potential future work about my research and my project:

- In Chapter 4, the advantages of a power divider with good isolation are demonstrated. In the future, the power divider with the load in multilayer SICL structure based on embedded PCB resistor technology to improve the isolation is a potential and attractive field to research.

- In Chapter 7, the multilayer SICL PCB design and manufacture are still challenging, which need to use back-drilling vias to manufacture. Multilayer SICL feeding network with wideband performance and feasible solutions to design and fabricate multilayer PCBs with many types of buried vias could be an attractive research interest.

- Beamforming system with multilayer SICL feeding network combined with the phase and gain control sections (beamforming core chip) and power supply.

- Beamforming system with the multilayer SICL feeding network based on the SICL power divider with loads. Compare and analyze the advantages/disadvantages of the SICL feeding network based on the power divider with/without loads.

- Beamforming system with massive antenna array elements based on the reconfigurable structure in applications.

REFERENCES

[1] K. B. Kumar and T. Shanmuganantham, "One port to 4 port power divider using SIW technology for 60GHz applications," in 2017 IEEE Applied Electromagnetics Conference (AEMC), 19-22 Dec. 2017, pp. 1-2, doi: 10.1109/AEMC.2017.8325755.

[2] S. Mukherjee, "Design of Four-Way Substrate Integrated Coaxial Line (SICL) Power Divider for K Band Applications," in 2017 IEEE MTT-S International Microwave and RF Conference (IMaRC), 11-13 Dec. 2017, pp. 1-4, doi: 10.1109/IMaRC.2017.8449663.

[3] F. Gatti, M. Bozzi, L. Perregrini, K. Wu, and R. G. Bosisio, "A Novel Substrate Integrated Coaxial Line (SICL) for Wide-Band Applications," in 2006 European Microwave Conference, 10-15 Sept. 2006, pp. 1614-1617, doi: 10.1109/EUMC.2006.281409.

[4] A. Tiwari, U. Pattapu, and S. Das, "A wideband 1:2 T-junction power divider for antenna array with optimum results," in 2018 3rd International Conference on Microwave and Photonics (ICMAP), 9-11 Feb. 2018, pp. 1-2, doi: 10.1109/ICMAP.2018.8354594.

[5] I. Sakagami, X. Wang, M. Fujii, and M. Tahara, "Planar dual-frequency three-way Wilkinson power dividers with open-circuited stubs," in 2013 European Microwave Conference, 6-10 Oct. 2013, pp. 144-147, doi: 10.23919/EuMC.2013.6686611.

[6] S. Parvez and M. N. Mollah, "Quarter wavelength open stub band pass filter based on dumbbell annular ring resonator for UWB applications," in 2017 IEEE Region 10 Humanitarian Technology Conference (R10-HTC), 21-23 Dec. 2017 2017, pp. 827-830, doi: 10.1109/R10-HTC.2017.8289083.

[7] P. B. Saha, R. Kumar Dash and D. Ghoshal, "A Compact Uplink-Downlink Band Switchable Wideband Antenna for C-band Satellite Applications," 2020 7th International Conference on Signal Processing and Integrated Networks (SPIN), 2020, pp. 262-266, doi: 10.1109/SPIN48934.2020.9071293. J. Clerk Maxwell, A Treatise on Electricity and Magnetism, 3rd ed., vol. 2. Oxford: Clarendon, 1892, pp.68-73.

[8] S. Cakaj and K. Malaric, "Isolation measurement between uplink and downlink antennas at low earth orbiting satellite ground station," 2007 19th International Conference on Applied

Electromagnetics and Communications, 2007, pp. 1-4, doi: 10.1109/ICECOM.2007.4544490.

[9] M. Sarkar and A. Majumder, "A Novel Broadband Microstrip to Waveguide Transition atWband with High Manufacturing Tolerance Suitable for MMIC Packaging," 2018 IEEE MTT-S International Microwave and RF Conference (IMaRC), 2018, pp. 1-4, doi: 10.1109/IMaRC.2018.8877214.

[10] X. Dai, "An Integrated Millimeter-Wave Broadband Microstrip-to-Waveguide Vertical Transition Suitable for Multilayer Planar Circuits," in IEEE Microwave and Wireless Components Letters, vol. 26, no. 11, pp. 897-899, Nov. 2016, doi: 10.1109/LMWC.2016.2614973.

[11] E. Topak, J. Hasch and T. Zwick, "Compact Topside Millimeter-Wave Waveguide-to-Microstrip Transitions," in IEEE Microwave and Wireless Components Letters, vol. 23, no. 12, pp. 641-643, Dec. 2013, doi: 10.1109/LMWC.2013.2284824.

[12] A. Artemenko, A. Maltsev, R. Maslennikov, A. Sevastyanov and V. Ssorin, "Design of wideband waveguide to microstrip transition for 60 GHz frequency band," 2011 41st European Microwave Conference, 2011, pp. 838-841, doi: 10.23919/EuMC.2011.6101966.

[13] M. Jiang, W. Hong, Y. Zhang and H. Zhou, "A broadband waveguide to substrate integrated coaxial line (SICL) transition for w-band applications," 2014 Asia-Pacific Microwave Conference, 2014, pp. 70-72.

[14] Y. Chen, K. Ma and Y.Wang, "A Ka-Band Substrate Integrated Suspended Line to Rectangular Waveguide Transition," in IEEE Microwave and Wireless Components Letters, vol. 28, no. 9, pp. 744-746, Sept. 2018, doi: 10.1109/LMWC.2018.2849203.

[15] K. Erkelenz, L. P. P. B. Bohl, A. Sieganschin and A. F. Jacob, "A Compact K-/Ka-Band Rectangular-to-Coplanar Waveguide Transition With Integrated Diplexer," in IEEE Microwave and Wireless Components Letters, vol. 31, no. 6, pp. 642-645, June 2021, doi: 10.1109/LMWC.2021.3064673.

[16] H. A. Diawuo and Y. -B. Jung, "Waveguide-to-Stripline Transition Design in Millimeter-Wave Band for 5G Mobile Communication," in IEEE Transactions on Antennas and Propagation, vol. 66, no. 10, pp. 5586-5589, Oct. 2018, doi: 10.1109/TAP.2018.2854364.

[17] S. Yamaguchi et al., "Development of 28GHz band Massive MIMO Antenna RF Frontend Module for 5G," 2018 IEEE International Symposium on Antennas and Propagation & USNC/URSI National Radio Science Meeting, 2018, pp. 629-630, doi: 10.1109/APUSNCURSINRSM. 2018.8608770.

[18] H. Al-Saedi, J. K. Ali, W. M. Abdel-Wahab, S. Gigoyan and S. Safavi-Naeini, "A dual circularly polarized patch antenna for broadband millimeter wave (MMW) communication systems," 2016 IEEE International Symposium on Antennas and Propagation (APSURSI), 2016, pp. 593- 594, doi: 10.1109/APS.2016.7696005.

[19] M. Farahani, M. Akbari, M. Nedil, A. -R. Sebak and T. A. Denidni, "Millimeter-Wave Dual Left/Right-Hand Circularly Polarized Beamforming Network," in IEEE Transactions on Antennas and Propagation, vol. 68, no. 8, pp. 6118-6127, Aug. 2020, doi: 10.1109/TAP.2020.2986678.

[20] Y. Cai, Y. Zhang, Z. Qian, W. Cao and S. Shi, "Compact Wideband Dual Circularly Polarized Substrate Integrated Waveguide Horn Antenna," in IEEE Transactions on Antennas and Propagation, vol. 64, no. 7, pp. 3184-3189, July 2016, doi: 10.1109/TAP.2016.2554627.

[21] F. Bongard, M. Gimersky, S. Doherty, X. Aubry and M. Krummen, "3Dprinted Ka-band waveguide array antenna for mobile SATCOM applications," 2017 11th European Conference on Antennas and Propagation (EUCAP), 2017, pp. 579-583, doi: 10.23919/EuCAP.2017.7928705.

[22] H. -. Zhang, W. Wang, Z. Zheng, M. -. Jin, X. Fang and G. Huang, "Design of A Beamforming Circular-polarization Waveguide Antenna Array," 2018 IEEE Asia-Pacific Conference on Antennas and Propagation (APCAP), 2018, pp. 64-65, doi: 10.1109/APCAP.2018.8538115.

[23] Guru, Bhag Singh; Hüseyin R. Hızıroğlu (2004). Electromagnetic Field Theory Fundamentals, 2nd Ed. Cambridge Univ. Press. pp. 422–423. ISBN 978-1139451925.

[24] Pozar, D. M., Microwave Engineering, John Wiley & Sons, Inc., 2005, third ed., pp. 315- 322.

[25] Balanis, C.A. (2005) Antenna theory analysis and design : 3rd ed. Hoboken, N.J.: Wiley.

[26] I. J. Bahl and D. K. Trivedi, "A Designer's Guide to Microstrip Line", Microwaves, May 1977, pp. 174-182.

[27] E. O. Hammerstad (1975). Equations for Microstrip Circuit Design. 1975 5th European Microwave Conference. pp. 268–272. doi:10.1109/EUMA.1975.332206.

[28] Liu, Q., Liu, Y., Wu, Y., Shen, J., Li, S., Yu, C., & Su, M. (2013). A Substrate Integrated Waveguide to Substrate Integrated Coaxial Line Transition. Progress in Electromagnetics Research C, 36, 249-259.

[29] K. Ning, X. -C. Li and J. Mao, "A Compact Ridged Substrate Integrated Coaxial Line," 2020 IEEE MTT-S International Wireless Symposium (IWS), 2020, pp. 1-3, doi: 10.1109/IWS49314.2020.9360170.

[30] S. K. Idury and S. Mukherjee, "A Wideband DC Isolated Substrate Integrated Coaxial Line Transition for System Integration," 2020 50th European Microwave Conference (EuMC), 2021, pp. 731-734, doi: 10.23919/EuMC48046.2021.9338113.

[31] K. Dong, X. Li, K. Ning and J. Mao, "Formula Derivation of Characteristic Impedance of Substrate Integrated Coaxial Line," 2019 International Conference on Microwave and Millimeter Wave Technology (ICMMT), 2019, pp. 1-3, doi: 10.1109/ICMMT45702.2019.8992241.

[32] Q. Wu, W. Wei, H. Wang, C. Yu and W. Hong, "Approximate SICL synthesis method," 2015 Asia-Pacific Microwave Conference (APMC), 2015, pp. 1-3, doi: 10.1109/APMC.2015.7411639.

[33] M. K. Hammood, "Impedance of Stripline," Tikrit Journal of Pure Science 17 (4), 2012, ISSN: 1813 - 1662.

[34] J. R. Reid, E. D. Marsh and R. T. Webster, "Micromachined rectangular-coaxial transmission lines," in IEEE Transactions on Microwave Theory and Techniques, vol. 54, no. 8, pp. 3433-3442, Aug. 2006, doi: 10.1109/TMTT.2006.879133.

[35] J. K. Richardson, "An Approximate Formula for Calculating Z/sub 0/ of a Symmetric Strip Line (Correspondence)," in IEEE Transactions on Microwave Theory and Techniques, vol. 15, no. 2, pp. 130-131, February 1967, doi: 10.1109/TMTT.1967.1126393.

[36] S. Serpaud, S. Tran, Y. Poiré and T. Cotxet, "High speed electronics on Printed Circuit Board characterisation of embedded capacitors and resistors," 2011 8th Workshop on Electromagnetic Compatibility of Integrated Circuits, 2011, pp. 131-136.

[37] S. Rathod, S. Y. Kumar, G. Tejaswini, K. Sreenivasulu, K. S. Beenamole and K. P. Ray, "Compact Dual T/R Module Controller Board Design using Embedded Resistor Technique," 2019 International Conference on Range Technology (ICORT), 2019, pp. 1-5, doi: 10.1109/ICORT46471.2019.9069654.

[38] C. Wu, Y. Zhang, Y. Xu, B. Yan and R. Xu, "Millimeter-Wave Waveguide-to-Microstrip Transition With a Built-In DC/IF Return Path," in IEEE Transactions on Microwave Theory and Techniques, vol. 69, no. 2, pp. 1295-1304, Feb. 2021, doi: 10.1109/TMTT.2020.3041257.

[39] Z. Xu, J. Xu and C. Qian, "Novel In-Line Microstrip-to-Waveguide Transition Based on E-Plane Probe T-Junction Structure," in IEEE Microwave and Wireless Components Letters, vol. 31, no. 9, pp. 1051-1054, Sept. 2021, doi: 10.1109/LMWC.2021.3083281.

[40] Y. Ren, K. Li, F. Wang, B. Gao and H. Wu, "A Broadband Magnetic Coupling Microstrip to Waveguide Transition Using Complementary Split Ring Resonators," in IEEE Access, vol. 7, pp. 17347-17353, 2019, doi: 10.1109/ACCESS.2019.2895159.

[41] Hui-Wen Yao, A. Abdelmonem, Ji-Fuh Liang and K. A. Zaki, "Analysis and design of microstrip-to-waveguide transitions," in IEEE Transactions on Microwave Theory and Techniques, vol. 42, no. 12, pp. 2371-2380, Dec. 1994, doi: 10.1109/22.339769.

[42] "IEEE Standard for Definitions of Terms for Antennas," in IEEE Std 145-2013 (Revision of IEEE Std 145-1993) , vol., no., pp.1-50, 6 March 2014, doi: 10.1109/IEEESTD.2014.6758443.

[43] Srivastava, Sakshi & Khandelwal, Ankit & Sharma, Dr. (2014). Microstrip Patch Antenna: A Survey. IOSR Journal of Electrical and Electronics Engineering. 9. 07-13. 10.9790/1676-09420713.

[44] Nikita Sharma, Bhawana Jain, Pradeep Singla, Raj Ranjan Prasad. (2014). RECTANGULAR PATCH MICRO STRIP ANTENNA: A SURVEY. International

Advanced Research Journal in Science, Engineering and Technology. Vol. 1, Issue 3, November 2014. ISSN (Print) 2394-1588.

[45] Ashyap, Adel & Al-ashwal, Wadhah & Shire, Abdirahman & Jenu, Mohd & Zainal Abidin, Zuhairiah & Dahlan, S.H.. (2016). A comparison between rectangular and C-shapep patch antenna for bandwidth improvement at 5.2 GHz for WLAN applications. 11. 3923-3928.

[46] D. Colles and D. Arakaki, "Multi-technique broadband microstrip patch antenna design," 2014 IEEE Antennas and Propagation Society International Symposium (APSURSI), 2014, pp. 1879-1880, doi: 10.1109/APS.2014.6905266.

[47] S. Sharma, M. Kumar, H. Nigam and M. Mathur, "Dual Band Circular Patch Coplaner Microstrip Patch Antenna for X band and Ku band Applications," 2021 IEEE Indian Conference on Antennas and Propagation (InCAP), 2021, pp. 344-346, doi: 10.1109/InCAP52216.2021.9726406.

[48] H. Ai, C. Wu and S. Zhou, "Design and Simulation of Rectangular Microstrip Patch Antenna with 5Gmm-wave Coaxial Line Back-Feed and Microstrip Line Side-Feeds," 2020 5th International Conference on Information Science, Computer Technology and Transportation (ISCTT), 2020, pp. 179-182, doi: 10.1109/ISCTT51595.2020.00039.

[49] M. Burtowy, A. Paszkowski, P. Kurgan and M. Nojman, "Microstrip patch antenna with wide beamwidth for AESA TRM diagnostics," 2020 23rd International Microwave and Radar Conference (MIKON), 2020, pp. 80-83, doi: 10.23919/MIKON48703.2020.9253806.

[50] J. Saini and S. K. Agarwal, "Design a single band microstrip patch antenna at 60 GHz millimeter wave for 5G application," 2017 International Conference on Computer, Communications and Electronics (Comptelix), 2017, pp. 227-230, doi: 10.1109/COMPTELIX.2017.8003969.

[51] Xiaoang Li and Chao Li, "Design of high gain multiple U-slot microstrip patch antenna for wireless system," International Conference on Computational Problem-Solving, 2010, pp. 256-259.

[52] J. Zhang and J. Mao, "A High-Gain Ka-Band Microstrip Patch Antenna with Simple Slot Structure," 2020 International Conference on Microwave and Millimeter Wave Technology (ICMMT), 2020, pp. 1-3, doi: 10.1109/ICMMT49418.2020.9386991.

[53] W. Lin, Z. Zhang and G. Fu, "Design of a High Gain and Low Cross-Polarization Tri-Band Horn Antenna," 2018 International Conference on Microwave and Millimeter Wave Technology (ICMMT), 2018, pp. 1-3, doi: 10.1109/ICMMT.2018.8563910.

[54] A. Elboushi and A. Sebak, "High-Gain Hybrid Microstrip/Conical Horn Antenna for MMW Applications," in IEEE Antennas and Wireless Propagation Letters, vol. 11, pp. 129-132, 2012, doi: 10.1109/LAWP.2012.2184256.

[55] Y. Chen, L. Zhang, Y. He, S. -W. Wong, W. Li and S. Gao, "A Broadband High-Gain H-plane SIW Horn Antenna," 2020 International Conference on Microwave and Millimeter Wave Technology (ICMMT), 2020, pp. 1-3, doi: 10.1109/ICMMT49418.2020.9386535.

[56] H. Jamshidi-Zarmehri and M. H. Neshati, "Design and Development of High-Gain SIW H-Plane Horn Antenna Loaded With Waveguide, Dipole Array, and Reflector Nails Using Thin Substrate," in IEEE Transactions on Antennas and Propagation, vol. 67, no. 4, pp. 2813-2818, April 2019, doi: 10.1109/TAP.2019.2896445.

[57] M. Asaadi and A. Sebak, "Broadside high gain H-plane substrate integrated horn antenna for future 5G applications," 2016 IEEE International Symposium on Antennas and Propagation (APSURSI), 2016, pp. 1491-1492, doi: 10.1109/APS.2016.7696452.

[58] Y. Yin, B. Zarghooni and K. Wu, "A compact substrate integrated waveguide circularly polarized horn antenna," 2016 International Symposium on Antennas and Propagation (ISAP), 2016, pp. 394-395.

[59] W. -Y. Li, W. Chung and J. -H. Chou, "Highly-Integrated Wideband 28 GHz and 39 GHz Array Antennas for 5G Mobile Phone Applications," 2020 IEEE International Symposium on Antennas and Propagation and North American Radio Science Meeting, 2020, pp. 1581-1582, doi: 10.1109/IEEECONF35879.2020.9330360.

[60] L. Jihao, "Antenna on board package for 5G millimeter wave phased array antenna," 2020 21st International Conference on Electronic Packaging Technology (ICEPT), 2020, pp. 1-5, doi: 10.1109/ICEPT50128.2020.9202652.

[61] K. Y. Kapusuz, Y. Şen, M. Bulut, İ. Karadede and U. Oğuz, "Low-profile scalable phased array antenna at Ku-band for mobile satellite communications," 2016 IEEE International Symposium on Phased Array Systems and Technology (PAST), 2016, pp. 1-4, doi: 10.1109/ARRAY.2016.7832648.

[62] Y. C. M. Tan and N. Guan Hong, "64-Elements mmWave Detachable Phased Array Antenna for 5G 26GHz Band," 2020 IEEE International Symposium on Antennas and Propagation and North American Radio Science Meeting, 2020, pp. 1317-1318, doi: 10.1109/IEEECONF35879.2020.9329940.

[63] A. K. Pandey, "Phased Array Antenna with Beamforming Network for 5G mmWave Communication System," 2020 50th European Microwave Conference (EuMC), 2021, pp. 364-367, doi: 10.23919/EuMC48046.2021.9338222.

[64] "Die Strassburger Versuche über gerichtete drahtlose Telegraphie" (The Strassburg experiments on directed wireless telegraphy), Elektrotechnische und Polytechnische Rundschau (Electrical technology and polytechnic review [a weekly]), (1 November 1905). This article is summarized (in German) in: Adolf Prasch, ed., Die Fortschritte auf dem Gebiete der Drahtlosen Telegraphie [Progress in the field of wireless telegraphy] (Stuttgart, Germany: Ferdinand Enke, 1906), vol. 4, pages 184–185.

[65] K. Benson, "Phased Array Beamforming ICs Simplify Antenna Design, " 2019.

[66] K. Zarb-Adami, A. Faulkner, J. G. B. de Vaate, G. W. Kant and P. Picard, "Beamforming techniques for large-N aperture arrays," 2010 IEEE International Symposium on Phased Array Systems and Technology, 2010, pp. 883-890, doi: 10.1109/ARRAY.2010.5613258.

[67] Z. R. Omam, W. M. Abdel-Wahab, S. Gigoyan and S. Safavi-Naeini, "High Gain 4×4 SIW Passive Phased Array Antenna," 2020 IEEE International Symposium on Antennas and Propagation and North American Radio Science Meeting, 2020, pp. 45-46, doi: 10.1109/IEEECONF35879.2020.9329752.

[68] Y. Wei, X. Zhang, Y. Bai and L. Tang, "LFM Pulse Compression of Wideband Passive Phased Array Based on True Time Delay," 2012 International Conference on Control

Engineering and Communication Technology, 2012, pp. 436-439, doi: 10.1109/ICCECT.2012.233.

[69] L. Li, W. Hong, P. Chen, Y. Zhang, Z. Chen and W. Yang, "A planar active antenna array for hybrid phased array-MIMO system," 2014 IEEE International Wireless Symposium (IWS 2014), 2014, pp. 1-4, doi: 10.1109/IEEE-IWS.2014.6864239.

[70] S. Yamaguchi, H. Nakamizo, S. Shinjo, K. Tsutsumi, T. Fukasawa and H. Miyashita, "Development of active phased array antenna for high SHF wideband massive MIMO in 5G," 2017 IEEE International Symposium on Antennas and Propagation & USNC/URSI National Radio Science Meeting, 2017, pp. 1463-1464, doi: 10.1109/APUSNCURSINRSM.2017.8072774.

[71] D. You et al., "A Ka-Band 16-Element Deployable Active Phased Array Transmitter for Satellite Communication," 2021 IEEE MTT-S International Microwave Symposium (IMS), 2021, pp. 799-802, doi: 10.1109/IMS19712.2021.9574795.

[72] L. Jiang and H. Jafarkhani, "Multi-User Analog Beamforming in Millimeter Wave MIMO Systems Based on Path Angle Information," in IEEE Transactions on Wireless Communications, vol. 18, no. 1, pp. 608-619, Jan. 2019, doi: 10.1109/TWC.2018.2883279.

[73] V. Venkateswaran and A. van der Veen, "Analog Beamforming in MIMO Communications With Phase Shift Networks and Online Channel Estimation," in IEEE Transactions on Signal Processing, vol. 58, no. 8, pp. 4131-4143, Aug. 2010, doi: 10.1109/TSP.2010.2048321.

[74] X. Wang, J. Xu, H. Tang, N. Chen and X. Zhang, "Oversampling Based Analog Beamforming for Initial Access With a Large Number of Receive Antennas," in IEEE Transactions on Vehicular Technology, vol. 69, no. 8, pp. 8613-8626, Aug. 2020, doi: 10.1109/TVT.2020.2998122.

[75] X. Xin, Y. Qinghong, S. Zhaolin, L. Qingjiang, W. Yinan and L. Wenli, "The Realization of Digital Beamforming Based on FPGA and DSP," 2010 International Conference on Intelligent System Design and Engineering Application, 2010, pp. 713-716, doi: 10.1109/ISDEA.2010.418.

[76] A. Patyuchenko et al., "Highly integrated dual-band digital beamforming Synthetic Aperture Radar," 2015 European Radar Conference (EuRAD), 2015, pp. 1-4, doi: 10.1109/EuRAD.2015.7346222.

[77] S. Han, C. -L. I, Z. Xu and S. Wang, "Reference Signals Design for Hybrid Analog and Digital Beamforming," in IEEE Communications Letters, vol. 18, no. 7, pp. 1191-1193, July 2014, doi: 10.1109/LCOMM.2014.2317747.

[78] M. C. Tan, M. Li, Q. H. Abbasi and M. Imran, "A Flexible Low-Cost Hybrid Beamforming Structure for Practical Beamforming Applications," 2019 IEEE International Symposium on Radio-Frequency Integration Technology (RFIT), 2019, pp. 1-3, doi: 10.1109/RFIT.2019.8929162.

[79] R. Singh and P. Chawla, "Performance Analysis of Hybrid Beamforming Algorithm for massive MIMO," 2021 2nd International Conference for Emerging Technology (INCET), 2021, pp. 1-4, doi: 10.1109/INCET51464.2021.9456265.

[80] M. N. Hamdy, "Beamformers Explained," pp. 11-12.

[81] P. K. Bailleul, "A New Era in Elemental Digital Beamforming for Spaceborne Communications Phased Arrays," in Proceedings of the IEEE, vol. 104, no. 3, pp. 623-632, March 2016, doi: 10.1109/JPROC.2015.2511661.

[82] S. Zhang, C. Guo, T. Wang and W. Zhang, "ON–OFF Analog Beamforming for Massive MIMO," in IEEE Transactions on Vehicular Technology, vol. 67, no. 5, pp. 4113-4123, May 2018, doi: 10.1109/TVT.2018.2789661.

[83] H. Chahrour, S. Rajan, R. Dansereau and B. Balaji, "Hybrid beamforming for interference mitigation in MIMO radar," 2018 IEEE Radar Conference (RadarConf18), 2018, pp. 1005-1009, doi: 10.1109/RADAR.2018.8378698.

[84] S. -L. Ju, N. -I. Kim, S. -Q. Lee, J. Kim and K. -S. Kim, "Hybrid Beamforming Scheme for Millimeter-wave Massive MIMO and Dense Small Cell Networks," 2019 25th Asia-Pacific Conference on Communications (APCC), 2019, pp. 301-304, doi: 10.1109/APCC47188.2019.9026487.

[85] Y. Wei, C. Arnold and J. Hong, "A K/Ka-Band Substrate Integrated Coaxial Line Power Divider for 4-input and 16-output Beamforming Multi-Layer Feeding Network," 2020 IEEE Asia-Pacific Microwave Conference (APMC), 2020, pp. 929-931, doi: 10.1109/APMC47863.2020.9331438.

[86] ANALOG DEVICES ADAR3000 documentation.

https://www.analog.com/en/products/adar3000.html.

[87] ANALOG DEVICES ADAR3001 documentation.

https://www.analog.com/en/products/adar3001.html

[88] Yan, Z., Ma, Z., Shi, G. and Che, M. (2013) 'A Novel Segmented Modeling Method of Via including the Effect of Power/Ground Plane Pair', International journal of antennas and propagation, 2013, pp. 1–16. doi:10.1155/2013/389516.

[89] J. R. Montejo-Garai, L. Marzall and Z. Popovi´c, "Octave Bandwidth High-Performance Microstrip-to-Double-Ridge-Waveguide Transition," in IEEE Microwave and Wireless Components Letters, vol. 30, no. 7, pp. 637-640, July 2020, doi: 10.1109/LMWC.2020.3000283.

[90] M. A. Nasr and A. A. Kishk, "Vertical Coaxial-to-Ridge Waveguide Transitions for Ridge and Ridge Gap Waveguides With 4:1 Bandwidth," in IEEE Transactions on Microwave Theory and Techniques, vol. 67, no. 1, pp. 86-93, Jan. 2019, doi: 10.1109/TMTT.2018.2873312.

[91] C. Wang, Y. Yao, J. Wang, X. Cheng, J. Yu and X. Chen, "A Wideband Contactless CPW to W -Band Waveguide Transition," in IEEE Microwave and Wireless Components Letters, vol. 29, no. 11, pp. 706-709, Nov. 2019, doi: 10.1109/LMWC.2019.2945242.

[92] Y. Ding, Y. Jin, G. Zhu, Z. Zou, E. Ren and G. Yang, "A K-band Wideband Low Insertion Loss SIW-to-Waveguide Transition," 2021 IEEE 4th International Conference on Electronics Technology (ICET), 2021, pp. 692-695, doi: 10.1109/ICET51757.2021.9451100.

[93] J. Jakob, R. Sammer, F. X. Röhrl, W. Bogner and S. Zorn, "WR12 to planar transmission line transition on organic substrate," 2019 49th European Microwave Conference (EuMC), 2019, pp. 288-291, doi: 10.23919/EuMC.2019.8910843.

[94] E. Hassan et al., "Multilayer Topology Optimization of Wideband SIWto-Waveguide Transitions," in IEEE Transactions on Microwave Theory and Techniques, vol. 68, no. 4, pp. 1326-1339, April 2020, doi: 10.1109/TMTT.2019.2959759.

[95] E. Arnieri, F. Greco, L. Boccia, C. Mustacchio and G. Amendola, "Dual Band Topside Waveguide-to-Stripline Transition in Multilayer Substrate," 2021 IEEE International Symposium on Antennas and Propagation and USNC-URSI Radio Science Meeting (APS/URSI), 2021, pp. 691-692, doi: 10.1109/APS/URSI47566.2021.9703769.

[96] S. Ghosh and M. Dadel, "Horn Antenna using Substrate Integrated Waveguide: Design of H-Plane X-Band Horn Antenna," 2016 International Conference on Wireless Communications, Signal Processing and Networking (WiSPNET), 2016, pp. 661-664, doi: 10.1109/WiSPNET.2016.7566215.

[97] F. Filice, N. Nachabe, C. Luxey and F. Gianesello, "3D-Printed Double-Ridged Waveguide Array Antenna targeting High-Efficiency Ku-band SatCom on The Move Applications," 2019 USNC-URSI Radio Science Meeting (Joint with AP-S Symposium), 2019, pp. 17-18, doi: 10.1109/USNC-URSI.2019.8861755.

[98] S. Bhardwaj and J. L. Volakis, "Circularly-polarized horn antennas for terahertz communication using differential-mode dispersion in hexagonal waveguides," 2017 IEEE International Symposium on Antennas and Propagation & USNC/URSI National Radio Science Meeting, 2017, pp. 2571-2572, doi: 10.1109/APUSNCURSINRSM.2017.8073328.